Development of a Hypersonic Aerothermoelastic Framework and Its Application to Flutter and Aerothermoelastic Scaling of Skin Panels

by

Daning Huang

A dissertation submitted in partial fulfillment
of the requirements for the degree of
Doctor of Philosophy
(Aerospace Engineering)
in the University of Michigan
2019

Doctoral Committee:

Professor Peretz P. Friedmann, Chair
Professor Carlos E. S. Cesnik
Professor Bogdan Epureanu
Professor Joaquim R. R. A. Martins

Daning Huang

dnhuang@umich.edu

ORCID iD: 0000-0001-7049-3494

To future humans as a multi-planetary species.

Acknowledgments

This dissertation marks a significant milestone in my career. I wish to thank all who made this work possible.

First, I wish to sincerely thank my advisor Professor Peretz Friedmann for his guidance and support throughout my graduate studies. His wisdom and insights have significantly influenced my research philosophy and prepared me better to become an independent researcher. I am grateful to the members of my doctoral committee, Professor Carlos Cesnik, Professor Joaquim Martins, and Professor Bogdan Epureanu, for their time and effort spent on this research. Particularly, Prof. Cesnik is the first person to introduce me into the field of aeroelasticity and has continuously supported my academic career; Prof. Martins has been very helpful and responsive to my technical and academic requests over the years; Prof. Epureanu's students have provided valuable insights into my research. I would also like to thank the Aerospace faculty, especially Profs. Anthony Waas and Karthik Duraisamy, for their help in my academic career.

This research was funded through the Francois-Xavier Bagnoud Center for Rotary and Fixed Wing Air Vehicle Design. Partial support was provided by the Rackham Predoctoral Fellowship awarded by the University of Michigan.

I would like to express my gratitude to the Multidisciplinary Design Optimization Laboratory, led by Prof. Martins, for allowing me to use the ADflow code; also to Dr. Gaetan Kenway and Eirikur Jonsson for their professional help and advice in computational aeroelasticity and general software engineering. Dr. Tomer Rokita, who I had the privilege to work with for the past few years, is deeply thanked for his insight and friendship. Prof. Jack McNamara and Dr. Ahbijit Gogulapati are acknowledged for their help and advice concerning aerothermoelasticity. Dr. Ryan Klock is thanked for providing me with ABAQUS user functions for aerothermoelastic analysis. I would like to thank all my colleagues in my research group with Prof. Friedmann, for their continued support and understanding throughout our years together: Dr. Michael Chia, Dr. Nicolas Lamorte, Dr. Eric Muir, Dr. Ashwani Padthe, Ryan Patterson, Abhinav Sharma, and Puneet Singh. I would also like to express my appreciation for the kindness and helpfulness of the Aerospace Department staff, especially Denise Phelps, who has been of great help and constant support with the administrative affairs.

I am also grateful to the friends here at the University of Michigan and across the world for enlightening interactions and friendship. I decided not to put any names here - an exhaustive list would be too long for this section while any omissions would be unfair and inappropriate. The life has been amazing. As a chaotic dynamical system, it brings about the crossing of our trajectories that originate from different parts of the world.

Finally, I owe immense gratitude to my parents, Guanle Huang and Minjian Pan, for bringing me to this exciting world and helping me get this far. Last but certainly not least, I thank my significant other, Junyi Geng, for her unwavering love, support, and understanding, since our encounter a decade ago.

TABLE OF CONTENTS

LIST OF FIGURES

FIGURE

LIST OF TABLES

TABLE

LIST OF APPENDICES

APPENDIX

LIST OF ACRONYMS

2D Two-Dimensional

3D Three-Dimensional

ADflow Automatic Differentiation flow

ALE Arbitrary Lagrangian-Eulerian

AM Analytical Models

ARMA Auto Regressive Moving Average

ASL Aerothermoelastic Scaling Laws

BHCJ Boeing Hypersonic Commercial Jet

BL Boundary Layer

BO Bayesian Optimization

CC Cox-Crabtree

CFD Computational Fluid Dynamics

CSD Computational Structural Dynamics

DCS9 Doubly-Curved Shallow 9-noded shell element

DNS Direct Numerical Simulation

DOFs Degrees Of Freedom

EE Eckert's reference Enthalpy method

EGO Efficient Global Optimization

EI Expected Improvement

FE Finite Element

FSDT First-order Shear Deformation Theory

FSI Fluid-Structure Interaction

FSTI Fluid-Structural-Thermal Interaction

GCL Geometric Conservation Law

GEP Generalized Eigenvalue Problem

HTF Hypersonic Tunnel Facility

HVEI HyperVolume Expected Improvement

HVLCB HyperVolume Lower Confidence Bound

HVPoI HyperVolume Probability of Improvement

HTSH Heat Transfer in shallow SHell element

HYPATE HYPersonic AeroThermoElasticity simulation environment

LC Loosely-Coupled

LCB Lower Confidence Bound

LCO Limit Cycle Oscillation

LES Large Eddy Simulation

LS Linearized Supersonic theory

LSA Linearized Stability Analysis

LTLT Layer-wise Thermal Lamination Theory

MO Multi-objective Optimization

MOBO Multi-Objective Bayesian Optimization

NASP National AeroSpace Plane

NRMSE Normalized Root-Mean-Squared Error

NS Navier-Stokes

ODE Ordinary Differential Equation

OLH Optimal Latin Hypercube

PEP Polynomial Eigenvalue Problem

PGMRES Preconditioned Generalized Minimal RESidual method

POD Proper Orthogonal Decomposition

PoI Probability of Improvement

PSD Power Spectral Density

PT Piston Theory

RANS Reynolds-Averaged Navier Stokes

ROM Reduced Order Model

SA Spalart-Allmaras

SBO Surrogate-Based Optimization

SO Single-objective Optimization

TC Tightly-Coupled

TPS Thermal Protection System

WM Weighted Metric

WS Weighted Sum

LIST OF SYMBOLS

Latin Symbols

$\mathbf{A}, A_{xx}$	Extensional stiffness matrix for composite shell and its first element
A_1, A_2	Differential coefficients of a doubly-curved shell
$\mathbf{a}, \mathbf{b}$	Modal coordinates of structural and thermal distributions, respectively
a, b	Panel dimensions
a_∞	Speed of sound
$\mathbf{B}, B_{xx}$	Extension-bending stiffness matrix for composite shell and its first element
Bi	Biot number
$\bar{B}$	Nose bluntness similarity parameter
$\mathbf{C}$	Damping matrix
$\mathbf{C}_A$	Aerodynamic damping matrix
$\mathbf{C}_T$	heat capacity matrix
C	Acquisition function
$\mathbf{c}$	Flight conditions
$\mathbf{c}_E, \mathbf{c}_I$	Equality and inequality constraints
c_v, c_p	Specific heat capacities at constant volume and at constant pressure, respectively
c_u, c_T	Weights for structural and thermal objectives
$\mathbf{D}, D_{xx}$	Bending stiffness matrix for composite shell and its first element
$\mathcal{D}$	Data set
$\mathbf{d}$	Design variables
d	Radius of the blunt nose of a slender body
d_{CFD}	Distance between two CFD solutions
$\mathbb{E}$	Statistical expectation
E	Young's modulus
δE	Artificial energy of a coupling scheme
$\mathbf{F}_I, \mathbf{F}_T$	Internal and thermal force vectors
$\mathbf{F}_c, \mathbf{F}_v$	Discretized convective and viscous fluxes in the RANS equations
$\mathcal{F}$	Pareto front
$\overline{\mathcal{F}}$	Pareto set, i.e. a set of Pareto optimal solutions
F_c, F_d, F_s	Convective, diffusive, and source fluxes in the RANS equations
Fo	Fourier number
$\mathbf{f}$	Regression function in kriging
$\mathbf{f}^{cor}$	Correction function in fluid ROM
f_1	The lowest natural frequency of a structure
$\mathbf{G}$	Stiffness matrices in lamina constitutive relation

$\mathbf{H}$	Interpolation matrix for information exchange
$\mathcal{H}$	Hypervolume of Pareto front
H	Altitude
$\mathbf{h}, h_i$	Thicknesses of lamina of a composite shell, and the ith laminae
h	Shell thickness
h_c	Heat convection coefficient
$\mathbf{I}$	Identity matrix or tensor
$\mathcal{I}$	Improvement function
I_1, I_2, I_3	Moments of inertia of the composite shell
$I_{\mathcal{H}}$	Hypervolume indicator of Pareto front
$\mathbf{J}$	Vector of objectives
J_u, J_T, J_s	Errors in the nondimensional aerothermoelastic response
$\mathbf{K}_A$	Aerodynamic stiffness matrix
$\mathbf{K}_L, \mathbf{K}_N$	Linear and nonlinear components of a stiffness matrix
$\mathbf{K}_T$	Thermal conductivity matrix
$\mathbf{k}, k$	Thermal conductivity
k_F	Force ratio
$\mathbf{L}$	Interpolation matrices in finite element formulation
$\mathbf{L}_{\mathbf{\Phi}}$	Cholesky decomposition of a symmetric matrix $\mathbf{\Phi}$
L	Characteristic length
L_{le}	Length of rigid wall upstream of the panel
l_1, l_2	Distance between stiffeners in 1- and 2-directions
$\mathbf{M}$	Mass matrix
$\mathbf{M}_E$	Elastic internal in-plane moments
$\mathbf{M}_T, M_{Tx}$	Thermal internal in-plane moments and the first element
M	Mach number
M_n	Normal Mach number
$\mathbf{N}_E$	Elastic internal in-plane forces
$\mathbf{N}_T, N_{Tx}$	Thermal internal in-plane forces and the first element
$\mathcal{N}$	Gaussian distribution
N	Shape function
N_b	Number of nodes on boundary
N_d, N_y	Dimensions of input and output vectors, respectively
N_F	Number of flight conditions
N_i	Number of iterations
N_S, N_T	Numbers of structural and thermal modes, respectively
N_s	Number of samples
N_t	Number of time steps
$\mathbf{n}$	Normal vector
$\mathbf{P}$	Preconditioner
P	Probability
Pr	Prandtl number
p	Pressure
p_I, p_O	In-phase and out-of-phase pressure components
$\mathbf{Q}$	Stiffness matrix in lamina constitutive relation

$\mathbf{Q}_I = \mathbf{K}_T\mathbf{T}$	Internal heat flux vector
$\mathbf{Q}_T$	Thermal loading vector
q	Dynamic pressure
$\dot{\mathbf{q}}, \dot{q}$	Heat flux
$\mathbf{R}, \mathbf{r}, r$	Correlation function in kriging
$\mathcal{R}$	Residual
R	Universal gas constant
R_i	Curvature in i direction
R_{12}	Stiffness ratio
R_δ	Coefficient for boundary layer correction
r_f	Recovery factor
$\boldsymbol{Re}$	Reynolds number
$\mathbf{S}, S_{xx}$	Transverse shear stiffness matrix for composite shell and its first element
$\mathcal{S}, \mathcal{S}_g$	Function for combining multiple objectives
St	Stanton number
$\mathbf{T}, T$	Temperature
$\mathbf{T}_E$	Transverse shear force
$\mathbf{T}_w, T_w$	Wall temperature
$\mathcal{T}$	Kinetic energy
T_{ini}	Initial temperature
T_{rad}	Radiation temperature
T_{cr}	Temperature associated with the first buckling mode
ΔT	Temperature increase
t	Time
t_1, t_2	Thickness of stiffeners in 1- and 2-directions
t_{AE}, t_{AT}	Aeroelastic and aerothermal characteristic times
t_{CFD}	Computational cost of CFD
t_F, t_S, t_T	Characteristic times for the fluid, structural and thermal responses
Δt	Time step size
$\mathbf{U}, U$	Cell volume
$\mathcal{U}$	Strain energy
$\mathbf{u}$	Structural displacements
$\mathbf{u}_F, u_F$	Deformation of the wall boundary in the fluid problem
u, v, w	Displacements of a shell
$\mathbf{V}, V$	Flow velocity
$\mathbf{v}_g, v_g$	Mesh velocity
$\mathcal{W}$	External work
$\mathbf{w}, w$	Solutions of RANS equations
$\mathbf{x} = [x, y, z]$	Cartesian coordinates
$\mathbf{y}$	Output vector
y^+	Dimensionless wall distance
Z	Local deviation in kriging
Δz	Grid size in wall-normal direction

Greek Symbols

$\boldsymbol{\alpha}, \alpha$	Thermal expansion coefficients
$\bar{\alpha}$	Coefficient for the Crank-Nicolson method
$\alpha^f, \alpha^m, \bar{\beta}, \bar{\gamma}, \bar{\rho}$	Coefficients for the generalized-α method
$\boldsymbol{\beta}_f, \boldsymbol{\beta}_r$	Coefficient matrices in kriging
β	Flow orientation angle
$\boldsymbol{\gamma}$	Transverse shear strain on the middle surface
γ	Heat capacity ratio
δ	Boundary layer thickness
$\delta_{,x}$	Slope of boundary layer thickness distribution in stream-wise direction
$\boldsymbol{\epsilon}$	Membrane strain of the shell
ϵ	Error
ε	Surface emissivity
ζ	Damping, real part of the eigenvalue of an aerothermoelastic mode
ζ_M, ζ_K	Coefficients for proportional damping
θ	Inclination angle
ϑ, φ	Coefficients in mesh interpolation scheme
$\boldsymbol{\kappa}, \bar{\boldsymbol{\kappa}}$	Normal velocity of CFD mesh cell face, and its weighted average
κ	Shear correction factor
$\bar{\lambda}_F$	Nondimensional dynamic pressure
$\boldsymbol{\Lambda}_p, \boldsymbol{\Lambda}_u$	Diagonal matrices in the Jacobians associated with fluid reduced-order model
λ	Bulk viscosity
λ_g, λ_p	Eigenvalues of GEP and PEP, respectively
$\boldsymbol{\mu}$	Mean of Gaussian distribution
μ	Viscosity
$\boldsymbol{\nu}, \bar{\boldsymbol{\nu}}$	Normal of CFD mesh cell face, and its weighted average
ν	Poisson's ratio
$\bar{\Xi}$	Boundary layer similarity parameter
ξ	Geometric scale
ρ	Density
$\boldsymbol{\Sigma}, \boldsymbol{\sigma}$	Covariance matrix of Gaussian distribution, and the vector of standard deviations
$\boldsymbol{\sigma}_E$	In-plane stress of the shell
σ	Standard deviation in Gaussian distribution
σ_b	Stefan-Boltzmann constant
$\boldsymbol{\tau}_E$	Transverse shear stress of the shell
$\boldsymbol{\tau}$	Viscous stress tensor
υ	Coefficient for exploitation-exploration balance
$\boldsymbol{\Phi}$	Jacobian of a residual function
$\boldsymbol{\phi}$	Residual vector
Φ, ϕ	Cummulative and probabilistic density functions, respectively
$\boldsymbol{\chi}$	Curvature strain on the middle surface
$\chi, \tilde{\chi}$	Moving and stationary CFD meshes, respectively

$\mathbf{\Psi}$	Projection matrix whose columns are orthonormal
Ψ	Gas specific energy
ψ	Gas specific internal energy
ψ_x, ψ_y	Rotational displacements in the shell
ω	Frequency, imaginary part of the eigenvalue of an aerothermoelastic mode

Subscripts

aw	Quantities related to adiabatic wall
e	Quantities at the edge of boundary layer
ext	Quantities related to external loading
F	Quantities related to the fluid solution
le	Distance from leading edge
P	Quantities related to the POD method
ref	Quantities for reference
S	Quantities related to the structural solution
T	Quantities related to the thermal solution
w	Quantities related to the wall boundary condition of the NS equations
∞	Quantities related to freestream
0	Quantities related to stagnation state

Superscripts

c	Matrices and vectors for constraints in finite element formulation
E	Estimated quantities
e	Quantities related to a finite element
f	Properties of the fluid
h	Homogenized quantities
krg	Quantities related to the kriging method
m	Quantities related to the scaled model
$n-1, n, n+1$	Quantities at time steps $n-1$, n, $n+1$, respectively
p	Quantities related to the prototype
pk	Quantities related to the POD-kriging method
qs	Quasi-steady components
s	Properties of the solid
std	Steady components
sur	Quantities related to surrogate
u	Unconstrained matrices and vectors in finite element formulation
uns	Unsteady components

Others

$\widehat{\square}$	Reference quantity for non-dimensionalization
$\overline{\square}$	Non-dimensional quantity
$\square'$	Quantities related to turbulence

$[\Box]_i$	The ith component of a vector
$O(\Box)$	On the order of a quantity
$\dfrac{\mathrm{D}\Box}{\mathrm{D}t}$	Material derivative, defined in Eq. (2.2)
$\dot{\Box} = \dfrac{\mathrm{d}\Box}{\mathrm{d}t}$	Time derivative
$\mathring{\Box}$	Derivative with respect to nondimensional time
$\|\|\mathbf{f}\|\| = (\sum_i f_i^2)^{1/2}$	The l^2 norm

ABSTRACT

In the past decade, there has been a strong interest in reusable air-breathing hypersonic vehicles for in both civil and military applications. However, there are still the unresolved technical challenges associated with this class of vehicles, and one of the challenges is hypersonic aerothermoelasticity. Enhancing the understanding of the aerothermoelastic behavior of hypersonic structures is the ultimate goal of this dissertation.

A computational framework is developed for efficient and accurate aerothermoelastic simulation over extended flight time. The framework is accelerated using two novel techniques. First, the fluid solver is accelerated using a reduced order model augmented with a correction and scaling technique, which accounts for non-uniform temperature distribution, varying flight conditions, and geometric scales. Secondly, a tightly-coupled scheme and linearized stability analysis are developed to enable near-real-time aerothermoelastic simulation of extended flight time and automatic identification of aerothermoelastic instabilities, respectively. The computational framework is applied to study the aeroelastic and aerothermoelastic response of a generic skin panel. The effects of aspect ratio and boundary layer thickness are found to have a significant influence on the critical flutter parameter and the aerothermoelastic stability boundary, i.e. the time elapsed before the onset of structural failure. Furthermore, a proper combination of flow orientation angle and material orientation can significantly extend the aerothermoelastic stability boundary.

Subsequently, an optimization framework is developed for generating hypersonic aerothermoelastic scaling laws using a novel two-pronged approach, which combines the classical dimensional analysis with augmentation from numerical simulations of the specific problem. From the comparison and adjustment of the full-scale prototype and the scaled model,

the "numerical similarity solutions" are generated to replace the analytical similarity solutions for refinement of the scaling laws. The search for an aerothermoelastically scaled model is formulated as a multi-objective optimization problem, which is solved using a surrogate-based optimization algorithm. The effectiveness of the two-pronged approach is demonstrated by its application to the refined hypersonic aerothermoelastic scaling of a composite skin panel configuration.

This study represents a substantial contribution toward an improved understanding of the aeroelastic and aerothermoelastic behavior of hypersonic skin panels. The findings provide practical implication on the structural design of hypersonic vehicles. Furthermore, the demonstration of the numerical scaling approach shows that it can be eventually applied to testing various components of a hypersonic vehicle. It has the potential for saving considerable funds in the development process of future hypersonic vehicles by replacing some flight tests with wind tunnel experiments.

CHAPTER 1

Introduction, Background and Objectives

1.1 Challenges in Air-Breathing Hypersonic Flight

Air-breathing hypersonic vehicles have the potential to revolutionize global transportation by vastly reducing the traveling time between distant locations. The past decade has witnessed strong, revived interest in reusable air-breathing hypersonic launch vehicles for low-cost space exploration as well as rapid response to global military threats [7–11]. Typical design of these vehicles is based on a lifting body configuration with small control surfaces, and an integrated airframe-propulsion system [12–16]. Several examples are illustrated in Fig. 1.1, including two flown experimental vehicles, NASA X-43 and Boeing X-51 Waverider, as well as two conceptual vehicles, Lockheed Martin SR-72 and Boeing hypersonic commercial jet (BHCJ).

While decades of intermittent research have been devoted to hypersonic flight, there are still several unresolved technical challenges associated with this class of vehicles, including propulsion technology, material science, and structural design and analysis [7–10, 12, 15, 16]. The outstanding challenges of modeling and testing in the structural aspect of air-breathing hypersonic vehicles have been pointed out in the report on the national aerospace plane (NASP) [17] in the 1980's,

> Because of the uncertainties ... in aerodynamic loads and heating, ... precision of computation and lack of ground test facilities to replicate thermal and

structural flight loads, the current ability to meet the structural designers requirements are marginal to non existent.

Over the past three decades, the aerospace industry has enjoyed technology advances in computational and experimental capabilities. However, the development of air-breathing hypersonic vehicles is still facing the challenges associated with the modeling and testing of hypersonic structures.

(a) X-43 experimental vehicle ©NASA

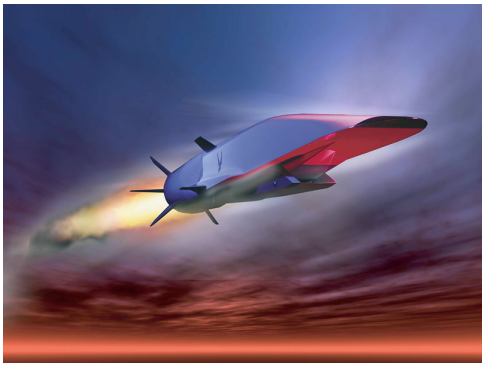

(b) X-51 Waverider ©Boeing

(c) SR-72 hypersonic vehicle ©Lockheed Martin

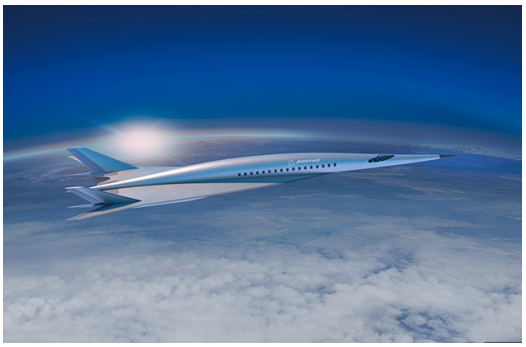

(d) Hypersonic commercial jet ©Boeing

Figure 1.1: Example air-breathing hypersonic vehicles

The challenges in modeling stems from the multidisciplinary nature of air-breathing hypersonic vehicles. The aerodynamic, structural and thermal responses are tightly coupled and interact with the control and propulsion systems, as illustrated in Fig. 1.2. Due to the high speeds, the vehicle is exposed to extreme aerothermodynamic environment involving high aerodynamic loading and heating. The high heating rates lead to degradation

of material properties. The thermal stresses introduced by the temperature gradients and geometrical constraints affect structural integrity and cause structural instabilities, including buckling and flutter. Therefore, successful design of air-breathing hypersonic vehicles requires a combined multi-physics model where the disciplines of aerodynamics, structural dynamics, and heat transfer are strongly coupled, producing a fluid-structural-thermal interaction (FSTI) problem, denoted by the term *aerothermoelasticity*. High-fidelity aerothermoelastic simulation over extended time periods is a key ingredient for the stability and reliability analysis of hypersonic vehicles, especially for the accurate prediction of aerothermoelastic stability boundary, i.e. the time elapsed before the onset of structural failure.

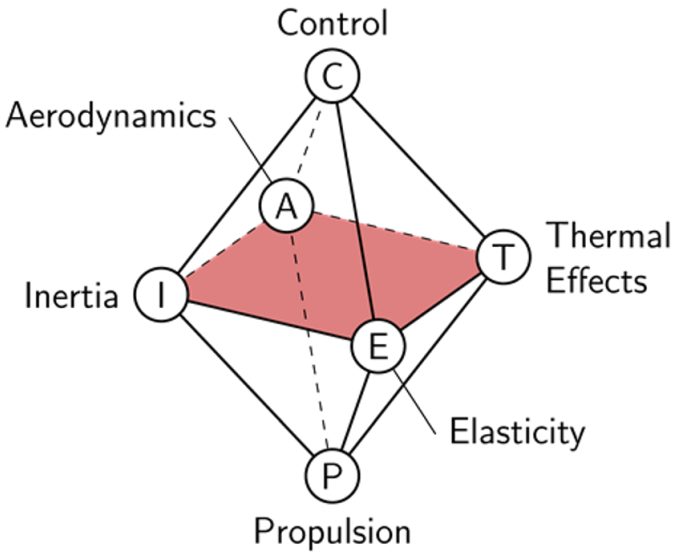

Figure 1.2: Aerothermoelasticity octahedron [1]

The major difficulties associated with the extended time aerothermoelastic analysis are two-fold. The first difficulty is the inherently complex hypersonic flows, which involves phenomena that are not present in supersonic conditions, including: dissociations, chemically reacting flow, viscous interactions and elevated levels of aerodynamic heat flux [18, 19]. A high-fidelity fluid solver based on computational fluid dynamics (CFD) is required for capturing the essential properties of the complex hypersonic flow physics. The

second difficulty is the disparity of characteristic times of different physical domains. The fluid characteristic time is several orders of magnitude smaller than the structural characteristic time, and the structural characteristic time is several orders of magnitude smaller than the thermal characteristic time [20]. The characteristic time disparity introduces the complexity associated with the different coupling mechanisms between and within the underlying aerothermal and aeroelastic subsystems [1, 8, 21].

The CFD-based transient aerothermoelastic simulation of an actual hypersonic flight trajectory is intractable on commercial workstation computers having 10-20 processors and has to be carried out on large-scale computer facilities. Assuming full availability of a mid-size computer cluster having 10^3-10^4 processors, the typical computational cost of a CFD solution per time step is 10^0-10^1s [2, 22]. The hypersonic flight may last for 10^3s, while the typical time step size of the CFD-based simulation is 10^{-3}s due to the requirement of numerical stability. As a result, the CFD-based transient aerothermoelastic simulation corresponding to a vehicle trajectory would take 10^6 time steps and 10^6-10^7s, i.e. several weeks or months, to finish on a typical large-scale computer facility. However, it is impractical to employ large-scale computer facilities for the extensive number of high-fidelity aerothermoelastic simulations that are required for the exploratory and parametric design and analysis of the structural components of a hypersonic vehicle [7, 9, 23]. In order to effectively incorporate the high-fidelity computational tools into the hypersonic vehicle design, the computational cost of high-fidelity aerothermoelastic simulations has to be reduced by at least four orders of magnitude, so that such simulations can be carried out on typical workstation computers, instead of large-scale computer facilities. Possible approaches to computational cost reduction include: (1) accelerating the fluid solver to reduce computer time per time step, and (2) developing advanced computational schemes to vastly increase the time step size.

Besides the challenges in modeling, the design of hypersonic vehicles is hindered by the lack of hypersonic aerothermoelastic scaling laws (ASL) for aerothermoelastic testing.

Aerothermoelastic testing implies the construction of a scaled down replica of the prototype vehicle and its direct insertion into a high-stagnation-temperature wind tunnel where the aerothermoelastic model can be subjected to aerodynamic heating and airloads simultaneously. Once such scaling laws were available, the test data obtained on scaled models could be extrapolated to full-size vehicles, resulting in a dramatic reduction in the cost of hypersonic aerothermoelastic flight testing, as well as a shortened design cycle of hypersonic vehicles. Work conducted on hypersonic vehicles in early 1960's has resulted in a landmark paper [24] where ASL were analytically derived to enable wind tunnel tests up to $M_\infty \leq 3.5$ and $T_0 \leq 1000^\circ F \approx 811\mathrm{K}$. However, modern hypersonic vehicles are expected to operate at much higher Mach numbers and in wider range of temperatures, as illustrated in Fig. 1.3. Experimental vehicles such as the X-43 [13] and the X-51 [25] have flown over Mach 4.5-6 at altitudes from 15 km to 33.5 km. The SR-72 is expected to cruise at Mach 6 at an altitude of 24.3 km [26]. The BHCJ is expected to cruise at Mach 5 at an altitude of 27 km [27]. As a result, the range of aerothermoelastic testing has to be extended from the high supersonic flow regime to the hypersonic flow regime $M_\infty \leq 10$ and $T_0 \leq 3000\mathrm{K}$. However, the study in the 1960's has concluded that complete similarity is impossible to achieve for scale ratios that differ from unity.

In addition to the lack of scaling laws, another issue associated with hypersonic aerothermoelastic testing is the scarcity of appropriate wind tunnel facilities for the tests beyond the high supersonic flow regime. An ideal wind tunnel has to meet three basic requirements: (1) high stagnation pressure ($p_0 \geq 0.5\mathrm{MPa}$), (2) high stagnation temperature ($T_0 \geq 800\mathrm{K}$), and (3) sufficiently long operating time period (at least on the order of minutes). The first two requirements ensure the simultaneous reproduction of the hypersonic aerodynamic loading and heating conditions and the third requirement ensures sufficient time for the development of the thermal responses in the scaled model that is critical to aerothermoelastic testing. Figure 1.4 illustrates the typical operational time period and stagnation temperature of different types wind tunnels [28, 29]. Only some of the blow-down and continuous

wind tunnels can potentially satisfy the basic requirements of hypersonic aerothermoelastic testing. Furthermore, two additional requirements are desirable: (1) the test section should be sufficiently large to accomodate the scaled model; (2) the working fluid should be inert gas, e.g. dry air or Nitrogen-Oxygen mixture, to avoid reactive products [29]. When accounting for these requirements, there are only a limited number of wind tunnels that can be potentially used for hypersonic aerothermoelastic testing [3, 29–31], as illustrated in Fig. 1.5.

The goal of this study is to address the challenges in modeling and testing associated with the aeroelastic and aerothermoelastic studies of representative hypersonic structures. The objectives are (1) to develop an integrated computational framework for fast, high-fidelity simulation of the aerothermoelastic response over extended time periods corresponding to a vehicle trajectory, and (2) to apply the computational framework to develop hypersonic ASL, so as to enable the wind tunnel testing of hypersonic structures.

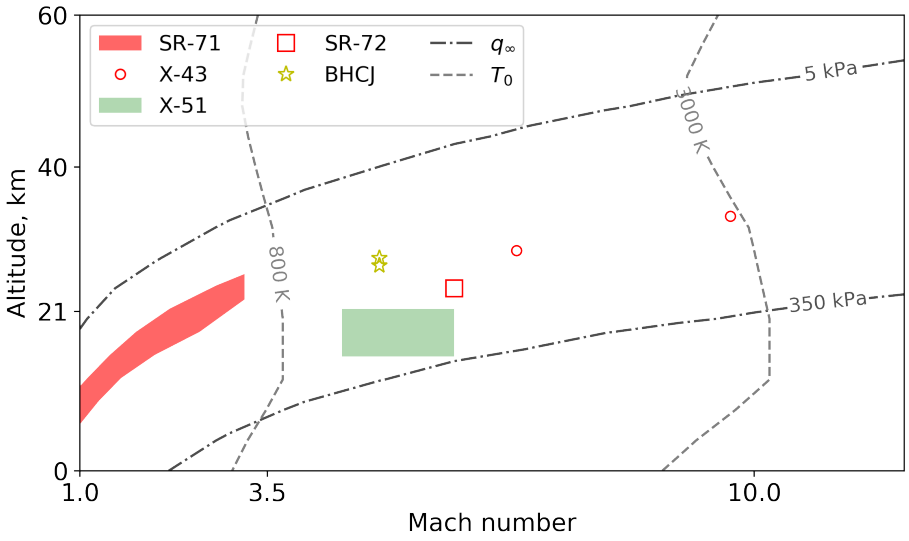

Figure 1.3: Flight envelopes of typical supersonic and hypersonic vehicles

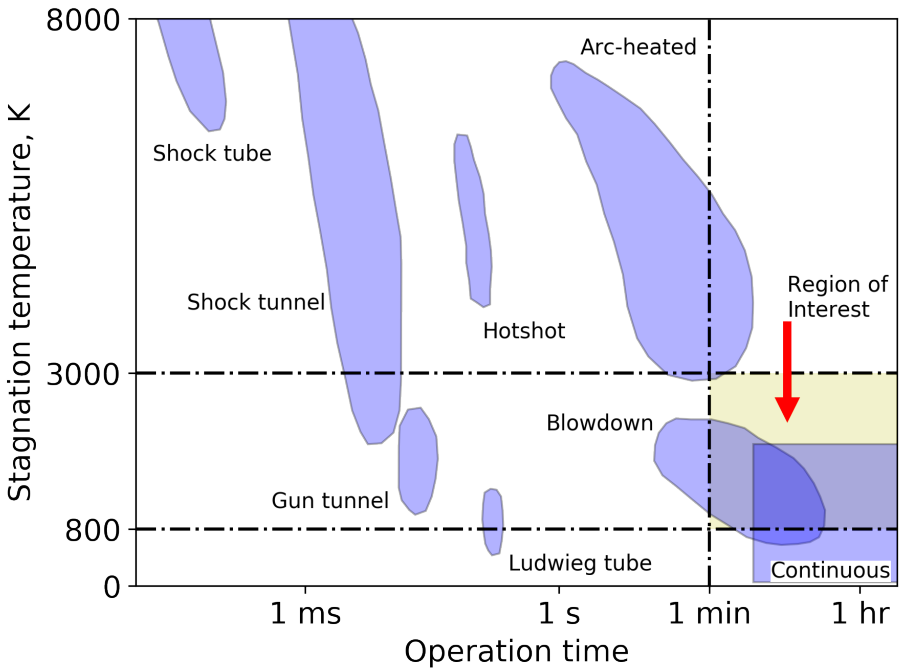

Figure 1.4: Capabilities of various types of wind tunnels

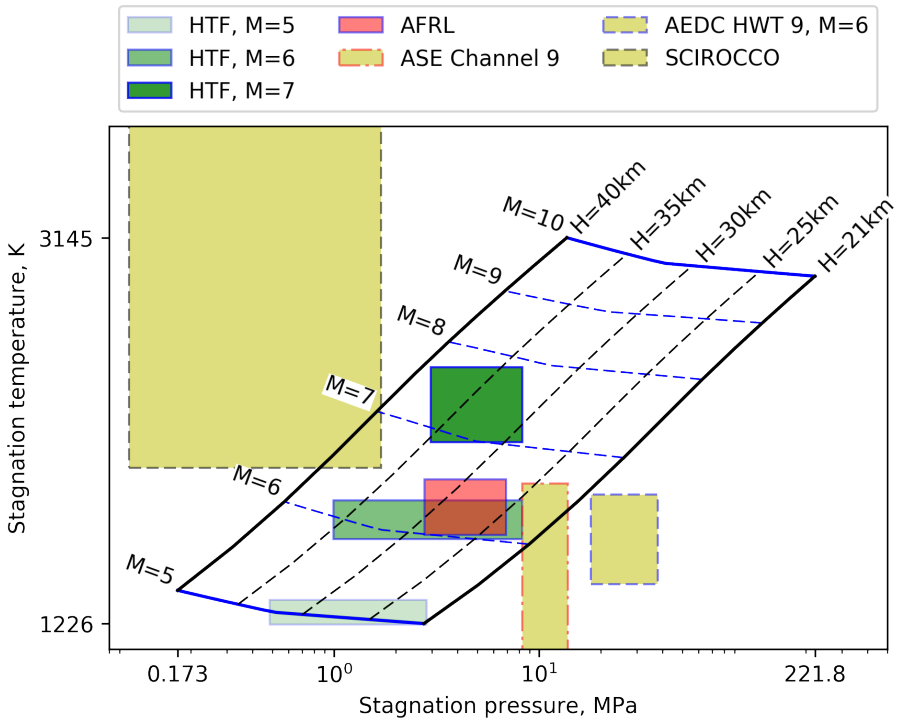

Figure 1.5: Envelope of testing conditions of several wind tunnels

1.2 Literature Review

1.2.1 Design and Analysis of Hypersonic Structures

In hypersonic flight, the vehicle operates in extreme and complex aerothermodynamic environment. The surface of the vehicle, particularly the skin panels that maintain the aerodynamic shape of the vehicle, are exposed to combined aerodynamic, thermal and acoustic loads [7, 9]. Traditionally, the ablative thermal protection system (TPS) has been successfully applied to mitigate the thermal loads in hypersonic flight, e.g. for reentry capsules and space shuttles [32, 33]. However, the ablative TPS is infeasible for air-breathing hypersonic vehicles, as it increases the vehicle weight, reduces the effective payload, and decreases the vehicle maintainability and reusability [34, 35].

The development of the NASP program has motived the concept of light-weight load-carrying hot structures [36–38] as an alternative configuration for the skin panel on air-breathing hypersonic vehicles. Some preliminary studies have been conducted on the design of such structures. In Refs. [39, 40], it was found that the corrugated panel is a promising configuration for lightweight load carrying structure, which is capable of sustaining thermal expansion without developing high thermal stresses. In Refs. [41–43], an integrated TPS based on a corrugated core sandwich panel was optimized for minimal weight while satisfying both the structural and thermal load constraints.

The detailed structural design of hypersonic vehicles, especially the skin panels, are discussed in Refs. [7, 9, 44], and the critical technology and knowledge gaps are identified. In Ref. [44], through the review of four hypersonic programs (SR-71, NASP, Lockheed Martin X-33, and DARPA Falcon project), it was concluded that coupled aerothermal and structural design methodologies are critical to the detailed design of hypersonic vehicles. In Ref. [7], a generic hypersonic vehicle was investigated and the limitations of existing analysis methodology were identified. It was found that the thermal analysis and CFD-based load predictions have to be integrated into the design process of the structural components.

Furthermore, in Ref. [9], four panels of a representative hypersonic cruise vehicle were designed using the state-of-the-art methods and tools to verify structural response and life predictive capabilities. It was found that, depending on the location, the panel design had to consider different combinations of extreme environments, including aeroelastic loading, material property change, thermally induced stress, mechanical and acoustical loading. This implies that the accurate prediction of aeroelastic and aerothermoelastic behavior of skin panels is critical to the systematic and comprehensive design of the skin panel structure.

The aeroelastic behavior of skin panels of high-speed vehicles have been studied extensively since late 1950s, as shown in a comprehensive review [45]. Early studies relied on relatively simple models [46–50]: Galerkin methods based on von Karman plate theory combined with piston theory (PT) [51, 52] or potential flow for the aerodynamic loading [49, 50]. Later, more sophiscated models were employed in panel flutter studies. In Refs. [53–55], finite-element-based structural models combined with piston theory were employed to examine the effects of temperature increment as well as composite materials on panel flutter. In Refs. [56, 57], Galerkin-based plate model combined with CFD-based Euler and Navier-Stokes (NS) aerodynamics was employed to study panel flutter with emphasis on the thermal effect and the curvature effect. In Ref. [58], the aeroelastic stability boundary of an internally pressurized circular cylindrical shell is studied using a structural model based on the finite element (FE) method combined with PT aerodynamics. Finally, CFD-based fluid-structure interaction (FSI) computational frameworks have also been developed and applied to panel flutter problems [59–61] and shock impingement problems [62–65].

Fewer studies are devoted to the aerothermoelastic behavior of skin panels. In Refs. [1, 66], an FSTI computational framework was developed using simplistic models: piston theory for pressure, Eckert's reference enthalpy method (EE) for heat flux [67], Galerkin-based von Karman plate model, and heat conduction model using finite difference method.

The framework was applied to study the aerothermoelastic behavior of a two-dimensional (2D) skin panel, which is a very simplified version of a realistic hypersonic structure. In Ref. [20], the framework was expanded using structural and thermal models based on the FE method, and the framework was applied to study the impact of structural bounary conditions and flight trajectories on the aerothermoelastic behavior of a three-dimensional (3D) skin panel configuration based on the NASP. In Ref. [23], a high-fidelity CFD-based computational framework was developed and employed to study the aerothermoelastic response of a stiffened panel mounted on a notional hypersonic vehicle. The findings highlight counter-intuitive aerothermoelastic deformation patterns caused by the local buckling modes due to the presence of stiffeners.

The aeroelastic and aerothermoelastic studies discussed above have several limitations. First, theoretical study has shown that significant differences exist in aeroelastic responses of 2D and 3D panels [68]. The impact of aspect ratio on the aerothermoelastic response has not been explored carefully. Second, theoretical and numerical studies have shown that the boundary layer has significant impact on the aeroelastic panel response [49, 61]. However, the impact of boundary layer on the aerothermoelastic panel response is not well understood. Finally, these studies focus primarily on the response of a flat isotropic panel with edges aligned to flow direction. This does not necessarily represent actual operating conditions. The direction of the flow rarely coincides with that of the panel edges and the panel may not be isotropic due to the application of composite materials and stiffeners. The effects of flow orientation angle and material orthotropicity can have considerable influence on its dynamical behavior, as shown in Refs. [48, 55], but have never been examined using a fully-coupled FTSI approach.

1.2.2 Fully-Coupled Analysis of Fluid-Structural-Thermal Interaction

A key component in the high-fidelity aeroelastic and aerothermoelastic analysis is the coupling scheme for CFD and computational structural dynamics (CSD) [69–72]. The cou-

pling is best addressed using a partitioned approach with loose-coupling [73–76]. In a partitioned approach, the responses of different physical domains are computed by separate solvers and coupling is achieved by exchanging boundary data at the interfaces of the domains. A loosely-coupled (LC) scheme, which exchanges information between solvers only once every time step, is computationally efficient and maintains accuracy and stability of the multi-physics solution when carefully designed [75]. Furthermore, when there is disparity in characteristic times of two physical domains, the subcycling approach can be employed to enhance the computational efficiency of the loosely-coupled scheme by initiating two solvers simultaneously and advancing one solver with a multiple of the time step associated with the other solver [73].

For FSI problems, it was shown in Refs. [77, 78] that the energy transfer between the fluid and structural solvers at their interface is essential for the numerical stability of partitioned schemes. The "artificial energy", which is the sum of the work done on the structure by fluid and the work done on the fluid by structure, should be zero based on physical considerations. However, due to the staggered implementation of the solvers, the artificial energy can be non-zero in partitioned schemes, thus leading to spurious solutions and numerical instability. Artificial energy is a measure of numerical error introduced by the staggered schemes. With proper combination of estimators for aerodynamic loading and structural displacement, the order of time accuracy of artificial energy and thus the stability of the numerical solution can be improved [78]. An estimator can be a predictor that extrapolates existing data to next time step, or a corrector that interpolates existing data to previous time step.

The loosely-coupled partitioned scheme has been extended to aerothermoelastic analysis [20, 66, 79–82]. In Ref. [79], a serial staggered procedure was developed for FSTI with trivial estimators, which pass the data between the solvers without extrapolation or interpolation over the time steps. In Refs. [20, 66], while simple analytical aerothermodynamic models were employed instead of a CFD solver, the importance of the coupling

between deformation and aerodynamic heat flux for the aerothermoelastic response of a panel is demonstrated. In Refs. [80–82], the transient aerothermoelastic problem was decomposed into the aerothermal and aeroelastic subproblems, and the subcycling technique was employed to enhance the computational efficiency of the staggered procedure. Three different time steps were used for the fluid, structural, and thermal solvers. The subcycling technique was applied in the coupling between fluid and structural solvers, and the coupling between thermal and aeroelastic solvers. Furthermore, the loosely-coupled scheme with subcycling was enhanced by using a combination of estimators, which improves the time accuracy from first-order to second-order [80–82].

Nevertheless, the loosely-coupled scheme with subcycling for aerothermoelastic analysis has two defficiencies. One defficiency is that, the subcycling approach relies on the quasi-steady assumption in hypersonic flow, which is not necessarily true. For example, in the shock wave/boundary layer interaction on a compliant structure, the shock wave motion introduces a dominant flow component with a frequency that is comparable to the structural frequency [83, 84]. Therefore, a loosely-coupled scheme without subcycling is desirable for obtaining general hypersonic aerothermoelastic responses. By extending the work done on FSI problem in Ref. [78], it is possible to develop a theoretical analysis tool to guide the design of a loosely-coupled scheme with improved time accuracy and numerical stability for aerothermoelastic analysis.

The other defficiency of the loosely-coupled scheme is that the aeroelastic response has to be resolved using a sufficiently small time step size that is typically one or two orders of magnitude smaller than the aerothermal time step size. However, in an actual hypersonic vehicle, the structural components have to be designed so as to avoid the onset of unstable response that impact the aerothermoelastic stability boundary. When the aerothermoelastic response is stable, the aeroelastic response is quasi-steady and driven by the thermal stress due to the aerothermal response [23]. This aeroelastic response can be resolved using an aerothermal time step size, instead of an aeroelastic time step size. Therefore, it is possible

to design a specialized coupling scheme that is more efficient for quasi-steady aerothermoelastic responses, in place of the general loosely-coupled scheme, to vastly improve the efficiency of long-time-duration aerothermoelastic simulations.

Finally, another missing component in the high-fidelity aerothermoelastic analysis is an approach for efficient and automatic identification of the aerothermoelastic stability boundary. Some stability analysis methods are available for aeroelastic analysis [85], which are divided into two categories, *a priori* and *a posteriori* methods. When a simple aerodynamic model is employed, it is possible to use an *a priori* method, such as the p-method [85], to determine the stability of an aeroelastic system by solving an eigenvalue problem, instead of generating the transient aeroelastic responses. The *a priori* method has been applied to the stability analysis of panel flutter response based on piston theory [54, 55]. However, when a high-fidelity aerodynamic model is employed in the aeroelastic analysis, the only practical choice is to use the *a posteriori* methods. The *a posteriori* methods are applied after a period of transient aeroelastic response is generated, and the response is examined to identify any aeroelastic instabilities. Typical *a posteriori* methods include the least-square fit method [86], the auto regressive moving average (ARMA) method [87, 88], and system identifications methods based on generalized aerodynamic loads and generalized degrees of freedom [89]. The ARMA method developed in Ref. [87] has also been used in hypersonic aeroelastic problems [1, 90]. For aerothermoelastic analysis, there is no available *a priori* method for the identification of instabilities. In the conventional approach [81, 91], the stability boundary is determined *after* the time domain simulation by examining the response as in the *a posteriori* methods. For such cases, simulation has to be carried out for adequate time, so that the solution includes both the stable (quasi-steady) and unstable (oscillatory) structural responses. The onset of unstable response represents the aerothermoelastic stability boundary during the postprocessing stage of the response obtained from the simulation. By extending the p-method for aeroelastic stability analysis, it is possible to develop a new *a priori* method for the automatic identification of aerothermoelastic

instabilities. Using the new method, the simulation is terminated upon the onset of instability, thus there is no need to continue the simulation into the unstable region, resulting in significant saving of computer time.

1.2.3 Reduced Order Modeling for Hypersonic Aerothermodynamics

As discussed in Section 1.1, while high-fidelity aerothermoelastic simulation is required for capturing the complex physics and multi-physical interactions of vehicle structures during hypersonic flight, the direct CFD-based aerothermoelastic simulation over the time scale of flight is intractable due to its high computational cost. A reduced order model (ROM) has to be employed to accelerate the CFD-based fluid solver. The goal of the ROM is to provide fast and accurate predictions of the responses of a high-dimensional dynamical system, i.e. a full-order model, to a given set of input parameters. In the context of aerothermoelastic simulation, the full-order model is the CFD-based fluid solver, which is typically a complex computer code. The ROM techniques are divided into the intrusive and non-intrusive methods, as described next.

The intrusive ROM method approximates the full-order model by reducing the number of governing equations and unknowns. It requires the modification of the computer code for the full-order model and hence the term "intrusive". The intrusive model order reduction is usually achieved through a projection process [92]. First, a small number of dominant components of the full-order responses are identified and used as "basis vectors". Next, the solution to the full-order model is approximated using a linear combination of the basis vectors. A typical approach for identifying the dominant components is the proper orthogonal decomposition (POD) method [93, 94]. The intrusive ROM methods have been successfully applied to problems in aerodynamics [95, 96] and aeroelasticity [97, 98]. However, the intrusive methods have two limitations. First, the numerical stability, accuracy, and convergence of the intrusive ROM are not guaranteed in general. Remedies for this limitation have been proposed, but they are not always effective [99, 100]. Second, the implementa-

tion of an intrusive ROM requires extensive modifications of the original computer code, which can be time-consuming or even infeasible. As a result, in the current study, the intrusive methods are not used for the construction of the ROM for the CFD solver.

In the non-intrusive ROM approach, the full-order model is replaced by a parametrized, black-box, function that is easy to compute. The parameters of the non-intrusive ROM are determined from the so-called training data set that consists of collection of full-order responses associated with different combinations of input parameters. The accuracy and convergence of a non-intrusive ROM depends on the use of sufficient number of training data samples provided for the ranges of parameters of interest. Common non-intrusive ROM methods include surrogates [91, 101–103] and Volterra series [104]. The surrogates approximate a full-order model by an interpolation model, such as radial basis functions, neural networks, polynomial response surfaces, and kriging [105–107]. In the Volterra series method, it is assumed that the response of any nonlinear system is exactly represented by an infinite series expansion of convolution integrals of Volterra kernels, and the ROM is represented by a truncated set of these kernels [104]. The Volterra series method is suitable for problems with strong unsteadiness, but hypersonic aerothermodynamic responses are typically quasi-steady. While the Volterra series method was applied to develop ROMs for aerodynamics from the subsonic flow regime to the high supersonic flow regime [108, 109], the surrogate-based methods are more commonly used for the reduced order modeling of hypersonic aerothermodynamics.

In Ref. [110], the kriging method was used to model the static force coefficients on a double-wedge typical section as a function of flight conditions and pitch angle. In a follow-up study [91], a kriging surrogate was constructed to predict the pressure and heat flux distributions on a 2D skin panel. The input to the surrogate consists of flight conditions, structural modal coordinates and wall temperature distribution characterized using a set of polynomials. The approach in Ref. [91] was combined with the POD method to generate the fluid ROM of a control surface [103], where the pressure and heat flux distribu-

tions were represented using the POD modes generated from the snapshots of CFD-based solution. Note that the POD modes were used only for dimension reduction, not for the projection of full-order models. The approach in Ref. [91] was also employed in the heat flux prediction on a three-dimensional control surface [102], where the wall temperatue distribution was characterized using POD modes of thermal response that were obtained from precomputed coupled aerothermoelastic simulation results. In Ref. [111], the kriging method was used to predict the boundary layer thickness on a deformed two-dimensional skin panel, which was subsequently used to compute the pressure distribution on the panel using the piston theory and the concept of effective shape [112].

As illustrated in the above studies [91, 102, 103], the ROM techniques have enabled the acceleration of the fluid solver by a factor of 10^3-10^4, while retaining the accuracy of a CFD solver. However, the fluid ROMs discussed in the above are limited by two issues: *characterization* and *generalization*. First, the characterization issue is associated with the representation of the wall temperature distribution. The polynomial thermal modes [91, 103] are usually too simplistic and lack the accuracy required for nonuniform wall temperature distribution present in an actual aerothermoelastic problem [113, 114]. The POD thermal modes [102] yield accurate representation of the temperature distribution, but the construction of such modes requires the use of expensive coupled aerothermoelastic analysis. Second, the generalization issue is due to the fact that the fluid ROM is representative of a particular geometrical configuration. This limitation precludes its generalization to other geometrical configurations of interest. To conduct the aerothermoelastic analysis of a series of geometrical configurations, one would need to build a different ROM for each configuration of interest. Construction of multiple ROM's incurs a heavy computational burden for the sample generation of high-fidelity fluid solutions.

In Refs. [2, 113, 114], a two-stage fluid ROM was proposed in an attempt to resolve the characterization issue. First, the heat flux distribution associated with uniform wall temperature was generated using a kriging surrogate. Subsequently, the heat flux distribution

was corrected by a pointwise model accounting for the discrepancy between the uniform temperature and the actual non-uniform temperature distribution. The two-stage fluid ROM produced accurate heat flux prediction associated with arbitrary wall temperature distribution, including the non-smooth distribution due to the presence of boundary layer transition and shock wave/boundary layer interaction [114], as well as complex structural deformation [2]. However, this approach has two limitations. First, it relies on the tuning of empirical coefficients that are dependent on flight conditions and geometrical configurations and has to be curvefitted from CFD solutions. Second, the correction factors are computed by solving an ordinary differential equation (ODE), which is computationally more expensive than other fluid ROMs [91, 102, 103] and may introduce potential numerical instabilities associated with the ODE solver. For the cases where the temperature distribution is expected to be smooth, it is possible to employ a simpler but more versatile correction model that is free of empirical coefficients and ODE's.

1.2.4 Scaling Laws for Aeroelastic and Aerothermoelastic Testing

The scaling laws characterize the proportionality relations between the parameters associated with a system and its length scale. The classical dimensional analysis for generating scaling laws has been established as early as 1920's [115, 116]. The idea central to the classical dimensional analysis is best summarized using the Buckingham's Π theorem. It states that, the characteristics or properties of a system can be expressed through combinations of various parameters so that each group is dimensionless [115]. Thus, any change in scale does not affect the magnitudes of these quantities and the performance of a system can be predicted from the results obtained on the performance of a similar system, but of different size.

Scaling laws have played an important role in the study of aeroelasticity. The scaling laws enable the construction of aeroelastically scaled wind tunnel models and allow one to relate small-scale wind tunnel test results to the behavior of a full-scale vehicle. The

fundamentals of aeroelastic scaling methods are described in the last three chapters of the classical textbook on aeroelasticity by Bisplinghoff et al. [117], which covers classical aeroelastic model theory, model design and construction, and testing techniques. The topic of aeroelastic scaling is further expanded in the AGARD Manual on Aeroelasticity [118] with a provision of details on model construction and testing. The classical aeroelastic scaling approach has been practiced extensively at the Transonic Dynamic Tunnel at NASA Langley Research Center, which is a dedicated facility for testing aeroelastically scaled models [119].

In Ref. [117], aeroelastic scaling laws are developed for *linear* structures by dimensional analysis of the governing equations, which establishes the scaling parameters required for designing aeroelastically scaled models. Two key requirements for dynamic aeroelastic testing are established by the authors. First, the aerodynamic shape should be geometrically scaled, so as to achieve similitude in the aerodynamic response. Second, two dimensionless parameters, nondimensional natural frequencies and mode shapes, have to be matched in order to achieve similitude in the structural dynamic response. As pointed out in Ref. [117], typical aeroelastic testing models do not have the same structural configuration as the full-scale prototype. The structural configuration scaled according to analytical scaling laws would either require materials having nonphysical properties or pose prohibitive manufacturing specifications. One alternative is to redesign the internal structure of the scaled model such that its structural dimensionless parameters are consistent with the full scale prototype.

In the last six decades, a considerable amount of research efforts have been devoted to the development of aeroelastic scaling techniques, so as to enable the wind tunnel testing of aeroelastic problems of increasing complexity.

Following the methodology in Ref. [117], approaches based on modal optimization and stiffness matching have been developed to systematically generate scaled models for linear aeroelastic problems [120–123]. In Refs. [120, 121], a two-step optimization ap-

proach was developed for the dynamic aeroelastic scaling of a low-aspect-ratio wing. First, the structure stiffness was matched by minimizing the differences in static deflections between the model and the prototype. Subsequently, the distribution of non-structural mass was optimized to minimize the difference in mode shapes and match the reduced modal frequencies. In Ref. [122], the two-step approach was compared with a one-step approach, where the natural frequencies and mode shapes were optimized by simultaneously adjusting the distribution of structural stiffnesses and nonstructural masses. It was concluded that both approaches converged to an acceptable result for wind tunnel testing, but the one-step approach was computationally more expensive. In Ref. [123], a multidisciplinary optimization framework was employed to develop aeroleastically scaled model using the one-step approach, which also accounted for the case where flow similarity cannot be achieved in the wind tunnel.

The optimization approach has also been extended for nonlinear aeroelastic scaling problems [124–126]. In Ref. [124], a nonlinear aeroelastic scaled model of a joined-wing aircraft was developed. The structure was designed by simultaneously matching not only the reduced natural frequencies and mode shapes, but also the nondimensionalized buckling eigenvalue. The aeroelastic frequencies and damping of the resulting scaled model matched well with the prototype throughout the flight conditions of interest. In Ref. [125], the aeroelastic scaling of a highly flexible flying wing aircraft with large deformations and prestress was considered. It was shown that nonlinear aeroelastically scaled models can be obtained by the matching of a set of carefully selected similarity parameters, including the Froude number. The scaled model demonstrated both linear and nonlinear aeroelastic responses that agreed reasonably well with the full-scale prototype. In Ref. [126], an aeroelastic scaling methodology was developed using a concept of equivalent static loads. Nonlinear aeroelastically scaled models of a joined-wing configuration were developed by matching vibration and buckling modes and eigenvalues, as well as the static structural responses. The new nonlinear scaled model was compared with a scaled model obtained by

classic scaling methodology. The new model showed improved match in the nondimensional deflections and reduced aeroelastic frequencies, but a loss of accuracy in the reduced flutter speed.

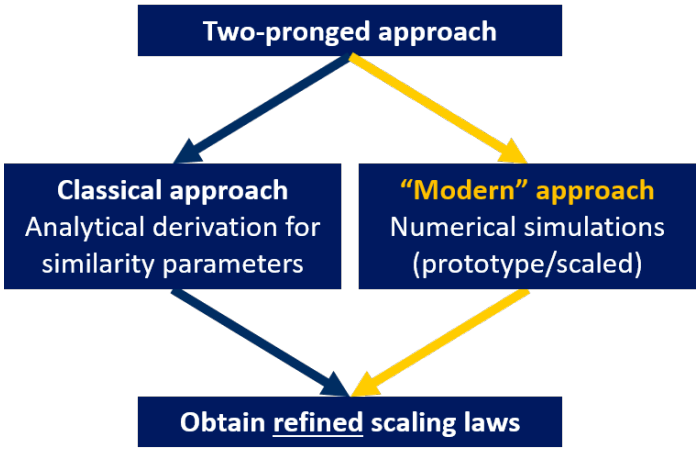

Figure 1.6: Schematic illustration of the two-pronged approach

In parallel to the studies in aeroelastic scaling, scaling laws for aeroservoelasticity have also been developed in the literature. In Ref. [127], an aeroservoelastic scaling procedure for a transonic wind tunnel model was developed. The scaling laws were obtained through the application of dimensional analysis the aeroelastic equations extended with the experimental spring mounting system. Satisfactory agreement was achieved between the root loci of the full size prototype and the scaled model. An innovative and more systematic scaling methodology, called the two-pronged approach, was proposed for aeroservoelastic scaling problems [128–131]. The two-pronged approach combines the classical dimensional analysis with modern numerical simulation methods, as illustrated in Fig. 1.6. On the left-hand branch, basic scaling requirements are established using dimensional analysis, in a manner that resembles the classical procedure. On the right-hand branch, complete aeroelastic/aeroservoelastic solutions for the prototype as well as the scaled model are obtained using numerical simulation. From the comparison and adjustment of these two models, the "numerical similarity solutions" are generated to replace the analytical similarity solutions

for refinement of the scaling laws. The two-pronged approach has been applied to obtain the scaling laws associated with active flutter suppression of a two-dimensional wing section [128–130]. In Ref. [131], it was also demonstrated that aeroservoelastic scaling laws for rotary-wing aircraft can be obtained in a manner similar to fixed-wing aircraft.

While scaling methodologies have been developed for aeroelastic problems with geometric nonlinearities and active control systems, the scaling of aerothermoelastic problems have been considered impossible in the literature. A few attempts have been made in the past to incorporate heat transfer effects into the aeroelastic scaling laws, such as Refs. [132, 133]. While scaling laws for hypersonic aerothermodynamics have been successfully established [19, 134, 135], only partial successes were achieved in the development of hypersonic ASL [24, 136, 137]. The similarity parameters that need to be satisfied are derived from the dimensional analysis of the general equations for stress, displacement and temperature distribution of a body immersed in a hot, flowing gas. As discussed in the previous section, these studies have come to the conclusion that, complete aerothermoelastic similarity is impossible to achieve for scale ratios that differ from unity for hypersonic Mach numbers and temperatures.

Lack of hypersonic ASL has resulted in the use of "restricted purpose" testing approaches and "incomplete" aerothermoelastic testing [24, 137]. Restricted purpose testing implies a study of the aerothermoelastic problem assuming that the coupling between the aerodynamic pressure, aerodynamic heating, heat conduction and stress-deflection phenomena is weak. However, the fluid-thermal-structural interactions cannot be decoupled in modern hypersonic vehicles since they are based on an integrated airframe-propulsion concept, which enhances the interactions between the various components [138]. Incomplete aerothermoelastic testing refers to the use of additional means, other than aerodynamics, to provide loading or heating. This requires *a priori* knowledge of the loading and heating on the full-scale vehicle, as well as the ability to accurately apply these loads at the appropriate locations as a function of time, which is difficult to achieve in practice. The

barriers associated with hypersonic aerothermoelastic testing have been one of the factors contributing to problems encountered during the development of air-breathing hypersonic vehicles in the past, such as failures in flight as well as high temperature structural testing.

Recently, there is renewed interest in developing models for aerothermoelastic testing in high supersonic and hypersonic wind tunnels [29, 139]. In these studies, scaled skin panel models are designed with the aid of numerical simulation tools so as to obtain the desired aerothermoelastic response in the wind tunnel. However, the primary goal of these studies is not to achieve aerothermoelastic scaling. Instead, the goal is to develop skin panel models that are quite flexible, such that the interaction between the high-speed flow and the panel deformation becomes observable in the wind tunnel. However, response observed on such wind tunnel models is not representative of the realistic aerothermoelastic response of the skin panels on a hypersonic vehicle.

To summarize, success in the development of scaling laws for hypersonic aerothermoelasticity has not been achieved yet. However, using the modern numerical simulation tools, it is possible to employ the two-pronged approach [131] to generate refined scaling laws that can be employed to develop aerothermoelastically scaled models for wind tunnel testing.

1.3 Objectives

Based on the introduction and literature review, it is evident there are major challenges in the modeling and testing of the aeroelastic and aerothermoelastic behavior of hypersonic vehicles. On the modeling side, there is need for an efficient and versatile computational approach for fast long-time-duration simulation of hypersonic aerothermoelasticity, a critical ingredient in the performance and reliability analysis of hypersonic vehicles. On the testing side, the hypersonic ASL have been missing for decades, thus hypersonic aerothermoelastic testing has been non-existent. This situation limits substantially our understand-

ing of the aerothermoelastic behavior of hypersonic structures. This dissertation addresses these challenges, by providing a major contribution towards solving these long-standing problems. The specific goals of this dissertation are:

1. Development of efficient fully-coupled solvers for transient and quasi-steady hypersonic aerothermoelastic simulation of the responses of a hypersonic configuration over extended time duration corresponding to a hypersonic flight trajectory.
2. Examination of the aeroelastic and aerothermoelastic behavior of hypersonic skin panels using high-fidelity simulation tools, with an emphasis on the effects of boundary layer thickness, aspect ratio, flow orientation angle, and material orthotropicity.
3. Development of a two-pronged approach and demonstration of its capability to generate aerothermoelastically scaled models of a composite skin panel in hypersonic flow that are suitable for testing under realistic wind tunnel conditions.

1.4 Key Novel Contributions

Accomplishment of the objectives stated above has resulted in several unique contributions towards the modeling and testing of representative structures of hypersonic vehicles. The contributions unique to this study are listed below:

1. Development of an integrated, modularized computational framework, hypersonic aerothermoelasticity simulation environment (HYPATE), that combines finite-element-based solvers for structural and thermal behavior with fluid solvers having multiple levels of fidelities.
2. Construction of an efficient fluid ROM based on POD-kriging method and enhanced by a novel approach for correction and scaling, which enables the extrapolation of a ROM to different geometric scales, flight conditions and arbitrary wall temperature distritbutions while reducing the number of input parameters.
3. A new tightly-coupled (TC) scheme for ROM-based aerothermoelastic simulation of

a typical hypersonic structure over extended time periods, combined with a new *a priori* stability analysis approach for the automatic identification of aerothermoelastic instabilities.

4. A systematic dimensional analysis of the aerothermoelastic response of a modern composite hypersonic structure.
5. A multi-objective optimization framework using the two-pronged approach that enables the generation of refined ASL for the first time in the literature of hypersonic aerothermoelasticity.

1.5 Outline of the Document

The dissertation is divided into 10 chapters. The motivations, literature review, and objectives are given in Chapter 1.

Second, Chapters 2-5 present the computational framework for hypersonic aerothermoelasticity, HYPATE. Chapter 2 provides a general discussion of the governing equations for hypersonic flow and its dimensional anlaysis, as well as the modeling approaches for hypersonic aerothermodynamics, including a CFD solver, analytical models, and a fluid ROM enhanced by a correction and scaling technique. Chapters 3 and 4 describe the finite element formulation and dimensional analysis of the structural and thermal problems, respectively. Chapter 5 describes the solution procedure of the fully-coupled aerothermoelastic analysis, highlighting loosely-coupled schemes for transient responses, tightly-coupled schemes for quasi-steady responses, and a linearized stability analysis method for the identification of the onset of aerothermoelastic instability.

Next, Chapter 6 presents the two-pronged approach to generating the refined ASL, which combines the classical dimensional analysis with modern computational framework. Chapter 6 also provides an extensive description of multi-objective Bayesian optimization algorithm that is employed to solve the optimization problem resulting from the two-

pronged approach.

Subsequently, Chapters 7-9 present the major results of the dissertation. Chapter 7 provides the verification results for the computational framework, including the verification of the enhanced fluid ROM, as well as aeroelastic and aerothermoelastic responses using CFD-based and ROM-based fluid solvers. Chapter 8 presents the aerothermoelastic analysis results of a generic skin panel highlighting the effects of boundary layer thickness, aspect ratio, flow orientation angle, and material orthotropicity. Chapter 9 presents the scaling results of the two-pronged approach. It is applied to reproduce the aeroelastic scaling laws associated with a heated panel and generate the refined ASL associated with a composite panel.

Finally, Chapter 10 provides the conclusions and recommendations for future research.

CHAPTER 2

Approaches to Modeling Hypersonic Aerothermodynamics

A key component in the aerothermoelastic simulation is the fluid solver required for the prediction of the aerodynamic and thermal loads acting on the hypersonic vehicle structure. The fluid solver has to strike a balance between predictive accuracy and computational efficiency. In this study, three fluid solvers having different levels of fidelity are developed and used. A fluid solver based on analytical models (AM), such as piston theory and Eckert's reference method, is developed for the verification of fully-coupled aerothermoelastic simulation. The next level up is a ROM-based fluid solver having a higher fidelity, which is the primary means for the reduction of computational cost in the hypersonic aerothermoelastic simulation. The high-fidelity fluid solver is a CFD solver that is used to carry out the high-fidelity aeroelastic and aerothermoelastic simulations and provide the data samples used for the development of the ROM. This chapter describes (1) the governing equations for hypersonic flow and its dimensional analysis, a requirement for the development of ASL generated in the subsequent chapters, and (2) the detailed formulation of the three fluid solvers employed in this study.

2.1 Governing Equations

2.1.1 The Navier-Stokes Equations

The two principal aerodynamic quantities required for aerothermoelastic modeling are the pressure and heat flux applied on the deforming structure by the external hypersonic flow. The flow field is governed by the NS equations describing the conservation of mass, momentum, and energy for a compressible, viscous, heat-conducting ideal gas (pp. 266–272 of Ref. [19]),

$$\frac{\mathrm{D}\rho^f}{\mathrm{D}t} + \rho^f \nabla \cdot \mathbf{V} = 0 \tag{2.1a}$$

$$\rho^f \frac{\mathrm{D}\mathbf{V}}{\mathrm{D}t} = -\nabla p + \nabla \cdot \boldsymbol{\tau} \tag{2.1b}$$

$$\rho^f \frac{\mathrm{D}\Psi}{\mathrm{D}t} = -\nabla \cdot (k^f \nabla T) - \nabla \cdot (p\mathbf{V}) + \nabla \cdot (\boldsymbol{\tau} \cdot \mathbf{V}) \tag{2.1c}$$

where the material derivative is

$$\frac{\mathrm{D}}{\mathrm{D}t} = \frac{\mathrm{d}}{\mathrm{d}t} + \mathbf{V} \cdot \nabla \tag{2.2}$$

and the viscous stress tensor is

$$\boldsymbol{\tau} = \mu(\nabla \mathbf{V} + \nabla \mathbf{V}^T) + \lambda(\nabla \cdot \mathbf{V})\mathbf{I} \tag{2.3}$$

Employing Stokes hypothesis, the bulk viscosity λ is related to the viscosity μ by

$$\lambda = -\frac{2}{3}\mu \tag{2.4}$$

To complete the system of equations, the specific energy Ψ, temperature T, pressure p,

and density ρ^f are related using the equations of state for ideal gas,

$$p = \rho^f RT \tag{2.5a}$$

$$\Psi = \psi + \frac{1}{2}\mathbf{V}\cdot\mathbf{V} \tag{2.5b}$$

$$\psi(T) = c_v(T)T \tag{2.5c}$$

$$c_v(T) = \frac{c_p(T)}{\gamma(T)} = \frac{R}{\gamma(T)-1} \tag{2.5d}$$

If the gas is calorically perfect, the specific heats are constant, and Eqs. (2.5c) and (2.5d) becomes,

$$\psi = c_v T$$

$$c_v = \frac{c_p}{\gamma} = \frac{R}{\gamma - 1}$$

Finally, two sets of boundary conditions are imposed on the governing equations. For free-stream condition,

$$\|\mathbf{V}\| = V_\infty, \quad \rho^f = \rho_\infty, \quad T = T_\infty \tag{2.6}$$

On the surface of the deforming structure, the velocity, temperature, and heat flux at the solid-fluid boundary have to match,

$$\mathbf{V} = \frac{\mathrm{d}\mathbf{u}_w}{\mathrm{d}t} \tag{2.7a}$$

$$T = T_w \tag{2.7b}$$

$$\mathbf{n}\cdot(k^f\nabla T) = \mathbf{n}\cdot(\mathbf{k}^s\cdot\nabla T^s) \tag{2.7c}$$

2.1.2 Dimensional Analysis of the Fluid Problem

For hypersonic flow, the following nondimensional quantities are introduced to non-dimensionalize the governing equations for the fluid problem Eqs. (2.1), (2.5)-(2.7),

$$\bar{x}_i = \frac{x_i}{\hat{L}}, \quad \bar{t} = \frac{t}{\hat{t}}, \quad \bar{T} = \frac{T}{\hat{T}_F}, \quad \overline{\mathbf{V}} = \frac{\mathbf{V}}{\hat{V}}, \quad \bar{\rho}^f = \frac{\rho^f}{\hat{\rho}^f}, \quad \bar{p} = \frac{p}{\hat{p}} \tag{2.8a}$$

$$\bar{\mu} = \frac{\mu}{\hat{\mu}}, \quad \bar{c}_p^f = \frac{c_p^f}{\hat{c}_p^f}, \quad \bar{k}^f = \frac{k^f}{\hat{k}^f} \tag{2.8b}$$

As suggested in Ref. [137], in hypersonic flow, it is more convenient to non-dimensionalize the NS equations using the stagnation conditions, instead of the free-stream conditions, because the following high-M_∞ approximations are available at the stagnation point,

$$T_0 \approx \frac{V_\infty^2}{2c_{p0}^f f_T}, \quad f_T = \int_0^1 \bar{c}_p^f \mathrm{d}\left(\frac{T}{T_0}\right) \tag{2.9a}$$

$$p_0 \approx \frac{\gamma+3}{2(\gamma+1)}\rho_\infty V_\infty^2 \tag{2.9b}$$

The following quantities are chosen as the reference values,

$$\hat{V} = V_\infty, \quad \hat{\rho}^f = \rho_\infty, \quad \hat{p} = p_0 \tag{2.10a}$$

$$\hat{\mu} = \mu_0, \quad \hat{c}_p^f = c_{p0}^f, \quad \hat{k}^f = k_0^f \tag{2.10b}$$

Using Eqs. (2.8)-(2.10), Eq. (2.1) is non-dimensionalized as,

$$\frac{\mathrm{D}\bar{\rho}^f}{\mathrm{D}\bar{t}} + \bar{\rho}^f \overline{\nabla} \cdot \overline{\mathbf{V}} = 0 \tag{2.11a}$$

$$\bar{\rho}^f \frac{\mathrm{D}\overline{\mathbf{V}}}{\mathrm{D}\bar{t}} = -\frac{\gamma+3}{2(\gamma+1)}\overline{\nabla}\bar{p} + \frac{1}{\boldsymbol{Re}_0}\overline{\nabla}\cdot\bar{\boldsymbol{\tau}} \tag{2.11b}$$

$$\begin{aligned}\bar{\rho}^f \frac{\mathrm{D}\bar{\Psi}}{\mathrm{D}\bar{t}} = &-\frac{1}{2f_T \boldsymbol{Pr}_0 \boldsymbol{Re}_0}\frac{\hat{T}_F}{T_0}\overline{\nabla}\cdot(\bar{k}^f\overline{\nabla}\bar{T}) \\ &-\frac{\gamma+3}{2(\gamma+1)}\overline{\nabla}\cdot(\bar{p}\overline{\mathbf{V}}) + \frac{1}{\boldsymbol{Re}_0}\overline{\nabla}\cdot(\bar{\boldsymbol{\tau}}\cdot\overline{\mathbf{V}})\end{aligned} \tag{2.11c}$$

where,

$$\overline{\nabla} = \hat{L}\nabla = \left[\frac{\partial}{\partial \bar{x}_1}, \frac{\partial}{\partial \bar{x}_2}, \frac{\partial}{\partial \bar{x}_3}\right] \tag{2.12a}$$

$$\frac{\mathrm{D}}{\mathrm{D}\bar{t}} = \frac{\hat{L}}{\hat{V}}\frac{\mathrm{D}}{\mathrm{D}t} = \frac{\hat{L}}{V_\infty \hat{t}}\frac{\mathrm{d}}{\mathrm{d}\bar{t}} + \overline{\mathbf{V}} \cdot \overline{\nabla} \tag{2.12b}$$

$$\bar{\boldsymbol{\tau}} = \frac{\hat{L}}{\hat{\mu}\hat{V}}\boldsymbol{\tau} = \bar{\mu}\left[\overline{\nabla \mathbf{V}} + \overline{\nabla \mathbf{V}}^T - \frac{2}{3}(\overline{\nabla} \cdot \overline{\mathbf{V}})\mathbf{I}\right] \tag{2.12c}$$

$$\bar{\Psi} = \frac{1}{\hat{V}^2}\Psi = \frac{1}{2\gamma f_T}\frac{\hat{T}_F}{T_0}\bar{c}_v^f \bar{T} + \frac{1}{2}\overline{\mathbf{V}} \cdot \overline{\mathbf{V}} \tag{2.12d}$$

The boundary conditions are non-dimensionalized as,

$$\overline{\mathbf{V}} = \frac{\hat{u}}{\hat{V}\hat{t}}\frac{\mathrm{d}\bar{\mathbf{u}}_w}{\mathrm{d}\bar{t}} \tag{2.13a}$$

$$\bar{T} = \bar{T}_w \tag{2.13b}$$

$$\frac{\hat{k}^f}{\hat{k}^s}\mathbf{n} \cdot (\hat{k}^f \overline{\nabla}\bar{T}) = \mathbf{n} \cdot (\bar{\mathbf{k}}^s \cdot \overline{\nabla}\bar{T}_w) \tag{2.13c}$$

where $\hat{u}$ is the reference amplitude of deflection.

The similarity parameters for the NS equations are identified from Eqs. (2.11)-(2.13),

$$\frac{V_\infty \hat{t}}{\hat{L}}, \frac{\hat{T}_F}{T_0} \tag{2.14a}$$

$$Re_0 = \frac{\rho_\infty V_\infty \hat{L}}{\hat{\mu}}, Pr_0 = \frac{\hat{c}_p^f \hat{\mu}}{\hat{k}^f}, \gamma \tag{2.14b}$$

$$\bar{\mu}, \bar{c}_p^f, \bar{k}^f \tag{2.14c}$$

$$\bar{\mathbf{u}}_w = \frac{\mathbf{u}_w}{\hat{u}} \tag{2.14d}$$

In Eq. (2.14a), the first quantity defines the time scale of the fluid problem, and the second quantity defines the reference temperature. The quantities in Eq. (2.14b) require similarity in the flow properties. Note that the freestream Mach number M_∞ does not appear and this is a result of the Mach number independence principle in the hypersonic flow (pp. 107–111 of Ref. [19]). Equation (2.14c) requires the similarity in the gas properties as functions of temperature. Finally, the geometric similarity between the model and prototype is required.

The similarity parameters in Eq. (2.14) are rewritten for a slender body [134, 135], where concept of boundary layer can be used. The slender body is characterized by a small thickness ratio $\frac{\hat{u}}{\hat{L}} \ll 1$, which is typical of a skin panel. Note that the thickness distribution $\mathbf{u}_w$ accounts for both the geometry and the deformation. With a few simplifying assumptions for hypersonic flow and boundary layer, the similarity parameters for the surface pressure and the heat flux on a slender body are [137],

$$\frac{\hat{V}\hat{t}}{\hat{L}}, \quad \frac{\hat{T}_F}{T_0}, \quad \bar{T}_w = \frac{T_w}{\hat{T}_F}, \quad \bar{\mathbf{u}}_w \tag{2.15a}$$

$$\frac{\hat{p}\hat{L}}{\gamma p_\infty M_\infty \hat{u}}, \quad \boldsymbol{Re}_0\boldsymbol{Pr}_0 \frac{\hat{k}^f \hat{V}^2}{\hat{q}\hat{c}_p^f \hat{L}} \tag{2.15b}$$

$$\bar{\Xi} = \frac{\hat{L}^2}{\hat{u}^2\sqrt{\boldsymbol{Re}_0}}, \quad \bar{B} = k_B M_\infty^3 \frac{\hat{d}}{\hat{L}} \tag{2.15c}$$

$$\boldsymbol{Pr}_0, \quad \gamma \tag{2.15d}$$

Four new similarity parameters are introduced in Eqs. (2.15a)-(2.15d). The two quantities in Eq. (2.15b) define the reference magnitudes of the pressure and the heat flux, respectively. In Eq. (2.15c), $\bar{\Xi}$ requires similarity in the boundary layer thickness. The parameter $\bar{\Xi}$ is important when the viscous interaction is strong, i.e. when the pressure distribution is significantly modified by the boundary layer. The parameter $\bar{B}$ is introduced to characterize the nose bluntness of the slender body, i.e. the sharpness of the leading edge, because the pressure distribution on the slender body is sensitive to the geometry of the nose, or the cross-section of the leading edge [24, 135]. In the parameter $\bar{B}$, $\hat{d}$ is the characteristic radius of the nose, and k_B is a constant that depends on the nose geometry.

Finally, note that a few simplifying assumptions, such as laminar flow and perfect gas law, have been used when deriving the similarity parameters in Eq. (2.15) [24, 137]. Therefore, when more complex effects are present in the fluid problem, e.g. turbulent boundary layer and real gas effect, the similarity parameters in Eqs. (2.14) and (2.15) may not represent the correct scaling requirements for constructing a scaled model that satisfies hyper-

sonic aerothermodynamic similarity.

2.2 Computational Fluid Dynamics

2.2.1 Compressible Reynolds-Averaged Navier-Stokes Equations

One approach to obtaining the aerodynamic pressure and heat flux on a deforming structure in hypersonic flow is to numerically solve the NS equations using a CFD solver. There are several CFD formulations representing different levels of fidelity: direct numerical simulation (DNS), large eddy simulation (LES), and reynolds-averaged Navier Stokes (RANS) simulation. The DNS and LES generate fluid solutions of very high fidelity that provide high spatial and temporal resolution of the flow field. However, the computational costs of DNS and LES are intractable for aerothermoelastic simulations of any significantly long time duration [140]. The RANS simulation provides a less expensive alternative to DNS and LES. In the RANS simulation, the flow is modelled by a time-averaged mean flow field, plus additional time-dependent components accouting for the impact of the transient flow fluctuations, i.e. turbulence, on the mean flow field. In the hypersonic aerothermoelastic simulations, the fluid characteristic time is much smaller than the structural characteristic time, and the structural response is of primary interest. The time-averaged fluid solution from a RANS solver can provide sufficiently time accurate predictions of the pressure and heat flux load for hypersonic aeroelastic and aerothermoelastic simulations [1, 21, 81, 90].

The RANS simulation consists of two components, the compressible RANS equations and a turbulence model. The compressible RANS equations are transformed from the NS equations using the Favre averaging method [141]. It contains variables characterizing the mean flow field, as well as the flow fluctuations. A turbulence model is a set of additional equations to provide closure to the compressible RANS equations by associating flow fluctuation variables to the mean flow field variables. In this study, the Spalart-Allmaras (SA) turbulence model [142] is employed for the RANS simulation. This turbulence model is

considered a reasonable one-equation model for representing turbulent hypersonic flow [143] and it has been employed in several past hypersonic aeroelastic studies in Refs. [1, 90, 144].

The compressible RANS equations [141], in a form that is suitable for the SA turbulence model, are as follows,

$$\frac{\mathrm{D}\rho^f}{\mathrm{D}t} + \rho^f \nabla \cdot \mathbf{V} = 0 \tag{2.16a}$$

$$\rho^f \frac{\mathrm{D}\mathbf{V}}{\mathrm{D}t} = -\nabla p + \nabla \cdot (\boldsymbol{\tau} + \boldsymbol{\tau}') \tag{2.16b}$$

$$\begin{aligned} \rho^f \frac{\mathrm{D}(\Psi + \Psi')}{\mathrm{D}t} = {} & \nabla \cdot \left[\left(k^f + \frac{\mu' c_p}{Pr'} \right) \nabla T + \left(\mu + \frac{\mu'}{\sigma} \right) \nabla E' \right] \\ & - \nabla \cdot (p\mathbf{V}) + \nabla \cdot [(\boldsymbol{\tau} + \rho^f \boldsymbol{\tau}') \cdot \mathbf{V}] \end{aligned} \tag{2.16c}$$

The variables ρ^f, $\mathbf{V}$, Ψ, p, and T are the flow quantities associated with the mean flow field. Several new variables are introduced to characterize the turbulent flow fluctuations, including the Reynolds stress tensor $\boldsymbol{\tau}'$, the turbulent kinetic energy Ψ', turbulent eddy viscosity μ' and turbulent Prandtl number Pr'.

In the SA model [142, 143], the Reynolds stress tensor is expressed in a manner similar to the viscous stress tensor Eq. (2.3),

$$-\boldsymbol{\tau}' = \nu' \left[\nabla \mathbf{V} + \nabla \mathbf{V}^T - \frac{2}{3} (\nabla \cdot \mathbf{V}) \mathbf{I} \right] \tag{2.17}$$

where the kinematic eddy viscosity ν' is a new scalar variable that has to be solved via a transport equation,

$$\begin{aligned} \frac{\mathrm{D}\nu^*}{\mathrm{D}t} = {} & c_{b1}(1 - f_{t2}) S^* \nu^* + \frac{1}{\sigma} \left[\nabla \cdot ((\nu + \nu^*) \nabla \nu^*) + c_{b2} (\nabla \nu^*)^2 \right] \\ & - \left(c_{w1} f_w - \frac{c_{b1}}{\kappa^2} f_{t2} \right) \left(\frac{\nu^*}{d} \right)^2 \end{aligned} \tag{2.18}$$

where d is the distance from the closest wall surface, and

$$\nu' = \nu^* f_{v1}, \quad f_{v1} = \frac{\xi^3}{\xi^3 + c_{v1}^3}, \quad \xi = \frac{\nu'}{\nu} \tag{2.19a}$$

$$S^* = S + \frac{\nu}{\kappa^2 d^2} f_{v2}, \quad S = ||\nabla \mathbf{V} - \nabla \mathbf{V}^T||, \quad f_{v2} = 1 - \frac{\xi}{1 + \xi f_{v1}} \tag{2.19b}$$

$$f_w = g\left(\frac{1 + c_{w3}^6}{g^6 + c_{w3}^6}\right)^{\frac{1}{6}}, \quad g = r[1 + c_{w2}(r^5 - 1)], \quad r = \min\left(\frac{\mu^*}{S^* \kappa^2 d^2}, 10\right) \tag{2.19c}$$

$$f_{t2} = c_{t3} \exp(-c_{t4} \xi^4), \quad c_{w1} = \frac{c_{b1}}{\kappa^2} + \frac{1 + c_{b2}}{\sigma} \tag{2.19d}$$

The coefficients associated with the SA model are provided in Table 2.1. In addition, the turbulent viscosity at the inflow boundary of the fluid domain is set to be five times of the gas viscosity, so as to guarantee a *fully-turbulent* boundary layer.

Table 2.1: Coefficients in the SA turbulence model

σ	κ	c_{b1}	c_{b2}	c_{w2}	c_{w3}	c_{v1}	c_{t3}	c_{t4}
2/3	0.41	0.1355	0.622	0.3	2.0	7.1	1.2	0.5

2.2.2 Arbitrary Lagrangian-Eulerian Formulation

For fully-coupled aerothermoelastic simulation, the geometry of the flow field changes due to the structural deformation. Therefore, a dynamic mesh capability is required for the RANS CFD solver. In the coupled simulation, the structural response results in the deformation of the fluid domain and hence the motion of the CFD mesh. The mesh motion requires an appropriate implementation of an arbitrary Lagrangian-Eulerian (ALE) formulation in the CFD solver [69]. The central problem in ALE formulation is the implementation of the geometric conservation law (GCL) condition, first proposed in Ref. [145] for structured grids and finite difference schemes. The GCL states that a flow field initialized with uniform distribution of flow states should remain unchanged during an unsteady CFD solution where mesh motion is present. The violation of GCL degrades time accuracy of

the solution [70]. Moreover, it is pointed out in Ref. [74] that, satisfying GCL is a necessary and sufficient condition for a numerical scheme to preserve the stability of its fixed grid counterpart. There are two approaches for correct implementation of GCL in an ALE formulation. In the first approach, a source term is added to the fluid equation, so that GCL is enforced when the equation is discretized, as shown in Refs. [71] and [72]. In the second approach, a grid velocity is computed using a carefully designed interpolation scheme, as proposed in Ref. [146]. In this study, the GCL is implemented using the mesh interpolation scheme presented in Ref. [146] and modified in Ref. [147], which enables stable and second-order time-accurate unsteady simulation involving mesh deformation.

The RANS equation with the ALE formulation [69] is written formally as,

$$\left.\frac{\partial Uw}{\partial t}\right|_{\tilde{\chi}} + U\nabla\cdot[F_c(w) - v_g w] = U\nabla\cdot F_d(w) + UF_s(w) \tag{2.20}$$

where F_c, F_d, F_s are the terms for convective flux, diffusive flux, and the source, respectively.

$$v_g = \left.\frac{\partial\chi}{\partial t}\right|_{\tilde{\chi}} \tag{2.21}$$

$$U = \left|\frac{\partial\chi}{\partial\tilde{\chi}}\right| \tag{2.22}$$

The major difference between Eq. (2.20) and RANS equations for stationary mesh is the inclusion of mesh velocity v_g, which describes the motion of mesh χ relative to the reference frame $\tilde{\chi}$. The mesh χ in the nth step is determined by the wall deformation $\mathbf{u}_F$, i.e. $\chi^n = \chi(\mathbf{u}_F^n)$.

Using the mesh interpolation scheme, Eq. (2.20) is discretized as,

$$\frac{3(\mathbf{Uw})^{n+1} - 4(\mathbf{Uw})^n + (\mathbf{Uw})^{n-1}}{2\Delta t} + \mathbf{F}_c(\mathbf{w}^{n+1}, \bar{\boldsymbol{\nu}}, \bar{\boldsymbol{\kappa}}) = \mathbf{F}_v(\mathbf{w}^{n+1}, \chi^{n+1}, \dot{\mathbf{u}}_F^{n+1}, \mathbf{T}_w^{n+1}) \tag{2.23}$$

If the mesh is stationary, the convective flux term $\mathbf{F}_c$ can be computed using the mesh

cell face normal $\bar{\boldsymbol{\nu}}$ of the current mesh χ^{n+1}, and the normal velocity of the cell face $\bar{\boldsymbol{\kappa}}$ is zero. When mesh motion is present, the quantities $\bar{\boldsymbol{\nu}}$ and $\bar{\boldsymbol{\kappa}}$ have to be computed using the weighted average of meshes from current and previous time steps.

$$\bar{\boldsymbol{\nu}} = \sum_{k=1}^{4} \vartheta_k \boldsymbol{\nu}(\chi^{(k)}) \tag{2.24}$$

$$\bar{\boldsymbol{\kappa}} = \sum_{k=1}^{4} \vartheta_k \mathbf{v}_g^{(k)} \boldsymbol{\nu}(\chi^{(k)}) \tag{2.25}$$

where $\boldsymbol{\nu}$ maps the mesh to the cell surface normal, and

$$\chi^{(k)} = \varphi_k^{n+1}\chi^{n+1} + \varphi_k^{n}\chi^{n} + \varphi_k^{n-1}\chi^{n-1} \tag{2.26}$$

$$\mathbf{v}_g^{(1)} = \mathbf{v}_g^{(2)} = \frac{\chi^{n+1} - \chi^{n}}{\Delta t}, \quad \mathbf{v}_g^{(3)} = \mathbf{v}_g^{(4)} = \frac{\chi^{n} - \chi^{n-1}}{\Delta t} \tag{2.27}$$

The following set of parameters is used to satisfy GCL and achieve second-order time accuracy [146],

$$\begin{aligned}
&\varphi_1^{n+1} = K_1, \quad \varphi_1^{n} = K_2, \quad \varphi_1^{n-1} = 0, \quad \varphi_2^{n+1} = K_2, \quad \varphi_2^{n} = K_1, \quad \varphi_2^{n-1} = 0,\\
&\varphi_3^{n+1} = 0, \quad \varphi_3^{n} = K_1, \quad \varphi_3^{n-1} = K_2, \quad \varphi_4^{n+1} = 0, \quad \varphi_4^{n} = K_2, \quad \varphi_4^{n-1} = K_1,
\end{aligned}$$

$$\vartheta_1 = \vartheta_2 = \frac{3}{4}, \quad \vartheta_3 = \vartheta_4 = -\frac{1}{4}, \text{ and } K_1 = \frac{1}{2}\left(1 + \frac{1}{\sqrt{3}}\right), \quad K_2 = \frac{1}{2}\left(1 - \frac{1}{\sqrt{3}}\right)$$

In the viscous flux and the source terms $\mathbf{F}_v$, no-slip condition has to be enforced to match local velocity of the wall boundary $\dot{\mathbf{u}}_F$. Instead of directly providing the boundary velocity to the fluid solver, the velocity is interpolated from the current and the previous meshes using a three-point backward differencing formula [148],

$$\dot{\mathbf{u}}_F^{n+1} = \frac{3\mathbf{u}_F^{n+1} - 4\mathbf{u}_F^{n} + \mathbf{u}_F^{n-1}}{2\Delta t} \tag{2.28}$$

In this manner, only a single piece of information, the displacement, has to be transferred

from the structural solver to the CFD solver at every time step, which is convenient in code implementation.

The fluid solution $\mathbf{w}$ is solved using Eq. (2.23) and depends on the wall deformation of the current and previous steps, and the wall temperature of the current step. The aerodynamic pressure $\mathbf{p}$ and heat flux $\dot{\mathbf{q}}$ on the deforming wall surface obtained from the fluid solution are symbolically represented as,

$$\dot{\mathbf{q}}^{n+1} = \dot{\mathbf{q}}^{CFD}(\mathbf{u}_F^{n+1}, \mathbf{u}_F^{n}, \mathbf{u}_F^{n-1}, \mathbf{T}_w^{n+1}) \tag{2.29a}$$

$$\mathbf{p}^{n+1} = \mathbf{p}^{CFD}(\mathbf{u}_F^{n+1}, \mathbf{u}_F^{n}, \mathbf{u}_F^{n-1}, \mathbf{T}_w^{n+1}) \tag{2.29b}$$

2.2.3 Overview of the ADflow Code

The RANS CFD solver used in this study is based on the code Automatic Differentiation flow (ADflow) [149, 150]. The ADflow solver is a multi-block solver for Euler, laminar NS and RANS equations with steady, unsteady, and time-periodic temporal modes. The ADflow code is Message Passing Interface compatible, allowing for massively parallel computations on multiple CPU clusters. A finite volume numerical method combined with the Roe flux scheme is employed to yield a second-order accurate spatial discretization. A three-point backward difference formula is employed for second-order time-accurate unsteady simulation. The CFD mesh is deformed according to the moving boundary using an explicit computationally-efficient interpolation scheme. The discretized RANS equations are solved using the dual time-stepping approach, which is accelerated using the the multigrid scheme and Newton-Krylov method.

The ADflow code is capable of accounting for both perfect gas and ideal gas models. For stability bounary calculations, the differences between the predictions of the perfect gas and ideal gas models are negligible [1]. Therefore, the perfect gas model is employed for the flow field calculation due to its simplicity.

The ADflow solver has the restart capability, which is important for both steady/un-

steady hypersonic simulations. In hypersonic regime, if the flow solution is initialized uniformly using the free stream condition, the simulation takes thousands of iterations to converge, i.e. to develop boundary layers and shock structures. When the solver is restarted, the flow simulation is initialized with a converged flow solution. Therefore, the restarted simulation is already nearly convergent, and the computational cost is reduced significantly. Furthermore, when the solution is nearly convergent, the solver is numerically stable, so that acceleration techniques, such as the Newton-Krylov method, can be applied to accelerate the convergence. The restart capability is used extensively for sample generation in the fluid ROM, as will be presented in Section 2.4.5.

Finally, note that a RANS CFD solver generates a time-averaged flow solution and therefore cannot capture the high-frequency pressure fluctuation due to turbulent boundary layer (TBL), known as the TBL load [151]. As a result, the effect of TBL load is not modeled in the current aerothermoelastic analysis framework.

2.3 Analytical Models

Analytical models provide pointwise analytical representation for the pressure and the heat flux. This means that the fluid solution at a point only depends on the properties of the wall boundary and the freestream at that point.

2.3.1 Pressure Distribution

2.3.1.1 Piston Theory

Piston theory is based on the simplification of Euler aerodynamics at the high Mach number limit [51]. It became a popular analytical model for unsteady aerodynamic pressure prediction [52], and has been employed for the flutter boundary calculation of a typical wing section in hypersonic flow [90]. It outperformed other analytical models when compared with the CFD-based solution.

The formulation of the full-order piston theory is [52],

$$p^{PT}(u_F, \dot{u}_F) = p_\infty \left(1 + \frac{\gamma - 1}{2} M_n\right)^{\frac{2\gamma}{\gamma-1}} - p_\infty \tag{2.30}$$

where the normal Mach number M_n is the Mach number associated with the flow velocity component that is perpendicular to the deforming surface,

$$M_n = M_\infty u_{F,x} + \frac{\dot{u}_F}{a_\infty} \tag{2.31}$$

The PT is applicable to any geometric scale and flight conditions with $M_\infty > \sqrt{2}$ [45, 52] and it is independent of the wall temperature. However, the formulation is only applicable for $M_n \ll 1$ [45, 52].

There are two variants of the PT, namely the first-order and third-order piston theory, that are based on the Taylor series expansion of Eq. (2.30) [52, 110]

$$\text{First-order PT:} \quad p^{PT1}(u_F, \dot{u}_F) = \gamma p_\infty M_n \tag{2.32a}$$

$$\text{Third-order PT:} \quad p^{PT3}(u_F, \dot{u}_F) = \gamma p_\infty M_n \left[1 + \frac{1+\gamma}{4} M_n + \frac{1+\gamma}{12} M_n^2\right] \tag{2.32b}$$

Both the first-order and third-order PT have been employed in the flutter boundary calculation of hypersonic vehicle structures, such as the skin panel [45] and the control surface [110]. However, in the current study, only the full-order PT Eq. (2.30) is employed in the flutter boundary calculation, due to its simplicity in the mathematical formulation. Equations (2.32a) and (2.32b) are introduced to assist the mathematical formulation of the fluid ROM, which will be discussed in the next section.

2.3.1.2 Modified Piston Theory With Effective Shape

Another variation of piston theory that accounts for the presence of the boundary layer utilizes the concept of effective shape [110, 112], where the normal displacement of the

structure is augmented by the presence of the boundary layer, whose thickness changes along the structure is

$$M_n = M_\infty(u_{F,x} + \delta_{,x}) + \frac{\dot{u}_F}{a_\infty} \tag{2.33}$$

The growth of 2D boundary layer can be characterized by the Cox-Crabtree (CC) formulation [152] for compressible boundary layer on a flat panel,

$$\delta^{CC}(\mathbf{c}, T_w, x) = \frac{\gamma - 1}{\gamma + 1}\left(\delta^{**}(x) + \delta^{*}(x)\frac{T_w}{T_0}\right) M_\infty^2 C_w^m \tag{2.34}$$

where $\mathbf{c}$ is the freestream condition, $C_w = \frac{\mu(T_w)T_\infty}{\mu_\infty T_w}$ is the Chapman-Rubesin coefficient, and m is a coefficient depending on the momentum and displacement thicknesses $\delta^{**}(x)$ and $\delta^{*}(x)$. For fully turbulent boundary layer [153],

$$\delta^{**}(x) = \frac{0.016}{Re_x^m}x, \quad \delta^{*}(x) = \frac{0.020}{Re_x^m}x, \quad m = \frac{1}{7} \tag{2.35}$$

where the 1/7th power law velocity profile is assumed in the turbulent boundary layer.

The strip theory is employed to model the growth of 3D boundary layer in hypersonic flow. It is assumed that the growth of the boundary layer along the freestream direction is weakly affected by the variation of flow properties along the cross-flow direction [112]. Therefore, the growth of 3D boundary layer is characterized by applying the 2D CC formulation Eq. (2.34) along the freestream flow direction,

$$\delta^{CC,3D}(\mathbf{c}, T_w, x, y) = \delta^{CC}(\mathbf{c}, T_w, \cos\beta x + \sin\beta y) \tag{2.36}$$

where β is the flow orientation angle.

2.3.1.3 Linearized Supersonic Theory

In supersonic flow regime, $\sqrt{2} \leq M_\infty \leq 5$, another approximation for inviscid pressure is provided by linearized supersonic theory (LS) [46],

$$p^{LS}(u_F, \dot{u}_F) = \frac{\gamma p_\infty M_\infty}{\sqrt{M_\infty^2 - 1}} \left(M_\infty u_{F,x} + \frac{M_\infty^2 - 2}{M_\infty^2 - 1} \frac{\dot{u}_F}{a_\infty} \right) \tag{2.37}$$

At the limit of high Mach number, i.e. $M_\infty \gg 1$,

$$\frac{M_\infty}{\sqrt{M_\infty^2 - 1}} \approx 1, \quad \frac{M_\infty^2 - 2}{M_\infty^2 - 1} \approx 1 \tag{2.38}$$

Equation (2.37) reduces to the first-order piston theory Eq. (2.32a).

Same as the piston theory, the LS is only applicable when $M_\infty u_{F,x} \ll 1$ and $\frac{\dot{u}_F}{a_\infty} \ll 1$. In this study, the LS is employed in the verification of the aeroelastic portion of the HYPATE framework, which will be presented in Chap. 7.

2.3.2 Heat Flux Distribution

The aerodynamic heat flux is computed using Eckert's reference enthalpy method [67]. The method is based on a compressible bounary layer solution over a flat plate with uniform wall temperature. The Eckert's method has been widely employed in the aerodynamic heat flux calculation in aerothermoelastic analysis [20, 66]. The formulation of Eckert's reference enthalpy method is

$$\dot{q}^{EE}(u_F, T_w) = St(T_r)\rho(T_r)V_e[H_{aw}(T_r) - H(T_w)] \tag{2.39}$$

where the enthalpy H, air density ρ and Stanton number St are temperature dependent,

$$St(T) = \frac{c_f(T)}{2Pr(T)^{2/3}} \tag{2.40}$$

$$H_{aw}(T) = H(T_e) + Pr(T)^{r_f}\frac{V_e^2}{2} \tag{2.41}$$

The recovery factor r_f and the skin friction coefficient c_f are,

$$\begin{cases} r_f = \frac{1}{3}, \quad c_f(T) = 0.370[\log_{10} Re(T, x_{le})]^{-2.584}, & \text{for turbulent flow} \\ r_f = \frac{1}{2}, \quad c_f(T) = 0.664 Re(T, x_{le})^{-0.5}, & \text{for laminar flow} \end{cases} \tag{2.42}$$

where $Re(T, x_{le}) = \frac{\rho(T)V_e x_{le}}{\mu(T)}$ and x_{le} is the distance from the leading edge. The reference temperature T_r satisfies,

$$H(T_r) = H(T_e) + 0.50[H(T_w) - H(T_e)] + 0.22[H_{aw}(T_r) - H(T_e)] \tag{2.43}$$

At the edge of the boundary layer, the pressure p_e is assumed to be equal to the wall pressure, which is computed using the piston theory Eq. (2.30). The other flow properties T_e and V_e satisfy,

$$\frac{T_e}{T_\infty} = \left(\frac{p_e}{p_\infty}\right)^{\frac{\gamma-1}{\gamma}} = \frac{1 + \frac{\gamma-1}{2}M_\infty^2}{1 + \frac{\gamma-1}{2}M_e^2}, \quad V_e = M_e\sqrt{\gamma R T_e} \tag{2.44}$$

2.4 Reduced Order Modeling

2.4.1 Modeling Strategies

The ROM techniques are applied to accelerate the CFD-based fluid solver in the HYPATE framework. The fluid solver evaluates the pressure $\mathbf{p}$ and heat flux $\dot{\mathbf{q}}$ on the structural surface given the surface deformation $\mathbf{u}_F$, surface velocity $\dot{\mathbf{u}}_F$, wall temperature $\mathbf{T}_w$ and

the flight condition $\mathbf{c}$,

$$\mathbf{c} = [M_\infty, p_\infty, T_\infty]^T \tag{2.45}$$

The ROM for the fluid solver is based on the assumption that the flow is quasi-steady. The quasi-steady flow assumption is due to the disparity of characteristic times in a hypersonic aerothermoelastic problem, and its justification is provided by an order-of-magnitude analysis of the characteristic times [20], as presented next.

The characteristic time for the fluid response is determined by Eq. (2.14a),

$$t_F = \frac{L}{M_\infty a_\infty} \tag{2.46}$$

The characteristic time for the structural response is determined by the lowest natural frequency,

$$t_S = \frac{1}{f_1} \tag{2.47}$$

For a skin panel,

$$f_1 = C\sqrt{\frac{Eh^2}{\rho^s L^4}} \tag{2.48}$$

where $C \sim 1$ is a constant that depends on the Poisson's ratio and the panel geometry.

The characteristic time for the structural response is determined by the Fourier number, which characterizes how fast the thermal response reaches equilibrium [20, 154],

$$t_T = \frac{\rho^s c_p^s h^2}{k^s} \tag{2.49}$$

For a typical metallic skin panel in hypersonic flow,

$$\begin{gathered} \rho^s \sim 10^3 \mathrm{kg/m^3}, \quad k^s \sim 10^1 \mathrm{W/mK}, \quad c_p^s \sim 10^2 \mathrm{J/kgK}, \quad E \sim 10^{11} \mathrm{Pa}, \\ L \sim 1\mathrm{m}, \quad h \sim 10^{-2}\mathrm{m}, \quad M_\infty \sim 10^1, \quad a_\infty \sim 10^2 \mathrm{m/s} \end{gathered} \tag{2.50}$$

Therefore, the orders of magnitude of the characteristic times are,

$$t_F \sim 10^{-3}\text{s}, \quad t_S \sim 10^{-2}\text{s}, \quad t_T \sim 1\text{s} \tag{2.51}$$

The results in Eq. (2.51) lead to two approximations. First, since the thermal characteristic time is much larger than the fluid and structural characteristic times, the surface heat flux is assumed to be independent of any terms associated with time derivatives, including structural velocity,

$$\dot{\mathbf{q}}(\mathbf{c}, \mathbf{u}_F, \dot{\mathbf{u}}_F, \mathbf{T}_w) = \dot{\mathbf{q}}(\mathbf{c}, \mathbf{u}_F, \mathbf{T}_w) \tag{2.52}$$

Second, the ratio between the fluid and structural characteristic times, i.e. the reduced frequency, is a small parameter,

$$\frac{t_F}{t_S} = \frac{Lf_1}{M_\infty a_\infty} \sim 10^{-1} \tag{2.53}$$

A small value of reduced frequency indicates that the aerodynamic pressure on the structure is quasi-steady, i.e. the pressure is weakly coupled with structural velocity (pp. 251-281 of [117]). The pressure distribution is decomposed into steady and unsteady components and modeled separately.

$$\mathbf{p}(\mathbf{c}, \mathbf{u}_F, \dot{\mathbf{u}}_F, \mathbf{T}_w) = \mathbf{p}^{std}(\mathbf{c}, \mathbf{u}_F, \mathbf{T}_w) + \mathbf{p}^{uns}(\mathbf{c}, \mathbf{u}_F, \dot{\mathbf{u}}_F) \tag{2.54}$$

The steady pressure component $\mathbf{p}^{std}$ and the heat flux $\dot{\mathbf{q}}$ are modeled using the POD-kriging method combined with the correction and scaling methodology, which will be detailed in the following sections. The unsteady pressure component $\mathbf{p}^{uns}$ is referred to as the unsteady correction and is evaluated using piston theory [101],

$$p^{uns}(u_F, \dot{u}_F) = p^{PT}(u_F, \dot{u}_F) - p^{PT}(u_F, \dot{u}_F = 0) \tag{2.55}$$

2.4.2 The POD-Kriging Method

In the POD-kriging method, a nonlinear interpolation model for the problem is constructed from a set of data sample points $\mathcal{D} = \{\mathbf{d}_i, \mathbf{y}_i\}_{i=1}^{N_s}$, where input vector $\mathbf{d} \in \mathbb{R}^{N_d}$ and output vector $\mathbf{y} \in \mathbb{R}^{N_y}$. In the context of a fluid ROM, the input vector typically contains $N_d = 10 \sim 20$ parameters characterizing $\mathbf{c}$, $\mathbf{u}_F$ and $\mathbf{T}_w$. The optimal latin hypercube (OLH) sampling method [155] is used to generate the uniformly and randomly distributed sample inputs in the parameter space of interest. The output vector can be either the steady component of the pressure $\mathbf{p}^{std}$ or the heat flux $\dot{\mathbf{q}}$.

The POD-kriging interpolation model for the data set $\mathcal{D}$ is expressed as,

$$\mathbf{y}^{pk}(\mathbf{d}) = \mathbf{\Psi}_P \mathbf{y}^{krg}(\mathbf{d}) \tag{2.56}$$

where the POD modes $\mathbf{\Psi}_P$ represents the dominant patterns in the output vectors, which are extracted from the data set using the snapshot method [93],

$$\mathbf{y}_P = \mathbf{\Psi}_P^T \mathbf{y}, \quad \mathbf{y} \approx \mathbf{\Psi}_P \mathbf{y}_P \tag{2.57}$$

The kriging method [107, 110] is used to construct a nonlinear interpolation model between $\mathbf{d}$ and $\mathbf{y}_P$. The model is characterized by two terms,

$$\mathbf{y}^{krg}(\mathbf{d}) = \boldsymbol{\beta}_f^T \mathbf{f}(\mathbf{d}) + \boldsymbol{\beta}_r^T \mathbf{r}(\mathbf{d}) \tag{2.58}$$

where $\mathbf{f}(\mathbf{d})$ is a regression function representing the global trend of the unknown function, and $\mathbf{r}(\mathbf{d})$ is a correlation function representing the local deviation of the regression function with respect to the actual sampled data. The mathematical details of the POD method and the kriging are provided in Appendix A.

The Jacobian of the POD-kriging model w.r.t. the input is,

$$\frac{\partial \mathbf{y}^{pk}}{\partial \mathbf{d}} = \mathbf{\Psi}_P \frac{\partial \mathbf{y}^{krg}}{\partial \mathbf{d}} = \mathbf{\Psi}_P \boldsymbol{\beta}_f^T \frac{\partial \mathbf{f}}{\partial \mathbf{d}} + \mathbf{\Psi}_P \boldsymbol{\beta}_r^T \frac{\partial \mathbf{r}}{\partial \mathbf{d}} \tag{2.59}$$

where the Jacobians of $\mathbf{f}$ and $\mathbf{r}$ w.r.t. $\mathbf{d}$ can be computed analytically from their definitions Eq. (A.7).

2.4.3 Conventional ROM and Its Limitations

In previous studies [91, 102, 103], the steady component of the pressure $\mathbf{p}^{std}$ and the heat flux $\dot{\mathbf{q}}$ are modeled using the POD-kriging method directly. An extensive list of input parameters has to be included in the POD-kriging models to account for a range of flight conditions of interest, structural deformation and non-uniform wall temperature distribution. The flight conditions include N_F parameters, such as M_∞ and T_∞. The structural deformation and the wall temperature are represented using a linear combination of N_S structural modes and N_T thermal modes, respectively,

$$\mathbf{u}_F = \mathbf{\Psi}_S \mathbf{a} \tag{2.60a}$$

$$\mathbf{T}_w = \mathbf{\Psi}_T \mathbf{b} \tag{2.60b}$$

The conventional POD-kriging models are

$$\mathbf{p}^{std}(\mathbf{c}, \mathbf{u}_F, \mathbf{T}_w) = \mathbf{p}^{pk}(\mathbf{d}) \tag{2.61a}$$

$$\dot{\mathbf{q}}(\mathbf{c}, \mathbf{u}_F, \mathbf{T}_w) = \dot{\mathbf{q}}^{pk}(\mathbf{d}) \tag{2.61b}$$

where the input vector for this approach has $(N_F + N_S + N_T)$ entries,

$$\mathbf{d}^T = [\mathbf{c}^T, \mathbf{a}^T, \mathbf{b}^T] = [\mathbf{c}^T, \mathbf{u}_F^T \mathbf{\Psi}_S, \mathbf{T}_w^T \mathbf{\Psi}_T] \tag{2.62}$$

However, the conventional POD-kriging-based fluid ROM has three limitations. The first two limitations are the issues of characterization and generalization, as discussed in Section 1.2.3. The limitation in generalization is due to the *a priori* assumption on the form of the wall temperature, such as simple polynomials [91, 103] and POD modes of a low-fidelity thermal solution [102]. The simplifying assumption usually proves to be inaccurate for the nonuniform wall temperature distribution in an actual aerothermoelastic problem [113, 114]. The limitation in characterization is due to the fact that the model is only suitable for a fixed geometrical configuration, since the sample data set is generated for a particular geometrical configuration. Finally, the third limitation is the curse of dimensionality, caused by the numerous parameters needed for representing the flight conditions and the wall temperature. The sample data for generating the model has to cover the parameter space of interest. The requirement of coverage of the parameter space causes the number of samples to grow exponentially with the number of entries in the ROM input vector $\mathbf{d}$, which would dramatically increase the computational cost for ROM generation.

Previous studies [114] have suggested a pointwise correction model for the heat flux, which is based on a generalized Chapman–Rubesin solution for turbulent flow over a flat surface. This approach predicts accurately the heat flux with respect to arbitrary temperature distributions, including the non-smooth distribution due to the presence of boundary layer transition and shock wave/boundary layer interaction. However, this approach relies on the tuning of empirical coefficients that depends on flight conditions and geometrical configurations. For the cases considered in the current study, where the temperature distribution is expected to be smooth, a new correction model that does not rely on empirical coefficients is developed. The new correction model is advantageous due to its simplicity and analytical form. It can be conveniently implemented for engineering applications and serves as an alternative to the more comprehensive but more complex pointwise correction model proposed in Ref. [114].

2.4.4 Scaled and Corrected Fluid ROM Formulation

A methodology for correction and scaling is developed to overcome the three limitations of the conventional POD-kriging method, as indicated earlier. First, the POD-kriging models for aerodynamic pressure and heat flux are generated for *fixed* reference flight conditions $\mathbf{c}_{ref}$, *uniform* wall temperature $\overline{T}_w$ and a *fixed* geometrical configuration with a characteristic length L_{ref}. Subsequently, the models are corrected to account for both non-uniform temperature distribution and for extrapolation to different flow conditions or geometric scale. The correction for a scaled configuration with a characteristic length L, an arbitrary flight condition $\mathbf{c}$ and with an arbitrary non-uniform wall temperature distribution $\mathbf{T}_w$ has the following form,

$$\dot{\mathbf{q}}(\mathbf{c}, \mathbf{u}_F, \mathbf{T}_w; L) = \mathbf{f}_q^{cor}(\dot{\mathbf{q}}^{pk}(\mathbf{d}); \mathbf{c}, \mathbf{u}_F, \mathbf{T}_w, \xi) \tag{2.63a}$$

$$\mathbf{p}^{std}(\mathbf{c}, \mathbf{u}_F, \mathbf{T}_w; L) = \mathbf{f}_p^{cor}(\mathbf{p}^{pk}(\mathbf{d}); \mathbf{c}, \mathbf{u}_F, \mathbf{T}_w, \xi) \tag{2.63b}$$

where $\xi = L_{ref}/L$ is the geometric scale ratio, and the subscripts q and p indicate the correction factor for heat flux and pressure, respectively. The input vector of the POD-kriging model for this approach is reduced to $(N_S + 1)$ entries:

$$\mathbf{d}^T = [\xi \mathbf{a}^T, \overline{T}_w] \tag{2.64}$$

The correction is based on recognizing that, the analytical models, such as the piston theory and the Eckert's method, have been widely used in the aerothermoelastic analysis and have generated physically meaningful results for engineering applications. The analytical models do not provide results with *absolute* accuracy comparable to the high-fidelity CFD results. However, they capture the trends with respect to the input parameters with sufficient accuracy. Therefore, the *ratio* of two analytical solutions, at two different states, can be used as a correction factor.

Utilizing this concept with Eckert's reference enthalpy method, a pointwise correction is yielded for heat flux,

$$[\mathbf{f}_q^{cor}(\dot{\mathbf{q}}^{pk};\mathbf{c},\mathbf{u}_F,\mathbf{T}_w,\xi)]_i = \frac{\dot{q}^{EE}(\mathbf{c},[\mathbf{u}_F]_i,[\mathbf{T}_w]_i)}{\dot{q}^{EE}(\mathbf{c}_{ref},\xi[\mathbf{u}_F]_i,\overline{T}_w)}[\dot{\mathbf{q}}^{pk}]_i \tag{2.65}$$

The combination of piston theory and POD-kriging-based pressure suggests the following correction,

$$[\mathbf{f}_p^{PT}(\mathbf{p}^{pk};\mathbf{c},\mathbf{u}_F,\mathbf{T}_w,\xi)]_i = \frac{p^{PT}(\mathbf{c},[\mathbf{u}_F]_i,[\mathbf{T}_w]_i)}{p^{PT}(\mathbf{c}_{ref},\xi[\mathbf{u}_F]_i,\overline{T}_w)}[\mathbf{p}^{pk}]_i \tag{2.66}$$

Using the first-order piston theory Eq. (2.32a) and assuming that the heat capacity ratio γ is constant, the correction Eq. (2.66) is simplified as,

$$[\mathbf{f}_p^{PT}(\mathbf{p}^{pk};\mathbf{c},\mathbf{u}_F,\mathbf{T}_w,\xi)]_i = \frac{\gamma p_\infty M_\infty [\mathbf{u}_{F,x}]_i}{\gamma p_{ref} M_{ref}[\mathbf{u}_{F,x}]_i}[\mathbf{p}^{pk}]_i \approx \frac{p_\infty M_\infty}{p_{ref}M_{ref}}[\mathbf{p}^{pk}]_i \tag{2.67}$$

Equation (2.67) is denoted the *PT correction*.

A noteworthy aspect of piston theory is that it does not take account of the boundary layer effect. An alternative correction for pressure is based on the modified piston theory with effective shape, which accounts for the geometrical shape change due to the boundary layer. Since the flow is inviscid outside the boundary layer, the piston theory is applied to compute the pressure on the effective shape [110, 112]. Alternatively, if the surface pressure is provided by the ROM, the slope of effective shape can be estimated using Eqs. (2.30) and (2.33),

$$\delta_{,x}^{PT}(p^{pk};\mathbf{c}_{ref},\xi u_F,\overline{T}_w) = \frac{2}{(\gamma-1)M_{ref}}\left[\left(1+\frac{p^{pk}}{p_{ref}}\right)^{\frac{\gamma-1}{2\gamma}}-1\right] - u_{F,x} \tag{2.68}$$

The slope of the boundary layer $\delta_{,x}^{pk}$ is associated with the geometrical configuration of the reference ROM, and it is corrected to account for the changes in flight conditions and

geometric scales using Eq. (2.34),

$$f^{cor}_{\delta,x}(p^{pk};\mathbf{c},u_F,T_w,\xi) = R_\delta \delta^{PT}_{,x}(p^{pk}) \tag{2.69}$$

where R_δ is a correction factor based on the Cox-Crabtree formulation,

$$R_\delta = \frac{\delta^{CC}_{,x}(\mathbf{c},x)}{\delta^{CC}_{,x}(\mathbf{c}_{ref},\xi x)} \tag{2.70}$$

Finally, the new pressure is computed using the modified PT with effective shape, Eqs. (2.30) and (2.33),

$$[\mathbf{f}^{BL}_p(\mathbf{p}^{pk};\mathbf{c},\mathbf{u}_F,\mathbf{T}_w,\xi)]_i = p_\infty \left[1 + \frac{\gamma-1}{2} M_\infty \left([\mathbf{u}_{F,x}]_i + f^{cor}_{\delta,x}([\mathbf{p}^{pk}]_i)\right)\right]^{\frac{2\gamma}{\gamma-1}} - p_\infty \tag{2.71}$$

The correction based on the modified piston theory with effective shape is denoted as the *boundary layer (BL) correction*. Combining Eqs. (2.68-2.71), the BL correction is formulated as,

$$\begin{aligned}[\mathbf{f}^{BL}_p(\mathbf{p}^{pk};\mathbf{c},\mathbf{u}_F,\mathbf{T}_w,\xi)]_i = p_\infty \Bigg\{ & 1 + (1-R_\delta)\frac{\gamma-1}{2} M_\infty [\mathbf{u}_{F,x}]_i \\ & + R_\delta \frac{M_\infty}{M_{ref}} \left[\left(1 + \frac{[\mathbf{p}^{pk}]_i}{p_{ref}}\right)^{\frac{\gamma-1}{2\gamma}} - 1 \right] \Bigg\}^{\frac{2\gamma}{\gamma-1}} - p_\infty \end{aligned} \tag{2.72}$$

The corrections for pressure and heat flux take care of the discrepancy in the wall temperature and flight conditions without introducing any empirical coefficients. Moreover, the models account for the geometric scaling using a new parameter ξ. Such a correction is important because it expands the applicability of the ROM to a wider range of applications, and greatly reduces the cost for ROM generation by reducing the number of required input parameters and resulting in the reduction of the number of samples.

The final forms of the fluid ROM are represented by the following relations,

$$\dot{\mathbf{q}}(\mathbf{c}, \mathbf{u}_F, \dot{\mathbf{u}}_F, \mathbf{T}_w) = \mathbf{f}_q^{cor}(\dot{\mathbf{q}}^{pk}(\mathbf{d}); \mathbf{c}, \mathbf{u}_F, \xi) \tag{2.73a}$$

$$\mathbf{p}(\mathbf{c}, \mathbf{u}_F, \dot{\mathbf{u}}_F, \mathbf{T}_w) = \mathbf{f}_p^{cor}(\mathbf{p}^{pk}(\mathbf{d}); \mathbf{c}, \mathbf{u}_F, \xi) + \mathbf{p}^{uns}(\mathbf{c}, \mathbf{u}_F, \dot{\mathbf{u}}_F) \tag{2.73b}$$

where $\mathbf{f}_p^{cor}$ can be the PT correction $\mathbf{f}_p^{PT}$ or the BL correction $\mathbf{f}_p^{BL}$.

For PT correction, the Jacobians of the pressure w.r.t. the displacement and the velocity are determined analytically from Eqs. (2.55), (2.67) and (2.73b),

$$\frac{\partial \mathbf{p}}{\partial \mathbf{u}_F} = \frac{p_\infty M_\infty}{p_{ref} M_{ref}} \frac{\partial \mathbf{p}^{pk}(\mathbf{d})}{\partial \mathbf{d}} \frac{\partial \mathbf{d}}{\partial \mathbf{u}_F} \tag{2.74a}$$

$$\frac{\partial \mathbf{p}}{\partial \dot{\mathbf{u}}_F} = \frac{\partial \mathbf{p}^{uns}(\mathbf{c}, \mathbf{u}_F, \dot{\mathbf{u}}_F)}{\partial \dot{\mathbf{u}}_F} \tag{2.74b}$$

For BL correction, the Jacobian of the pressure w.r.t. the velocity is the same as Eq. (2.74b). The Jacobian of the pressure w.r.t. the displacement is determined analytically using Eq. (2.72),

$$\frac{\partial \mathbf{p}}{\partial \mathbf{u}_F} = \mathbf{\Lambda}_u \left[(1 - R_\delta) \frac{\gamma - 1}{2} p_\infty M_\infty \frac{\partial \mathbf{u}_{F,x}}{\partial \mathbf{u}_F} + R_\delta \frac{p_\infty M_\infty}{p_{ref} M_{ref}} \mathbf{\Lambda}_p \frac{\partial \mathbf{p}^{pk}(\mathbf{d})}{\partial \mathbf{d}} \frac{\partial \mathbf{d}}{\partial \mathbf{u}_F} \right] \tag{2.75}$$

where $\mathbf{\Lambda}_u$ and $\mathbf{\Lambda}_p$ are diagonal matrices and their ith diagonal element are, respectively,

$$[\mathbf{\Lambda}_u]_{ii} = \left[1 + \frac{\gamma - 1}{2} M_\infty \left([\mathbf{u}_{F,x}]_i + f_{\delta,x}^{cor}([\mathbf{p}^{pk}]_i) \right) \right]^{\frac{\gamma+1}{\gamma-1}} \tag{2.76a}$$

$$[\mathbf{\Lambda}_p]_{ii} = \left(1 + \frac{[\mathbf{p}^{pk}]_i}{p_{ref}} \right)^{\frac{-\gamma-1}{2\gamma}} - 1 \tag{2.76b}$$

2.4.5 Efficient ROM Sample Generation

Over 95% of the time for generating a fluid ROM is spent on the computation of the sample fluid solutions. The smart ordering scheme accelerates the computation of the samples, and reduces the computational cost of ROM generation by a factor of 2.

The scheme utilizes the "restart" capability of the CFD solver. The fluid simulation is initialized using a reference solution $\mathbf{w}^*$, and converges to the actual solution $\mathbf{w}$ after a certain number of iterations. When the reference solution is similar to the actual solution, the solver converges in fewer iterations and requires less computer time. The smart ordering scheme initializes a sample solution $\mathbf{w}$ using another sample solution $\mathbf{w}^*$ that is the most similar to $\mathbf{w}$, so that the computational cost of $\mathbf{w}$ is minimized. The similarity between the reference solution $\mathbf{w}^*$ and the actual solution $\mathbf{w}$ is characterized by the "distance" between the two fluid solutions.

The fluid solution depends on the flight conditions, structural deformation, and wall temperature,

$$\mathbf{w} = \mathbf{w}(\mathbf{c}, \mathbf{u}_F, \mathbf{T}_w) \tag{2.77}$$

Assuming that the computational cost of the fluid solution is proportional to the difference between the reference and actual solutions, one has,

$$\begin{aligned} t_{CFD}(\mathbf{w}) &\propto ||\mathbf{w} - \mathbf{w}^*|| \\ &= ||\mathbf{w}(\mathbf{c}, \mathbf{u}_F, \mathbf{T}_w) - \mathbf{w}(\mathbf{c}^*, \mathbf{u}_F^*, \mathbf{T}_w^*)|| \\ &\leq C_1||\mathbf{c} - \mathbf{c}^*|| + C_2||\mathbf{u}_F - \mathbf{u}_F^*|| + C_3||\mathbf{T}_w - \mathbf{T}_w^*|| \end{aligned} \tag{2.78}$$

where C_1, C_2, C_3 are constants in the Taylor series expansion of $\mathbf{w}(\mathbf{c}, \mathbf{u}_F, \mathbf{T}_w)$.

In the POD-kriging ROM, the structural deformation and wall temperature are represented using shape functions provided by Eqs. (2.60a)-(2.60b). Assuming the shape functions are orthogonal and normalized,

$$||\mathbf{u}_F - \mathbf{u}_F^*|| = \|\mathbf{\Psi}_S\mathbf{a} - \mathbf{\Psi}_S\mathbf{a}^*\| = \|\mathbf{a} - \mathbf{a}^*\| \tag{2.79}$$

$$||\mathbf{T}_w - \mathbf{T}_w^*|| = \|\mathbf{\Psi}_T\mathbf{b} - \mathbf{\Psi}_T\mathbf{b}^*\| = \|\mathbf{b} - \mathbf{b}^*\| \tag{2.80}$$

Combining equations (2.78)-(2.80), the distance between two fluid solutions is defined

as,

$$d_{CFD}(\mathbf{w}, \mathbf{w}^*) = \sqrt{\sum_{i=1}^{N_F} D_{1i}(c_i - c_i^*)^2 + D_2||\mathbf{a} - \mathbf{a}^*|| + D_3||\mathbf{b} - \mathbf{b}^*||} \tag{2.81}$$

where D_{1i}, D_2, D_3 are empirical constants for nondimensionalization, so that the quantities with different dimensions, such as the structural and thermal modal amplitudes $\mathbf{a}$ and $\mathbf{b}$, can be combined.

The total computational cost of computing the ROM samples $\mathcal{D}$ is proportional to the sum of the distances between the fluid solutions and their reference solutions.

$$t_{CFD}(\mathcal{D}) \propto \sum_{i=1}^{N_s} d_{CFD}(\mathbf{w}_i, \mathbf{w}_i^*) \tag{2.82}$$

The reference solution $\mathbf{w}_i^*$ can be a naive fluid solution $\mathbf{w}_0$ defined as one that represents the flow field for the undeformed panel with uniform wall temperature. The naive fluid solution is computed before the ROM generation. The reference solution can also be one of the sample fluid solutions. The best reference solution $\mathbf{w}_i^*$ is the one that is the closest to the ith sample $\mathbf{w}_i$, so that the computation cost of $\mathbf{w}_i$ is minimized. In conventional ROM generation, the samples are always restarted using the naive fluid solution $\mathbf{w}_0$.

The algorithm for smart ordering scheme is presented in Appendix B. The samples are ordered such that:

1. The first sample solution is restarted using the naive fluid solution $\mathbf{w}_0$.
2. The reference solution for the jth sample $\mathbf{w}_j$ is chosen to be the ith sample $\mathbf{w}_i$ that minimizes $d_{CFD}(\mathbf{w}_i, \mathbf{w}_j)$, and the sample $\mathbf{w}_i$ is always computed before $\mathbf{w}_j$.
3. Multiple samples might use the same sample solution as reference solution.

The comparison of the computational cost using the conventional method and the smart ordering scheme is given in Table 2.2. For simplicity, the fluid solution is described using 3 structural modes only, i.e. $N_F = 0, N_S = 3, N_T = 0$. One hundred 3D solutions are generated. Using smart ordering scheme, the sample generation is accelerated by a factor of two, approximately.

Table 2.2: Computational cost for sample generation

	Conventional	Smart ordering	Acceleration
Euler	1.2 hrs	0.7 hrs	1.7
RANS	2 hrs	0.9 hrs	2.2

CHAPTER 3

Structural Dynamic Model

In this chapter, the structural dynamic model is developed for an anisotropic doubly-curved shallow shell, including the effects of transverse shear deformations, geometric nonlinearity and thermal stress. Next, a dimensional analysis is applied to Hamilton's principle to identify the similarity parameters for the structural problem, which are required for the development of ASL described in the following chapters. Finally, the finite element discretization of the structural dynamic equations is presented together with its solution.

3.1 Governing Equations

3.1.1 Basic Assumptions

The skin panel of a hypersonic vehicle may undergo moderate deflections [8, 49] in some cases and the transverse shear effect is significant when employing composite materials for construction [45]. Therefore, doubly-curved shallow shell equations with first-order shear deformation theory (FSDT) and von Karman strain (pp. 621-626 of [156]) are used in the current study. The assumptions made:

1. The panel is thin, i.e. the thickness-to-span ratio of the panel is less than 1/20 [157], therefore FSDT is appropriate.
2. The curvature of the panel is shallow, i.e. the span-to-radius ratio of the panel is less than 0.5 [157], therefore shallow shell theory is applicable.

3. The panel undergoes moderate rotation with small strain, thus von Karman strain is appropriate for representing the deformations.
4. No change in thickness due to external loading, i.e. total normal strain in thickness direction is neglected.
5. Under non-uniform thermal loading, the traditional composite constitutive relation with thermal strain can be used.

3.1.2 Kinematics and Constitutive Relations

The displacement field of the shell is characterized by five variables illustrated in Fig. 3.1: the transverse displacement w, the in-plane displacement u, v of the middle surface, and the rotation ψ_x, ψ_y w.r.t. the middle surface. For a doubly-curved shallow shell, the membrane strain and the transverse shear strain by FSDT are (pp. 621-626 of [156]),

$$\boldsymbol{\epsilon} = [\epsilon_{xx}, \epsilon_{yy}, \gamma_{xy}]^T = \boldsymbol{\epsilon}_l + \boldsymbol{\epsilon}_{nl} + z\boldsymbol{\chi} \tag{3.1a}$$

$$\boldsymbol{\gamma} = [\gamma_{xz}, \gamma_{yz}]^T \tag{3.1b}$$

where,

$$\boldsymbol{\epsilon}_l = \begin{bmatrix} u_{,x} + \dfrac{w}{R_x} \\ v_{,y} + \dfrac{w}{R_y} \\ u_{,y} + v_{,x} \end{bmatrix}, \quad \boldsymbol{\epsilon}_{nl} = \begin{bmatrix} \frac{1}{2}w_{,x}^2 \\ \frac{1}{2}w_{,y}^2 \\ w_{,x}w_{,y} \end{bmatrix}, \quad \boldsymbol{\chi} = \begin{bmatrix} \psi_{x,x} \\ \psi_{y,y} \\ \psi_{x,y} + \psi_{y,x} \end{bmatrix}, \quad \boldsymbol{\gamma} = \begin{bmatrix} -\dfrac{u}{R_x} + w_{,x} + \psi_x \\ -\dfrac{v}{R_y} + w_{,y} + \psi_y \end{bmatrix} \tag{3.2}$$

The von Karman strain $\boldsymbol{\epsilon}_{nl}$ is used to describe moderate shell deflections. Furthermore, $\boldsymbol{\epsilon}_0 = \boldsymbol{\epsilon}_l + \boldsymbol{\epsilon}_{nl}$ is defined as the total membrane strain.

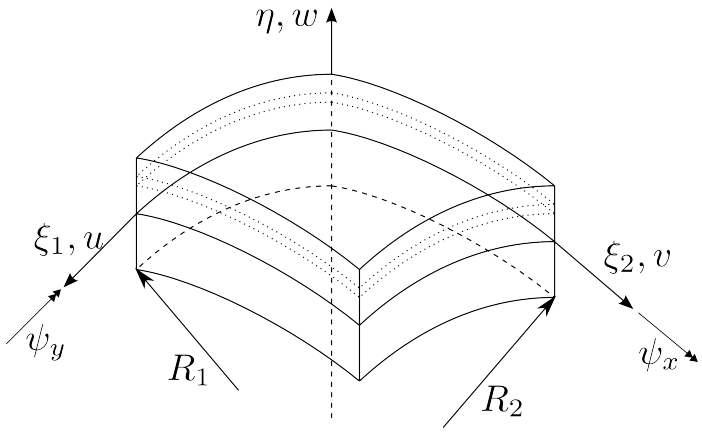

Figure 3.1: Local curvilinear coordinate system (ξ_1, ξ_2, ζ) in doubly-curved shallow shell of laminated composites

Consider the ith lamina in a laminated composite shell, which extends from h_i to h_{i+1} in the thickness direction. The constitutive relation is,

$$\boldsymbol{\sigma}_E = \mathbf{Q}_i(\boldsymbol{\epsilon} + z\boldsymbol{\chi} - \boldsymbol{\alpha}_i \Delta T), \quad \boldsymbol{\tau}_E = \mathbf{G}_i \boldsymbol{\gamma} \tag{3.3}$$

where,

$$\boldsymbol{\sigma}_E = \begin{bmatrix} \sigma_{xx} \\ \sigma_{yy} \\ \sigma_{xy} \end{bmatrix}, \quad \mathbf{Q}_i = \begin{bmatrix} Q^i_{11} & Q^i_{12} & Q^i_{13} \\ Q^i_{12} & Q^i_{22} & Q^i_{23} \\ Q^i_{13} & Q^i_{23} & Q^i_{66} \end{bmatrix}, \quad \boldsymbol{\alpha}_i = \begin{bmatrix} \alpha^i_{xx} \\ \alpha^i_{yy} \\ \alpha^i_{xy} \end{bmatrix} \tag{3.4}$$

and,

$$\boldsymbol{\tau}_E = \begin{bmatrix} \sigma_{yz} \\ \sigma_{xz} \end{bmatrix}, \quad \mathbf{G}_i = \begin{bmatrix} Q^i_{44} & Q^i_{45} \\ Q^i_{45} & Q^i_{55} \end{bmatrix} \tag{3.5}$$

where Q_{ij} are elastic constants, α_i are thermal expansion coefficients of the ith lamina and ΔT is a temperature increment.

Assuming a known temperature distribution in the structure, integration of Eq. (3.3) through the thickness produces the in-plane forces $\mathbf{N}_E = [N_{Ex}, N_{Ey}, N_{Exy}]^T$, moments

$\mathbf{M}_E = [M_{Ex}, M_{Ey}, M_{Exy}]^T$ and transverse shear forces $\mathbf{T}_E = [T_{Ey}, T_{Ex}]^T$.

$$(\mathbf{N}_E, \mathbf{M}_E, \mathbf{T}_E) = \int_{-h/2}^{h/2} (\boldsymbol{\sigma}_E, z\boldsymbol{\sigma}_E, \boldsymbol{\tau}_E) \mathrm{d}z \tag{3.6}$$

Since $\mathbf{Q}_i$ and $\boldsymbol{\alpha}_i$ vary from layer to layer, the integration over $[-\frac{h}{2}, \frac{h}{2}]$ has to be performed in a piecewise manner. After the integration, one has,

$$\begin{aligned} \begin{bmatrix} \mathbf{N}_E \\ \mathbf{M}_E \end{bmatrix} &= \begin{bmatrix} \mathbf{A} & \mathbf{B} \\ \mathbf{B} & \mathbf{D} \end{bmatrix} \begin{bmatrix} \boldsymbol{\epsilon} \\ \boldsymbol{\chi} \end{bmatrix} - \begin{bmatrix} \mathbf{N}_T \\ \mathbf{M}_T \end{bmatrix} \\ \mathbf{T}_E &= \mathbf{S}\boldsymbol{\gamma} \end{aligned} \tag{3.7}$$

where, $\mathbf{A}, \mathbf{B}, \mathbf{D}$ are extensional, extension-bending and bending matrices, respectively, $\mathbf{S}$ is transverse shear stiffness matrix, and $\mathbf{N}_T, \mathbf{M}_T$ are forces and moments due to thermal effect.

$$(\mathbf{A}, \mathbf{B}, \mathbf{D}) = \sum_{i=1}^{N_l} \int_{h_i}^{h_{i+1}} (1, z, z^2) \mathbf{Q}_i \mathrm{d}z \tag{3.8a}$$

$$\mathbf{S} = \kappa \left(\sum_{i=1}^{N_l} \int_{h_i}^{h_{i+1}} \mathbf{G}_i \mathrm{d}z \right) \tag{3.8b}$$

$$(\mathbf{N}_T, \mathbf{M}_T) = \sum_{i=1}^{N_l} \int_{h_i}^{h_{i+1}} (1, z) \mathbf{Q}_i \boldsymbol{\alpha}_i \Delta T \mathrm{d}z \tag{3.8c}$$

Note that a shear correction factor κ is used in the calculation of $\mathbf{S}$. The actual transverse shear stress distribution across the thickness is non-uniform. For example, in homogeneous beams and plates, the distribution is parabolic. However, the shear stress distribution is assumed to be constant in FSDT. To correct this discrepancy, the transverse shear strain energy predicted by FSDT is multiplied by a factor κ, so that the modified transverse shear strain energy is equal to the actual transverse shear strain energy. In current study, $\kappa = \frac{5}{6}$ (pp. 135-136 of [156]).

When the temperature is non-uniform and material properties are temperature-dependent, and the integrations defining $\mathbf{A}, \mathbf{B}, \mathbf{D}, \mathbf{S}, \mathbf{N}_T$, and $\mathbf{M}_T$ are approximated using Simpson's

rule. For example,

$$\mathbf{A} = \sum_{i=1}^{N} \int_{h_i}^{h_{i+1}} \mathbf{Q}_i \mathrm{d}z \approx \sum_{i=1}^{N} \left\{ \frac{h_{i+1} - h_i}{6} \left[\mathbf{Q}_i(h_i) + 4\mathbf{Q}_i \left(\frac{h_i + h_{i+1}}{2} \right) + \mathbf{Q}_i(h_{i+1}) \right] \right\} \tag{3.9}$$

where $\mathbf{Q}_i(z) \equiv \mathbf{Q}_i(\Delta T(z))$.

3.1.3 Hamilton's Principle

Using constitutive relation Eq. (3.7), the strain energy $\mathcal{U}$ of the shell is,

$$\mathcal{U} = \frac{1}{2} \int_A \left(\boldsymbol{\epsilon}^T \mathbf{N}_E + \boldsymbol{\chi}^T \mathbf{M}_E + \boldsymbol{\gamma}^T \mathbf{T}_E \right) \mathrm{d}A \tag{3.10}$$

The variation of the strain energy is,

$$\delta\mathcal{U} = \int_A \left(\delta\boldsymbol{\epsilon}^T \mathbf{A} \boldsymbol{\epsilon} + \delta\boldsymbol{\epsilon}^T \mathbf{B} \boldsymbol{\chi} + \delta\boldsymbol{\chi}^T \mathbf{B} \boldsymbol{\epsilon} + \delta\boldsymbol{\chi}^T \mathbf{D} \boldsymbol{\chi} + \delta\boldsymbol{\gamma}^T \mathbf{S} \boldsymbol{\gamma} - \frac{1}{2} \delta\boldsymbol{\epsilon}^T \mathbf{N}_T - \frac{1}{2} \delta\boldsymbol{\chi}^T \mathbf{M}_T \right) \mathrm{d}A \tag{3.11}$$

The kinetic energy $\mathcal{T}$ of the shell is,

$$\begin{aligned} \mathcal{T} &= \int_A \int_h \frac{1}{2} \rho^s(\mathbf{x}, T) \left[(\dot{u} + z\dot{\psi}_x)^2 + (\dot{v} + z\dot{\psi}_y)^2 + \dot{w}^2 \right] \mathrm{d}z \mathrm{d}A \\ &= \frac{1}{2} \int_A \left[I_1 \left(\dot{u}^2 + \dot{v}^2 + \dot{w}^2 \right) + 2I_2 \left(\dot{u}\dot{\psi}_x + \dot{v}\dot{\psi}_y \right) + I_3 \left(\dot{\psi}_x^2 + \dot{\psi}_y^2 \right) \right] \mathrm{d}A \end{aligned} \tag{3.12}$$

where,

$$I_k = \int_h \rho^s(\mathbf{x}, T) z^{k-1} \, \mathrm{d}z \tag{3.13}$$

The variation of the kinetic energy is,

$$\delta\mathcal{T} = \int_A I_1(\delta\dot{u}\dot{u} + \delta\dot{v}\dot{v} + \delta\dot{w}\dot{w}) + I_2(\delta\dot{u}\dot{\psi}_x + \delta\dot{\psi}_x\dot{u} + \delta\dot{v}\dot{\psi}_y + \delta\dot{\psi}_y\dot{v}) + I_3(\delta\dot{\psi}_x\dot{\psi}_x + \delta\dot{\psi}_y\dot{\psi}_y)\mathrm{d}A \tag{3.14}$$

The distributed loading $p(x, y)$ in the z-direction is considered in the aerothermoelastic problem. The loading is provided either by the aerodynamic pressure p_F, or other external pressure loading p_{ext}. The virtual work done by $p(x, y)$ per unit area is,

$$\delta\mathcal{W} = \int_A p(x, y)\delta w\mathrm{d}A \tag{3.15}$$

Applying Hamilton's principle to Eqs. (3.11) , (3.14) and (3.15),

$$0 = \int_{t_1}^{t_2}\int_A (\delta\mathcal{T} - \delta\mathcal{U} + \delta\mathcal{W})\ \mathrm{d}A\mathrm{d}t \tag{3.16}$$

yields the governing equations of the composite shell response associated with the variables u, v, w, ψ_x, ψ_y. The boundary conditions are obtained by further manipulating Eq. (3.16) using integration by parts. However, these governing equations are not of major interest and not presented in detail. In this study, Eq. (3.16) is only used for dimensional analysis and finite element formulation, as presented in the following.

3.1.4 Dimensional Analysis of the Structural Problem

The structural similarity parameters are derived by non-dimensionalizing the strain energy and the kinetic energy associated with the composite shallow shell theory with FSDT and geometric nonlinearity.

The following nondimensional quantities are introduced,

$$(\bar{x},\bar{y},\bar{R}_x,\bar{R}_y)=\frac{(x,y,R_x,R_y)}{\hat{L}},\quad \bar{z}=\frac{z}{\hat{h}},\quad \bar{h}(x,y)=\frac{h(x,y)}{\hat{h}},\quad \bar{t}=\frac{t}{\hat{t}} \tag{3.17a}$$

$$(\bar{u},\bar{v},\bar{w})=\frac{(u,v,w)}{\hat{w}},\quad (\bar{\psi}_x,\bar{\psi}_y)=\frac{\hat{w}}{\hat{L}}(\psi_x,\psi_y),\quad \bar{p}(x,y)=\frac{p(x,y)}{\hat{p}} \tag{3.17b}$$

The strain components $\boldsymbol{\epsilon}$, $\boldsymbol{\chi}$ and $\boldsymbol{\gamma}$ are,

$$\boldsymbol{\epsilon}=\frac{\hat{w}}{\hat{L}}\begin{bmatrix}\left(\dfrac{\partial\bar{u}}{\partial\bar{x}}+\dfrac{\bar{w}}{\bar{R}_x}\right)+\dfrac{1}{2}\dfrac{\hat{w}}{\hat{L}}\left(\dfrac{\partial\bar{w}}{\partial\bar{x}}\right)^2\\ \left(\dfrac{\partial\bar{v}}{\partial\bar{y}}+\dfrac{\bar{w}}{\bar{R}_y}\right)+\dfrac{1}{2}\dfrac{\hat{w}}{\hat{L}}\left(\dfrac{\partial\bar{w}}{\partial\bar{y}}\right)^2\\ \left(\dfrac{\partial\bar{u}}{\partial\bar{y}}+\dfrac{\partial\bar{v}}{\partial\bar{x}}\right)+\dfrac{\hat{w}}{\hat{L}}\dfrac{\partial\bar{w}}{\partial\bar{x}}\dfrac{\partial\bar{w}}{\partial\bar{y}}\end{bmatrix}\equiv\frac{\hat{w}}{\hat{L}}\overline{\boldsymbol{\epsilon}} \tag{3.18a}$$

$$\boldsymbol{\chi}=\frac{\hat{w}}{\hat{L}^2}\begin{bmatrix}\dfrac{\partial\bar{\psi}_x}{\partial\bar{x}}\\ \dfrac{\partial\psi_y}{\partial\bar{y}}\\ \dfrac{\partial\bar{\psi}_x}{\partial\bar{y}}+\dfrac{\partial\bar{\psi}_y}{\partial\bar{x}}\end{bmatrix}\equiv\frac{\hat{w}}{\hat{L}^2}\overline{\boldsymbol{\chi}} \tag{3.18b}$$

$$\boldsymbol{\gamma}=\frac{\hat{w}}{\hat{L}}\begin{bmatrix}-\dfrac{\bar{u}}{\bar{R}_x}+\dfrac{\partial\bar{w}}{\partial\bar{x}}+\bar{\psi}_x\\ -\dfrac{\bar{v}}{\bar{R}_y}+\dfrac{\partial\bar{w}}{\partial\bar{y}}+\bar{\psi}_y\end{bmatrix}\equiv\frac{\hat{w}}{\hat{L}}\overline{\boldsymbol{\gamma}} \tag{3.18c}$$

Using Eqs. (3.3-3.7), (3.18) and (3.11), the variation of the strain energy is,

$$\begin{aligned}\delta\mathcal{U}=&\frac{\widehat{D}_{xx}\hat{w}^2}{\hat{L}^4}\int_A\left[\frac{\widehat{A}_{xx}\hat{L}^2}{\widehat{D}_{xx}}\delta\overline{\boldsymbol{\epsilon}}^T\overline{\mathbf{A}}\overline{\boldsymbol{\epsilon}}+\frac{\widehat{B}_{xx}\hat{L}}{\widehat{D}_{xx}}\left(\delta\overline{\boldsymbol{\epsilon}}^T\overline{\mathbf{B}}\overline{\boldsymbol{\chi}}+\delta\overline{\boldsymbol{\chi}}^T\overline{\mathbf{B}}\overline{\boldsymbol{\epsilon}}\right)+\delta\overline{\boldsymbol{\chi}}^T\overline{\mathbf{D}}\overline{\boldsymbol{\chi}}\right.\\ &\left.+\frac{\widehat{S}_{xx}\hat{L}^2}{\widehat{D}_{xx}}\delta\overline{\boldsymbol{\gamma}}^T\overline{\mathbf{S}}\overline{\boldsymbol{\gamma}}-\frac{\widehat{N}_{Tx}\hat{L}^3}{\widehat{D}_{xx}\hat{w}}\frac{1}{2}\delta\overline{\boldsymbol{\epsilon}}^T\overline{\mathbf{N}}_T-\frac{\widehat{M}_{Tx}\hat{L}^2}{\widehat{D}_{xx}\hat{w}}\frac{1}{2}\delta\overline{\boldsymbol{\chi}}^T\overline{\mathbf{M}}_T\right]\mathrm{d}A\\ \equiv&\frac{\widehat{D}_{xx}\hat{w}^2}{\hat{L}^4}\delta\overline{\mathcal{U}}\end{aligned} \tag{3.19}$$

where,

$$\overline{\mathbf{A}} = \frac{\mathbf{A}}{\widehat{A}_{xx}}, \quad \overline{\mathbf{B}} = \frac{\mathbf{B}}{\widehat{B}_{xx}}, \quad \overline{\mathbf{D}} = \frac{\mathbf{D}}{\widehat{D}_{xx}}, \quad \overline{\mathbf{S}} = \frac{\mathbf{S}}{\widehat{S}_{xx}}$$
$$\overline{\mathbf{N}}_T = \frac{\mathbf{N}_T}{\widehat{N}_{Tx}}, \quad \overline{\mathbf{M}}_T = \frac{\mathbf{M}_T}{\widehat{M}_{Tx}} \tag{3.20}$$

The reference values are

$$(\widehat{A}_{xx}, \widehat{B}_{xx}, \widehat{D}_{xx}) = \int_{\hat{h}} (1, z, z^2) Q_{11}(\mathbf{x}, \hat{T}_S) \mathrm{d}z \tag{3.21a}$$

$$\widehat{S}_{xx} = \kappa \int_{\hat{h}} G_{11}(\mathbf{x}, \hat{T}_S) \mathrm{d}z \tag{3.21b}$$

$$\widehat{N}_{Tx} = \int_{\hat{h}} Q_{11}(\mathbf{x}, \hat{T}_S) \alpha_1(\mathbf{x}, \hat{T}_S) \mathrm{d}z \hat{T}_S \tag{3.21c}$$

$$\widehat{M}_{Tx} = \widehat{N}_{Tx} \hat{h} \tag{3.21d}$$

Using Eq. (3.11)), the variation of the kinetic energy is,

$$\begin{aligned}
\delta\mathcal{T} = \frac{\hat{I}\hat{w}^2}{\hat{t}^2} \int_A \Bigg[& \bar{I}_1 \left(\delta\mathring{\hat{u}}\mathring{\hat{u}} + \delta\mathring{\hat{v}}\mathring{\hat{v}} + \delta\mathring{\hat{w}}\mathring{\hat{w}} \right) + \frac{\hat{h}}{\hat{L}} \bar{I}_2 \left(\delta\mathring{\hat{u}}\mathring{\bar{\psi}}_x + \delta\mathring{\bar{\psi}}_x\mathring{\hat{u}} + \delta\mathring{\hat{v}}\mathring{\bar{\psi}}_y + \delta\mathring{\bar{\psi}}_y\mathring{\hat{v}} \right) \\
& + \left(\frac{\hat{h}}{\hat{L}} \right)^2 \bar{I}_3 \left(\delta\mathring{\bar{\psi}}_x\mathring{\bar{\psi}}_x + \delta\mathring{\bar{\psi}}_y\mathring{\bar{\psi}}_y \right) \Bigg] \mathrm{d}A \\
\equiv & \frac{\hat{I}\hat{w}^2}{\hat{t}^2} \delta\overline{\mathcal{T}}
\end{aligned} \tag{3.22}$$

where,

$$\bar{I}_i = \frac{I_i}{\hat{I}\hat{h}^{i-1}}, \quad \hat{I} = \int_{\hat{h}} \rho^s(\mathbf{x}, \hat{T}_S) \, \mathrm{d}z \tag{3.23}$$

Using Eq. (3.15)), the virtual work done by transverse loading is,

$$\begin{aligned}
\delta\mathcal{W} &= \hat{p}\hat{w} \int_A \bar{p}(x, y) \delta\bar{w} \mathrm{d}A \\
&\equiv \hat{p}\hat{w} \delta\overline{\mathcal{W}}
\end{aligned} \tag{3.24}$$

Combining Eqs. (3.19) , (3.22) and (3.24) with the Hamilton's principle Eq. (3.16),

$$
\begin{aligned}
0 &= \int_{t_1}^{t_2} \int_A \left(\frac{\hat{I}\hat{w}^2}{\hat{t}^2}\delta\overline{\mathcal{T}} - \frac{\widehat{D}_{xx}\hat{w}^2}{\hat{L}^4}\delta\overline{\mathcal{U}} + \hat{p}\hat{w}\delta\overline{\mathcal{W}} \right) \mathrm{d}A\mathrm{d}t \\
0 &= \int_{t_1}^{t_2} \int_A \left(\frac{\hat{I}\hat{L}^4}{\widehat{D}_{xx}\hat{t}^2}\delta\overline{\mathcal{T}} - \delta\overline{\mathcal{U}} + \frac{\hat{p}\hat{L}^4}{\widehat{D}_{xx}\hat{w}}\delta\overline{\mathcal{W}} \right) \mathrm{d}A\mathrm{d}t
\end{aligned} \tag{3.25}
$$

The similarity parameters for the structural problem are identified from Eqs. (3.19), (3.22), (3.24), and (3.25), as shown in the following,

$$\frac{\hat{I}\hat{L}^4}{\widehat{D}_{xx}\hat{t}^2}, \quad \bar{R}_x, \quad \bar{R}_y \tag{3.26a}$$

$$\bar{I}_1, \quad \frac{\hat{h}\bar{I}_2}{\hat{L}}, \quad \frac{\hat{h}^2\bar{I}_3}{\hat{L}^2} \tag{3.26b}$$

$$\overline{\mathbf{A}}, \quad \overline{\mathbf{B}}, \quad \overline{\mathbf{D}}, \quad \overline{\mathbf{S}}, \quad \overline{\mathbf{N}}_T, \quad \overline{\mathbf{M}}_T \tag{3.26c}$$

$$\frac{\widehat{A}_{xx}\hat{L}^2}{\widehat{D}_{xx}}, \quad \frac{\widehat{B}_{xx}\hat{L}}{\widehat{D}_{xx}}, \quad \frac{\widehat{S}_{xx}\hat{L}^2}{\widehat{D}_{xx}}, \quad \frac{\widehat{N}_{Tx}\hat{L}^3}{\widehat{D}_{xx}\hat{w}}, \quad \frac{\widehat{M}_{Tx}\hat{L}^2}{\widehat{D}_{xx}\hat{w}} \tag{3.26d}$$

$$\frac{\hat{p}\hat{L}^4}{\widehat{D}_{xx}\hat{w}}, \quad \bar{p}, \quad \frac{\hat{w}}{\hat{L}} \tag{3.26e}$$

In Eq. (3.26a), the first quantity defines the time scale of the structural problem, and the next two quantities represent the similarity in the geometrical configuration. The quantities in Eqs. (3.26b) and (3.26c) require similarity in material properties as functions of temperature and spatial coordinates. Note that $\overline{\mathbf{A}}$, $\overline{\mathbf{B}}$ and $\overline{\mathbf{D}}$ are 3×3 symmetric matrices, $\overline{\mathbf{S}}$ is a 2×2 symmetric matrix, and $\overline{\mathbf{N}}_T$ and $\overline{\mathbf{M}}_T$ are 3×1 vectors. Therefore, $\overline{\mathbf{A}}$, $\overline{\mathbf{B}}$ and $\overline{\mathbf{D}}$ each contain 6 independent similarity parameters, while $\overline{\mathbf{S}}$, $\overline{\mathbf{N}}_T$ and $\overline{\mathbf{M}}_T$ each contain 3 independent similarity parameters. The quantities in Eq. (3.26d) requires the similarity in the ratios of various elastic properties. Finally, in Eq. (3.26e), the first two quantities require the similarity in the distribution and the magnitude of the external loading. The quantity $\frac{\hat{w}}{\hat{L}}$ requires the similarity in the magnitude of the nonlinear deformation. The reference structural temperature $\hat{T}_S$, which is contained in the definitions of $\widehat{A}_{xx}$, $\widehat{B}_{xx}$, $\widehat{D}_{xx}$, $\widehat{S}_{xx}$, $\widehat{N}_{Tx}$,

$\widehat{M_{Tx}}$ and $\hat{I}$, is determined from the consideration of the aerothermoelastic problem.

In the case of thin, isotropic, and homogeneous plate, the 41 similarity parameters in Eq. (3.26) reduce to 13 parameters,

$$\frac{\hat{I}\hat{L}^4}{\widehat{D}_{xx}\hat{t}^2} \tag{3.27a}$$

$$\bar{I}_1 \tag{3.27b}$$

$$\overline{A}_{xx}, \quad \overline{D}_{xx}, \quad \overline{N}_{Tx}, \quad \overline{M}_{Tx}, \quad \nu \tag{3.27c}$$

$$\frac{\widehat{A}_{xx}\hat{L}^2}{\widehat{D}_{xx}}, \quad \frac{\widehat{N}_{Tx}\hat{L}^3}{\widehat{D}_{xx}\hat{w}}, \quad \frac{\widehat{M}_{Tx}\hat{L}^2}{\widehat{D}_{xx}\hat{w}} \tag{3.27d}$$

$$\frac{\hat{p}\hat{L}^4}{\widehat{D}_{xx}\hat{w}}, \quad \bar{p}, \quad \frac{\hat{w}}{\hat{L}} \tag{3.27e}$$

The set of similarity parameters in Eq. (3.27) is equivalent to the classical results in Ref. [24] if the reference value for the elastic portion of the in-plane force is defined as,

$$\widehat{N} = \widehat{A}_{xx}\frac{\hat{w}}{\hat{L}} \tag{3.28}$$

3.2 Finite Element Formulation

In HYPATE, the shell element is implemented using the shallow shell equations given in the energy principle represented by Eq. (3.16). The finite element is referred to as the doubly-Curved shallow 9-noded shell element (DCS9). The nodes are shown in Fig. 3.2, four at corners, four at midpoints and one at the center. The numbers enclosed by circles are the nodes. Every node has five degrees of freedom (DOFs): three displacements and two rotations. Second-order Lagrangian shape functions are used to interpolate the nodal variables.

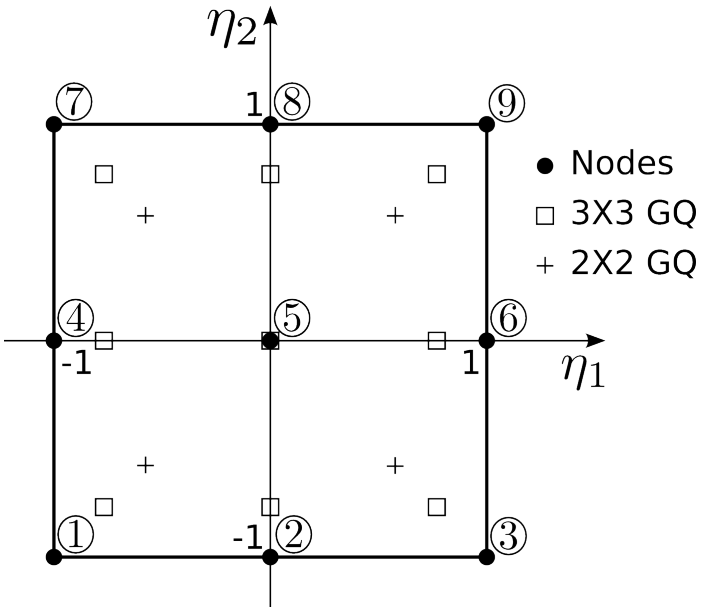

Figure 3.2: The DCS9 element in parametric coordinates, GQ means Gaussian Quadrature

3.2.1 Element Matrices and Loading Vectors

For each element, the displacement field $\mathbf{u}(x, y) = [u, v, w, \psi_x, \psi_y]^T$ is interpolated by the shape functions N_i and nodal values $\mathbf{u}^e = [u_1, v_1, w_1, \psi_{x1}, \psi_{y1}, \cdots, u_9, v_9, w_9, \psi_{x9}, \psi_{y9}]^T$,

$$\mathbf{u} = \mathbf{L}_0 \mathbf{u}^e \tag{3.29}$$

where,

$$\mathbf{L}_0 = \left[\begin{array}{c|ccccc|c} & N_i & 0 & 0 & 0 & 0 & \\ & 0 & N_i & 0 & 0 & 0 & \\ \cdots & 0 & 0 & N_i & 0 & 0 & \cdots \\ & 0 & 0 & 0 & N_i & 0 & \\ & 0 & 0 & 0 & 0 & N_i & \end{array}\right], \quad i = 1, \cdots, 9 \tag{3.30}$$

and

$$N_{i+3j-3} = f_i(\eta) f_j(\xi), \quad i,j = 1,2,3 \tag{3.31}$$
$$f_1(x) = \frac{1}{2}x(x-1)$$
$$f_2(x) = 1 - x^2$$
$$f_3(x) = \frac{1}{2}(1+x)x$$

The strains are,

$$\boldsymbol{\epsilon}_l = \mathbf{L}_1 \mathbf{u}^e, \quad \boldsymbol{\epsilon}_{nl} = \frac{1}{2}\mathbf{L}_w \mathbf{u}^e, \quad \boldsymbol{\chi} = \mathbf{L}_2 \mathbf{u}^e, \quad \boldsymbol{\gamma} = \mathbf{L}_3 \mathbf{u}^e \tag{3.32}$$

where,

$$\mathbf{L}_1 = \left[\begin{array}{c|ccccc|c} & N_{i,x} & 0 & \frac{N_i}{R_x} & 0 & 0 & \\ \cdots & 0 & N_{i,y} & \frac{N_i}{R_y} & 0 & 0 & \cdots \\ & N_{i,y} & N_{i,x} & 0 & 0 & 0 & \end{array}\right]$$

$$\mathbf{L}_2 = \left[\begin{array}{c|ccccc|c} & 0 & 0 & 0 & N_{i,x} & 0 & \\ \cdots & 0 & 0 & 0 & 0 & N_{i,y} & \cdots \\ & 0 & 0 & 0 & N_{i,y} & N_{i,x} & \end{array}\right]$$

$$\mathbf{L}_w = \left[\begin{array}{c|ccccc|c} & 0 & 0 & w_{,x}N_{i,x} & 0 & 0 & \\ \cdots & 0 & 0 & w_{,y}N_{i,y} & 0 & 0 & \cdots \\ & 0 & 0 & w_{,y}N_{i,x} + w_{,x}N_{i,y} & 0 & 0 & \end{array}\right]$$

$$\mathbf{L}_3 = \left[\begin{array}{c|ccccc|c} & 0 & -\frac{N_i}{R_y} & N_{i,y} & 0 & N_i & \\ \cdots & -\frac{N_i}{R_x} & 0 & N_{i,x} & N_i & 0 & \cdots \end{array}\right]$$

From the variation of strain energy, Eq. (3.11), the stiffness matrices and thermal load-

ing vector is obtained,

$$\begin{aligned}\delta\mathcal{U} &= \int_A \left(\delta\boldsymbol{\epsilon}_0^T\mathbf{A}\boldsymbol{\epsilon} + \delta\boldsymbol{\epsilon}_0^T\mathbf{B}\boldsymbol{\chi} + \delta\boldsymbol{\chi}^T\mathbf{B}\boldsymbol{\epsilon}_0 + \delta\boldsymbol{\chi}^T\mathbf{D}\boldsymbol{\chi} + \delta\boldsymbol{\gamma}^T\mathbf{S}\boldsymbol{\gamma}\right)\,\mathrm{d}A - \int_A \left(\delta\boldsymbol{\epsilon}_0^T\mathbf{N}_T + \delta\boldsymbol{\chi}^T\mathbf{M}_T\right)\,\mathrm{d}A \\ &\equiv \left(\delta\mathbf{u}^e\right)^T\left\{\left[\mathbf{K}_{L1}^e + \mathbf{K}_{L2}^e + \mathbf{K}_N^e(\mathbf{u}^e)\right]\mathbf{u}^e - \mathbf{F}_T^e\right\}\end{aligned} \tag{3.33}$$

where,

$$\mathbf{K}_{L1}^e = \int_A \left(\mathbf{L}_1^T\mathbf{A}\mathbf{L}_1 + \mathbf{L}_1^T\mathbf{B}\mathbf{L}_2 + \mathbf{L}_2^T\mathbf{B}\mathbf{L}_1 + \mathbf{L}_2^T\mathbf{D}\mathbf{L}_2\right)\,\mathrm{d}A \tag{3.34a}$$

$$\mathbf{K}_{L2}^e = \int_A \left(\mathbf{L}_3^T\mathbf{S}\mathbf{L}_3\right)\,\mathrm{d}A \tag{3.34b}$$

$$\begin{aligned}\mathbf{K}_N^e(\mathbf{u}^e) = \int_A \Bigg[&\mathbf{L}_1^T\mathbf{A}\left(\frac{1}{2}\mathbf{L}_w\right) + \mathbf{L}_w^T\mathbf{A}\mathbf{L}_1 + \mathbf{L}_w^T\mathbf{A}\left(\frac{1}{2}\mathbf{L}_w\right) \\ &+ \mathbf{L}_w^T\mathbf{B}\mathbf{L}_2 + \mathbf{L}_2^T\mathbf{B}\left(\frac{1}{2}\mathbf{L}_w\right)\Bigg]\,\mathrm{d}A\end{aligned} \tag{3.34c}$$

$$\mathbf{F}_T^e = \int_A \left[(\mathbf{L}_1^T + \mathbf{L}_w^T)\mathbf{N}_T + \mathbf{L}_2^T\mathbf{M}_T\right]\,\mathrm{d}A \tag{3.34d}$$

The term $\mathbf{F}_T^e$ is thermal loading vector. The terms $\mathbf{K}_{L1}^e$ and $\mathbf{K}_{L2}^e$ correspond to the linear part of the element stiffness matrix. Gaussian quadrature with selective reduced integration scheme is used to evaluate the integrations associated with $\mathbf{K}_{L1}^e$ and $\mathbf{K}_{L2}^e$, as shown in Fig. 3.2. For $\mathbf{K}_{L1}^e$, a set of 3×3 Gaussian quadrature points is used ("full integration"); for $\mathbf{K}_{L2}^e$, a set of 2×2 Gaussian quadrature points is used ("reduced integration"). This procedure avoids the "shear locking" problem in FE analysis (pp. 327-330 of [158]). The term $\mathbf{K}_N^e(\mathbf{u}^e)$ is the nonlinear part of the element stiffness matrix, which depends on the nodal displacements of the element. Full integration is used for its numerical evaluation.

Combining the linear and nonlinear parts of the element stiffness matrix and loading

vector yields the element stiffness matrix and internal force vector,

$$\mathbf{K}^e(\mathbf{u}^e) = \mathbf{K}^e_{L1} + \mathbf{K}^e_{L2} + \mathbf{K}^e_N(\mathbf{u}^e) \equiv \mathbf{K}^e_L + \mathbf{K}^e_N(\mathbf{u}^e) \tag{3.35}$$

$$\mathbf{F}^e_I(\mathbf{u}^e) = \mathbf{K}^e(\mathbf{u}^e)\mathbf{u}^e - \mathbf{F}^e_T \tag{3.36}$$

The consistent mass matrix required for dynamic modeling is obtained from the kinetic energy $\mathcal{T}$ in Eq. (3.12),

$$\mathcal{T} = \frac{1}{2}(\mathbf{u}^e)^T \mathbf{M}^e \mathbf{u}^e \tag{3.37}$$

where $\mathbf{M}^e$ is the element consistent mass matrix generated using the same shape functions that were used for the element stiffness matrix evaluation,

$$\begin{aligned} \mathbf{M}^e &= \mathbf{L}_0^T \mathbf{I}^e \mathbf{L}_0 \\ \mathbf{I}^e &= \begin{bmatrix} I_1 & 0 & 0 & I_2 & 0 \\ 0 & I_1 & 0 & 0 & I_2 \\ 0 & 0 & I_1 & 0 & 0 \\ I_2 & 0 & 0 & I_3 & 0 \\ 0 & I_2 & 0 & 0 & I_3 \end{bmatrix} \end{aligned} \tag{3.38}$$

Finally, distributed loading $p(x, y)$ in the z-direction is considered. Using the virtual work in Eq. (3.15), the element loading vector $\mathbf{F}^e_S$ in the z-direction is,

$$\mathbf{F}^e_S = \int_A \mathbf{L}_0^T [0, 0, p(x, y), 0, 0]^T \, \mathrm{d}A \tag{3.39}$$

3.2.2 Equations of Motion for the Structural Problem

The element stiffness and mass matrices and loading vectors are assembled into the linear stiffness matrix $\mathbf{K}_L$, total mass matrix $\mathbf{M}$, and unconstrained total internal and loading vectors, $\mathbf{F}^u_I$ and $\mathbf{F}^u_S$. Suppose N_b DOFs of the structure are constrained: the displacement

of k_ith DOFs u_{k_i} is set to be $u_b^{k_i}$, $i = 1, 2, \cdots, N_b$. The penalty method is used to apply the boundary conditions (pp. 143-146 of [159]) to obtain the total stiffness matrix and loading vector,

$$\mathbf{F}_I(\mathbf{u}) = \mathbf{F}_I^u(\mathbf{u}) + \mathbf{K}^c\mathbf{u} \tag{3.40}$$

$$\mathbf{F}_S = \mathbf{F}_S^u + \mathbf{F}^c \tag{3.41}$$

where,

$$[\mathbf{K}^c]_{ij} = \begin{cases} \tilde{\alpha}, & i = j \in \{1, 2, \cdots, N_b\} \\ 0, & \text{else} \end{cases}$$

$$[\mathbf{F}^c]_i = \begin{cases} \tilde{\alpha} u_b^i, & i \in \{1, 2, \cdots, N_b\} \\ 0, & \text{else} \end{cases}$$

In practice, $\tilde{\alpha}$ is set to be,

$$\tilde{\alpha} = \tilde{\alpha}_0 \max_{i,j}([\mathbf{K}^u]_{ij}) \tag{3.42}$$

where $\tilde{\alpha}_0$ is set to 10^6 to guarantee that $\tilde{\alpha}$ is much larger than the largest entry in the unconstrained stiffness matrix.

Using the total mass matrix and the total internal force and loading vectors, the equations of motion are,

$$\mathbf{M}\ddot{\mathbf{u}} + \mathbf{C}\dot{\mathbf{u}} + \mathbf{F}_I(\mathbf{u}, \mathbf{T}) = \mathbf{F}_S(\mathbf{u}, \dot{\mathbf{u}}) \tag{3.43}$$

The damping matrix $\mathbf{C}$ is introduced using the proportional damping approach [158],

$$\mathbf{C} = \zeta_M\mathbf{M} + \zeta_K\mathbf{K} \tag{3.44}$$

where ζ_M introduces stronger damping on the low-frequency modes, while ζ_K introduces stronger damping on the high-frequency modes.

3.2.3 Solution of the Nonlinear Structural Problem

Several second-order time accurate numerical schemes are available for the temporal discretization of Eq. (3.43), including the Newmark-β scheme [160], the Hilber-Hughes-Taylor scheme [161], and the generalized-α scheme [162]. The generalized-α scheme is preferred over the other two schemes, because it allows for tunable energy dissipation of high frequency responses, while minimizing the dissipation of low frequency responses and maintaining second-order time accuracy.

Equation (3.43) is discretized in time using the generalized-α scheme [162],

$$\mathcal{R}_S(\mathbf{u}^{n+1}) = \mathbf{M}\ddot{\mathbf{u}}^{n+1-\alpha_m} + \mathbf{C}\dot{\mathbf{u}}^{n+1-\alpha_f} + \mathbf{F}_I^{n+1-\alpha_f} = \mathbf{F}_S^{n+1-\alpha_f} \tag{3.45}$$

where,

$$\begin{aligned}
\mathbf{u}^{n+1} &= \mathbf{u}^n + \Delta t\dot{\mathbf{u}}^n + (1-2\bar{\beta})\frac{\Delta t^2}{2}\ddot{\mathbf{u}}^n + \bar{\beta}\Delta t^2\ddot{\mathbf{u}}^{n+1} \\
\dot{\mathbf{u}}^{n+1} &= \dot{\mathbf{u}}^n + (1-\bar{\gamma})\Delta t\ddot{\mathbf{u}}^n + \bar{\gamma}\Delta t\ddot{\mathbf{u}}^{n+1} \\
\mathbf{u}^{n+1-\alpha_f} &= (1-\alpha_f)\mathbf{u}^{n+1} + \alpha_f\mathbf{u}^n \\
\dot{\mathbf{u}}^{n+1-\alpha_f} &= (1-\alpha_f)\dot{\mathbf{u}}^{n+1} + \alpha_f\dot{\mathbf{u}}^n \\
\ddot{\mathbf{u}}^{n+1-\alpha_m} &= (1-\alpha_m)\ddot{\mathbf{u}}^{n+1} + \alpha_m\ddot{\mathbf{u}}^n \\
\mathbf{F}_I^{n+1-\alpha_f} &= (1-\alpha_f)\mathbf{F}_I(\mathbf{u}^{n+1}, \mathbf{T}^{n+1}) + \alpha_f\mathbf{F}_I(\mathbf{u}^n, \mathbf{T}^n) \\
\mathbf{F}_S^{n+1-\alpha_f} &= (1-\alpha_f)\mathbf{F}_S(\mathbf{u}^{n+1}, \dot{\mathbf{u}}^{n+1}) + \alpha_f\mathbf{F}_S(\mathbf{u}^n, \dot{\mathbf{u}}^n)
\end{aligned}$$

The coefficients α_f and α_m are determined by a user-specified parameter $\bar{\rho} \in [0, 1]$. For second-order time accuracy and unconditional stability (in the linear sense),

$$\alpha_f = \frac{\bar{\rho}}{\bar{\rho}+1}, \quad \alpha_m = \frac{2\bar{\rho}-1}{\bar{\rho}+1}, \quad \bar{\gamma} = \frac{1}{2} - \alpha_m + \alpha_f, \quad \bar{\beta} = \frac{1}{4}(1-\alpha_m+\alpha_f)^2$$

The parameter $\bar{\rho}$ characterizes the numerical dissipation of the generalized-α scheme. A lower value of $\bar{\rho}$ means a higher decay rate for the high-frequency components of the structural response [162]. A typical value of $\bar{\rho} = 0.95$ is chosen to obtain transient struc-

tural response. When $\bar{\rho} = 0$, the *quasi-steady* structural response is obtained [163], where $\ddot{\mathbf{u}}$ and $\dot{\mathbf{u}}$ are negligible.

Equation (3.45) is solved using the Newton-Raphson algorithm with line search,

1. Start with solution from last time step $\mathbf{u}^n$, maximum number of iterations N_i, tolerance ϵ
2. Set initial guess $\mathbf{u}^0 = 0$
3. Iteration for a maximum of N_i steps:
   (a) Newton-Raphson step: Solve $\Delta\mathbf{u}$ from

$$\left(\frac{\partial \mathcal{R}_S}{\partial \mathbf{u}^i} - \frac{\partial \mathbf{F}_S^{n+1-\alpha_f}}{\partial \mathbf{u}^i}\right)\Delta\mathbf{u} = -(\mathcal{R}_S(\mathbf{u}^i) - \mathbf{F}_S^{n+1-\alpha_f}) \tag{3.46}$$

   (b) Line search step: Find a scalar θ such that

$$\theta = \text{argmin}_\theta \, ||\mathcal{R}_S(\mathbf{u}^i + \theta\Delta\mathbf{u}) - \mathbf{F}_S^{n+1-\alpha_f}|| \tag{3.47}$$

   (c) Update solution: $\mathbf{u}^{i+1} = \mathbf{u}^i + \theta\Delta\mathbf{u}$
   (d) If $||\mathcal{R}_S(\mathbf{u}^{i+1}) - \mathbf{F}_S^{n+1-\alpha_f}|| < \epsilon$ break, otherwise continue.

The computational considerations associated with the residual equation, Eq. (3.46), are discussed in Section 5.4.4.

Assuming $\mathbf{M}$ and $\mathbf{C}$ are constant, the Jacobians in the Newton-Raphson algorithm Eq. (3.46) are,

$$\frac{\partial \mathcal{R}_S(\mathbf{u})}{\partial \mathbf{u}} = \mathbf{K}_m + (1-\alpha^f)\frac{\partial \mathbf{F}_I^{n+1}}{\partial \mathbf{u}} \tag{3.48a}$$

$$\frac{\partial \mathbf{F}_S^{n+1-\alpha_f}}{\partial \mathbf{u}} = (1-\alpha^f)\left[\frac{\partial \mathbf{F}_S^{n+1}}{\partial \mathbf{u}} + \frac{\bar{\gamma}}{\bar{\beta}\Delta t}\frac{\partial \mathbf{F}_S^{n+1}}{\partial \dot{\mathbf{u}}}\right] \tag{3.48b}$$

where

$$\mathbf{K}_m = \frac{1-\alpha^m}{\bar{\beta}\Delta t^2}\mathbf{M} + \frac{\bar{\gamma}(1-\alpha^f)}{\bar{\beta}\Delta t}\mathbf{C} \tag{3.49}$$

To obtain the explicit forms that are suitable for programming, the Jacobians associated

with $\mathbf{F}_I$ and $\mathbf{F}_S$ in Eq. (3.48) need further elaboration. Note that $\mathbf{F}_I$ and $\mathbf{F}_S$ are linear combinations of their element counterparts. Therefore one can calculate Jacobians of the element force vectors and assemble them to obtain the Jacobians of the assembled system.

For the internal force vector of an element,

$$\frac{\partial \mathbf{F}_I^e}{\partial \mathbf{u}^e} = \mathbf{K}^e(\mathbf{u}^e) + \frac{\partial \mathbf{K}_N^e(\mathbf{u}^e)}{\partial \mathbf{u}^e}\mathbf{u}^e - \frac{\partial \mathbf{F}_T^e(\mathbf{u}^e)}{\partial \mathbf{u}^e} \tag{3.50}$$

The first term in Eq. (3.50) is given by Eq. (3.35). The second term is written explicitly as,

$$\frac{\partial \mathbf{K}_N^e(\mathbf{u}^e)}{\partial \mathbf{u}^e}\mathbf{u}^e = \left[\begin{array}{c|c|c|c|c|c} \dfrac{\partial \mathbf{K}_N^e(\mathbf{u}^e)}{\partial u_1}\mathbf{u}^e & \dfrac{\partial \mathbf{K}_N^e(\mathbf{u}^e)}{\partial v_1}\mathbf{u}^e & \dfrac{\partial \mathbf{K}_N^e(\mathbf{u}^e)}{\partial w_1}\mathbf{u}^e & \dfrac{\partial \mathbf{K}_N^e(\mathbf{u}^e)}{\partial \psi_{x1}}\mathbf{u}^e & \dfrac{\partial \mathbf{K}_N^e(\mathbf{u}^e)}{\partial \psi_{y_1}}\mathbf{u}^e & \cdots \end{array}\right] \tag{3.51}$$

Nonlinear terms in Eq. (3.51) are only associated with w_i, therefore the derivatives of $\mathbf{K}_N^e(\mathbf{u}^e)$ w.r.t. $u_i, v_i, \psi_{xi}, \psi_{y_i}$ are zero. Derivatives of $\mathbf{K}_N^e(\mathbf{u}^e)$ w.r.t. w_i are,

$$\begin{aligned} \frac{\partial \mathbf{K}_N^e(\mathbf{u}^e)}{\partial w_i}\mathbf{u}^e &= \int_A \frac{\partial}{\partial w_i}\left[\mathbf{L}_1^T\mathbf{A}\left(\frac{1}{2}\mathbf{L}_w\right) + \mathbf{L}_w^T\mathbf{A}\mathbf{L}_1 + \mathbf{L}_w^T\mathbf{A}\left(\frac{1}{2}\mathbf{L}_w\right)\right. \\ &\quad \left. + \mathbf{L}_w^T\mathbf{B}\mathbf{L}_2 + \mathbf{L}_2^T\mathbf{B}\left(\frac{1}{2}\mathbf{L}_w\right)\right]\mathbf{u}^e \,\mathrm{d}A \\ &= \int_A \left[\left(\mathbf{L}_1^T\mathbf{A} + \mathbf{L}_w^T\mathbf{A} + \mathbf{L}_2^T\mathbf{B}\right)\mathbf{L}_{w1} + \mathbf{L}_{w2}^T\mathbf{N}_E\right] \mathrm{d}A \end{aligned} \tag{3.52}$$

where,

$$\mathbf{L}_{w1} = \frac{\partial}{\partial w_i}\mathbf{L}_w\mathbf{u}^e = [N_{i,x}w_{,x}, N_{i,y}w_{,y}, N_{i,y}w_{,x} + N_{i,x}w_{,y}]^T \tag{3.53a}$$

$$\mathbf{L}_{w2} = \frac{\partial}{\partial w_i}\mathbf{L}_w = \left[\begin{array}{cccc|c} 0 & 0 & N_{i,x}N_{1,x} & 0 & 0 \\ 0 & 0 & N_{i,y}N_{1,y} & 0 & 0 \\ 0 & 0 & N_{i,y}N_{1,x} + N_{i,x}N_{1,y} & 0 & 0 \end{array}\right| \cdots \tag{3.53b}$$

For the last term in Eq. (3.50), using Eq. (3.34d) and noting that only derivatives w.r.t.

w_i are nonzero,

$$\begin{aligned}\frac{\partial \mathbf{F}_T^e}{\partial w_i} &= \frac{\partial}{\partial w_i}\left[\int_A (\mathbf{L}_1^T + \mathbf{L}_w^T)\mathbf{N}_T + \mathbf{L}_2^T \mathbf{M}_T \,\mathrm{d}A\right] \\ &= \int_A \frac{\partial}{\partial w_i}\mathbf{L}_w^T \mathbf{N}_T \,\mathrm{d}A \\ &= \int_A \mathbf{L}_{w2}^T \mathbf{N}_T \,\mathrm{d}A\end{aligned} \tag{3.54}$$

The Jacobian of the element loading vector is,

$$\frac{\partial \mathbf{F}_S^e(\mathbf{u}^e)}{\partial \mathbf{u}^e} = \left[\begin{array}{c|c|c|c|c|c|c} \dfrac{\partial \mathbf{F}_S^e(\mathbf{u}^e)}{\partial u_1} & \dfrac{\partial \mathbf{F}_S^e(\mathbf{u}^e)}{\partial v_1} & \dfrac{\partial \mathbf{F}_S^e(\mathbf{u}^e)}{\partial w_1} & \dfrac{\partial \mathbf{F}_S^e(\mathbf{u}^e)}{\partial \psi_{x1}} & \dfrac{\partial \mathbf{F}_S^e(\mathbf{u}^e)}{\partial \psi_{y1}} & \cdots \end{array}\right] \tag{3.55}$$

When the loading vector is independent of displacement, for example, $p(x, y) = const$ in Eq. (3.39), the Jacobian is zero. Otherwise, the Jacobian has to be evaluated explicitly.

CHAPTER 4

Heat Conduction Model

In this chapter, the governing equation for the heat conduction in a shallow composite shell is developed. Next, a dimensional analysis is applied to the heat conduction equations to identify the thermal similarity parameters, which are required for the development of ASL in the following chapters. Finally, the Galerkin's approach is employed to develop the nonlinear finite element formulation of the thermal problem accounting for temperature-dependent material properties.

4.1 Governing Equations

4.1.1 Heat Conduction in Shallow Shells

For the formulation of the heat conduction equation, following assumptions are made:

1. The panel is thin, i.e. the thickness-to-span ratio of the panel is less than 1/20 [157].
2. The curved structure is shallow, i.e. the span-to-radius ratio of the panel is less than 0.5 [157].
3. The panel remains shallow during moderate deflections.

Using the Fourier's law [164], the heat conduction equation in a solid body Ω_T is,

$$\rho^s c_p^s(\mathbf{x}, T)\dot{T} - \nabla \cdot (\mathbf{k}^s(\mathbf{x}, T) \cdot \nabla T) = 0 \quad \text{in } \Omega_T \tag{4.1a}$$

$$-\mathbf{n} \cdot \mathbf{k}^s(\mathbf{x}, T) \cdot \nabla T = \dot{q}_{bc}(\mathbf{x}, T, t) \quad \text{on } \Gamma_q \tag{4.1b}$$

$$T(\mathbf{x}) = T_{bc}(\mathbf{x}) \quad \text{on } \Gamma_T \tag{4.1c}$$

$$T(\mathbf{x})|_{t=0} = T_{ini}(\mathbf{x}) \quad \text{in } \Omega_T \tag{4.1d}$$

where Γ_q and Γ_T represent boundaries where heat flux and temperature are prescribed, respectively. In the formulation Eq. (4.1), the density, thermal capacity and conductivity are inhomogenous and temperature dependent. The surface heat flux $\dot{q}_{bc}$ is due to aerodynamic heating $\dot{q}_F$ and other heat sources $\dot{q}_{ext}$, such as radiation.

For a composite shell, the material is oriented along the curved surface, and the thermal conductivity matrix $\mathbf{k}^s$ is defined in a curvilinear coordinate system $\xi_1\xi_2\zeta$, as shown in Fig. 4.1,

$$\mathbf{k}^s = \begin{bmatrix} k_{\xi_1\xi_1} & k_{\xi_1\xi_2} & 0 \\ k_{\xi_2\xi_1} & k_{\xi_2\xi_2} & 0 \\ 0 & 0 & k_{\zeta\zeta} \end{bmatrix} \tag{4.2}$$

The gradient operator ∇ associated with the $\xi_1\xi_2\zeta$ coordinate system is,

$$\nabla = \left[\frac{1}{A_1}\frac{\partial}{\partial \xi_1}, \frac{1}{A_2}\frac{\partial}{\partial \xi_2}, \frac{\partial}{\partial \zeta} \right] \tag{4.3}$$

where,

$$A_1 = 1 + \frac{\zeta}{R_1}, \quad A_2 = 1 + \frac{\zeta}{R_2} \tag{4.4}$$

Since the shell is thin and shallow,

$$A_1 \approx 1, \quad A_2 \approx 1 \tag{4.5}$$

Furthermore, by assuming that the derivatives of temperature w.r.t. ξ_1, ξ_2, ζ are the same as derivatives w.r.t. x, y, z, the gradient operator simplifies as,

$$\nabla \approx \left[\frac{\partial}{\partial x}, \frac{\partial}{\partial y}, \frac{\partial}{\partial z}\right] \tag{4.6}$$

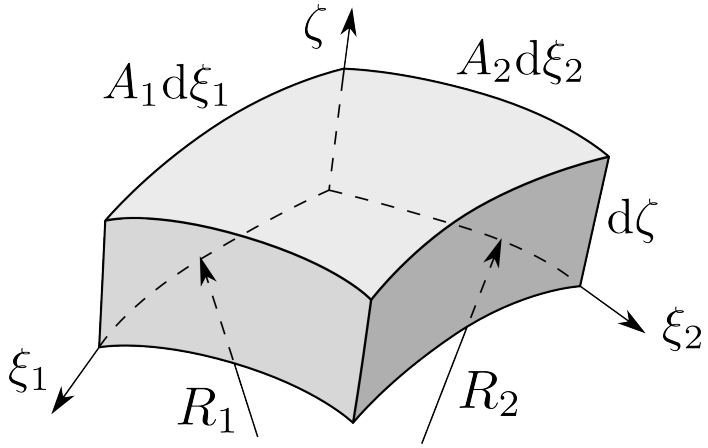

Figure 4.1: A differential volume in the $\xi_1\xi_2\zeta$ coordinate system

The analysis described above implies:

1. The shell curvatures have very little effect on the thermal solution, i.e. a thin shallow shell can be approximated by a thin flat plate.
2. The constitutive relations in the xyz coordinate system can be approximated by those in the $\xi_1\xi_2\zeta$ coordinate system.

Conclusion 1 can be extended to a more general case. Since the shell remains shallow under moderate deflection, shell deformation has very little effect on thermal solution. Therefore, thermal solution of a moderately-deformed thin shallow shell can be approximated by that of an *undeformed* thin flat plate.

4.1.2 Dimensional Analysis of the Thermal Problem

The governing equation for the thermal problem, Eq. (4.1), is non-dimensionalized by introducing the following nondimensional quantities,

$$\bar{x}_i = \frac{x_i}{\hat{L}_i}, \quad \bar{t} = \frac{t}{\hat{t}}, \quad \bar{T} = \frac{T}{\hat{T}_T}, \quad \bar{\dot{q}}_{bc} = \frac{\dot{q}_{bc}}{\hat{\dot{q}}} \tag{4.7a}$$

$$\bar{\mathbf{k}}^s = \frac{\mathbf{k}^s}{\hat{k}^s}, \quad \bar{\rho}^s \bar{c}_p^s = \frac{\rho^s c_p^s}{\hat{\rho}^s \hat{c}_p^s} \tag{4.7b}$$

Equation (4.1) is non-dimensionalized as,

$$\frac{\hat{\rho}^s \hat{c}_p^s \hat{L}_3^2}{\hat{k}^s \hat{t}} \bar{\rho}^s \bar{c}_p^s(\bar{\mathbf{x}}, T) \mathring{\bar{T}} - \overline{\nabla} \cdot (\bar{\mathbf{k}}^s(\bar{\mathbf{x}}, T) \cdot \overline{\nabla} \bar{T}) = 0 \quad \text{in } \Omega_T \tag{4.8a}$$

$$-\mathbf{n} \cdot \bar{\mathbf{k}}^s(\bar{\mathbf{x}}, T) \cdot \nabla \bar{T} = \frac{\hat{\dot{q}} \hat{L}_3}{\hat{k}^s \hat{T}_T} \bar{\dot{q}}_{bc}(\bar{\mathbf{x}}, T, t) \quad \text{on } \Gamma_q \tag{4.8b}$$

$$T(\mathbf{x}) = T_{bc}(\mathbf{x}) \quad \text{on } \Gamma_T \tag{4.8c}$$

$$\bar{T}(\bar{\mathbf{x}})|_{t=0} = \bar{T}_{ini}(\bar{\mathbf{x}}) \quad \text{in } \Omega_T \tag{4.8d}$$

where,

$$\overline{\nabla} = \left(\frac{\hat{L}_3}{\hat{L}_1} \frac{\partial}{\partial \bar{x}_1}, \frac{\hat{L}_3}{\hat{L}_2} \frac{\partial}{\partial \bar{x}_2}, \frac{\partial}{\partial \bar{x}_3} \right) \tag{4.9}$$

The similarity parameters for the thermal problem are identified from Eqs. (4.8),

$$\mathit{Fo} = \frac{\hat{k}^s \hat{t}}{\hat{\rho}^s \hat{c}_p^s \hat{L}_3^2}, \quad \mathit{Bi} = \frac{\hat{\dot{q}} \hat{L}_3}{\hat{k}^s \hat{T}_T}, \quad \frac{\hat{L}_3}{\hat{L}_1}, \quad \frac{\hat{L}_3}{\hat{L}_2} \tag{4.10a}$$

$$\bar{\rho}^s \bar{c}_p^s, \quad \bar{\mathbf{k}}^s, \quad \bar{T}_{ini}, \quad \bar{\dot{q}}_{bc} \tag{4.10b}$$

In Eq. (4.10a), the first quantity is the Fourier number, a dimensionless time representing the ratio between the rate of heat conduction to the rate of energy stored by capacitance [20, 38]. It defines the time scale of the thermal problem. The second quantity is the Biot number that characterizes the heat transfer resistance of the body. The quantities $\frac{\hat{L}_3}{\hat{L}_1}$ and $\frac{\hat{L}_3}{\hat{L}_2}$ require the similarity in geometrical configuration. In Eq. (4.10b), the first two quantities

require the similarity in the material properties as functions of temperature and spatial coordinates. Note that $\bar{\mathbf{k}}^s$ is a 3×3 symmetric matrix, and contains 6 independent similarity parameters. The last two quantities define the distribution of initial temperature field and the heat flux, respectively.

For heat transfer in a composite shell structure, one can choose $\hat{L}_1 = \hat{L}_2 = \hat{L}$ as the length scale of the shell and $\hat{L}_3 = \hat{h}$ as the thickness of the shell, simplifying the similarity parameters in Eq. (4.10),

$$\textit{Fo} = \frac{\hat{k}^s \hat{t}}{\hat{\rho}^s \hat{c}_p^s \hat{h}^2}, \quad \textit{Bi} = \frac{\hat{\dot{q}} \hat{h}}{\hat{k}^s \hat{T}_T}, \quad \frac{\hat{h}}{\hat{L}} \tag{4.11a}$$

$$\bar{\rho}^s \bar{c}_p^s, \quad \bar{\mathbf{k}}^s, \quad \bar{T}_{ini}, \quad \bar{\dot{q}}_{bc} \tag{4.11b}$$

For a composite shell, the reference values for $\rho^s c_p^s$ and $\mathbf{k}^s$ are defined as,

$$\hat{\rho}^s \hat{c}_p^s = \int_{\hat{h}} \rho^s(\mathbf{x}, \hat{T}_T) c_p^s(\mathbf{x}, \hat{T}_T) \mathrm{d}z \tag{4.12a}$$

$$\hat{k}^s = \left(\int_{\hat{h}} \frac{\mathrm{d}z}{k_{11}^s(\mathbf{x}, \hat{T}_T)} \right)^{-1} \hat{h} \tag{4.12b}$$

where k_{11}^s is the first element of $\mathbf{k}^s$, and the reference thermal temperature $\hat{T}_T$ will be determined by the dimensional analysis of the aerothermoelastic problem.

4.2 Finite Element Formulation

Several methods have been developed to simplify the FE modeling of heat transfer in composite shells [165]. These methods include first-order thermal lamination theory [166], layer-wise thermal lamination theory (LTLT) [167], and the method of homogenization [168]. The FE based on thermal lamination theory are shell elements that use ad hoc assumptions for the temperature distribution to simplify the heat transfer problem. The method of homogenization replaces the anisotropic thermal properties of the composite

shell with effective homogeneous thermal properties, so as to avoid modeling heat conduction layer by layer. To accurately capture the through-thickness temperature distribution and minimize computational cost, the LTLT method is employed in the current study.

In the LTLT based shell element, the nodes are distributed over the shell middle surface. The temperatures T_i at interfaces between the layers are unknowns at the node, as shown in Fig. 4.2. The through-the-thickness temperature distribution is approximated by piecewise linear interpolation for the unknowns. In Fig. 4.2, the gray dashed line is the middle surface of the shell.

In HYPATE, the LTLT based shell element is implemented using a solid element, which is referred to as the heat transfer in shallow shell element (HTSH). As illustrated in Fig. 4.3, the HTSH element is an 8-noded element with first-order Lagrangian shape function. The nodes are labelled by numbers enclosed by circles. Every node has one unknown, namely the temperature. A series of cells are stacked in the thickness direction, each representing one layer. Thus, the through-the-thickness temperature distribution is approximated by piecewise linear interpolation, as required by the LTLT based shell element.

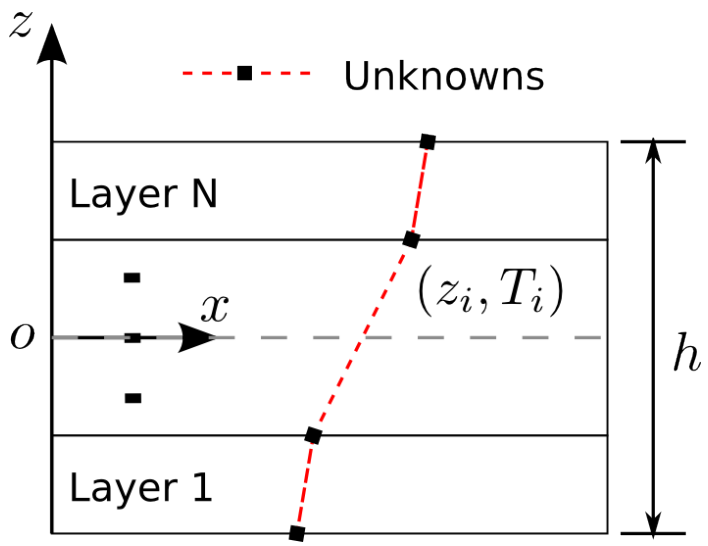

Figure 4.2: The LTLT based shell element using piecewise linear interpolation

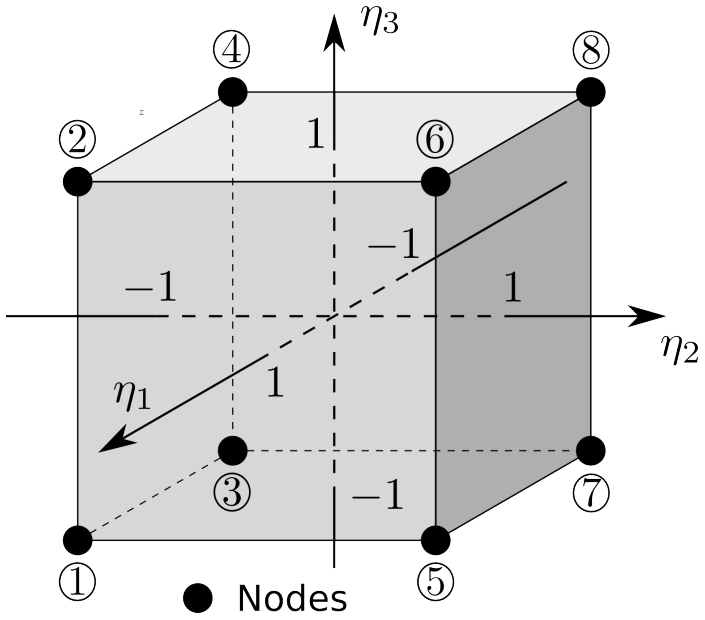

Figure 4.3: The HTSH element

4.2.1 Galerkin Formulation of the Governing Equation

Using Galerkin's method [169], multiply the governing equation by a shape function N and integrate by parts,

$$\int_V N\left[\rho^s c_p^s \dot{T} - \nabla\cdot(\mathbf{k}^s\cdot\nabla T)\right]\,\mathrm{d}V = 0$$
$$\int_V N\rho^s c_p^s \dot{T}\,\mathrm{d}V + \int_V \nabla N\cdot(\mathbf{k}^s\cdot\nabla T)\,\mathrm{d}V = \int_{\Gamma_q} N(-\dot{q}_{bc})\,\mathrm{d}\Gamma_q \tag{4.13}$$

where the differential volume is approximated using Eq. (4.5),

$$\mathrm{d}V = A_1A_2\mathrm{d}\xi_1\mathrm{d}\xi_2\mathrm{d}\zeta \approx \mathrm{d}x\mathrm{d}y\mathrm{d}z \tag{4.14}$$

Using Eqs. (4.6) and (4.14), the terms in Eq. (4.13) are simplified as,

$$\int_V N\rho^s c_p^s \dot{T}\,\mathrm{d}V \approx \int_V N\rho^s c_p^s \dot{T}\mathrm{d}x\mathrm{d}y\mathrm{d}z \tag{4.15}$$

$$\int_V \nabla N\cdot(\mathbf{k}^s\cdot\nabla T)\,\mathrm{d}V \approx \int_V \begin{bmatrix}\dfrac{\partial N}{\partial x} & \dfrac{\partial N}{\partial y} & \dfrac{\partial N}{\partial z}\end{bmatrix}\mathbf{k}^s\begin{bmatrix}\dfrac{\partial T}{\partial x}\\ \dfrac{\partial T}{\partial y}\\ \dfrac{\partial N}{\partial z}\end{bmatrix}\mathrm{d}x\mathrm{d}y\mathrm{d}z \tag{4.16}$$

4.2.2 Element Matrices and Loading Vectors

For each element, the temperature field is interpolated by shape functions $N_i, i = 1,\cdots,8$ and nodal values $\mathbf{T}^e = [T_1, T_2, \cdots, T_8]^T$,

$$T(\mathbf{x}) = [N_1, N_2, \cdots, N_8]\mathbf{T}^e \equiv \mathbf{L}_4\mathbf{T}^e \tag{4.17}$$

The shape functions are,

$$N_{i+2j+4k-6} = f_i(\eta_1)f_j(\eta_2)f_k(\eta_3), \quad i,j,k = 1,2 \tag{4.18}$$

where, $f_1(\eta) = \frac{1}{2}(1-\eta)$, $f_2(\eta) = \frac{1}{2}(1+\eta)$.

The temperature gradient is,

$$\left[\frac{\partial T}{\partial x}, \frac{\partial T}{\partial y}, \frac{\partial T}{\partial z}\right]^T = \mathbf{L}_5\mathbf{T}^e \tag{4.19}$$

where,

$$\mathbf{L}_5 = \begin{bmatrix} N_{1,x} & N_{2,x} & \cdots & N_{8,x}\\ N_{1,y} & N_{2,y} & \cdots & N_{8,y}\\ N_{1,z} & N_{2,z} & \cdots & N_{8,z}\end{bmatrix} \tag{4.20}$$

From Eqs. (4.15) and (4.16) are discretized as,

$$\int_V N\rho^s c_p^s \dot{T}\,\mathrm{d}V \approx \left\{\int_V N\rho^s c_p^s \mathbf{L}_4 \mathrm{d}x\mathrm{d}y\mathrm{d}z\right\}\dot{\mathbf{T}}^e \tag{4.21}$$

$$\int_V \nabla N\cdot(\mathbf{k}^s\cdot\nabla T)\,\mathrm{d}V \approx \left\{\int_V \begin{bmatrix}\frac{\partial N}{\partial x} & \frac{\partial N}{\partial y} & \frac{\partial N}{\partial z}\end{bmatrix}\mathbf{k}^s\mathbf{L}_5\mathrm{d}x\mathrm{d}y\mathrm{d}z\right\}\mathbf{T}^e \tag{4.22}$$

Replacing N using $N_i, i = 1,\cdots,8$, the element heat capacity matrix $\mathbf{K}_T^e$, thermal conductivity matrix $\mathbf{C}_T^e$, and the loading vector $\mathbf{Q}_T^e$ are obtained,

$$\mathbf{K}_T^e = \int_V \mathbf{L}_5^T\mathbf{k}^s\mathbf{L}_5\,\mathrm{d}V \tag{4.23a}$$

$$\mathbf{C}_T^e = \int_V \mathbf{L}_4^T\rho^s c_p^s\mathbf{L}_4\,\mathrm{d}V \tag{4.23b}$$

$$\mathbf{Q}_T^e = \int_{\Omega_q} \mathbf{L}_4^T(-\dot{q})\,\mathrm{d}\Omega_q \tag{4.23c}$$

where,

$$\dot{q} = \begin{cases} Q, & \text{Constant heat flux} \\ h_c(T-T_{aw}), & \text{Convection} \\ \varepsilon\sigma_b(T^4-T_{rad}^4), & \text{Radiation}\end{cases} \tag{4.24}$$

The volume integrations in Eqs. (4.23a) and (4.23b) are evaluated using $2\times2\times2$ Gaussian quadratures, while the surface integration in Eq. (4.23c) is evaluated using 2×2 Gaussian quadratures.

4.2.3 Equations of Motion for the Thermal Problem

The thermal conductivity and heat capacity matrices and loading vectors of the individual elements are assembled into unconstrained total thermal conductivity matrix $\mathbf{K}_T^u$, total heat capacity matrix $\mathbf{C}_T$, unconstrained total loading vector $\mathbf{Q}_T^u$, and total temperature vector $\mathbf{T}$. Note that both $\mathbf{K}_T$ and $\mathbf{C}_T$ are nonlinear when the material properties are temperature dependent.

The governing equations for heat transfer problem are,

$$\mathbf{C}_T(\mathbf{T})\dot{\mathbf{T}} + \mathbf{K}_T^u(\mathbf{T})\mathbf{T} = \mathbf{Q}_T^u(\mathbf{T}) \tag{4.25}$$

Next, the temperature boundary condition has to be enforced on Γ_T, i.e. on N_b nodes where the temperature is prescribed,

$$T_i = T_{bi}, \quad i \in \{1, 2, \cdots, N_b\} \tag{4.26}$$

Equation (4.25) is modified using the penalty method (pp. 459–478 of Ref. [158]),

$$\mathbf{C}_T(\mathbf{T})\dot{\mathbf{T}} + \mathbf{K}_T(\mathbf{T})\mathbf{T} = \mathbf{Q}_T(\mathbf{T}) \tag{4.27}$$

where $\mathbf{K}_T = \mathbf{K}_T^u + \mathbf{K}_T^c$ and $\mathbf{Q}_T = \mathbf{Q}_T^u + \mathbf{Q}_T^c$. The penalty terms $\mathbf{K}_T^c$ and $\mathbf{Q}_T^c$ are,

$$[\mathbf{K}_T^c]_{ij} = \begin{cases} \tilde{\alpha}, & i = j \in \{1, 2, \cdots, N_b\} \\ 0, & \text{else} \end{cases}$$

$$[\mathbf{Q}_T^c]_i = \begin{cases} \tilde{\alpha} T_{bc}, & i \in \{1, 2, \cdots, N_b\} \\ 0, & \text{else} \end{cases}$$

4.2.4 Solution of the Nonlinear Thermal Problem

Equation (4.27) is discretized in the time domain using the Crank-Nicolson scheme for second-order time accuracy (pp. 490–522 of Ref. [158]). The Newton-Raphson method is used to solve the resulting nonlinear equations.

Let $\mathbf{T}^\alpha = (1 - \bar{\alpha})\mathbf{T}^n + \bar{\alpha}\mathbf{T}^{n+1}$,

$$\mathcal{R}_T(\mathbf{T}^{n+1}) = \mathbf{C}_T(\mathbf{T}^\alpha)\frac{\mathbf{T}^{n+1} - \mathbf{T}^n}{\Delta t} + \mathbf{K}_T(\mathbf{T}^\alpha)\mathbf{T}^\alpha = \mathbf{Q}_T(\mathbf{T}^\alpha) \tag{4.28}$$

For unconditional stability, let $\bar{\alpha} = \frac{1}{2}$ in the calculation. However, this guarantees unconditional stability in linear systems; and in the nonlinear case, numerical instability may still occur.

Similar to the structural problem, Eq. (4.28) is solved using Newton-Raphson method with line search, which requires the solution of a series of linear systems,

$$\left(\frac{\partial \mathcal{R}_T(\mathbf{T}^i)}{\partial \mathbf{T}^i} - \frac{\partial \mathbf{Q}_T(\mathbf{T}^\alpha)}{\partial \mathbf{T}^i} \right) \Delta \mathbf{T} = -[\mathcal{R}_T(\mathbf{T}^i) - \mathbf{Q}_T(\mathbf{T}^\alpha)] \tag{4.29}$$

where $\mathbf{T}^i$ is the solution $\mathbf{T}^{n+1}$ at the ith iteration.

The Jacobians of the residual and the loading vector are,

$$\begin{aligned} \frac{\partial \mathcal{R}_T(\mathbf{T}^{n+1})}{\partial \mathbf{T}^{n+1}} = \frac{\bar{\alpha}}{\Delta t} \underbrace{\frac{\partial \mathbf{C}_T(\mathbf{T}^\alpha)}{\partial \mathbf{T}^\alpha} \Delta \mathbf{T}}_{\text{Term 1}} + \frac{1}{\Delta t} \mathbf{C}_T(\mathbf{T}^\alpha) \\ + \bar{\alpha} \underbrace{\frac{\partial \mathbf{K}_T(\mathbf{T}^\alpha)}{\partial \mathbf{T}^\alpha} \mathbf{T}^\alpha}_{\text{Term 2}} + \bar{\alpha} \mathbf{K}_T(\mathbf{T}^\alpha) \end{aligned} \tag{4.30a}$$

$$\frac{\partial \mathbf{Q}_T(\mathbf{T}^\alpha)}{\partial \mathbf{T}^{n+1}} = \bar{\alpha} \frac{\partial \mathbf{Q}_T(\mathbf{T}^\alpha)}{\partial \mathbf{T}^\alpha} \tag{4.30b}$$

where $\Delta \mathbf{T} = \mathbf{T}^{n+1} - \mathbf{T}^n$.

To obtain the explicit forms that are suitable for programming, the two terms identified by curved brackets in Eq. (4.30a) and the term in Eq. (4.30b) are clarified next. Note that $\mathbf{C}_T$, $\mathbf{K}_T$, and $\mathbf{Q}_T$ are linear combinations of element heat capacity and thermal conductivity matrices and loading vector, respectively. So one can calculate derivatives of element matrices and loading vector and assemble them to obtain the three terms in Eq. (4.30a). In

each element,

$$\frac{\partial \mathbf{C}_T^e}{\partial \mathbf{T}^\alpha}\Delta\mathbf{T} = \left[\begin{array}{c|c|c} \cdots & \dfrac{\partial \mathbf{C}_T^e}{\partial T_i^\alpha}\Delta\mathbf{T} & \cdots \end{array}\right], \quad \frac{\partial \mathbf{C}_T^e}{\partial T_i^\alpha} = \int_V \mathbf{L}_1^T \frac{\partial \rho^s c_p^s}{\partial T_i^\alpha}\mathbf{L}_1 \,\mathrm{d}V \tag{4.31a}$$

$$\frac{\partial \mathbf{K}_T^e}{\partial \mathbf{T}^\alpha}\mathbf{T}^\alpha = \left[\begin{array}{c|c|c} \cdots & \dfrac{\partial \mathbf{K}_T^e}{\partial T_i^\alpha}\mathbf{T}^\alpha & \cdots \end{array}\right], \quad \frac{\partial \mathbf{K}_T^e}{\partial T_i^\alpha} = \int_V \mathbf{L}_2^T \frac{\partial \mathbf{k}^s}{\partial T^\alpha i}\mathbf{L}_2 \,\mathrm{d}V \tag{4.31b}$$

$$\frac{\partial \mathbf{Q}_T^e}{\partial \mathbf{T}^\alpha} = \left[\begin{array}{c|c|c} \cdots & \dfrac{\partial \mathbf{Q}_T^e}{\partial T_i^\alpha} & \cdots \end{array}\right], \quad \frac{\partial \mathbf{Q}_T^e}{\partial T_i^\alpha} = \int_\Omega \mathbf{L}_1^T \left(-\frac{\partial \dot{q}}{\partial T_i^\alpha}\right)\mathbf{L}_1 \,\mathrm{d}\Gamma \tag{4.31c}$$

The derivative of $\dot{q}$ depends on the type of heat flux,

$$\frac{\partial \dot{q}}{\partial T_i^\alpha} = \begin{cases} 0, & \text{Constant heat flux} \\ h_c, & \text{Convection} \\ 4\varepsilon\sigma_b (T_i^\alpha)^3, & \text{Radiation} \end{cases} \tag{4.32}$$

CHAPTER 5

Fully-Coupled Aerothermoelastic Analysis

5.1 Overview of the HYPATE Framework

The HYPATE computational framework is developed for numerical simulation of aerothermoelastic responses using fluid solvers having different levels of fidelity. The code structure of the framework is shown in Fig. 5.1. The framework employs a partitioned approach using a loosely-coupled or a tightly-coupled scheme. Individual solvers are developed to compute the fluid, thermal and structural responses, as described in Chaps. 2-4. The coupling is achieved by exchanging boundary data at the interfaces of the physical domains. Moreover, a solver based on linearized stability analysis (LSA) is developed as an extension of the p-method commonly used in aeroelasticity [85]. The LSA is used to examine the stability of the deformed structure at every time step, so as to detect the onset of aerothermoelastic instability.

In the following sections, the various components of the HYPATE framework are described, including the information exchange between the solvers, the coupling schemes for transient and quasi-steady aerothermoelastic responses, and the LSA solver for the identification of aerothermoelastic instability.

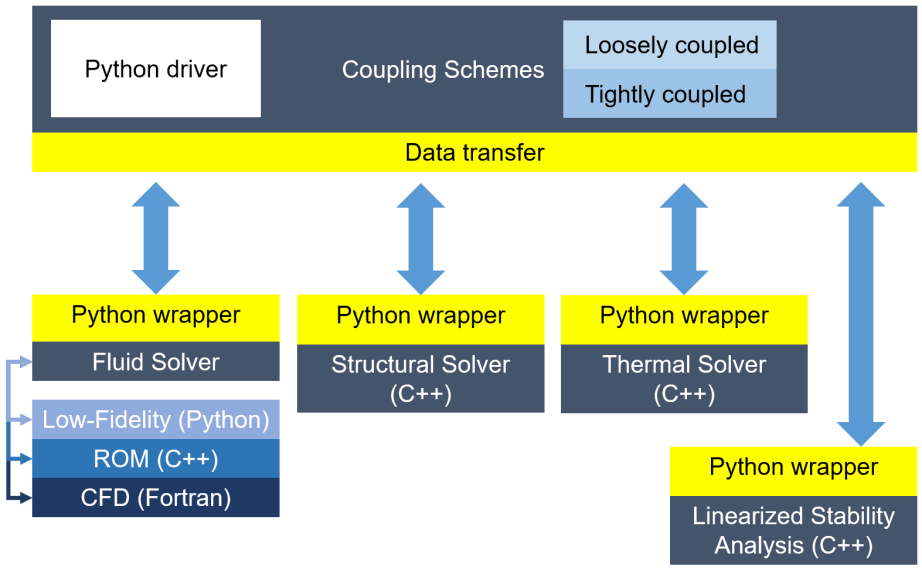

Figure 5.1: Code structure of the HYPATE framework

5.2 Exchange of Information Between the Physical Domains

At the fluid-solid boundary, the discretizations used for the solid and the fluid surfaces are usually mismatched. The nodes of fluid mesh are denser when compared to those of the solid mesh. Therefore, appropriate interpolation schemes are required for effective information exchange between the two domains. The displacements $\mathbf{u}$ and the temperature $\mathbf{T}$ are interpolated from the solid to the fluid mesh using a mortar element scheme [76]. The aerodynamic loading $\mathbf{p}$ and heat flux $\dot{\mathbf{q}}$ are interpolated from the fluid to the solid mesh using the quadrature projection scheme [170]. The combination of the mortar element and the quadrature projection scheme guarantees the conservation of the load and energy transfer at the fluid-solid boundary, a necessary requirement for the numerical stability of the coupled solver [76]. The interpolation schemes are expressed as linear transformations,

$$\mathbf{F}_S = \mathbf{H}_{SF}\mathbf{p} \tag{5.1a}$$

$$\mathbf{Q}_T = \mathbf{H}_{TF}\dot{\mathbf{q}} \tag{5.1b}$$

$$\mathbf{u}_F = \mathbf{H}_{FS}\mathbf{u} \tag{5.1c}$$

$$\mathbf{T}_w = \mathbf{H}_{FT}\mathbf{T} \tag{5.1d}$$

The transformation matrices in Eqs. (5.1a)-(5.1d) only need to be computed once, when the spatial discretization of the solid and the fluid domains is provided.

5.3 Transient Response

In Ref. [75], a theoretical framework for determining the time accuracy of a coupling scheme for FSI problems was developed. The framework is based on a three-field formulation. The formulation includes fluid domain, solid domain, and fluid-mesh-motion domain, and a pseudo-elastodynamic method is used to deform the mesh when solid boundaries move. In the current study, the framework is generalized for time accuracy analysis of a coupling scheme for FSTI problems.

As pointed out in section I, the numerical stability of a coupling scheme for FSI problems can be improved by a proper combination of estimators, i.e. predictors and correctors. The choice of estimators is facilitated by the energy balance analysis. In Ref. [77], the difference between the fluid work and the sum of kinetic energy and strain energy in an undamped system is examined by conducting numerical studies. The difference should equal the initial total energy when the artificial energy of the coupling scheme is zero. The method can be conveniently implemented numerically. However, it cannot be used to determine the order of time accuracy of the artificial energy. In Ref. [78], the energy balance analysis relies on the assumption of harmonic aeroelastic response, i.e. both structural and fluid responses are harmonic. The time accuracy of the artificial energy *per period*, which is defined as energy accuracy in Ref. [78], is analytically determined for the various coupling

schemes. However, the validity of the energy accuracy defined in this manner is limited to cases where the aeroelastic responses are harmonic. In the current study, a modified energy balance analysis is developed to quantify the energy accuracy. In this analysis framework, energy accuracy is defined as the time accuracy of the artificial energy *per time step*, so that energy accuracy of a coupling scheme can be determined analytically and is applicable to arbitrary aeroelastic responses.

Next, two typical loosely-coupled schemes for aerothermoelastic simulation are described. Subsequently, the framework proposed in Ref. [75] is modified to analyze the time accuracy of a loosely-coupled scheme. The modified energy balance analysis is developed to examine numerical stability of coupling schemes with different combinations of estimators. The first scheme is adapted from the scheme in Ref. [81] by removing the subcycling procedure, which will be referred to as the S1 scheme. The second scheme is the serial staggered procedure in Ref. [79] extended with a set of non-trivial estimators, which will be referred to as the S2 scheme.

5.3.1 Loosely-Coupled Schemes

In a typical aerothermoelastic coupling scheme [81], the solvers are initiated at the same physical time t. As the calculations commence, a series of operations are performed to advance the coupled system to next time step.

The coupling procedure of S1 scheme is, as illustrated in Fig. 5.2,

1. The thermal step:
   (a) Heat flux from the fluid solver is extrapolated and passed to the thermal solver,

$$\dot{\mathbf{q}}^{n+1/2,E} = \frac{3}{2}\dot{\mathbf{q}}^{n} - \frac{1}{2}\dot{\mathbf{q}}^{n-1} \tag{5.2}$$

   (b) The thermal solution $\mathbf{T}$ is updated to step $n+1$.
2. The aeroelastic step:

(a) The thermal solution is passed to the fluid solver and the structural solver.

(b) The pressure from fluid solver is extrapolated and passed to the structural solver,

$$\mathbf{p}^{n+1,E} = 2\mathbf{p}^{n} - \mathbf{p}^{n-1} \tag{5.3}$$

(c) The structural solution $\mathbf{u}$ is updated to step $n+1$.

(d) The displacement from the structural solver is passed to the the fluid solver,

$$\mathbf{u}^{n+1,E} = \mathbf{u}^{n+1} \tag{5.4}$$

(e) The fluid solutions $\mathbf{p}$ and $\dot{\mathbf{q}}$ are updated to step $n+1$.

3. Above steps are repeated until the end of the simulation.

The procedure for S2 scheme is illustrated in Fig. 5.3. The thermal step of the S2 scheme is the same as the S1 scheme, but the aeroelastic step is modified,

(2a) The thermal solution is passed to the fluid solver and the structural solver.

(2b) The displacement from the structural solver is extrapolated and passed to the fluid solver,

$$\mathbf{u}^{n+1,E} = \mathbf{u}^{n} + \Delta t \left(\frac{3}{2}\dot{\mathbf{u}}^{n} - \frac{1}{2}\dot{\mathbf{u}}^{n-1} \right) \tag{5.5}$$

(2c) The fluid solutions $\mathbf{p}$ and $\dot{\mathbf{q}}$ are updated to step $n+1$.

(2d) The pressure from fluid solver is passed to the structural solver,

$$\mathbf{p}^{n+1,E} = \mathbf{p}^{n+1} \tag{5.6}$$

(2e) The structural solution $\mathbf{u}$ is updated to step $n+1$.

For both aeroelastic schemes, a starting procedure is needed. In the current study,

following procedure is employed [80],

$$\dot{\mathbf{u}}^1 = \dot{\mathbf{u}}^0 + \Delta t \ddot{\mathbf{u}}^0 \tag{5.7a}$$

$$\mathbf{u}^1 = \mathbf{u}^0 + \Delta t \dot{\mathbf{u}}^0 + \frac{1}{2}\Delta t^2 \ddot{\mathbf{u}}^0 \tag{5.7b}$$

Subsequently the pressure and the heat flux at step 1 is calculated using $\mathbf{u}^1$ and $\dot{\mathbf{u}}^1$. The same starting procedure is used for both schemes so that their time accuracy can be compared on the same basis.

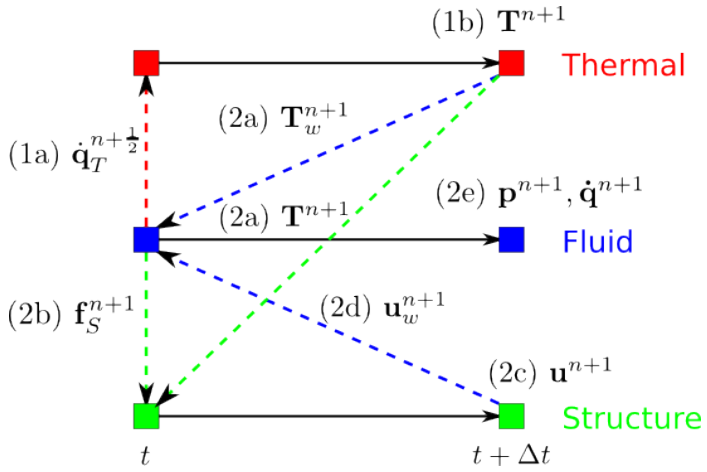

Figure 5.2: Schematic outline of the S1 scheme

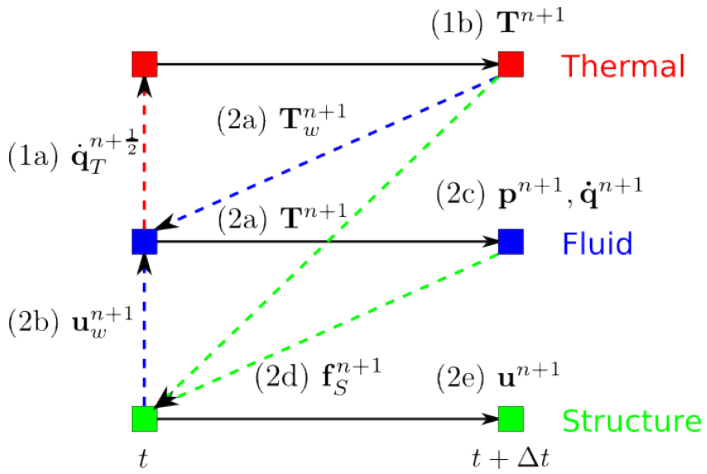

Figure 5.3: Schematic outline of the S2 scheme

5.3.2 Time Accuracy Analysis of Coupling Schemes

In the aeroelastic simulations, the fluid and structural solvers constructed using second-order time accurate schemes may not exhibit the same order of time accuracy in a loosely-coupled scheme [75]. The approach from Ref. [75] is adapted to determine the conditions under which the loosely-coupled scheme is second-order time accurate for aerothermoelastic simulations.

5.3.2.1 Fluid Solver

The fluid solution is represented symbolically in the form of Eqs. (2.29b) and (2.29a). In the loosely-coupled scheme, the pressure and the heat flux are represented as,

$$\mathbf{p}^{n+1} = \mathbf{p}(\mathbf{u}_F^{n+1,E}, \mathbf{u}_F^{n,E}, \mathbf{u}_F^{n-1,E}, \mathbf{T}_w^{n+1}) \tag{5.8a}$$

$$\dot{\mathbf{q}}^{n+1} = \dot{\mathbf{q}}(\mathbf{u}_F^{n+1,E}, \mathbf{u}_F^{n,E}, \mathbf{u}_F^{n-1,E}, \mathbf{T}_w^{n+1}) \tag{5.8b}$$

where the displacements $\mathbf{u}_w$ are provided by an estimator from the structural solver. Compared to Eq. (2.29b), the error in the pressure due to estimation in Eq. (5.8a) is

$$\begin{aligned}
\epsilon_p &= ||\mathbf{p}(\mathbf{u}_F^{n+1,E}, \mathbf{u}_F^{n,E}, \mathbf{u}_F^{n-1,E}, \mathbf{T}_w^{n+1}) - \mathbf{p}(\mathbf{u}_F^{n+1}, \mathbf{u}_F^{n}, \mathbf{u}_F^{n-1}, \mathbf{T}_w^{n+1})|| \\
&= O(|| \sum_{k=-1}^{1} \frac{\partial \mathbf{p}}{\partial \mathbf{u}_F^{n+k}} (\mathbf{u}_F^{n+k,E} - \mathbf{u}_F^{n+k})||) \\
&= O(\sum_{k=-1}^{1} ||\frac{\partial \mathbf{p}}{\partial \mathbf{u}_F^{n+k}}|| ||\mathbf{u}_F^{n+k,E} - \mathbf{u}_F^{n+k}||) \\
&= \sum_{k=-1}^{1} O(||\mathbf{u}^{n+k,E} - \mathbf{u}^{n+k}||)
\end{aligned} \tag{5.9}$$

where Taylor series expansion is employed to estimate the order of ϵ_p [75]. Using the same approach, the error in the heat flux due to estimation is,

$$\begin{aligned}\epsilon_{\dot{q}} &= ||\dot{\mathbf{q}}(\mathbf{u}_F^{n+1,E}, \mathbf{u}_F^{n,E}, \mathbf{u}_F^{n-1,E}, \mathbf{T}_w^{n+1}) - \dot{\mathbf{q}}(\mathbf{u}_F^{n+1}, \mathbf{u}_F^{n}, \mathbf{u}_F^{n-1}, \mathbf{T}_w^{n+1})|| \\ &= \sum_{k=-1}^{1} O(||\mathbf{u}^{n+k,E} - \mathbf{u}^{n+k}||)\end{aligned} \tag{5.10}$$

When $O(||\mathbf{u}^{n+k,E} - \mathbf{u}^{n+k}||) = O(\Delta t^2)$, i.e. displacement estimator is at least second-order time-accurate, the time accuracy of the fluid solver in the coupled scheme is preserved. Note that the wall temperature at time step $n+1$ is passed to fluid solver without estimation. As long as the thermal solution is second-order time-accurate, it would not effect the time accuracy of the fluid solution.

5.3.2.2 Structural Solver

From Eq. (3.43), the governing equation for structural domain is,

$$\mathbf{M}\ddot{\mathbf{u}}^{n+1} + \mathbf{C}\dot{\mathbf{u}}^{n+1} + \mathbf{F}_I(\mathbf{u}^{n+1}, \mathbf{T}^{n+1}) = \mathbf{F}_S^{n+1} \tag{5.11}$$

In coupled system, the loading is provided by the fluid solver via an estimator, such that

$$\mathbf{F}_S^{n+1} = \mathbf{H}_{SF}\mathbf{p}^{n+1} \approx \mathbf{H}_{SF}\mathbf{p}^{n+1,E} \tag{5.12}$$

The discretization error is,

$$\epsilon_S = \epsilon_t + \epsilon_f \tag{5.13}$$

where ϵ_t is the error associated with the discretization in time domain by the generalized-α scheme, which is second-order time accurate $\epsilon_t = O(\Delta t^2)$. The term ϵ_f is the error

associated with loading estimation,

$$\epsilon_f = O(||\mathbf{p}^{n+1,E} - \mathbf{p}^{n+1}||)$$

The total error due to discretization in the coupled scheme is,

$$\epsilon_S = O(||\mathbf{p}^{n+1,E} - \mathbf{p}^{n+1}||) + O(\Delta t^2) \tag{5.14}$$

Therefore when the pressure estimator is at least second-order time-accurate, the structural solution in the coupled scheme remains second-order time-accurate. Similar to the fluid solution, the temperature is passed to the structural solver without estimation and the thermal solution does not effect the time-accuracy of the structural solution.

5.3.2.3 Thermal Solver

From Eq. (4.27), the governing equation for thermal domain is,

$$\mathbf{C}_T(\mathbf{T}^{n+1/2})\dot{\mathbf{T}}^{n+1/2} + \mathbf{K}_T(\mathbf{T}^{n+1/2})\mathbf{T}^{n+1/2} = \mathbf{Q}_T^{n+1/2} \tag{5.15}$$

In coupled system, the heat flux $\dot{\mathbf{q}}_T^{n+1/2}$ is provided by the fluid solver via an estimator, such that,

$$\mathbf{Q}_T^{n+1/2} = \mathbf{H}_{TF}\dot{\mathbf{q}}^{n+1/2} \approx \mathbf{H}_{TF}\dot{\mathbf{q}}^{n+1/2,E} \tag{5.16}$$

The discretization error is,

$$\epsilon_T = \epsilon_t + \epsilon_q \tag{5.17}$$

where ϵ_t is the error associated with Crank-Nicolson scheme, which is second-order time accurate $\epsilon_t = O(\Delta t^2)$, and ϵ_q is the error associated with heat flux estimation,

$$\epsilon_q = O(||\dot{\mathbf{q}}^{n+1/2,E} - \dot{\mathbf{q}}^{n+1/2}||)$$

The total error due to discretization in the coupled scheme is,

$$\epsilon_T = O(||\dot{\mathbf{q}}^{n+1/2,E} - \dot{\mathbf{q}}^{n+1/2}||) + O(\Delta t^2) \tag{5.18}$$

Therefore as long as the heat flux estimator is at least second-order time-accurate, the thermal solver in coupled scheme remains second-order time-accurate.

5.3.2.4 Summary

Based on above discussion, the loosely coupled scheme for aerothermoelastic simulation is second-order time-accurate when,

1. The individual fluid, structural and thermal solvers are second-order time-accurate.
2. The displacement, force and heat flux estimators are second-order time-accurate.

Note that the aerothermoelastic coupling procedures using S1 and S2 schemes both produce second-order time-accurate solutions.

5.3.3 Energy Balance Analysis of Coupling Schemes

The aeroelastic portion of the loosely-coupled schemes is further characterized using an energy balance analysis. Using the definitions from Ref. [78], in a structural solver using the generalized-α scheme, which is a variant of the midpoint rule, the work done on the structure by the fluid δE_S is,

$$\delta E_S = \frac{1}{2}(\mathbf{F}_S^{n+1,E} + \mathbf{F}_S^{n,E})^T(\mathbf{u}^{n+1} - \mathbf{u}^n) = \frac{1}{2}(\mathbf{p}^{n+1,E} + \mathbf{p}^{n,E})^T\mathbf{H}_{SF}^T(\mathbf{u}^{n+1} - \mathbf{u}^n) \tag{5.19}$$

and the work done on the fluid by the structure δE_F in a second-order time-accurate fluid solver is,

$$\delta E_F = -\frac{1}{2}(\mathbf{p}^{n+1} + \mathbf{p}^n)^T\mathbf{H}_{SF}^T(\mathbf{u}^{n+1,E} - \mathbf{u}^{n,E}) \tag{5.20}$$

The artificial energy δE over one time step is,

$$\delta E = \delta E_S + \delta E_F \tag{5.21}$$

It is evident that the artificial energy is non-zero unless

$$\mathbf{p}^{n+1,E} = \mathbf{p}^{n+1}, \quad \mathbf{u}^{n+1,E} = \mathbf{u}^{n+1} \tag{5.22}$$

However, in loosely-coupled schemes, the values of $\mathbf{u}^{n+1}$ and $\mathbf{p}^{n+1}$ are unknown at the same time and either $\mathbf{u}^{n+1}$ or $\mathbf{p}^{n+1}$ is approximated. Therefore, in loosely-coupled schemes, artificial energy accumulates at each time step, resulting in error accumulation and eventual numerical instability.

The artificial energy can be quantified by its order of time accuracy. Use the combination of estimators in the S1 scheme as example,

$$\begin{aligned}\mathbf{p}^{n+1,E} &= 2\mathbf{p}^n - \mathbf{p}^{n-1} \\ \mathbf{u}^{n+1,E} &= \mathbf{u}^{n+1}\end{aligned}$$

Expand δE in Taylor series at the nth time step,

$$\begin{aligned}\delta E = &\frac{1}{2}(\mathbf{p}^n + \frac{1}{2}\mathbf{p}^{n-1} - \frac{1}{2}\mathbf{p}^{n-2})^T \mathbf{H}_{SF}^T (\mathbf{u}^{n+1} - \mathbf{u}^n) \\ &- \frac{1}{2}(\mathbf{p}^{n+1} + \mathbf{p}^n)^T \mathbf{H}_{SF}^T (\mathbf{u}^{n+1} - \mathbf{u}^n) \\ &\approx -(\ddot{\mathbf{p}}^n)^T \mathbf{H}_{SF}^T \dot{\mathbf{u}}^n \Delta t^3 = O(\Delta t^3)\end{aligned} \tag{5.23}$$

Therefore, the artificial energy in the S1 scheme is third-order time-accurate. For simplicity, we refer to a scheme as pth-order energy-accurate when its artificial energy per time step is pth-order time-accurate.

On the other hand, if the estimators in the S2 scheme are used,

$$\mathbf{p}^{n+1,E} = \mathbf{p}^{n+1}$$
$$\mathbf{u}^{n+1,E} = \mathbf{u}^{n} + \Delta t \left(\frac{3}{2}\dot{\mathbf{u}}^{n} - \frac{1}{2}\dot{\mathbf{u}}^{n-1} \right)$$

The S2 scheme is fourth-order energy-accurate with

$$\delta E \approx \frac{5}{12}(\mathbf{p}^{n})^{T}\mathbf{H}_{SF}^{T}\mathbf{u}^{(4),n}\Delta t^{4} = O(\Delta t^{4}) \tag{5.24}$$

which is one-order higher than that of the S1 scheme.

5.4 Quasi-Steady Response

The loosely-coupled scheme is developed for transient aerothermoelastic response and is suitable for both CFD-based and ROM-based simulations. However, the CFD-based fluid solver requires solving partial differential equations, i.e. the RANS equations, while the ROM-based fluid solver generates the aerodynamic pressure and heat flux by evaluating analytical expressions and does not require the solution of any differential equations. Therefore, it is possible to develop a coupling scheme for the ROM-based simulations that is more efficient than the loosely-coupled scheme.

5.4.1 Decomposition of Transient Aerothermoelastic Response

The governing equations for the ROM-based aerothermoelastic response are derived from the fluid ROM formulation Eq. (2.73), the equations of motion for structural and thermal responses Eqs. (3.43) and (4.27), and the interface conditions Eqs. (5.1a)-(5.1d). These seven equations are simplified into two equations in the following procedure.

First, the structural displacement $\mathbf{u}$ and body temperature $\mathbf{T}$ are transformed to the surface deformation and wall temperature in the fluid domain using Eqs. (5.1c) and (5.1d),

respectively, so as to obtain the pressure and heat flux from the fluid ROM Eq. (2.73),

$$\dot{\mathbf{q}} = \dot{\mathbf{q}}(\mathbf{u}_F, \mathbf{T}_w) = \dot{\mathbf{q}}(\mathbf{H}_{FS}\mathbf{u}, \mathbf{H}_{FT}\mathbf{T}) \tag{5.25a}$$

$$\mathbf{p} = \mathbf{p}(\mathbf{u}_F, \dot{\mathbf{u}}_F, \mathbf{T}_w) = \mathbf{p}(\mathbf{H}_{FS}\mathbf{u}, \mathbf{H}_{FS}\dot{\mathbf{u}}, \mathbf{H}_{FT}\mathbf{T}) \tag{5.25b}$$

Next, using Eq. (5.1b), the aerodynamic heat flux $\dot{\mathbf{q}}$ in Eq. (5.25a) is transformed to the external heat flux vector in the governing equation for thermal response Eq. (4.27),

$$\mathbf{C}_T(\mathbf{T})\dot{\mathbf{T}} + \mathbf{Q}_I(\mathbf{T}) = \mathbf{Q}_T = \mathbf{H}_{TF}\dot{\mathbf{q}} \tag{5.26}$$

Similarly, using Eq. (5.1a), the aerodynamic pressure $\mathbf{p}$ in Eq. (5.25b) is transformed to the external loading vector in the governing equation for structural response Eq. (3.43),

$$\mathbf{M}\ddot{\mathbf{u}} + \mathbf{C}\dot{\mathbf{u}} + \mathbf{F}_I(\mathbf{u}, \mathbf{T}) = \mathbf{F}_S = \mathbf{H}_{SF}\mathbf{p} \tag{5.27}$$

The governing equations for the ROM-based aerothermoelastic response are obtained by combining Eqs. (5.26) and (5.27),

$$\begin{cases} \mathbf{C}_T(\mathbf{T})\dot{\mathbf{T}} + \mathbf{Q}_I(\mathbf{T}) = \mathbf{Q}_T(\mathbf{u}, \mathbf{T}) & \text{(5.28a)} \\ \mathbf{M}\ddot{\mathbf{u}} + \mathbf{C}\dot{\mathbf{u}} + \mathbf{F}_I(\mathbf{u}, \mathbf{T}) = \mathbf{F}_S(\mathbf{u}, \dot{\mathbf{u}}, \mathbf{T}) & \text{(5.28b)} \end{cases}$$

Equations (5.28a) and (5.28b) represent the aerothermal and the aeroelastic subproblems of the ROM-based aerothermoelastic analysis, respectively.

The time scales for the aerothermal and aeroelatic subproblems are given by the thermal and structural characteristic times, respectively. From Eqs. (2.47), (2.49), and (2.51),

$$t_{AT} = t_T = \frac{\rho^s c_p^s h^2}{k^s} \sim 1\text{s} \tag{5.29a}$$

$$t_{AE} = t_S = C\sqrt{\frac{\rho^s L^4}{Eh^2}} \sim 10^{-2}\text{s} \tag{5.29b}$$

The fluid characteristic time no longer exists in the ROM-based aerothermoelastic response, due to the quasi-steady flow assumption employed in the fluid ROM formulation. It should be noted that, when the loosely-coupled scheme is employed to solve Eq. (5.28), the time step size has to be a fraction of t_{AE} to resolve the transient aerothermoelastic response.

The disparity in the characteristic time scales t_{AT} and t_{AE} allows the decomposition of the transient aerothermoelastic response into the quasi-steady and unsteady components,

$$\mathbf{T} = \mathbf{T}^{qs} + \mathbf{T}^{uns}, \quad \mathbf{u} = \mathbf{u}^{qs} + \mathbf{u}^{uns} \tag{5.30}$$

The quasi-steady aerothermoelastic response $(\mathbf{T}^{qs}, \mathbf{u}^{qs})$ satisfies,

$$\begin{cases} \mathbf{C}_T(\mathbf{T}^{qs})\dot{\mathbf{T}}^{qs} + \mathbf{Q}_I(\mathbf{T}^{qs}) = \mathbf{Q}_T(\mathbf{u}^{qs}, \mathbf{T}^{qs}) & \text{(5.31a)} \\ \mathbf{F}_I(\mathbf{u}^{qs}, \mathbf{T}^{qs}) = \mathbf{F}_S(\mathbf{u}^{qs}, 0, \mathbf{T}^{qs}) & \text{(5.31b)} \end{cases}$$

The variation of the quasi-steady components is negligible on the aeroelastic time scale. Therefore $\mathbf{T}^{uns} \approx 0$ and the unsteady structural response $\mathbf{u}^{uns}$ satisfies,

$$\mathbf{M}\ddot{\mathbf{u}}^{uns} + \mathbf{C}\dot{\mathbf{u}}^{uns} + \mathbf{F}_I(\mathbf{u}^{qs} + \mathbf{u}^{uns}, \mathbf{T}^{qs}) = \mathbf{F}_S(\mathbf{u}^{qs} + \mathbf{u}^{uns}, \dot{\mathbf{u}}^{uns}, \mathbf{T}^{qs}) \tag{5.32}$$

Equations (5.31a)-(5.31b) represent the quasi-steady aerothermoelastic response consisting of the heat conduction process in the structure combined with the static aeroelastic deformation. Equation (5.32) represents the unsteady *aeroelastic* response due to the aerodynamic loading and the temperature distribution $\mathbf{T}^{qs}$ that is constant on the aeroelastic time scale. Using Tikhonov's Theorem [171, 172] it can be shown that the unsteady components in Eq. (5.30) are negligible, i.e. $\mathbf{T}^{uns} \approx 0$ and $\mathbf{u}^{uns} \approx 0$, as long as the unsteady structural response $\mathbf{u}^{uns}$ is stable. A response is considered stable, if all the oscillatory components in the response decay in time.

The conclusion from Tikhonov's Theorem has two implications. First, to obtain the

aerothermoelastic response over extended time periods, one can solve Eq. (5.31) using a time step size $\Delta t \sim t_{AT}$, instead of solving Eq. (5.28) using a time step size $\Delta t \sim t_{AE}$. Neglecting the unsteady aerothermoelastic response $(\mathbf{T}^{uns}, \mathbf{u}^{uns})$ will result in a relative error of $O(\frac{t_{AE}}{t_{AT}}) \sim O(10^{-2})$, which is negligible as long as the aerothermoelastic response governed by Eq. (5.28) is stable. Second, the stability of the aerothermoelastic response is determined by the stability of the unsteady structural response $\mathbf{u}^{uns}$ governed by Eq. (5.32). Furthermore, the quasi-steady approximation of the aerothermoelastic response is invalid if the unsteady response $\mathbf{u}^{uns}$ becomes unstable.

5.4.2 Linearized Stability Analysis

The stability of the unsteady response $\mathbf{u}^{uns}$, governed by Eq. (5.32), is determined by solving the eigenvalue problem represented by Eq. (5.33),

$$[\lambda_p^2 \mathbf{M} + \lambda_p(\mathbf{C} - \mathbf{C}_A) + (\mathbf{K} - \mathbf{K}_A)]\mathbf{u} = 0 \tag{5.33}$$

where

$$\mathbf{K} = \frac{\partial \mathbf{F}_I(\mathbf{u}^{qs} + \mathbf{u}^{uns}, \mathbf{T}^{qs})}{\partial \mathbf{u}^{uns}}, \quad \mathbf{K}_A = \frac{\partial \mathbf{F}_S(\mathbf{u}^{qs} + \mathbf{u}^{uns}, \dot{\mathbf{u}}^{uns}, \mathbf{T}^{qs})}{\partial \mathbf{u}^{uns}}, \\ \mathbf{C}_A = \frac{\partial \mathbf{F}_S(\mathbf{u}^{qs} + \mathbf{u}^{uns}, \dot{\mathbf{u}}^{uns}, \mathbf{T}^{qs})}{\partial \dot{\mathbf{u}}^{uns}} \tag{5.34}$$

The aerodynamic matrices $\mathbf{C}_A$ and $\mathbf{K}_A$ are usually asymmetric, so $(\mathbf{C}-\mathbf{C}_A)$ and $(\mathbf{K}-\mathbf{K}_A)$ are asymmetric as well.

Equation (5.33) is a polynomial eigenvalue problem (PEP), where the eigenvalues always appear as complex conjugate pairs $(\lambda_{p1}, \lambda_{p2})$. The PEP formulation can be simplified for computational efficiency by employing two additional assumptions:

(1) There is no viscous damping, i.e. $\mathbf{C} = 0$.

(2) The aerodynamic damping is negligible, due to the quasi-steadiness of the aerodynamic loading, implying $\mathbf{C}_A = 0$.

With these assumptions, $(\mathbf{C} - \mathbf{C}_A) = 0$, and Eq. (5.33) simplifies to,

$$[\lambda_p^2 \mathbf{M} + (\mathbf{K} - \mathbf{K}_A)]\mathbf{u} = 0, \quad \text{or} \quad (\mathbf{K} - \mathbf{K}_A)\mathbf{u} = \lambda_g \mathbf{M}\mathbf{u} \tag{5.35}$$

where $\lambda_g = -\lambda_p^2$. Equation (5.35) represents the generalized eigenvalue problem (GEP) used in structural dynamics. Since $(\mathbf{K} - \mathbf{K}_A)$ is asymmetric, Eq. (5.35) yields complex eigenvalues. In Ref. [173], it was shown that the approximation $(\mathbf{C} - \mathbf{C}_A) = 0$ does not produce a discernible change in the eigenvalues. Therefore, the GEP formulation is used for the linearized stability analysis.

The GEP is solved using the Krylov-Schur algorithm. The Krylov-Schur algorithm is an iterative procedure for finding a limited number of the *largest* eigenvalues, and thus it is an efficient algorithm for large-scale problems [174, 175]. The Krylov-Schur algorithm can be combined with the spectral transformation (pp. 582–600 of Ref. [158]), so as to produce the *smallest* eigenvalues representing the first few structural modes of interest. The spectral transformation implies the solution of Eq. (5.36) instead of Eq. (5.35),

$$\begin{cases} (\mathbf{K} - \mathbf{K}_A)\mathbf{x} = \mathbf{M}\mathbf{u} & \text{(5.36a)} \\ \left(\dfrac{1}{\lambda_g}\right)\mathbf{u} = \mathbf{x} & \text{(5.36b)} \end{cases}$$

The computational considerations associated with the linear system Eq. (5.36a) are discussed in Section 5.4.4.

The real and imaginary parts of the eigenvalue are defined as the damping and frequency of the corresponding aerothermoelastic mode, respectively,

$$\zeta = Re(\lambda_p), \quad \omega = Im(\lambda_p) \tag{5.37}$$

Both the damping ζ and the frequency ω have the same unit of radian/second.

The structure is stable when $\zeta < 0$. Moreover, two types of instability can be identified

based on the properties of eigenvalues, shown in Table 5.1. When the eigenvalue has a positive real part and a nonzero imaginary part, the corresponding aerothermoelastic mode represents flutter instability that is driven by the aerodynamic loading. When the eigenvalue is positive real, the corresponding aerothermoelastic mode represents divergence, caused by the thermal force in the structure.

$\zeta < 0, \omega \neq 0$	Stable
$\zeta = 0, \omega \neq 0$	Neutrally stable
$\zeta > 0, \omega \neq 0$	Unstable (flutter)
$\omega = 0$	Unstable (divergence)

Table 5.1: Stability criteria for the linearized stability analysis

5.4.3 Tightly-Coupled Scheme

A tightly-coupled scheme is developed to obtain the quasi-steady aerothermoelastic response governed by Eq. (5.31). In the aeroelastic solver of the tightly-coupled scheme, at every time step, the fluid and structural solvers exchange information repeatedly until both solvers converge. The tightly-coupled scheme has higher computational cost compared to the loosely-coupled scheme for each time step. However, time step size of the tightly-coupled scheme is determined by the largest characteristic time and it retains the numerical stability of solution at a larger time step size. Note that the tightly-coupled scheme is limited due to the fact that it only works when the aerothermoelastic response is stable and quasi-steady. Therefore, at the end of each time step, LSA is employed to check the stability of the coupled system. If the aerothermoelastic instability is detected at several consecutive time steps, the aerothermoelastic stability boundary is reached and the simulation should be either terminated or switched to transient simulation using the loosely-coupled scheme.

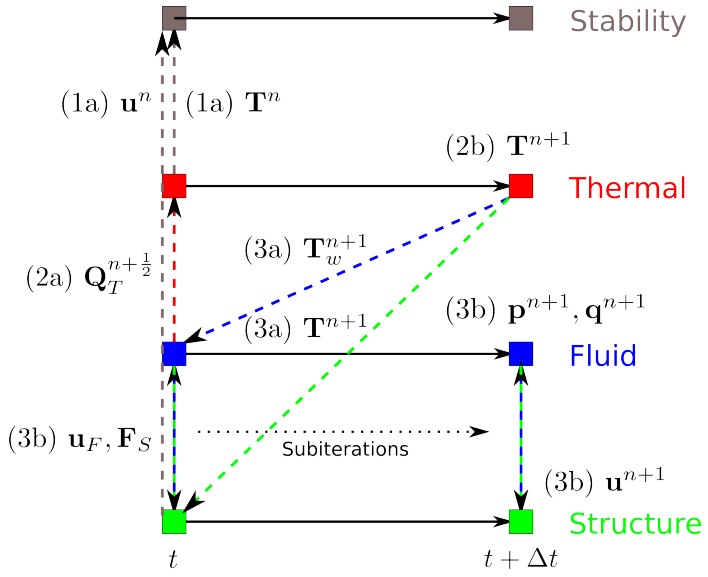

Figure 5.4: Tightly-coupled scheme for quasi-steady aerothermoelastic response

The procedure for the tightly-coupled scheme is illustrated in Fig. 5.4. The aerothermal steps of the loosely-coupled and tightly-coupled schemes are the same. However, a modified aeroelastic step and a new stability step are introduced to the tightly-coupled scheme.

1. Stability step:
   (a) The thermal solution $\mathbf{T}^n$ and the structural solution $\mathbf{u}^n$ are passed to the stability solver.
   (b) The stability of the aerothermoelastic response is checked using LSA.
   (c) If the structure is stable, continue to the next step, otherwise terminate the simulation or switch to loosely-coupled scheme.
2. Aerothermal step:
   (a) Heat flux from the fluid solver is extrapolated using Eq. (5.2)
   (b) The thermal solution $\mathbf{T}$ is updated to step $n+1$, with heat flux $\mathbf{Q}_T^{n+\frac{1}{2}} = \mathbf{H}_{TF}\mathbf{q}^{n+\frac{1}{2},E}$
3. Aeroelastic step:
   (a) The thermal solution is passed to the fluid solver using Eq. (5.1b) and the structural solver.

(b) The fluid and the structural solutions are simultaneously updated to step $n+1$ by solving Eqs. (5.28b) and (5.25b).

4. Above steps are repeated until the simulation is completed.

5.4.4 Computational Considerations

In the loosely-coupled scheme, the aerodynamic loading is provided by an external vector and is independent of the structural displacement and velocity. Therefore, in the Newton-Raphson step of the structural solver, an equation of the following form has to be solved,

$$\mathbf{\Phi x} = \boldsymbol{\phi} \tag{5.38}$$

where the residual Jacobian $\mathbf{\Phi}$ contains the mass and stiffness matrices only and these are sparse and symmetric. A sparse linear system like Eq. (5.38) can be solved efficiently using a direct solver, such as the MUMPS package [176] (MUltifrontal Massively Parallel Sparse direct Solver). The solution procedure of a direct solver [177] is shown in the following,

1. Given a $N \times N$ symmetric matrix $\mathbf{\Phi}$, residual vector $\boldsymbol{\phi}$.
2. Cholesky factorization with a computational cost of at most $O(N^2)$

$$\mathbf{\Phi} = \mathbf{L_\Phi L_\Phi^T} \tag{5.39}$$

3. Forward substitution with a computational cost of $O(N)$: Solve an intermediate variable $\mathbf{y}$

$$\mathbf{L_\Phi y} = \boldsymbol{\phi} \tag{5.40}$$

4. Back substitution with a computational cost of $O(N)$: Solve the final solution

$$\mathbf{L_\Phi^T x} = \mathbf{y} \tag{5.41}$$

When $\mathbf{\Phi}$ is sparse, overall computational cost is at most $O(N^2)$.

However, a numerical difficulty raises in the tightly-coupled scheme and the linearized stability analysis. It is due to the inclusion of the aerodynamic Jacobian in the Newton-Raphson step and the spectral transform of the eigenvalue solver. In both cases, an equation of the following form has to be solved,

$$(\mathbf{\Phi} - \mathbf{\Phi}_A)\mathbf{x} = \boldsymbol{\phi}, \quad \mathbf{\Phi}_A = \mathbf{K}_A + \frac{\partial \dot{\mathbf{u}}}{\partial \mathbf{u}}\mathbf{C}_A \tag{5.42}$$

Without loss of generality, Eq. (5.42) is examined for the case where $\mathbf{C}_A = 0$. Using Eqs. (2.57), (2.60a) and (5.25b), the aerodynamic Jacobian $\mathbf{\Phi}_A$ is simpilified as

$$\mathbf{\Phi}_A = \mathbf{H}_{SF}\frac{\partial \mathbf{p}}{\partial \mathbf{u}_F}\mathbf{H}_{FS} = (\mathbf{H}_{SF}\mathbf{\Psi}_P)\frac{\partial \mathbf{p}}{\partial \mathbf{u}_F}(\mathbf{\Psi}_S\mathbf{H}_{FS}) \equiv \tilde{\mathbf{\Psi}}_P\mathbf{\Phi}_{krg}\tilde{\mathbf{\Psi}}_S^T \tag{5.43}$$

where $\tilde{\mathbf{\Psi}}_P \in \mathbb{R}^{N\times N_P}$ contains N_P aerodynamic POD modes, $\tilde{\mathbf{\Psi}}_S \in \mathbb{R}^{N\times N_S}$ contains N_S structural modes, and $\mathbf{\Phi}_{krg} \in \mathbb{R}^{N_P\times N_S}$ is the Jacobian obtained from the kriging model. The computational cost of $\mathbf{\Phi}_A$ is $O(N^2)$, since $N_P, N_S \ll N$. Moreover, the full Jacobian $(\mathbf{\Phi} - \mathbf{\Phi}_A)$ becomes dense and asymmetric. The direct solver for Eq. (5.42) would have to utilize the LU factorization and the overall computational cost would be $O(N^3)$, which is undesirable for problems with over 1000 DOFs.

Therefore, it is necessary to replace the direct solver with an iterative solver that utilizes algorithms such as preconditioned generalized minimal residual method (PGMRES) [178]. The advantage of an iterative solver is that it replaces the expensive computation and factorization of $\mathbf{\Phi}_A$ by cheap matrix-vector multiplication of computational cost $O(N)$,

$$(\mathbf{\Phi} - \mathbf{\Phi}_A)\mathbf{x} = \mathbf{\Phi}\mathbf{x} - \tilde{\mathbf{\Psi}}_P\mathbf{\Phi}_{krg}\tilde{\mathbf{\Psi}}_S^T\mathbf{x} \tag{5.44}$$

Note that $\mathbf{\Phi}$ is a sparse matrix so the computational cost of multiplication $\mathbf{\Phi}\mathbf{x}$ is $O(N)$ instead of $O(N^2)$. For the PGMRES solver, it is also necessary to provide the iterative

solver with a preconditioner $\mathbf{P}$ that approximates the full Jacobian $(\mathbf{\Phi} - \mathbf{\Phi}_A)$, so as to accelerate the convergence of the algorithm. In the current study, $\mathbf{P}$ is set to $\mathbf{\Phi}$. The solution procedure of the PGMRES algorithm applied to Eq. (5.42) is shown below,

1. Given symmetric matrix $\mathbf{\Phi}$, residual vector $\boldsymbol{\phi}$, matrices $\tilde{\mathbf{\Psi}}_P$, $\mathbf{\Phi}_{krg}$ and $\tilde{\mathbf{\Psi}}_S$, maximum number of iterations N_i, tolerance ϵ
2. Choose $\mathbf{\Phi}$ as the preconditioner and set initial guess $\mathbf{x}^{(0)}$
3. Cholesky factorization, at most $O(N^2)$: $\mathbf{\Phi} = \mathbf{L}_{\mathbf{\Phi}}\mathbf{L}_{\mathbf{\Phi}}^T$
4. PGMRES iterations for maximum N_i steps:
   (a) Compute matrix-vector product $\mathbf{y} = (\mathbf{\Phi} - \mathbf{\Phi}_A)\mathbf{x}$ using Eq. (5.44) with computational cost $O(N)$.
   (b) Solve the preconditioned error $\mathbf{e}^{(i)}$ using forward and back substitution with computational cost $O(N)$,

$$\mathbf{L}_{\mathbf{\Phi}}\mathbf{L}_{\mathbf{\Phi}}^T\mathbf{e}^{(i)} = \boldsymbol{\phi} - \mathbf{y} \tag{5.45}$$

   (c) Update the solution $\mathbf{x}^{(i)}$ with the error $\mathbf{e}^{(i)}$ using the GMRES procedure with computational cost $O(N)$.
   (d) If $||(\mathbf{\Phi} - \mathbf{\Phi}_A)\mathbf{x} - \boldsymbol{\phi}|| < \epsilon$, break, otherwise continue.

The algorithm typically requires only a few dozens of iteration for the solution to converge, therefore the overall computational cost of solving Eq. (5.42) is reduced from $O(N^3)$ to at most $O(N^2)$.

CHAPTER 6

Refined Aerothermoelastic Scaling Laws

This chapter presents the development of analytical and refined ASL. First, classical dimensional analysis is employed to derive the analytical similarity parameters for the aerothermoelastic response of a modern composite hypersonic structure. Next, the conflicts in the analytical aerothermoelastic scaling are identified and possible solutions to these conflicts are discussed. Subsequently, a novel two-pronged approach is presented for the refinement of hypersonic ASL, which is formulated as a multi-objective optimization problem. Finally, the solution strategy for the optimization problem associated with the two-pronged approach is discussed.

6.1 Analytical Approach Revisited

6.1.1 Dimensional Analysis of the Aerothermoelastic Problem

The aerothermoelastic response of a hypersonic skin panel consists of the aeroelastic and aerothermal responses. The aeroelastic response is represented by the structural deformation and aerodynamic pressure distribution, while the aerothermal response is represented by the structural temperature and the aerodynamic heat flux distribution. This study focuses on the behavior of a typical structural component in hypersonic flow. Therefore, in the rest of this chapter, the similarity in aerothermoelastic response refers to the similarity in the time history of the structural deformation and temperature.

From Eqs. (2.15), (3.26) and (4.11), the similarity parameters for the aerothermoelastic response of a skin panel are,

$$\text{Geometry}: \quad \frac{\hat{h}}{\hat{L}}, \quad \bar{h}, \quad \frac{\hat{d}}{\hat{L}} \tag{6.1a}$$

$$\text{Time}: \quad \textit{Fo}, \quad \frac{\hat{I}\hat{L}^4}{\widehat{D}_{xx}\hat{t}^2}, \quad \frac{\hat{V}\hat{t}}{\hat{L}} \tag{6.1b}$$

$$\text{Coupling}: \begin{cases} \bar{\lambda}_F, \quad \textit{Bi}_F, \quad \dfrac{\hat{u}_w}{\hat{L}}, \quad \dfrac{T_w}{\hat{T}_S}, \quad \dfrac{\hat{T}_T}{\hat{T}_S}, \quad \dfrac{T_0}{\hat{T}_S}, \quad \dfrac{\hat{T}_F}{\hat{T}_S} \\ \bar{p}_F, \quad \bar{\dot{q}}_F, \quad \bar{\mathbf{u}}_w, \quad \bar{T}_w, \quad \bar{T} \end{cases} \tag{6.1c}$$

$$\text{Thermal}: \begin{cases} \textit{Bi}_{ext} = \dfrac{\hat{\dot{q}}_{ext}\hat{h}}{\hat{k}^s\hat{T}_T}, \ \bar{\dot{q}}_{ext} \\ \bar{\rho}^s\bar{c}_p^s, \ \bar{\mathbf{k}}^s \end{cases} \tag{6.1d}$$

$$\text{Structural}: \begin{cases} \dfrac{\widehat{A}_{xx}\hat{L}^2}{\widehat{D}_{xx}}, \ \dfrac{\widehat{B}_{xx}\hat{L}}{\widehat{D}_{xx}}, \ \dfrac{\widehat{S}_{xx}\hat{L}^2}{\widehat{D}_{xx}}, \ \dfrac{\widehat{N}_{Tx}\hat{L}^2}{\widehat{D}_{xx}}, \ \dfrac{\widehat{M}_{Tx}\hat{L}}{\widehat{D}_{xx}}, \ \bar{\lambda}_{ext} = \dfrac{\hat{p}_{ext}\hat{L}^3}{\widehat{D}_{xx}}, \ \bar{p}_{ext} \\ \overline{\mathbf{A}}, \ \overline{\mathbf{B}}, \ \overline{\mathbf{D}}, \ \overline{\mathbf{S}}, \ \overline{\mathbf{N}}_T, \ \overline{\mathbf{M}}_T, \ \bar{I}_1, \ \bar{I}_2, \ \bar{I}_3 \end{cases} \tag{6.1e}$$

$$\text{Fluid}: \begin{cases} M_\infty \dfrac{\hat{h}}{\hat{L}}, \ \textit{Re}_0 \\ \textit{Pr}_0, \ \gamma \end{cases} \tag{6.1f}$$

where,

$$\bar{\lambda}_F = \frac{\gamma p_\infty M_\infty \hat{L}^3}{\widehat{D}_{xx}} \tag{6.2a}$$

$$\textit{Bi}_F = \frac{\hat{k}^f}{\hat{k}^s}\textit{Re}_0\textit{Pr}_0\frac{\hat{V}^2}{\hat{c}_p^f\hat{T}_T} \tag{6.2b}$$

Equation (6.1a) requires the geometric similarity between the model and the prototype, which is easy to satisfy. In Eq. (6.1b), the three quantities provide conflicting requirements for the time scale, which can be reconciled depending on the type of problem. For example, to simulate long-term quasi-steady aerothermoelastic response, the first parameter representing the thermal characteristic time should be used to define the time scale, and the other two can be ignored.

Equation (6.1c) provides a group of similarity parameters related to the aerothermoelastic coupling. In the *first row*, the first parameter $\bar{\lambda}_F$ is the nondimensional dynamic pressure, representing the ratio of aerodynamic pressure and the bending stiffness. The second parameter Bi_F is the Biot number associated with the aerodynamic heat flux. The third parameter defines the magnitude of surface deformation, which is important when the panel undergoes moderate deformations. The last four parameters provide the requirements for the reference temperatures in the thermal, structural and fluid problems. The *second row* represents the requirements for the similarity in the distributions of the aerodynamic pressure and heat flux, surface deformation, wall temperature and body temperature. These requirements are automatically satisfied if all other similarity requirements are satisfied.

The parameters in Eqs. (6.1d)-(6.1f) are the similarity requirements for the individual disciplines. In each group, the *second row* represents the similarity requirements for material properties as a function of temperature. These requirements are approximately satisfied if the functions representing the temperature dependency of the material properties have a similar form. One example is the case where the material properties of the model and the prototype are proportional to the power of temperature T^{η} over the temperature range of interest, where the exponent η is curve-fitted from the material data [24]. The similarity requirements for the temperature-dependent material properties are approximately satisfied, if the difference between the values of η associated with the model and the prototype are sufficiently small.

In Eq. (6.1d), the first parameter, which requires the similarity in the initial temperature distribution, is easy to satisfy. The next two parameters represent the magnitude and distribution of the heat flux due to external heat source, which will be discussed later in this chapter. In Eq. (6.1e), first five parameters provide the similarity requirements in various stiffness constants. The parameters associated with $\widehat{B}_{xx}$, $\widehat{S}_{xx}$ and $\widehat{M}_{Tx}$ may be ignored if the panel is orthotropic and sufficiently thin. The last two parameters, which define the magnitude and distribution of the externally-applied loading, will be discussed later. In Eq.

(6.1f), the first parameter may be disregarded due to Mach number independence principle. The second parameter, the Reynolds number, governs the growth of the boundary layer and thus the distribution of pressure and heat flux.

Based on the preceeding discussion, for long-term quasi-steady aerothermoelastic response of skin panel, the similarity parameters in Eq. (6.1) are reduced and replaced by a simplified set given by Eqs. (6.3a)-(6.3d),

$$\textit{Fo} \tag{6.3a}$$

$$\frac{\hat{h}}{\hat{L}},\ \bar{h},\ \bar{\lambda}_F,\ \textit{Bi}_F,\ \textit{Re}_0,\ \frac{\widehat{A}_{xx}\hat{L}^2}{\widehat{D}_{xx}},\ \frac{\widehat{N}_{Tx}\hat{L}^2}{\widehat{D}_{xx}} \tag{6.3b}$$

$$\frac{T_w}{\hat{T}_S},\ \frac{\hat{T}_T}{\hat{T}_S},\ \frac{T_0}{\hat{T}_S},\ \frac{\hat{T}_F}{\hat{T}_S} \tag{6.3c}$$

$$\textit{Bi}_{ext},\ \bar{\dot{q}}_{ext},\ \bar{\lambda}_{ext},\ \bar{p}_{ext} \tag{6.3d}$$

6.1.2 Limitations of Complete Aerothermoelastic Scaling

The complete aerothermoelastic scaling requires that (1) all the similarity parameters in Eqs. (6.3b) and (6.3c) should be satisfied, and (2) the external loading and heating in Eq. (6.3d) is zero. Complete aerothermoelastic scaling cannot be achieved due to the conflict between the similarity requirements for the aeroelastic and the aerothermal responses, or specifically, structural stiffness and aerodynamic heating.

First, the quantities $\widehat{A}_{xx}$, $\widehat{N}_{Tx}$, and $\widehat{D}_{xx}$ are functions of the reference structural temperature $\hat{T}_S$. Therefore, from the similarity parameters $\frac{\widehat{A}_{xx}\hat{L}^2}{\widehat{D}_{xx}}$ and $\frac{\widehat{N}_{Tx}\hat{L}^2}{\widehat{D}_{xx}}$, $\hat{T}_S$ is determined. Next, the quantities $\bar{\lambda}_F$, $\textit{Re}_0$, and $\textit{Bi}_F$ are functions of the flow conditions p_∞, M_∞ and T_∞. Therefore, the flow conditions that satisfies aeroelastic similarity is determined from the combination of $\hat{T}_S$ and parameters $\bar{\lambda}_F$, $\textit{Re}_0$ and $\frac{T_0}{\hat{T}_S}$. However, a different set of flow conditions p_∞, M_∞ and T_∞ that satisfies aerothermal similarity is determined from the combination of $\hat{T}_S$ and parameters $\bar{\lambda}_F$, $\textit{Bi}_F$ and $\frac{\hat{T}_T}{\hat{T}_S}$. In general, the two sets of flow conditions are not the same and thus complete aerothermoelastic scaling fails.

6.1.3 Strategies for Refined Aerothermoelastic Scaling

The previous discussion has shown that it is impossible to develop a scaled model that satisfies all the aerothermoelastic similarity parameters in Eq. (6.1) or Eq. (6.3). However, various ad hoc assumptions have been introduced to facilitate the analytical derivation of the similarity parameters. Some complex but important factors in the aerothermoelastic problem have been ignored, including the turbulence and real gas effect in the fluid problem, geometric nonlinearity in the structural problem and the material nonlinearity in the structural and thermal problems. Therefore, while the similarity parameters derived using the classical approach provide useful information about aerothermoelastic scaling, they fail to accurately represent the requirements for constructing aerothermoelastically scaled models.

A refined aerothermoelastic scaling approach is developed in this study to reconcile the conflict that arises in conventional aerothermoelastic scaling, thus overcoming the limitations of the classical scaling approach. Instead of satisfying the aerothermoelastic similarity parameters, the scaled model is constructed by satisfying the similarity in the aerothermoelastic *response*, i.e. minimize the differences between the nondimensional aerothermoelastic responses of the prototype and the model. The aerothermoelastic responses generated using numerical simulation take account of all the complex factors that are ignored in the classical approach.

Two strategies can be employed in refined aerothermoelastic scaling:

1. *Parameter relaxation*: the scaled model is constructed so as to achieve approximate similarity in the aerothermoelastic responses, while matching a *partial* set of the aerothermoelastic similarity parameters between the prototype and the model, so as to produce the best fit agreement for all the aerothermoelastic similarity parameters.
2. *Incomplete testing*: represents a situation where external loading and heating is introduced in the wind tunnel test to compensate for the differences in the similarity parameters $\bar{\lambda}_F, Bi_F$ associated with the prototype and the model.

Both strategies are difficult to apply to the construction of the scaled model if the classical approach is used alone. However, the two strategies can be combined with the two-pronged approach to enable systematic model adjustment with the objective of achieving aerothermoelastic similarity. The process of model adjustment can be formulated as an optimization problem. The design variables are selected to correspond to the most important parameters needed for the refined simulation, and these design variables differ from those employed when generating the model based on classical similarity. Eventually, the numerical scaling law for the specialized cases can be obtained without recourse to the *ad hoc* assumptions used in the classical approach. Thus, the difficulties associated with hypersonic aerothermoelastic testing are resolved.

The selection of the design variables is problem-dependent. Typically, the design variables should include the freestream flow conditions in the wind tunnel, which cannot be determined using the classical approach due to the conflict between the aeroelastic and aerothermal similarity requirements. For a skin panel configuration, the design variables should also include the geometrical parameters of the scaled model, such as the panel thickness and the side length. The classical approach requires all the geometrical parameters to scale uniformly using the same scaling factor. However, it could be advantageous to scale the geometrical parameters using different scaling factors so as to achieve a better agreement between the nondimentional aerothermoelastic response of the prototype and the model [173].

6.2 Two-Pronged Approach for Refined Scaling Laws

6.2.1 Objectives

The two-pronged approach combines the classical dimensional analysis and the numerical simulation method to systematically adjust the wind tunel model properties so as to enable hypersonic aerothermoelastic testing. For a generic configuration, the adjustment process

is formulated as a constrained optimization problem that searches for a wind tunnel setup whose aerothermoelastic response could represent that of the full-scale prototype to the largest extent possible. The aerothermoelastic responses of the prototype and the model are computed using the HYPATE framework. The simulated aerothermoelastic response of the prototype is a time history of deformation and body temperature. The similarity of the solutions is measured using two objective functions, representing the differences between the nondimensional solutions to be minimized. For the deformation and temperature, the objective functions are defined, respectively, as:

$$J_u(\mathbf{d};\{\mathbf{u}_i^m\}) = \sqrt{\sum_{i=1}^{N_t} \left\| \mathbf{\Psi}_u^T \left(\frac{\mathbf{u}_i^m}{\hat{u}^m} - \frac{\mathbf{u}_i^p}{\hat{u}^p} \right) \right\|^2} \tag{6.4a}$$

$$J_T(\mathbf{d};\{\mathbf{T}_i^m\}) = \sqrt{\sum_{i=1}^{N_t} \left\| \mathbf{\Psi}_T^T \left(\frac{\mathbf{T}_i^m}{\hat{T}^m} - \frac{\mathbf{T}_i^p}{\hat{T}^p} \right) \right\|^2} \tag{6.4b}$$

where $\mathbf{d}$ is the vector of design variables. The projection matrices $\mathbf{\Psi}_u$ and $\mathbf{\Psi}_T$ converts the full aerothermoelastic responses to the quantities of interest, such as the modal components of the deformation and temperature.

The objectives are meaningful only when the differences between the nondimensional solutions are computed at the *same* nondimensional time. The matching of the nondimensional time is guaranteed by using the same nondimensional time step size for the prototype and the model. In other words, the time step size of the model Δt^m should be determined from the time step size of the prototype Δt^p by keeping one of the similarity parameters in Eq. (6.1b) constant. For example, for the case of long-term quasi-steady aerothermoelastic response, given Δt^p, the time step size Δt^m should be determined such that the Fourier numbers of the model and the prototype are the same,

$$\frac{[\hat{k}^s]^m \Delta t^m}{[\hat{\rho}^s \hat{c}_p^s]^m (\hat{h}^m)^2} = \frac{[\hat{k}^s]^p \Delta t^p}{[\hat{\rho}^s \hat{c}_p^s]^p (\hat{h}^p)^2} \quad \Rightarrow \quad \Delta t^m = \frac{[\hat{k}^s]^p [\hat{\rho}^s \hat{c}_p^s]^m}{[\hat{k}^s]^m [\hat{\rho}^s \hat{c}_p^s]^p} \left(\frac{\hat{h}^m}{\hat{h}^p} \right)^2 \Delta t^p \tag{6.5}$$

Table 6.1: Design variables for the optimization problem

Group	Design variables	Type	Lower limits	Upper limits
Flow conditions	M_∞	Disc.	N/A	
	p_0, T_0	Cont.	Wind tunnel	
Geometry	$\hat{L}, L_{le}, \theta$	Cont.	Manufacture	Wind tunnel
Composite layup	$\mathbf{Q}, \boldsymbol{\alpha}, \mathbf{k}^s, c_p^s$	Disc.	N/A	
	$\mathbf{h}$	Cont.	Manufacture	Wind tunnel
External loading	p_{ext}	Cont.	Wind tunnel	
	T_{rad}	Cont.	Wind tunnel	
	ε	Cont.	0	1
Temperatures	$\hat{T}_T, \hat{T}_S$	Cont.	Arbitrary	
	T_w	Cont.	Wind tunnel	

6.2.2 Design Variables and Constraints

For the case of skin panel, the design variables describing the full-scale prototype and the wind tunnel test model are summarized in Table 6.1. Note that external loading is introduced by p_{ext} and external heating is introduced by radiant heating specified by the radiation temperature T_{rad} and the surface emissivity ε [179]. Not all of the variables in the wind tunnel setup are continuous. First, in most hypersonic wind tunnels, the *freestream* flow conditions are given as constant, or can be selected from a very limited number of discrete options provided by using different nozzle configurations. Second, due to high loads and temperatures during aerothermoelastic testing, there are only a limited number of options for material properties, i.e. elastic constants $\mathbf{Q}$, thermal expansion coefficients $\boldsymbol{\alpha}$ and thermal properties $\mathbf{k}^s$ and c_p^s. Nevertheless, some wind tunnels do have the capability to adjust the stagnation temperature and pressure continuously [31]. Moverover, a continous range of *post-shock* flow conditions can be achieved by adjusting the geometrical inclination angle θ of the panel. Furthermore, the thickness of each lamina may be adjusted to tune the structural and thermal properties of the model. Finally, it is assumed that a continous range of the surface emissivity ε can be achieved by applying different coating to the surface of the scaled model, so as to adjust the magnitude of the radiative heat flux acting on the model.

Based on preceeding discussion, the design variables are divided into two groups,

$$\mathbf{d}_c = [p_0, T_0, \hat{L}, L_{le}, \theta, \mathbf{h}, p_{ext}, T_{rad}, \varepsilon, \hat{T}_T, \hat{T}_S, T_w] \tag{6.6a}$$

$$\mathbf{d}_d = [M_\infty, \mathbf{Q}, \boldsymbol{\alpha}, \mathbf{k}^s, c_p^s] \tag{6.6b}$$

where $\mathbf{d}_c$ and $\mathbf{d}_d$ are the vectors of the continuous and discrete design variables, respectively.

The design variables have to satisfy two sets of constraints, the equality and the inequality ones. The equality constraints are due to the requirement that the similarity parameters of the model and the prototype should be equal. When the parameter relaxation or incomplete testing strategy is employed, not all similarity parameters in Eqs. (6.3b) and (6.3c) are used as equality constraints. For example, the heat flux parameter Bi_F is excluded from the equality constraints if external heating is provided. The inequality constraints are due to practical limits and the factors characterizing the lower and upper limits of the inequality constraints are summarized in the last two columns of Table 6.1. The lower and upper limits of the geometrical quantities are determined by the limitations in model manufacture and the size of the wind tunnel, respectively. The feasible ranges of external loading and temperature are determined by the capabilities of the wind tunnel facility.

6.2.3 Formulation of Optimization Problem

Combining Eqs. (6.4) and (6.6), the two-pronged approach for refined scaling law is formulated as a constrained multi-objective optimization (MO) problem,

$$\text{Minimize} \quad \mathbf{J}(\mathbf{d}_c, \mathbf{d}_d) = [J_u(\mathbf{d}_c, \mathbf{d}_d), J_T(\mathbf{d}_c, \mathbf{d}_d)] \tag{6.7a}$$

$$\text{Subject to} \quad \mathbf{c}_E(\mathbf{d}_c, \mathbf{d}_d) = 0 \tag{6.7b}$$

$$\mathbf{c}_I(\mathbf{d}_c, \mathbf{d}_d) \leq 0 \tag{6.7c}$$

where Eqs. (6.7b) and (6.7c) represent the equality and inequality constraints, respectively. The optimization problem Eq. (6.7) is a mixed-integer optimization problem that is difficult to solve, due to the presence of both continuous and discrete design variables. However, since there is only a limited number of feasible values for the discrete design variables, the full problem Eq. (6.7) can be solved by an exhaustive search on all feasible values for $\mathbf{d}_d$. For each possible set of $\mathbf{d}_d$, the optimal solution is found by solving the continuous optimization problem w.r.t. $\mathbf{d}_c$,

$$\begin{aligned} \text{Minimize} \quad & \mathbf{J}(\mathbf{d}) = [J_u(\mathbf{d}), J_T(\mathbf{d})] && \text{(6.8a)} \\ \text{Subject to} \quad & \mathbf{c}_E(\mathbf{d}) = 0 && \text{(6.8b)} \\ & \mathbf{c}_I(\mathbf{d}) \leq 0 && \text{(6.8c)} \end{aligned}$$

where the subscript c of $\mathbf{d}_c$ is dropped for convenience.

6.3 Solution Strategies for the MO Problem

An MO problem typically has multiple solutions. Each solution of an MO problem is Pareto optimal, meaning that one objective cannot be decreased without increasing the other objectives. The set of all the Pareto optimal solutions is called the Pareto front $\mathcal{F}$. A typical pareto front for a two-objective optimization problem is illustrated in Fig. 6.1. The gray shaded area represents the solution space, which is the set of all possible combinations of the objective values. At points A and D, the objectives J_u and J_T achieve the minimum possible values in the solution space, respectively. The Pareto front is the subset of the boundary of the solution space between points A and D, represented by solid black curves. Note that the continuity of the Pareto front is not a requirement. In Fig. 6.1, Point B represents a combination of objectives in the solution space that is better than any point on the gray curve BC. As a result, the Pareto front is disconnected and consists of only the curves AB and CD, and not the curve BC. While multiple solutions are possible, the ulti-

mate goal is to identify *one* optimal solution from the Pareto front, referred to as the *design point* in the following discussion. The design point represents a wind tunnel configuration that minimizes the differences in the nondimensional aerothermoelastic responses of the prototype and the model.

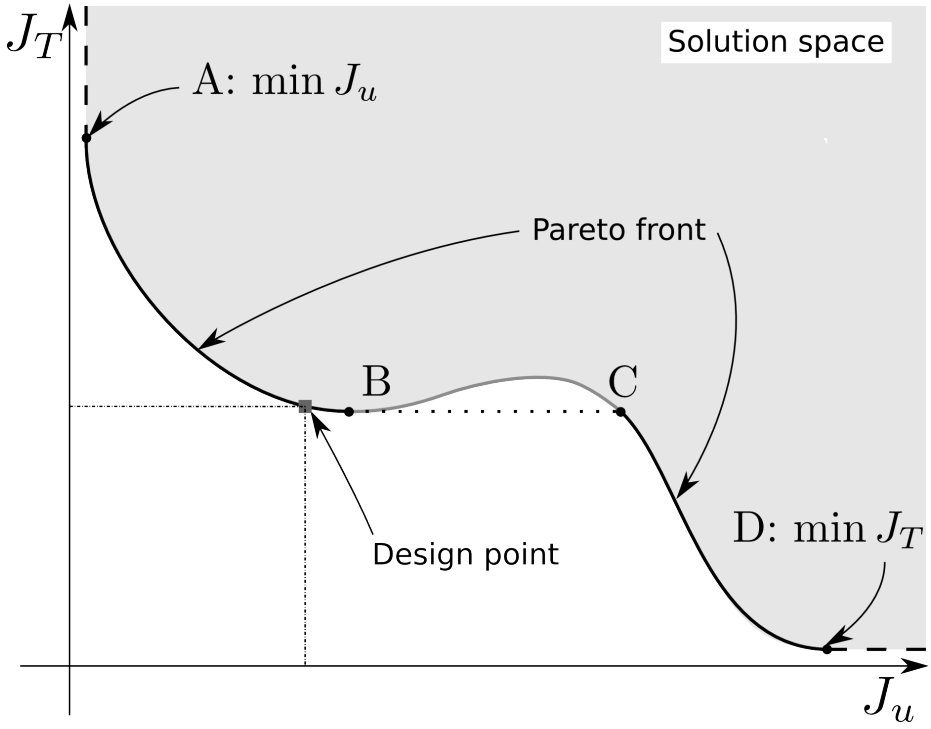

Figure 6.1: Illustration of a typical Pareto front of a two-objective problem

An additional challenge associated with the MO problem Eq. (6.8) is the expensive computational cost of the objectives, due to the aerothermoelastic simulation over the extended flight time. To solve the MO problem within a practical amount of time, the number of evaluations of the objectives has to be limited during optimization. As a result, there are two limitations on the optimization algorithm: (1) The design space cannot be explored by carrying out numerous *direct* evaluation of the objectives; (2) The derivative of the objectives w.r.t. design variables cannot be computed using the finite difference approach. To overcome the two limitations, the surrogate-based optimization (SBO) is employed in the current study [107]. Using the SBO algorithm, two approaches are employed to find the de-

sign point associated with the MO problem. The indirect approach produces a Pareto set $\overline{\mathcal{F}}$, i.e. a set of Pareto optimal solutions, that is representative of the Pareto front $\mathcal{F}$. The design point has to be selected from the Pareto set manually by the user. The direct approach does not produce a Pareto set. Instead, it only generates one Pareto optimal solution, identified as the design point.

In the rest of this section, the general procedure of the SBO algorithm is provided first. Next, the direct and indirect approaches using the SBO algorithm are presented and compared. Finally, the implementation details of the optimization algorithms are discussed.

6.3.1 Surrogate-Based Optimization

The SBO algorithms contain two key ingredients, a surrogate model and an acquisition function. The surrogate model is employed to approximate the expensive objectives. Since the surrogate is computationally efficient, it allows the fast evaluation of approximated objectives as well as its derivative w.r.t. the design variables. The acquisition function is a criterion for selecting the points in the design space that is potentially a solution to the optimization problem. It is designed to take into account two ingredients, namely *exploration*, i.e. sampling from areas of high uncertainty, and *exploitation*, i.e. sampling from areas likely to improve the objectives. A typical SBO algorithm contains the following steps,

1. Set the number of initial samples N_s, number of iterations N_i.
2. Generate initial sample points $\{\mathbf{d}_i\}_{i=1}^{N_s}$ in the design space using a sampling approach, e.g. the OLH method.
3. Generate a sample data set $\mathcal{D} = \{(\mathbf{d}_i, \mathbf{J}_i, \mathbf{c}_{Ei}, \mathbf{c}_{Ii})\}_{i=1}^{N_s}$ by evaluating the objectives and constraints $\mathbf{J}_i, \mathbf{c}_{Ei}, \mathbf{c}_{Ii}$ at the initial sample points.
4. Inner optimization for a maximum of N_i iterations:
   (a) Generate surrogates $\mathbf{J}^{sur}(\mathbf{d})$, $\mathbf{c}_E^{sur}(\mathbf{d})$, $\mathbf{c}_I^{sur}(\mathbf{d})$ for the objectives and constraints using the sample data set $\mathcal{D}$.
   (b) Find the candidate point $\mathbf{d}^*$ by solving an optimization problem that consists of

the surrogates and acquisition function.

(c) Evaluate the objective and constraint functions $\mathbf{J}_i^*, \mathbf{c}_{Ei}^*, \mathbf{c}_{Ii}^*$ at the candidate point $\mathbf{d}^*$.

(d) Update the surrogate using the sample data set augmented with the candidate solution $\mathcal{D}^* = \mathcal{D} \cup \{(\mathbf{d}^*, \mathbf{J}^*, \mathbf{c}_E^*, \mathbf{c}_I^*)\}$.

(e) Break if convergence criteria is met, otherwise continue.

The SBO algorithms are classified in two categories: the one-shot approach and the updating approach [106]. The one-shot approach only excutes the inner optimization step once. The candidate solution is accepted as the final solution regardless of the differences between the surrogate and the objectives at the candidate point. The one-shot approach might fail if the design space is not well represented by the sample data set and the uncertainty of the surrogate at the candidate point is high. In the updating approach, the inner optimization is executed until convergence or when the computational budget is exceeded. While the updating approach does not guarantee finding the global optimum point, it usually produces a better solution than the one-shot approach [106, 180]. In this thesis, the updating approach is employed.

Several surrogate models have been employed in SBO algorithms, including response surfaces [181], radial basis function method [182], and the kriging method [106, 180, 183]. The kriging method, or the Gaussian process regression model [105], is employed for SBO in this thesis, because it has a clear statistical interpretation that is beneficial in the construction of acquisition functions. The prediction of the kriging model at a candidate point $\mathbf{d}^*$ follows a joint Gaussian probability distribution,

$$\mathbf{J}^* = \mathbf{J}^{sur}(\mathbf{d}^*) \sim \mathcal{N}(\boldsymbol{\mu}(\mathbf{d}^*), \boldsymbol{\Sigma}(\mathbf{d}^*)) \tag{6.9}$$

where $\boldsymbol{\mu}$ is the predicted values of objectives and $\boldsymbol{\Sigma}$ is the covariance matrix quantifying the uncertainty of the prediction. The objectives are assumed to be independent and thus

$\boldsymbol{\Sigma}$ is a diagonal matrix. The standard deviations associated with the predicted values are denoted as $\boldsymbol{\sigma}$.

Note that the updating SBO algorithms using kriging method appear in the literature under multiple names, such as efficient global optimization (EGO) [180, 183] and Bayesian optimization (BO) [184, 185]. Throughout the rest of the thesis, the updating SBO algorithms is referred to as "Bayesian optimization", due to its statistical interpretation.

6.3.2 Multi-Objective Optimization Using the BO Algorithm

6.3.2.1 Direct Approach

In the direct approach, the MO problem is reformulated as a single-objective optimization (SO) problem and the design point is found by solving the SO problem only once,

$$\text{Minimize} \quad J_s(\mathbf{d}) = \mathcal{S}(\mathbf{J}(\mathbf{d})) \tag{6.10a}$$

$$\text{Subject to} \quad \mathbf{c}_E(\mathbf{d}) = 0 \tag{6.10b}$$

$$\mathbf{c}_I(\mathbf{d}) \leq 0 \tag{6.10c}$$

where a function $\mathcal{S}(\mathbf{J})$ is introduced to combine the vector of objectives into a scalar objective, typically using a weighted metric (WM) method. For the MO problem Eq. (6.8), the objectives J_u and J_T are combined as,

$$\mathcal{S}_g(\mathbf{J}) = \left[(c_u J_u)^g + (c_T J_T)^g\right]^{1/g} \tag{6.11}$$

where $g \in [1, \infty]$ and $0 \leq c_u, c_T \leq 1$. The weights c_u, c_T are determined empirically and more emphasis is placed on the objective with the larger weight.

Two special cases of WM method are illustrated in Figs. 6.2(a) and 6.2(b). The first special case is the WM method with $g = 1$, which is equivalent to the weighted sum (WS)

method [186],

$$\mathcal{S}_1(\mathbf{J}) = c_u J_u + c_T J_T \tag{6.12}$$

A Pareto optimal solution found by the WS method is illustrated by the point E in Fig. 6.2(a). The contours of the combined objective $\mathcal{S}_1(\mathbf{J})$ are a family of straight lines of slope $-\frac{c_u}{c_T}$. The WS method finds the point at which the contour of $\mathcal{S}_1$ is tangent to the Pareto front and the contour does not intersect with the rest of the solution space. However, the WS method can only find points on a partial set of a non-convex Pareto front. At point F of the Pareto front in Fig. 6.2(a), it is impossible to find a contour of $\mathcal{S}_1$ at F that does not intersect with the solution space.

The second special case is the WM method with $g = \infty$, where the objectives are combined as,

$$\mathcal{S}_\infty(\mathbf{J}) = \max(c_u J_u, c_T J_T) \tag{6.13}$$

The WM method with $g = \infty$ is capable of finding all the Pareto points on the Pareto front and its geometrical interpretation is provided in Fig. 6.2(b). The contours of the combined objective $\mathcal{S}_\infty(\mathbf{J})$ are a family of rectangles whose diagonals have a slope of $\frac{c_T}{c_u}$. The WM method with $g = \infty$ finds the point that is the only intersection between a contour of $\mathcal{S}_\infty$ and the solution space. The point is either the tangent point between the contour and the Pareto front, such as point B, or the corner point of the contour, such as point F.

While the WM method is employed for finding one Pareto optimal solution in the current study, it can also be used to generate a Pareto set by solving a series of SO problems associated with different combinations of weights [186]. However, this approach is inefficient because solving each SO problem requires generating a considerable amount of sample data in BO algorithm. Furthermore, the Pareto set may not be representative of the Pareto front. A uniform distribtuion of weights $\mathbf{c} = [c_u, c_T]$ typically does not result in a uniformly distributed Pareto set [187].

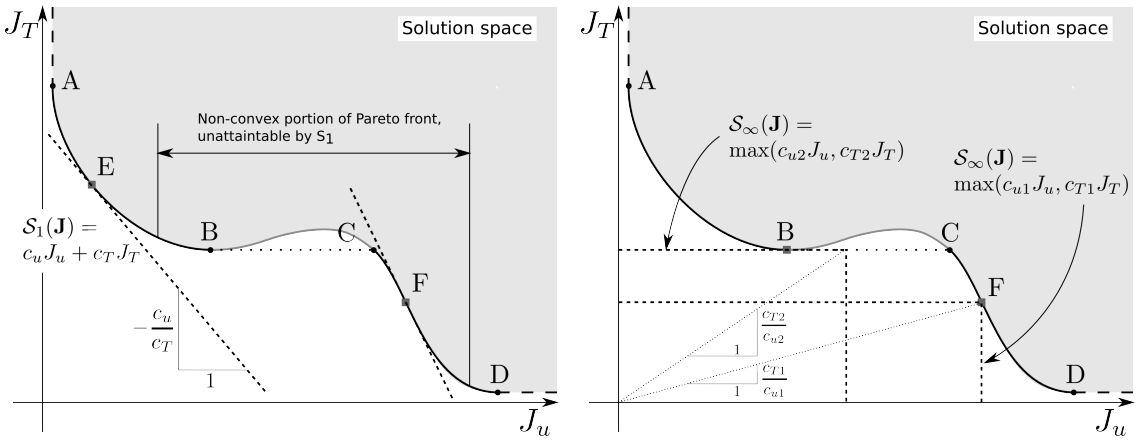

(a) Weighted metric with $g = 1$ **(b) Weighted metric with $g = \infty$**

Figure 6.2: Illustration of two typical WM methods

Surveys of acquisition functions for SO problems can be found in, for example, Refs. [183] and [188]. There are three basic acquisition functions: (1) probability of improvement (PoI) [189], (2) expected improvement (EI) [184, 190], (3) lower confidence bound (LCB) [191]. The formulation of these acquisition functions is presented next.

Probability of Improvement The PoI acquisition function is defined as the probability of the new design point $\mathbf{d}^*$ that represents a better value of the objective J^* when compared to the minimum objective in the sample data set $J_{\min} = \min J_i$.

$$C_{PoI}(\mathbf{d}^*) = P(J^* \leq J_{\min}) = 1 - \Phi(z_0) \tag{6.14}$$

where $z_0 = \frac{J_{\min} - \mu}{\sigma}$ and Φ is the cummulative distribution function of a standard Gaussian distribution. The gradient of C_{PoI} w.r.t. $\mathbf{d}$ is,

$$\frac{\partial C_{PoI}}{\partial \mathbf{d}} = \frac{1}{\sigma}\phi(z_0)\left(\frac{\partial \mu}{\partial \mathbf{d}} + z_0 \frac{\partial \sigma}{\partial \mathbf{d}}\right) \tag{6.15}$$

where ϕ is the probability density function, and the computation of $\frac{\partial \mu}{\partial \mathbf{d}}$ and $\frac{\partial \sigma}{\partial \mathbf{d}}$ are provided by Eqs. (A.8a) and (A.8b).

Expected Improvement The EI acquisition function is defined as the expectation of the improvement in the objective at the new design point. In the literature, EI has been generalized to include user-specified parameters that control the exploitation-exploration trade-off. The generalized EI is written as [190],

$$C_{EI}(\mathbf{d}^*) = \mathbb{E}[\mathcal{I}(\mathbf{d}^*)] \tag{6.16}$$

where $\upsilon \geq 0$ and $g \geq 1$ are the user-specified parameters, and

$$\mathcal{I}(\mathbf{d}) = \max(0, (J_{\min} - J^{sur}(\mathbf{d}) - \upsilon\sigma(\mathbf{d}))^g) \tag{6.17}$$

A larger g or υ will put more weight on the exploration. The classical form of EI is obtained with $\upsilon = 0$ and $g = 1$. When $\upsilon > 0$ and $g = 1$, the EI is equivalent to the weighted EI function developed in Ref. [106]. When $\upsilon = 0$ and $g = 0$, EI reduces to PoI. For a kriging model, the closed-form expression is available for C_{EI}. For the case $g = 1$,

$$C_{EI}(\mathbf{d}^*) = \int_0^\infty \mathcal{I} P(J^{sur} = J_{\min} - \upsilon\sigma - \mathcal{I}) \mathrm{d}\mathcal{I} \tag{6.18}$$

$$= \begin{cases} \sigma[z\Phi(z) + \phi(z)], & \sigma > 0 \\ 0, & \sigma = 0 \end{cases} \tag{6.19}$$

where $z = \frac{J_{\min} - \upsilon\sigma - \mu}{\sigma}$. The gradient of C_{EI} w.r.t. $\mathbf{d}$ is,

$$\frac{\partial C_{EI}}{\partial \mathbf{d}} = -\frac{\partial \mu}{\partial \mathbf{d}}\Phi(z) + \frac{\partial \sigma}{\partial \mathbf{d}}[\phi(z) - \upsilon\Phi(z)] \tag{6.20}$$

Lower Confidence Bound The LCB acquisition function is defined using the LCB concept of a Gaussian probability distribution,

$$C_{LCB}(\mathbf{d}^*) = \mu(\mathbf{d}^*) - \upsilon\sigma(\mathbf{d}^*) \tag{6.21}$$

where the probability of $J^{sur} < C_{LCB}$ is a constant controlled by the user-specified parameter $\upsilon > 0$. A larger υ will put more weight on the exploration. The gradient of C_{LCB} w.r.t. $\mathbf{d}$ is,

$$\frac{\partial C_{LCB}}{\partial \mathbf{d}} = \frac{\partial \mu}{\partial \mathbf{d}} - \upsilon \frac{\partial \sigma}{\partial \mathbf{d}} \tag{6.22}$$

The PoI acquisition function is purely exploitation, which is undesirable for global optimization. The EI and LCB acquisition functions are high when J^* approaches the optimum point, or the uncertainty of J^* is high. Therefore, both C_{EI} and C_{LCB} achieve a balance between exploitation and exploration. The LCB function is smoother than the EI function and thus more favorable for the inner optimization of the BO algorithm. Therefore, the LCB function is employed in the current study.

Finally, note that the exploitation-exploration trade-off of EI and LCB functions can be further tuned by a cooling scheme. In the cooling scheme, the optimization starts with a large user-specified parameter υ for more exploration and gradually decreases the parameter to focus on exploitation. However, the effect of this scheme is controversial [183, 192], and not employed in the study.

6.3.2.2 Indirect Approach

In the indirect approach, the original MO problem formulation Eq. (6.8) is retained. The acquisition functions suitable for multiple objectives are developed, so that each inner optimization step of the BO algorithm produces one Pareto optimal solution of the MO problem. The optimization algorithm generates a Pareto set and the user needs to select one of the Pareto optimal solutions as the final design point.

The PoI, EI and LCB acquisition functions for SO problems have been extended to MO problems using the concept of hypervolume $\mathcal{H}$ [193–195]. Figure 6.3 illustrates the hypervolume associated with a two-objective problem. Initially, the Pareto set $\overline{\mathcal{F}}_1$ consists of three Pareto optimal solutions labelled by the blue dots. All the points in the purple shaded region are worse than one or more solutions in $\overline{\mathcal{F}}_1$ and better than a reference solution labelled by a green square on the top right corner of Fig. 6.3. The area of the purple shaded region is defined as the hypervolume associated with the Pareto set $\overline{\mathcal{F}}_1$. A new Pareto set $\overline{\mathcal{F}}_2$ is generated by augmenting $\overline{\mathcal{F}}_1$ with a new solution $\mathbf{J}^*$. The hypervolume associated with $\overline{\mathcal{F}}_2$ is larger than $\overline{\mathcal{F}}_1$ due to the additional area introduced by $\mathbf{J}^*$, as represented by the gray rectangle. The area of the gray rectangle is defined as the hypervolume indicator $I_{\mathcal{H}}$, which quantifies the improvement of a Pareto set due to a new solution $\mathbf{J}^*$.

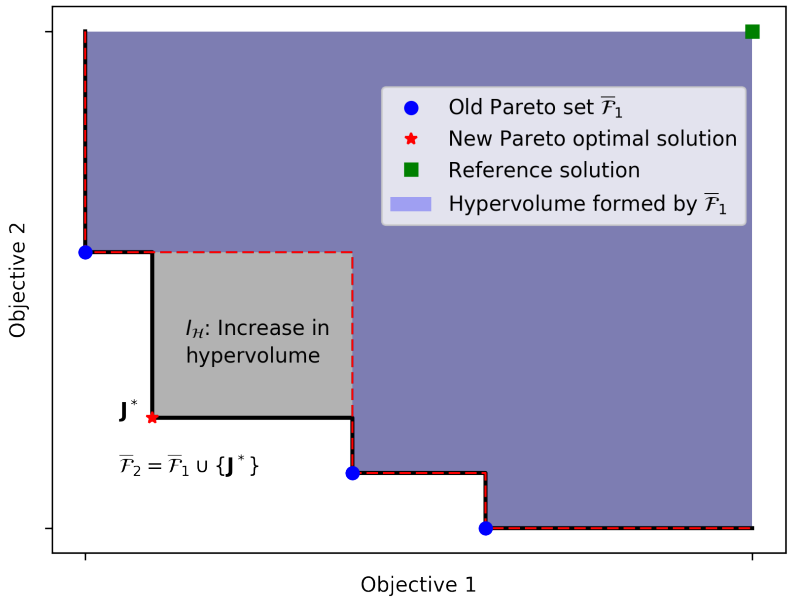

Figure 6.3: Illustration of the hypervolume indicator

Given a Pareto set $\overline{\mathcal{F}}$ and a new solution $\mathbf{J}^*$, the hypervolume indicator is written as,

$$I_{\mathcal{H}}(\mathbf{J}^*; \overline{\mathcal{F}}) = \mathcal{H}(\overline{\mathcal{F}} \cup \{\mathbf{J}^*\}) - \mathcal{H}(\overline{\mathcal{F}}) \tag{6.23}$$

When a new solution $\mathbf{J}^*$ fails to improve the existing Pareto set $\overline{\mathcal{F}}$, the hypervolume indicator associated with $\mathbf{J}^*$ is zero,

$$\mathcal{H}(\overline{\mathcal{F}} \cup \{\mathbf{J}^*\}) = \mathcal{H}(\overline{\mathcal{F}}) \quad \Rightarrow \quad I_{\mathcal{H}}(\mathbf{J}^*; \overline{\mathcal{F}}) = 0 \tag{6.24}$$

which means no improvement to $\overline{\mathcal{F}}$ is introduced by the new solution. The MO counterparts of the PoI, EI and LCB acquisition functions are defined based on the hypervolume indicator as presented in the following.

Hypervolume PoI The hypervolume probability of improvement (HVPoI) acquisition function is developed in Ref. [195], as the hypervolume counterpart of the PoI function. It is defined as follows,

$$C_{HVPoI}(\mathbf{d}) = \int \mathcal{I}(\mathbf{J}; \overline{\mathcal{F}}) P(\mathbf{J}^{sur} = \mathbf{J}) \mathrm{d}\mathbf{J} \tag{6.25}$$

where $\overline{\mathcal{F}}$ is the Pareto set of the current iteration, and

$$\mathcal{I}(\mathbf{J}; \overline{\mathcal{F}}) = \begin{cases} 1, & \text{if } I_{\mathcal{H}}(\mathbf{J}; \overline{\mathcal{F}}) > 0 \\ 0, & \text{otherwise} \end{cases} \tag{6.26}$$

Hypervolume EI The hypervolume expected improvement (HVEI) acquisition function is initially proposed under the name "S-metric expected improvement" in Refs. [187, 196] as an extension of the EI acqusition function of SO problems. The formulation is straightforward by replacing the improvement function in Eq. (6.18) with the hypervolume indicator,

$$C_{HVEI}(\mathbf{d}) = \int I_{\mathcal{H}}(\mathbf{J}; \overline{\mathcal{F}}) P(\mathbf{J}^{sur} = \mathbf{J}) \mathrm{d}\mathbf{J} \tag{6.27}$$

Hypervolume LCB The hypervolume lower confidence bound (HVLCB) acquisition function is initially proposed in Ref. [194] as an extension of the LCB acqusition func-

tion of SO problems. It was shown to outperform other popular MO algorithms, such as ParEGO [186], NSGA-II [197] and SPEA-2 [198]. This method is easy to implement and has been widely used. Assuming the Pareto set of the current iteration is $\overline{\mathcal{F}}$, the HV counterpart of the LCB function is defined as follows,

$$C_{HVLCB}(\mathbf{d}^*) = \begin{cases} I_{\mathcal{H}}(\mathbf{J}_0; \overline{\mathcal{F}}), & \text{if } I_{\mathcal{H}}(\mathbf{J}; \overline{\mathcal{F}}) > 0 \\ \min\limits_{\mathbf{J} \in \overline{\mathcal{F}}} \|\mathbf{J} - \mathbf{J}_0\|, & \text{otherwise} \end{cases} \tag{6.28}$$

where $\mathbf{J}_0 = \boldsymbol{\mu}(\mathbf{d}^*) - \upsilon\boldsymbol{\sigma}(\mathbf{d}^*)$.

Similar to the discussion in the direct approach, the HVLCB function is employed for the indirect approach due to its smoothness and the exploitation-exploration trade-off property.

6.3.2.3 Comparison of the Direct and Indirect Approaches

The comparison between the direct and indirect approaches is illustrated in Fig. 6.4. In the direct approach, the MO problem is reformulated as an SO problem and the design point is found by solving the SO problem only once. The direct approach is employed when there is sufficient preference information on the objectives, i.e. the knowledge about the relative importance of the objectives. The preference information provides the criterion for selecting the weights for objective combination as in Eq. (6.11). When the MO problem has objectives with limited user knownledge and the weights for objective combination cannot be determined easily, the indirect approach is employed to explore the design space associated with the MO problem. The indirect approach produces a set of representative Pareto optimal solutions and the user needs to manually pick one solution as the design point. In general, the direct approach is preferred whenever it is applicable, because the direct approach only requires solving one optimization problem and generally takes fewer iterations to converge when compared to the indirect approach.

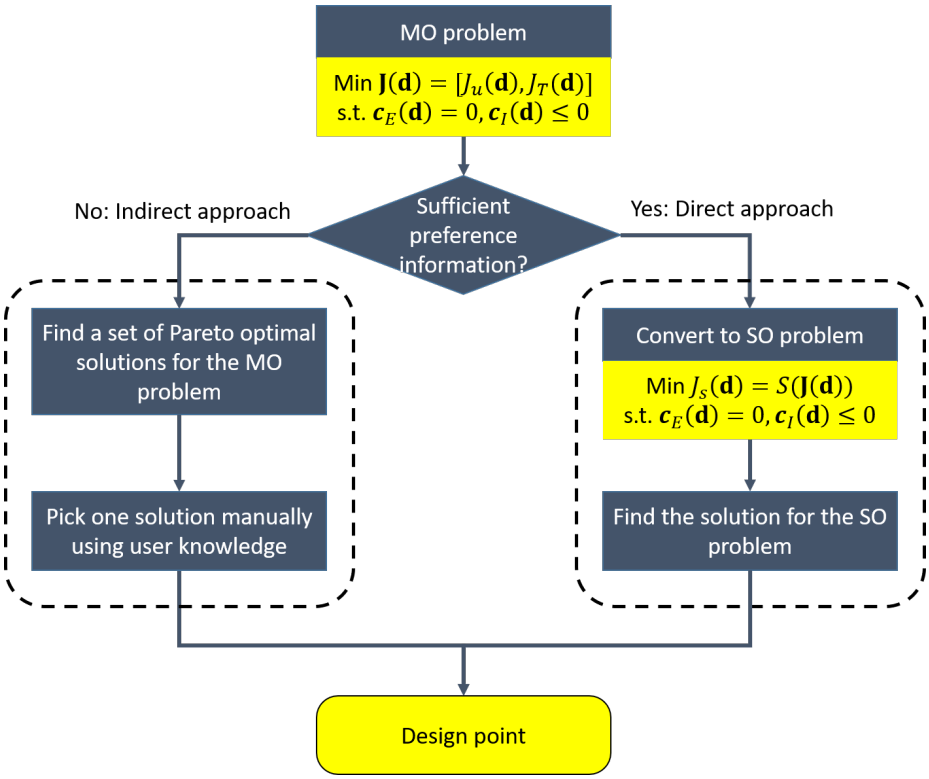

Figure 6.4: Illustration of direct and indirect approaches for solving the MO problem

6.3.3 Implementation Details

In the current study, both the direct and indirect approaches for the MO problems are implemented in a Python library, multi-objective Bayesian optimization (MOBO), that is developed at the University of Michigan. For the SO problem associated with the direct approach, BO algorithms employing PoI, EI, LCB acquisition functions are implemented. For the indirect approach, BO algorithms employing HVPoI and HVLCB acquisition functions are implemented. The kriging model is generated using the scikit-learn library [199].

No matter which surrogate model and acquisition function are used, eventually the BO algorithm boils down to a series of non-convex subproblems in the inner optimization step. It is hard to find the global optimum of a non-convex function. One choice is to use global optimization algorithms, such as the DIviding RECTangules (DIRECT) algorithm

[200]. Another choice is to apply local optimization algorithms, especially the gradient-based algorithms, with multiple starts. In practice, multiple restarts usually result in a good global sub-optimal point that is sufficient for the engineering purposes. Therefore, in the current study, the inner optimization step of the BO algorithm is solved using a gradient-based algorithm, Sequential Least-SQuares Programming (SLSQP), implemented in the SciPy library [201] with multiple starts. The initial starting points are generated using the OLH method at the beginning of every inner optimization step.

CHAPTER 7

Verification Results for the HYPATE Computational Framework

7.1 Results for Aerothermodynamic Solutions

The CFD solver based on ADflow has been verified extensively in the literature [149, 150]. This section will focus on the verification of the ROM-based fluid solver enhanced by the correction and scaling technique.

7.1.1 Case Description

For verification, a 2D panel configuration is considered, as shown in Fig. 7.1. The panel is simply supported at its leading and trailing edges, and its properties are: $a = 1\mathrm{m}$, $h = 0.0025\mathrm{m}$ and $L_{le} = 1\mathrm{m}$.

The CFD mesh for the 2D panel is shown in Fig. 7.2. The fluid domain is discretized using structured mesh. It consists of 170 points in the x-direction (65 of which are on the panel itself) and 105 points normal to the plate. The wall-normal spacing is $\Delta z/a = 10^{-5}$ for a sufficient resolution of the boundary layer.

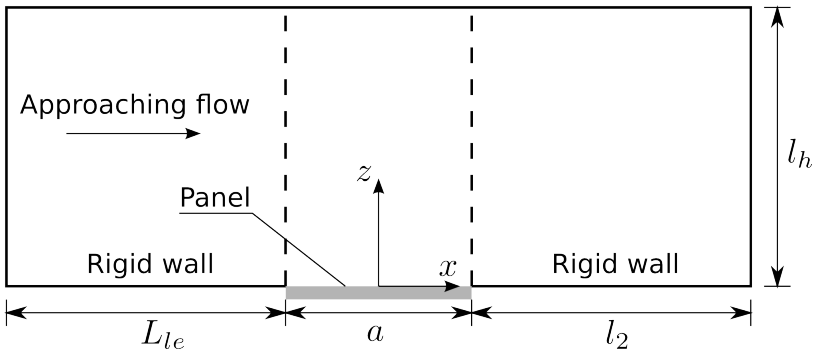

Figure 7.1: Geometrical configuration of a 2D panel

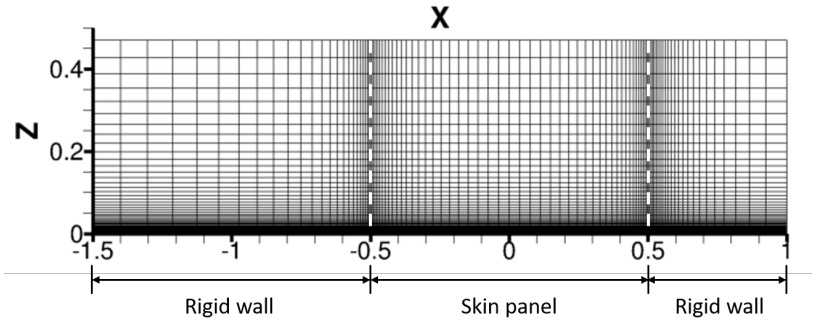

Figure 7.2: Computational grid of a 2D panel for the CFD solver

7.1.2 Generation of the Fluid ROM

Two ROMs are generated, in both cases, the panel deformation is characterized by six sinusoidal modes,

$$u_F(x)/h = \sum_{i=1}^{6} a_i \sin\left[i\pi\left(\frac{x}{a} + \frac{1}{2}\right)\right] \tag{7.1}$$

The distinction between the two ROMs is due to different wall temperature models. In the first ROM, denoted ROM/Poly, the wall temperature is characterized by a third-order polynomial,

$$T_w(x) = (b_1 + b_2 x + b_3 x^2 + b_4 x^3) \times 10^3 \mathrm{K} \tag{7.2}$$

In the second ROM, denoted ROM/Avr, the wall temperature of the panel is uniform,

$$T_w(x) = b_1 \times 10^3 \mathrm{K} \tag{7.3}$$

The ranges of the parameters in the sample CFD solutions are listed in Table 7.1. The sample parameters are generated using the OLH sampling method. For ROM/Poly, after the parameter sampling, the parameters b_1, b_2, b_3, b_4 are scaled to ensure that the temperature distributions given by Eq. (7.2) stay within the range of $[200, 900]K$.

the following procedure is used to scale the parameters b_1, b_2, b_3, b_4, to ensure that the temperature distributions given by Eq. (7.2) stay within the range of $[200, 900]K$.

$$b_1^{new} = (b_1 - T_{w,\min})\frac{T_{\max} - T_{\min}}{T_{w,\max} - T_{w,\min}} + T_{\min} \tag{7.4}$$

$$b_i^{new} = b_i \frac{T_{\max} - T_{\min}}{T_{w,\max} - T_{w,\min}}, \quad i = 2, 3, 4 \tag{7.5}$$

where $T_{w,\max} = \min(900K, \max(T_w(x)))$ and $T_{w,\min} = \max(200K, \min(T_w(x)))$.

Three sets of sample CFD solutions are generated. The first two data sets are for ROM generation and verification, which consists of the CFD solutions at the reference flow condition $M_\infty = 6$ and $H = 25\mathrm{km}$. For the ROM generation, 1100 and 500 samples are generated for ROM/Poly and ROM/Avr, respectively. For the verification of ROM convergence, 100 samples are generated for each ROM. The third data set is generated for the verification of ROM correction and scaling technique. The data set consists of $3 \times 15 \times 30$ sample CFD solutions, representing 3 geometric scales $\xi = 1, 2, 4$ and 15 flight conditions as a combination of Mach numbers $M_\infty = 4, 5, 6, 7, 8$ and altitudes $H = 20, 25, 30\mathrm{km}$. The deformation is characterized using the first three sinusoidal modes, while the wall temperature is characterized using three modes,

$$T_w(x) = [b_1 + b_2 x + b_5 \sin(2\pi x)] \times 10^3 \mathrm{K} \tag{7.6}$$

Note that wall temperature distribution includes a *non-polynomial* mode that is not present in the data set for ROM generation. Thirty combinations of panel deformation and temperature distribution are sampled from the ranges specified in Table 7.1.

Table 7.1: Ranges of sample parameters in the 2D ROM

	Data sets 1, 2		Data set 3
	ROM/Poly	ROM/Avr	
a_1	$[-6, 6]$	$[-6, 6]$	$[-6, 6]$
a_2	$[-2, 2]$	$[-2, 2]$	$[-2, 2]$
a_3	$[-2, 2]$	$[-2, 2]$	$[-2, 2]$
a_4	$[-2, 2]$	$[-2, 2]$	N/A
a_5	$[-1.5, 1.5]$	$[-1.5, 1.5]$	N/A
a_6	$[-1.5, 1.5]$	$[-1.5, 1.5]$	N/A
b_1	$[0.2, 0.9]$	$[0.2, 0.9]$	$[0.2, 0.9]$
b_2	$[-2, 2]$	N/A	$[-0.3, 0.3]$
b_3	$[-5, 5]$	N/A	N/A
b_4	$[-5, 5]$	N/A	N/A
b_5	N/A	N/A	$[-0.3, 0.3]$

The convergence of ROM/Poly and ROM/Avr is examined in Fig. 7.3. The ROMs are used to predict the pressure and the heat flux distributions in the second data set. The differences between the ROM prediction and the CFD solution are characterized using the normalized root-mean-squared error (NRMSE),

$$NRMSE = \frac{\sqrt{\frac{1}{L}\int_0^L (y_{CFD} - y_{ROM})^2 \mathrm{d}x}}{\max(y_{CFD}) - \min(y_{CFD})} \tag{7.7}$$

The convergence of the average NRMSE is shown in Fig. 7.3. For the pressure distribution, both ROMs achieve convergence using 200 samples with the average NRMSE less than 1%.

For the heat flux distribution, ROM/Avr converges with 200 samples, which is one fifth of the number of samples that are necessary for the convergence of ROM/Poly. The difference in the convergence rate is expected, as the polynomial temperature distribution introduces variations in the heat flux distribution, which requires more input parameters and thus more samples for ROM/Poly to converge.

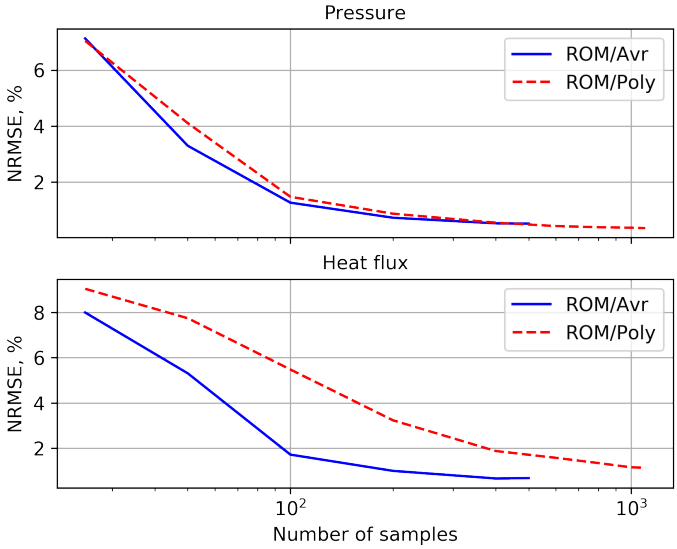

Figure 7.3: The NRMSE of the test cases

7.1.3 The ROM-Based Fluid Solutions

The capability of the ROM correction and scaling technique is demonstrated using a sample from data set 3. The panel deformation and the temperature distribution in the sample are illustrated in Fig. 7.4. The ROM results are presented in Fig. 7.5 for three cases ordered in increasing complexity. In the first case, the ROM/Poly and ROM/Avr results are compared against the CFD results for the reference flight conditions $M_\infty = 6$, $H = 25$km. In ROM/Poly, the temperature distribution is curve-fitted using a third-order polynomial. In ROM/Avr, the correction for non-uniform wall temperature is achieved using the BL correction. The ROM/Avr produces accurate predictions with an error of 1.1% in the pressure distribution and 7.0% in the heat flux distribution. Furthermore, the errors of the ROM/Avr

results are less than half of that of the ROM/Poly results. In the second case, compared to the first case, the flight conditions are changed to $M_\infty = 7$, $H = 30$km. The surface pressure and the heat flux decrease due to the decrease in the freestream pressure. The ROM correction captures the trend well, with an error of 2.3% in pressure and an error of 6.6% in the heat flux. In the third case, the flight conditions are identical to those in the second case, while the geometrical configuration is scaled with a factor of $\xi = 4$. Despite the moderate deviations in both the flight conditions and geometric scales, the corrected and scaled ROM results produce an error of 6.0% in the pressure distribution and 11.1% in the heat flux distributions, which are sufficient for engineering applications.

Finally, the PT and BL corrections for the ROM are compared in Figs. 7.6(a) and 7.6(b). The ROM results generated using the PT and BL corrections are denoted ROM/PT and ROM/BL, respectively. Figure 7.6(a) illustrates the distributions of the average NRMSE in the pressure for the flight conditions and geometric scales considered in data set 3. The NRMSE increases as the conditions deviate from the reference values. The BL correction results in lower NRMSE when compared to the PT correction in most of the cases. The difference is expected, since the BL correction takes into account the boundary layer effect that is ignored in the PT correction. Figure 7.6(b) illustrates the distributions of the average NRMSE for the heat flux. The distribution of the NRMSE follows a trend similar to the pressure. The NRMSE increases as the conditions deviate from the reference values. However, a better pressure correction in ROM/BL does not necessarily produce better correction in the heat flux. The discrepancy is attributed to the limitations in the analytical model for the heat flux correction. In general, given a ROM for $M_\infty = 6$, $H = 25$km, both PT and BL corrections provide a good correction for the pressure and the heat flux in the range of $M_\infty = 5 - 7$, $H = 20 - 30$km and $\xi = 1 - 4$ with an error of less than 10%. In particular, the BL correction is more accurate for pressure prediction, while the PT correction is more accurate for heat flux prediction.

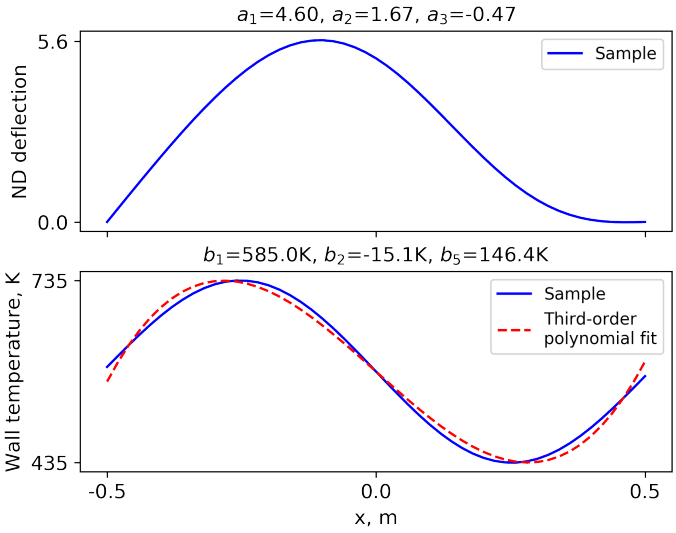

Figure 7.4: Distributions of deflection and temperature in the sample

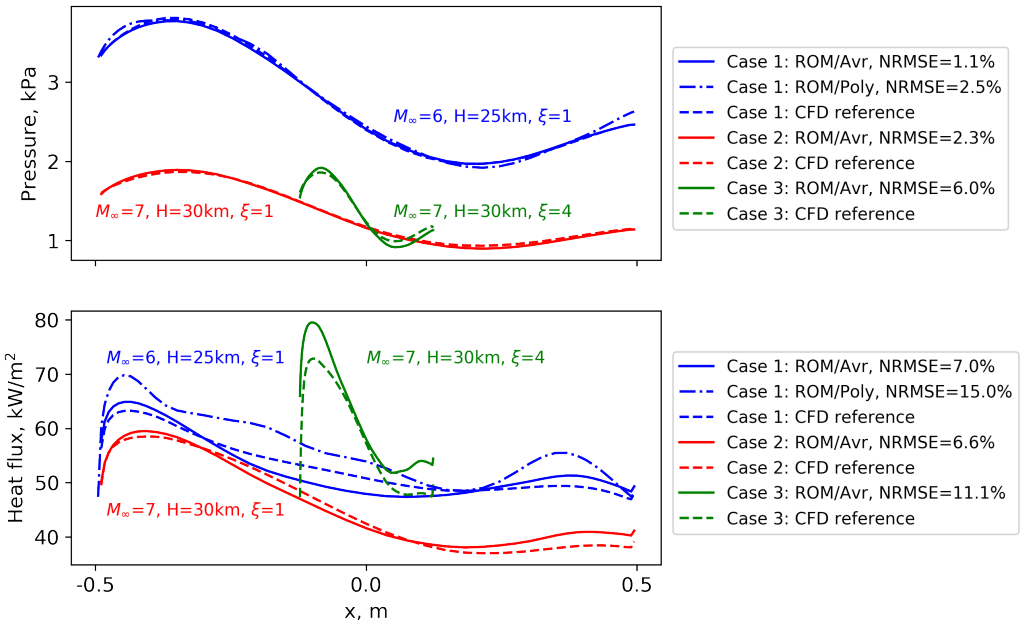

Figure 7.5: Correction and scaling of the ROM solution

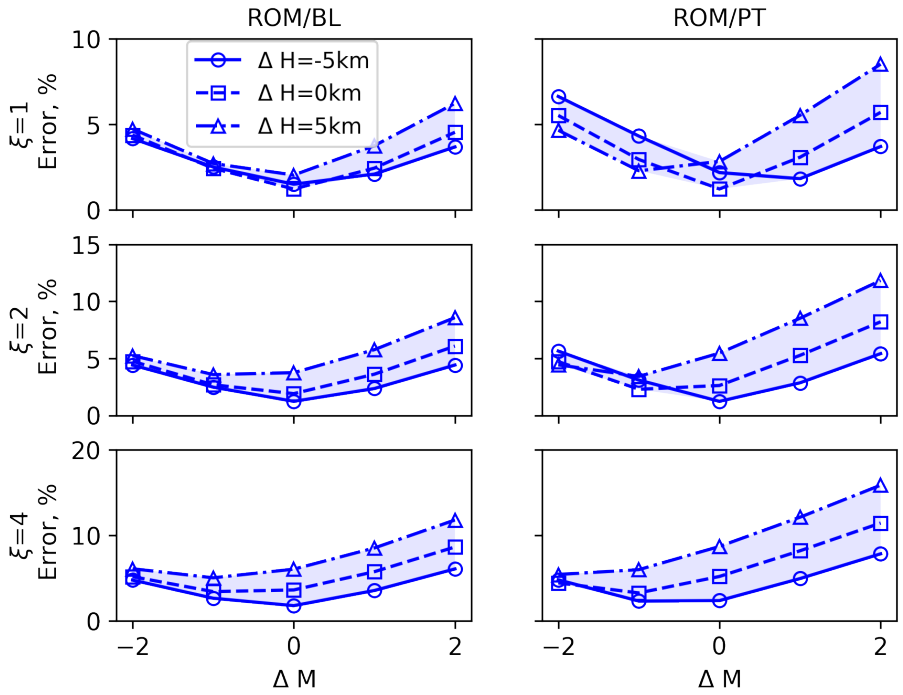

(a) Pressure

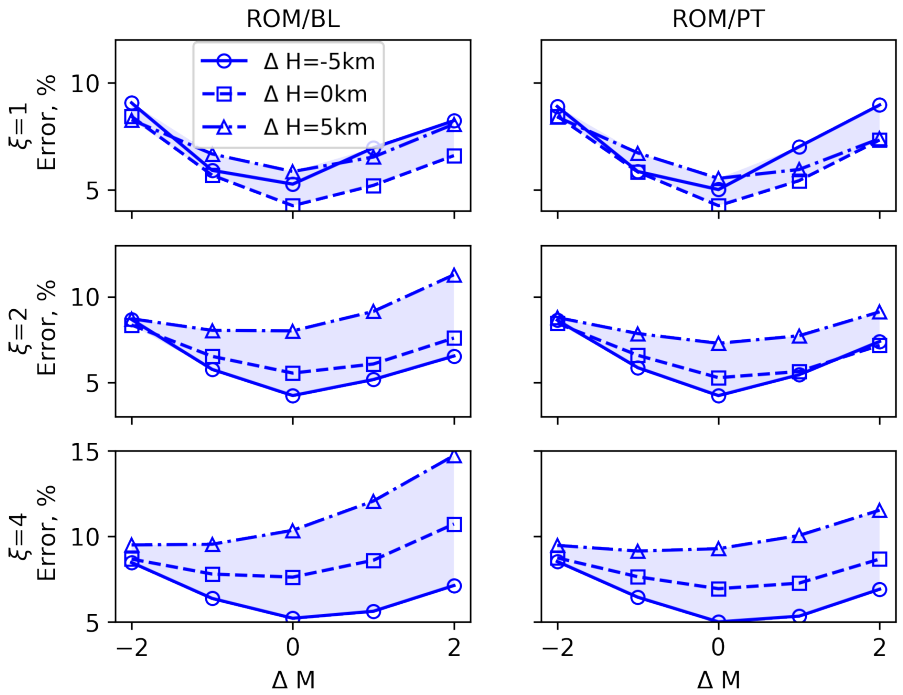

(b) Heat flux

Figure 7.6: Distribution of average NRMSE of the ROM/BL and ROM/PT solutions

7.2 Results for Aeroelastic Response

In this section, the aeroelastic portion of the HYPATE framework is verified. First, the CFD-based solutions are verified against computational and experimental results from literature. Next, the correctness and accuracy of the fluid ROM is illustrated by verifying the ROM-based aeroelastic solutions against the CFD-based solutions. Finally, the capability of the LSA method to predict the aeroelastic flutter boundary of a skin panel is demonstrated.

7.2.1 The CFD-Based Aeroelastic Solutions

7.2.1.1 Case Description

The configuration considered for 3D panel flutter is taken from Ref. [61], where a RANS-based tightly-coupled aeroelastic computational framework was developed and applied to panel flutter analysis over a range of $M_\infty = 1.1 - 2.4$. The panel configuration is based on the panel flutter test in Ref. [4] for $M_\infty = 1.05 - 1.4$ and $Re = 4 \times 10^6$. The geometrical parameters and material properties of the panel are shown in Table 7.2. The panel is clamped along its four edges. The natural frequencies of the panel agree well with data from literature, as shown in Table 7.3. The number in the bracket indicates the error with respect to the analytical values obtained from Ref. [4]. The natural frequencies in the current study are slightly higher than the analytical values, with errors less than 0.5%. In Ref. [61], a finite difference formulation was employed, which resulted in lower natural frequencies. The thickness of the boundary layer on the panel is controlled by the length L_{le} of the rigid wall in front of the panel. A larger value of L_{le} results in a thicker boundary layer.

Table 7.2: Properties for the 3D panel configuration [4]

a	b	h	ρ^s	E	ν
9in	18in	0.0401in	110.0 $\mathrm{lb/ft^3}$	5.6Mpsi	0.35

Table 7.3: Natural frequencies of the panel

Mode No.	Analytical, Hz [4]	Hashimoto, Hz [61]	Current, Hz
1	109.7	108.1 (1.46%)	110.0 (0.27%)
2	142.0	138.2 (2.68%)	142.4 (0.28%)
3	199.8	191.7 (4.05%)	200.3 (0.25%)
4	282.6	267.9 (5.20%)	283.4 (0.28%)
5	285.5	278.4 (2.49%)	286.4 (0.32%)

The computational model for the 3D panel is shown in Fig. 7.7. In the structural mesh, the panel is discretized using 10 elements in streamwise direction and 20 in spanwise direction. In the fluid mesh, the panel has 33 grid points in streamwise direction and 65 in spanwise direction. The y^+ value of the mesh is kept under 1.0 for adequate resolution of the boundary layer. The value of L_{le} is fixed, so that the boundary layer thickness at $x = 0$ is $\delta/a = 0.1$ at $M_\infty = 2.4$.

The simulation is initialized as follows. First, a steady solution is obtained for the undeformed panel. The resulting pressure distribution due to boundary layer is applied below the panel as the cavity pressure, which is fixed throughout the simulation. As discussed in Ref. [49] pp. 43–45, a high cavity pressure results in the static deformation of the panel and increases the critical flutter dynamic pressure. Using the pressure distribution over the undeformed panel eliminates the static deformation of the panel, and thus the effect of the cavity pressure. To initiate the unsteady flutter computation, a perturbation in deformation is imposed on the panel at the first time step. The perturbed deformation is obtained by applying a small uniform load in z direction and it is removed after the unsteady simulation

is initiated.

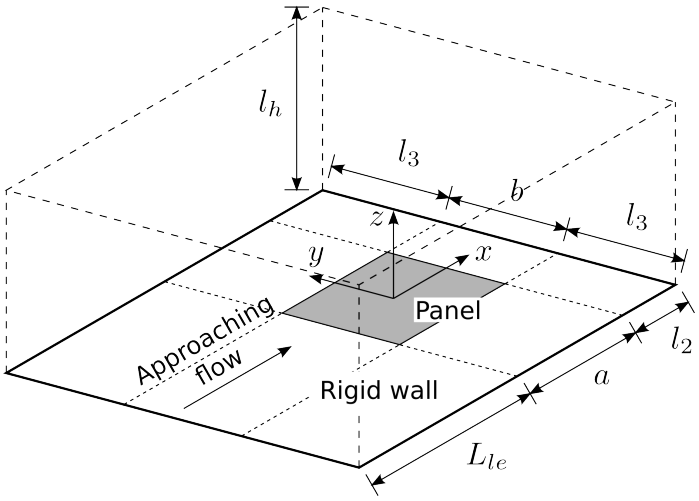

Figure 7.7: Geometrical configuration of a rectangular panel

7.2.1.2 Aeroelastic Flutter Boundary

The flutter boundary of the panel is shown in Fig. 7.8. The Euler and RANS results are shifted upward by approximately 5%, compared with the data from Ref. [61]. The Euler and LS results agree well with each other. The error could be due to the fact that the structure used in current study is slightly stiffer than that in the reference. A stiffer panel is expected to have higher flutter boundary. For the RANS results, another source of error is the boundary layer. The values of δ/a in the reference and current study do not match exactly. The difference in boundary layer thickness may result in the shift of flutter boundary.

The RANS and Euler results in Fig. 7.8 indicate that in high supersonic flow ($M_\infty \geq 2.0$), the turbulent boundary layer stabilizes the panel and could increase the flutter boundary by over 20%. This trend was also confirmed by Ref. [61]. It is worth noting that, in low supersonic flow, the effect of the turbulent boundary layer is less pronounced. In Ref. [60], it was found that, at $M_\infty = 1.2$, the flutter boundary with turbulent flow is in agreement with the results from the inviscid flow.

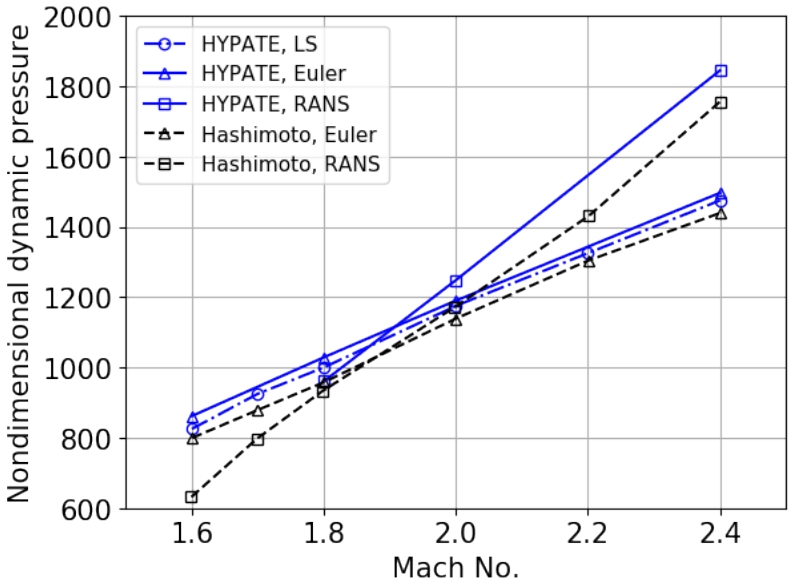

Figure 7.8: Flutter boundary for $M_\infty = 1.6 - 2.4$

7.2.2 The ROM-Based Aeroelastic Solutions

7.2.2.1 Case Description

A square panel configuration shown in Fig. 7.9 is considered. To enable a similar boundary layer thickness at an arbitrary flow orientation angle, an O-grid mesh is generated for the fluid domain in the computational model, as shown in Fig. 7.9. The distance of center of the panel to the inflow boundary is invariant, so the same boundary layer thickness on the panel is maintained for any orientation angle. In the fluid mesh, the panel has 41 grid points in both x- and y-directions and 73 grid points normal to the panel. The wall-normal spacing is $\Delta z/a = 10^{-6}$ for a sufficient resolution of the boundary layer.

The aeroelastic responses at $\beta = 30^\circ$ are examined for two cases: (1) $M_\infty = 6.0$, $H = 20\text{km}$, $\lambda = 10000$, (2) $M_\infty = 5.0$, $H = 25\text{km}$, $\lambda = 8000$. The panel temperature is uniformly 300K and fixed. In both cases, the panel is dynamically unstable and a small perturbation to the panel develops into a limit cycle oscillation (LCO).

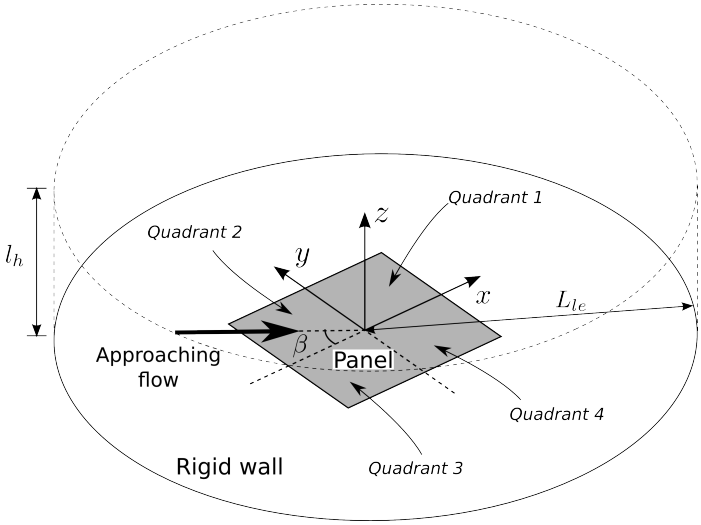

Figure 7.9: Geometrical configuration of the square panel with arbitrary flow orientation angles

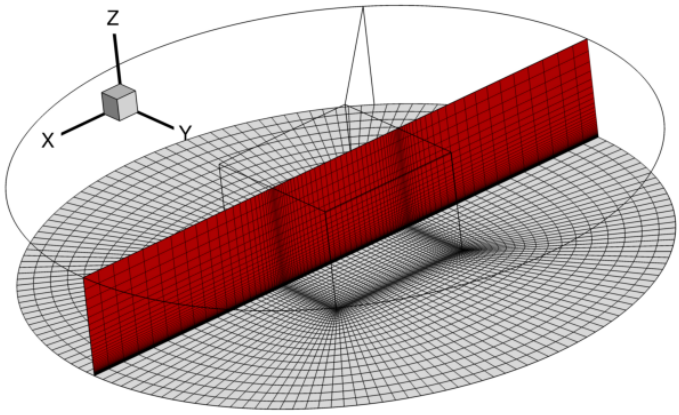

Figure 7.10: O-grid mesh for the fluid domain

7.2.2.2 Generation of the fluid ROM

Two fluid ROMs were generated for different flow orientation angles ($\beta = 0, 30°$) for the flight condition $M_\infty = 6.0$, $H = 20\text{km}$. The wall temperature of the panel is uniform and ranges from 250K to 350K. The panel deformation is characterized using 12 sinusoidal

Table 7.4: Nondimensionalized maximum modal amplitudes for the 3D ROMs

Amplitudes	a_{11}	a_{12}	a_{13}	a_{21}	a_{22}	a_{23}	a_{31}	a_{32}	a_{33}	a_{41}	a_{42}	a_{43}
$\beta = 0°$	6	N/A	2	2	N/A	1.5	1.5	N/A	1.0	1.0	N/A	0.5
$\beta = 30°$	6	0.75	0.75	1.25	0.35	0.35	1.25	0.3	0.3	0.25	0.25	0.25

modes,

$$u_F(x,y)/h = \sum_{i=1}^{4}\sum_{j=1}^{3} a_{ij}\sin(i\pi x/a)\sin(j\pi y/b) \tag{7.8}$$

In the ROM for $\beta = 30°$, all 12 modes are used; while in the ROM for $\beta = 0°$, only the 8 modes that are symmetric about the streamwise centerline are used. The maximum modal amplitudes in the samples are listed in Table 7.4. In this section and the rest of the paper, the BL correction is used for scaling the ROM results to different flight conditions and geometric scales.

7.2.2.3 Aeroelastic Response

In the following results, the structural response is plotted against the nondimensional time $\bar{t} = \frac{V_\infty t}{a}$, and the power spectral density (PSD) is plotted against the reduced frequency, or the Strouhal number, $St = \frac{\omega a}{V_\infty}$.

For the first case the flow conditions are identical to those used for the CFD samples from which the fluid ROM was generated. In Fig. 7.11(a), the time responses from the complete CFD and ROM solutions are in agreement and generate similar LCO amplitudes. The modal amplitudes of the structural responses after the panel enters LCO range are shown in Fig. 7.11(b). The CFD and the ROM results show a similar distribution of modal amplitudes. The 1st, 2nd and 4th sinusoidal modes dominate the structural response. The PSD of the LCO portion of the structural response is illustrated in Fig. 7.11(c). The ROM solution accurately captures the primary frequency component of the CFD solution at $St = 0.0913$ and approximates the secondary frequency component at $St = 0.279$ with an error of 4.0%.

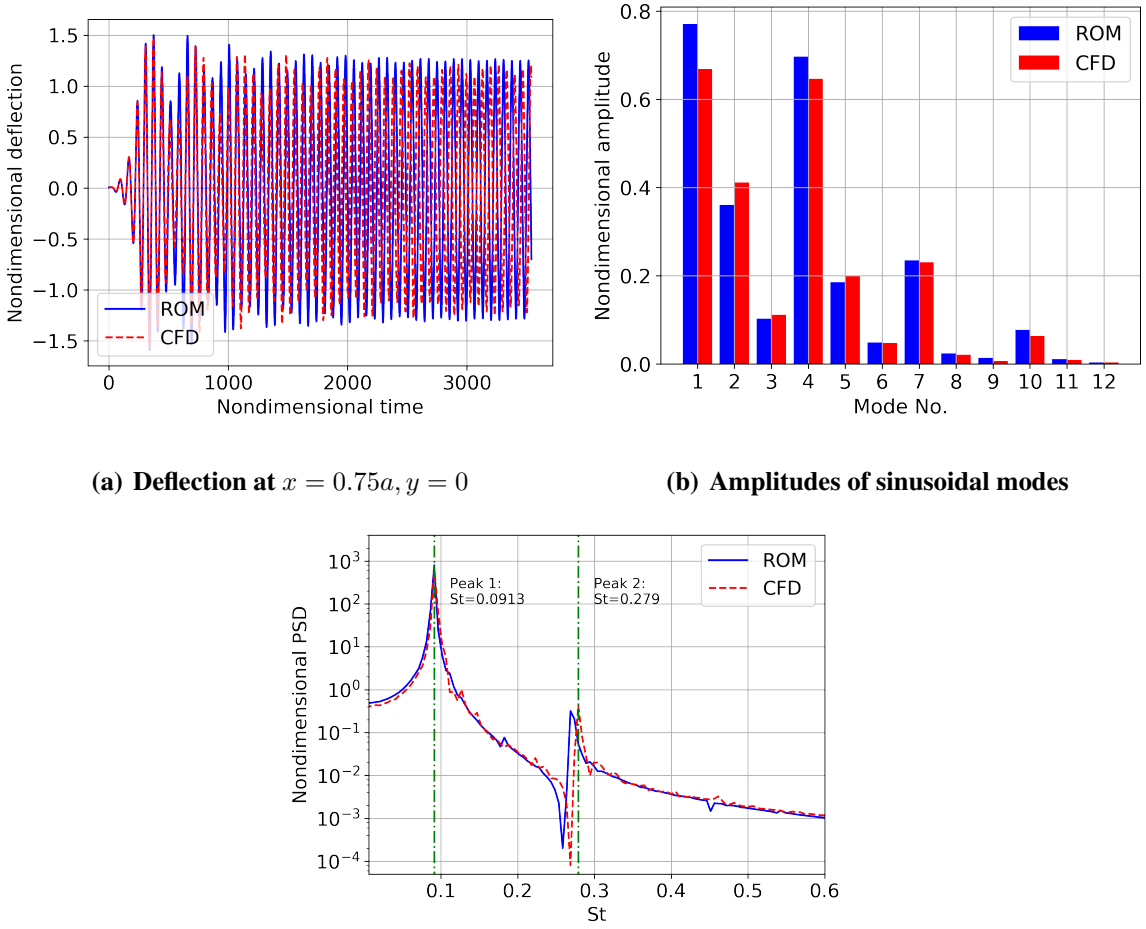

(a) Deflection at $x = 0.75a, y = 0$

(b) Amplitudes of sinusoidal modes

(c) PSD of the LCO response

Figure 7.11: Aeroelastic response at $M_\infty = 6$, $H = 20\text{km}$

The aeroelastic responses for the second case are shown in Figs. 7.12(a)-7.12(c). For this case the flow conditions are different from those used for the CFD samples from which the fluid ROM was generated. The ROM-based solution agrees well with the CFD-based solution both in the time response and the modal amplitudes. The ROM solution captures the frequency components of the CFD solution at $St = 0.0684$ and $St = 0.208$ with errors of 3.6% and 6.3%, respectively.

In-plane loads are not considered since the objective is to verify the ROM-based solutions. It is important to note that axial and thermal loads producing panel buckling have an

important effect on panel flutter resulting in LCO's that are not harmonic and can become aperiodic [49]. The combination of LCO and buckling represent conditions beyond the onset of instability. This is a topic worth further investigation in the future.

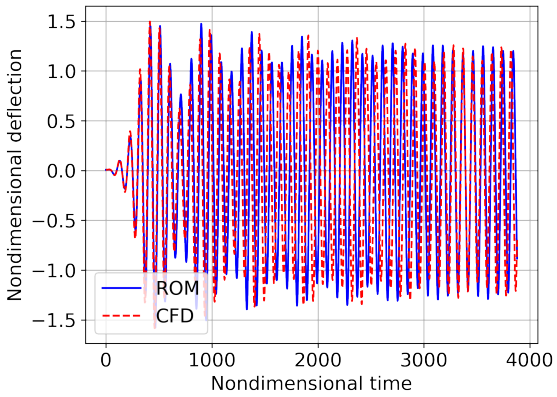

(a) Deflection at $x = 0.75a, y = 0$

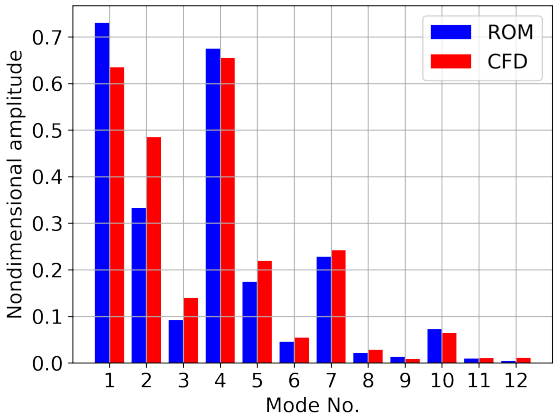

(b) Amplitudes of sinusoidal modes

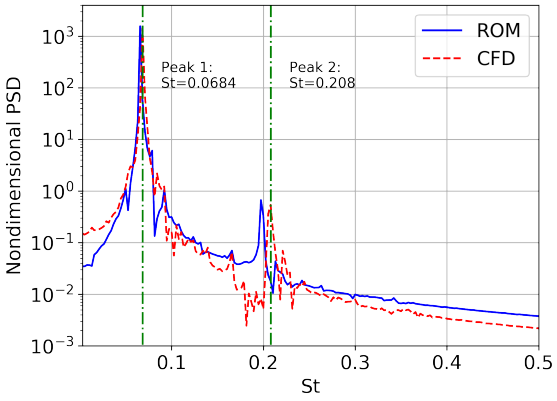

(c) PSD of the LCO response

Figure 7.12: Aeroelastic response at $M_\infty = 5$, $H = 25\text{km}$

7.2.3 Linearized Stability Analysis of Panel Flutter Problem

7.2.3.1 Case Description

The geometrical configuration is a simply supported square panel that is similar to the case shown in Fig. 7.7. The geometrical parameters are $a/h = 500$ and $a/b = 1$. The material

properties are $\nu = 0.3$ and $\alpha = 1.2 \times 10^{-6}/\mathrm{K}$. The mass ratio $\mu_F = 5.355 \times 10^{-4}$. The aerodynamic loads are obtained using the piston theory. Two cases with different temperature increments are considered: (1) $\Delta T = T_{cr}$, (2) $\Delta T = 2T_{cr}$.

The first set of results are obtained directly from temporal responses of the panel, as shown in Fig. 7.13. The amplitudes of LCO are computed at a series of dynamic pressures. At each dynamic pressure, the aeroelastic simulation is run for 5000 time steps so that the time response enters a stable state or a LCO state. The results are compared with those from Refs. [47, 57].

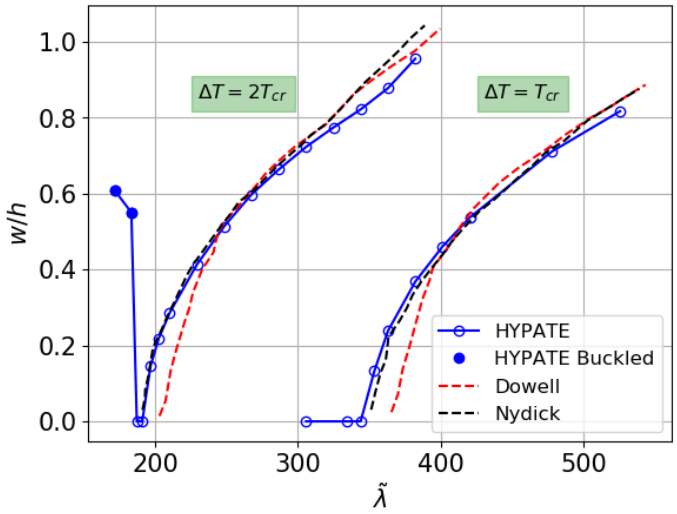

Figure 7.13: The LCO curves of the square panel

In general, the results from current study agree well with those from literature. The flutter points predicted by HYPATE are $\bar{\lambda}_F = 344.0$ for $\Delta T = T_{cr}$ and $\bar{\lambda}_F = 191.1$ for $\Delta T = 2T_{cr}$. Compared with the literature results, the errors are less than 1%. Moreover, the case $\Delta T = 2T_{cr}$ provides an illustration of three typical types of panel response [50]. The panel response is controlled by two types of forces, i.e. the thermally-induced inplane compressive force and the aerodynamic force. When the dynamic pressure is low ($\bar{\lambda}_F < 183.5$), the aerodynamic force is weaker than the compressive force and type I response occurs: The panel is thermally buckled but dynamically stable, as illustrated in Fig.

7.14(a). As the dynamic pressure increases ($183.5 < \bar{\lambda}_F < 191.1$), The two forces are both moderate and type II response occurs: The panel is stabilized and has zero LCO amplitude, as illustrated in Fig. 7.14(b). After the flutter point ($\bar{\lambda}_F > 191.1$), the aerodynamic force becomes stronger than the compressive force and the panel enters the LCO state.

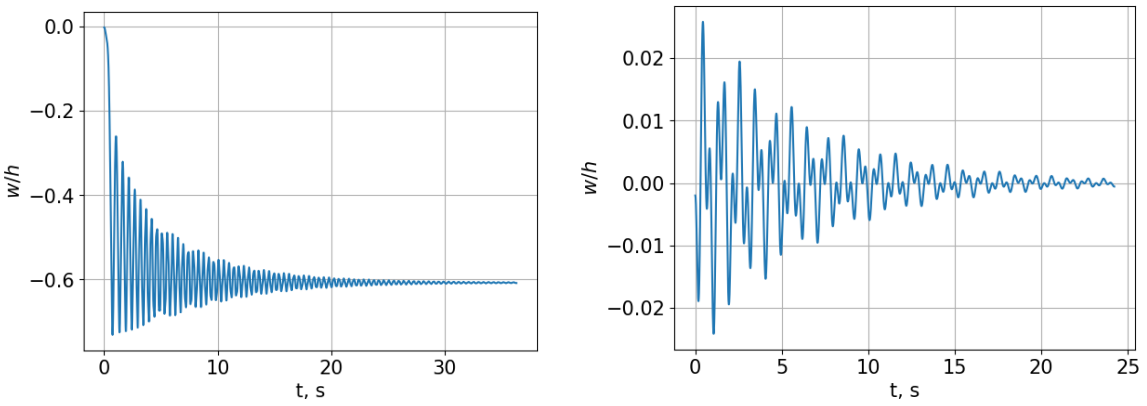

(a) Type I response at $\bar{\lambda}_F = 172.0$ **(b) Type II response at** $\bar{\lambda}_F = 187.3$

Figure 7.14: Typical panel responses before flutter when $\Delta T = 2T_{cr}$

The second set of results is obtained from the LSA using the PEP and GEP formulations. The frequencies ω and dampings ζ of the first six aeroelastic modes are computed at a series of dynamic pressures. The first two modes are found to be the source of instability and the higher modes are stable. By the definitions in Eq. (5.37), the frequency and damping have the same unit of radian/second, and therefore they are nondimensionalized by the natural frequency ω_o of the first structural mode of the unheated panel.

$$\bar{\omega} = \frac{\omega}{\omega_o}, \quad \bar{\zeta} = \frac{\zeta}{\omega_o} \tag{7.9}$$

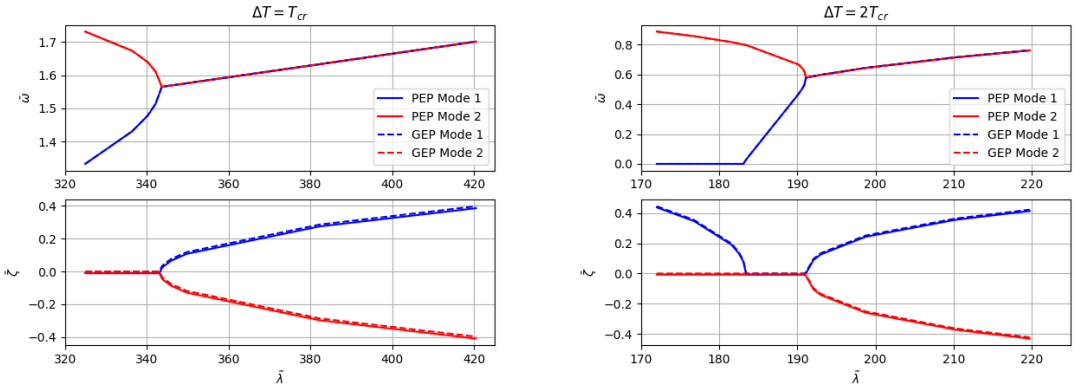

(a) Case 1: $\Delta T = T_{cr}$ **(b) Case 2:** $\Delta T = 2T_{cr}$

Figure 7.15: Linearized stability analysis results (PEP v.s. GEP)

Figure 7.15(a) illustrates the LSA results for the first case ($\Delta T = T_{cr}$). The frequencies of the two modes coalesce as the dynamic pressure increases. When the frequencies coalesce, the damping of one of the modes becomes positive, and the other becomes negative, indicating a flutter-type instability. The flutter point is $\bar{\lambda}_F = 343.3$, within 1% error compared with results from time-domain analysis.

Figure 7.15(b) illustrates the LSA results for the second case ($\Delta T = 2T_{cr}$). The flutter point is $\bar{\lambda}_F = 190.9$, where the damping becomes positive. Furthermore, the LSA results capture the two types of panel response before the flutter point. When $\bar{\lambda}_F < 183.4$, mode 1 has zero frequency and positive damping, indicating that the panel has divergence-type instability, which corresponds to the type I response in the time-domain analysis. When $183.4 < \bar{\lambda}_F < 190.9$, the modes have negative damping and the panel is stable, which corresponds to the type II response.

In Figs. 7.15(a) and 7.15(b), the PEP and GEP formulations produce almost identical results. The maximum error in the frequencies is less than 0.1%. Compared with PEP results, the damping computed by GEP is "shifted" upward by a small amount, typically 1% of the reference frequency. The shift in damping is caused by neglecting the aerodynamic damping matrix due to the quasi-steady assumption. The changes in the flutter points due to

the shift are negligible. The comparison between PEP and GEP results justifies the quasi-steady assumption in the hypersonic flow regime. Also, the results indicate that the positive damping in flutter-type instablity is mainly introduced by the aerodynamic stiffness matrix.

7.3 Results for Aerothermoelastic Response

7.3.1 Case Description

The structural configuration is a 2D skin panel, as shown in Fig. 7.1. The panel is simply supported at the leading and trailing edges. The geometrical parameters are $h = 2.5\mathrm{mm}$, $a = 1\mathrm{m}$, and $L_{le} = 1\mathrm{m}$. The panel is made of Al7075 and the material properties are temperature dependent. The properties at initial temperature ($T = 300K$) are shown in Table 7.5.

Table 7.5: Material properties for the 2D aerothermoelastic case [5]

ρ^s	E	ν	α	k^s	c_p^s
$2768.1\mathrm{kg/m^3}$	$72.86\mathrm{GPa}$	0.325	$2.236 \times 10^{-5}/\mathrm{K}$	$132.05\mathrm{W/mK}$	$850.99\mathrm{J/kgK}$

7.3.2 The CFD-Based Aerothermoelastic Response

The benchmark case is based on Ref. [202], where the aerothermoelastic response is generated using analytical models for aerodynamic pressure and heat flux. It is suitable for the verification of the aerothermoelastic solution and the accuracy of the coupling schemes. The flight conditions are $M_\infty = 4.0$, $p_\infty = 2087.2\mathrm{Pa}$, and $T_\infty = 266.7\mathrm{K}$.

7.3.2.1 Comparison of Coupling Schemes

Two sets of coupled solutions are generated using the S1 and S2 schemes, respectively, as shown in Fig. 7.16. In an actual hypersonic vehicle, the panel has to be designed so as to avoid any unstable behavior. Therefore, the responses up to the onset of aerothermoelastic

instability, indicating the stability boundary of the panel that has to be avoided in actual vehicle design, are presented in Fig. 7.16.

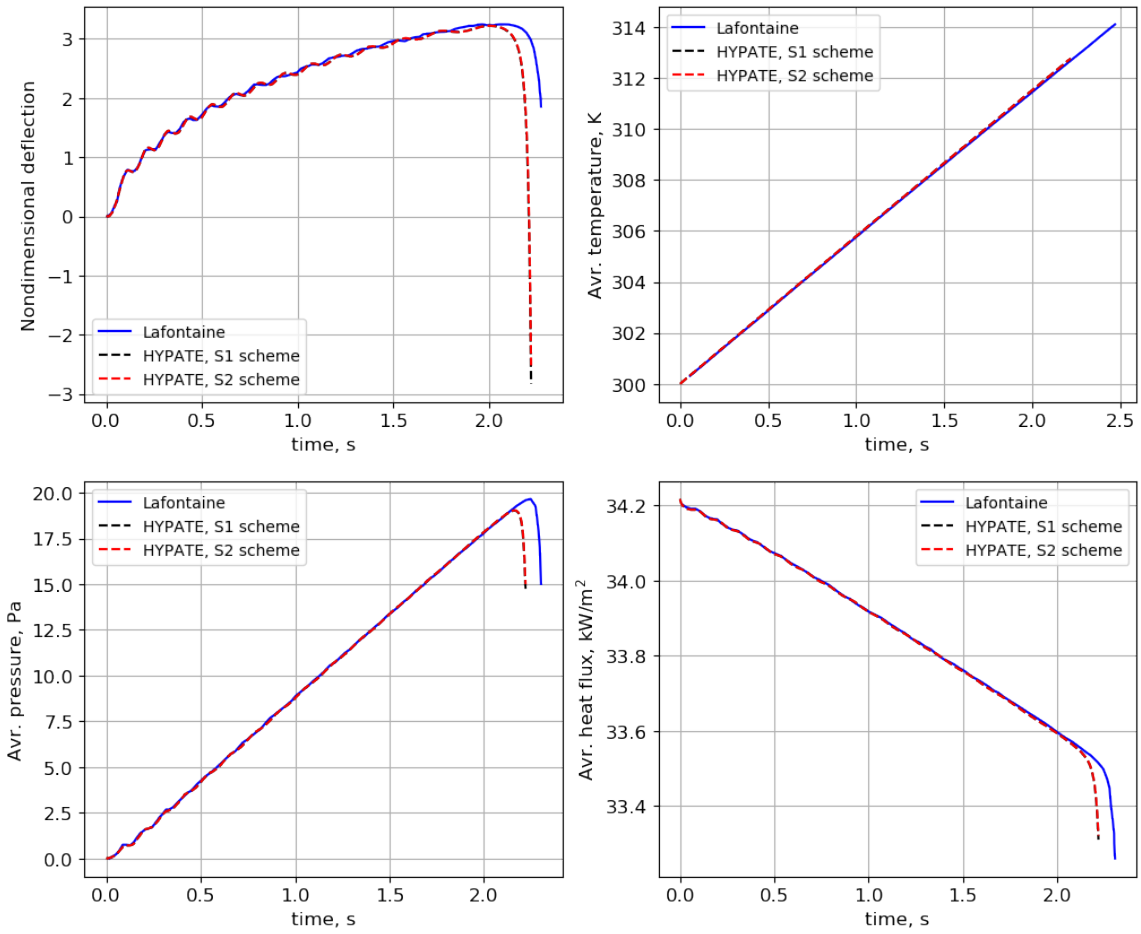

Figure 7.16: Aerothermoelastic response of the 2D panel for $M_\infty = 4.0, p_\infty = 2087.2\text{Pa}, T_\infty = 266.7\text{K}$

The results from the two schemes are almost identical. In the structural response, the mid-panel displacement is nondimensionalized by thickness. The panel undergoes a thermally-driven response, which causes the panel to deform into the flow. Near $t = 2.1s$, aerothermoelastic instability in the form of snap-through occurs, and the panel deforms out of the flow. The average pressure on the panel surface gradually increases as the panel deforms into the flow. Sufficiently large pressure causes the snap-through of the panel, which

in turn causes the sudden drop of the pressure itself. The heat flux gradually decreases as the panel heats up. The fluid, structural, and thermal solutions from HYPATE agree well with those from Ref. [202] up to the onset of the instability, and therefore verifies the correctness of the aerothermoelastic solution in the HYPATE framework.

7.3.2.2 Time Accuracy Analysis of Coupling Schemes

Next, the time accuracy of the coupling schemes is verified using the same benchmark case. To obtain the order of time accuracy, a series of aerothermoelastic simulations are conducted for 2.048 seconds using multiple time step sizes $\Delta t_i = 0.05 \times 2^i$ms ($i = 1, \cdots, 8$). The error is defined as the normalized difference between the solutions of two consecutive time step sizes,

$$\epsilon_i = ||\mathbf{f}(\Delta t_{i+1}) - \mathbf{f}(\Delta t_i)||/\epsilon_{ref} = O(\Delta t^p) \tag{7.10}$$

where $\mathbf{f}(\Delta t_i)$ is a numerical solution generated using time step size Δt_i, and the convergence rate p is the order of time accuracy. The normalization factor ϵ_{ref} is the difference between the solutions of Δt_7 and Δt_8 obtained by the S1 scheme,

$$\epsilon_{ref} = ||\mathbf{f}_{S1}(\Delta t_8) - \mathbf{f}_{S1}(\Delta t_7)|| \tag{7.11}$$

The factor ϵ_{ref} is chosen so that the errors of S1 scheme at the largest time step size are non-dimensionalized to be unity.

The convergence rates of displacement, temperature, aerodynamic pressure and heat flux are shown in Fig. 7.17. The results agree with theoretical prediction and the fluid, structural, and thermal solutions all display second-order time accuracy. While the two schemes have the same order of time accuracy, the S2 scheme has lower error in the numerical solution compared with that of S1 scheme. In particular, using the same time step size, the errors of the displacement, pressure, and heat flux of the S2 scheme are approximately one order of magnitude smaller than those of the S1 scheme. That indicates the S2

scheme converges at a larger time step compared with the S1 scheme. The faster convergence of the S2 scheme is attributed to its higher order energy accuracy, that smaller error is introduced into the numerical solution at every time step. This illustrates the superiority of the S2 scheme over the S1 scheme in terms of accuracy and convergence rate. One can therefore speculate that the S2 scheme may produce more accurate results for long-time-scale simulations than the S1 scheme. In the rest of this thesis, the S2 scheme is used as the loosely-coupled scheme for transient aerothermoelastic simulations.

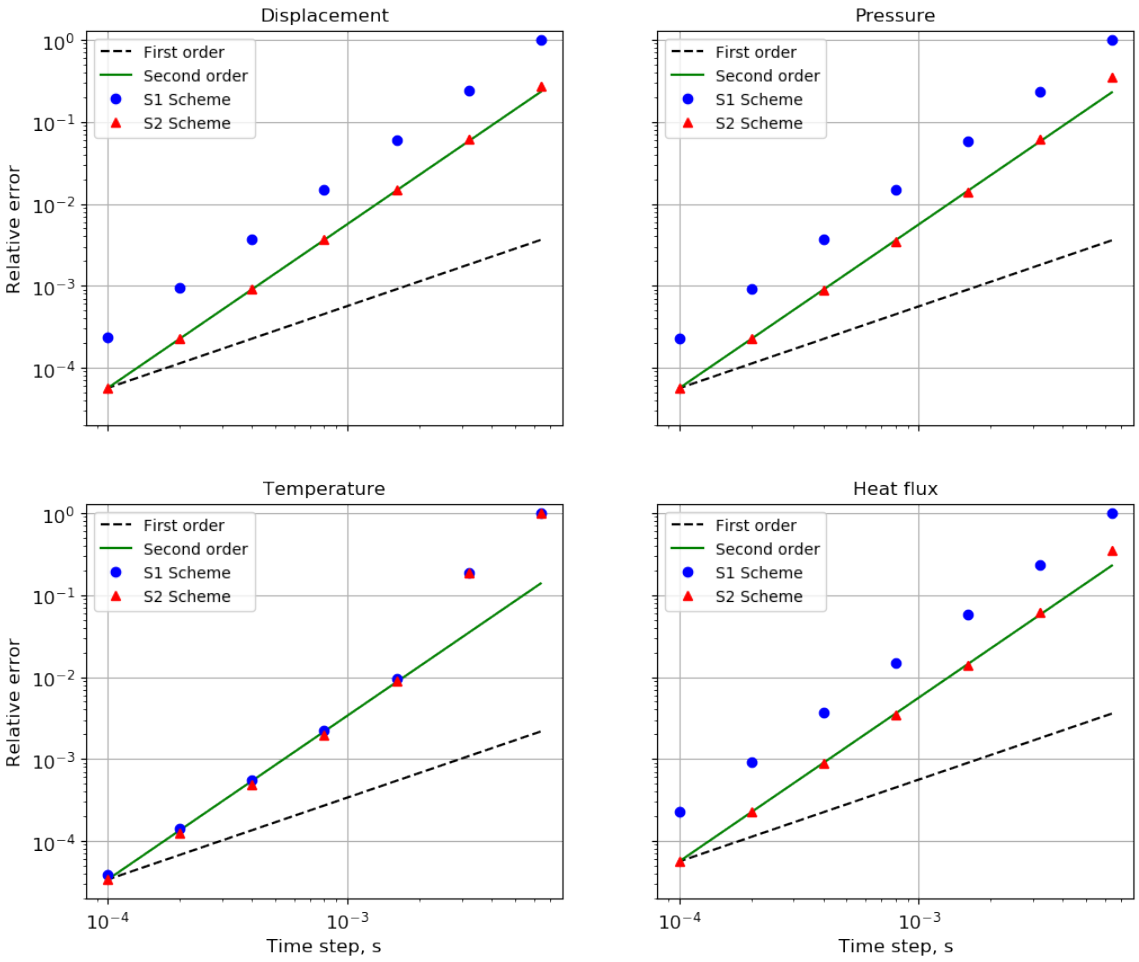

Figure 7.17: Convergence rate of the S1 and S2 schemes

7.3.3 The ROM-Based Aerothermoelastic Response

The ROM-based aerothermoelastic solutions are verified against the CFD-based solutions. The fluid ROM developed in Section 7.1.2 is employed. The aerothermoelastic responses are generated for two cases: (1) $M_\infty = 7.0, H = 20$km, $\xi = 1, 4$; (2) $M_\infty = 5.0, H = 30$km, $\xi = 1, 4$. Note that the flight conditions differ from the reference conditions of the ROM. In each case, the ROM-based transient and quasi-steady solutions are compared with the CFD-based transient solution. The transient and quasi-steady solutions are generated with time step sizes of 2.5ms and 25ms, respectively.

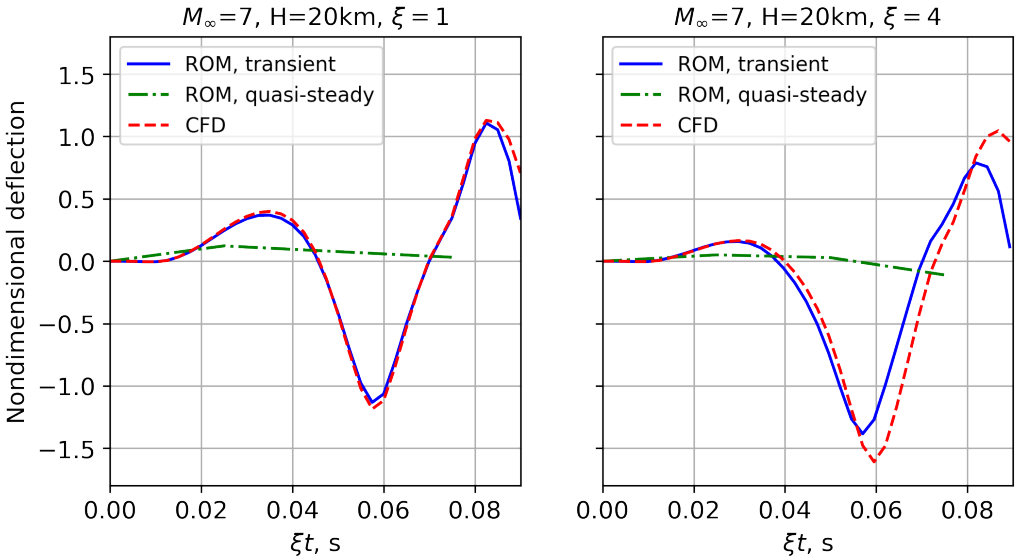

Figure 7.18: Structural response for $M_\infty = 7.0$, $H = 20$km

The results for case 1 are shown in Figs. 7.18-7.19. Figure 7.18 illustrates the structural response. The panel starts to flutter within 0.1s after the simulation starts for both cases of $\xi = 1$ and $\xi = 4$. The time responses of structural displacement from the CFD and transient ROM solutions agree well with each other up to the onset of flutter. The onset of flutter is identified by the quasi-steady ROM solution at the second time step and two more time steps are carried out before the simulation is terminated. The eigenvalue solution from the quasi-steady ROM-based response is shown in Fig. 7.19. The values of the frequency and

the damping are nondimensionalized by the natural frequency of the first structural mode. At the first time step, the damping of an aeroelastic mode becomes positive, indicating a flutter-type instability.

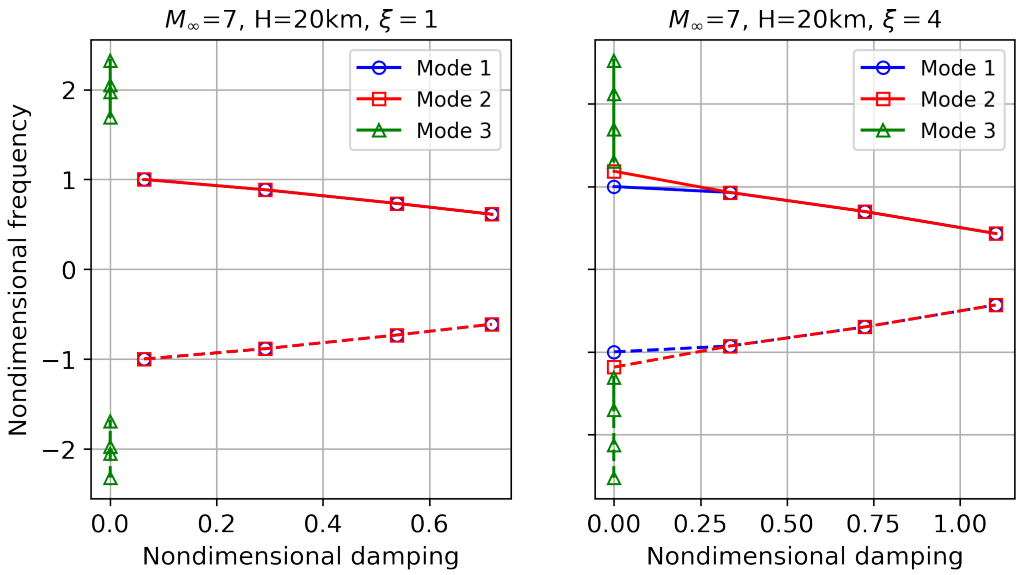

Figure 7.19: Eigenvalue solution on the complex plane for $M_\infty = 7.0$, $H = 20$km

The results for case 2 are shown in Figs. 7.20-7.21. Figure 7.20 illustrates the structural and thermal responses. The panel undergoes a thermally-driven response, which causes the panel to deform into the flow. The ROM-based transient and quasi-steady solutions agree with each other. In the case for $\xi = 4$, the panel deforms faster than that in the CFD solution. At the end of the simulation, the ROM-based response is 5% larger than the CFD-based response. The discrepancy is due to the difference in thermal solutions. Compared with the CFD solution, the heat flux in the ROM solution is 10% higher, producing a faster increase in the panel temperature, and larger thermal force in the structure, causing a larger deformation. The eigenvalue solution is shown in Fig. 7.21. The frequencies of all aeroelastic modes are positive and the dampings are zero, indicating that the panel stays stable throughout the simulation.

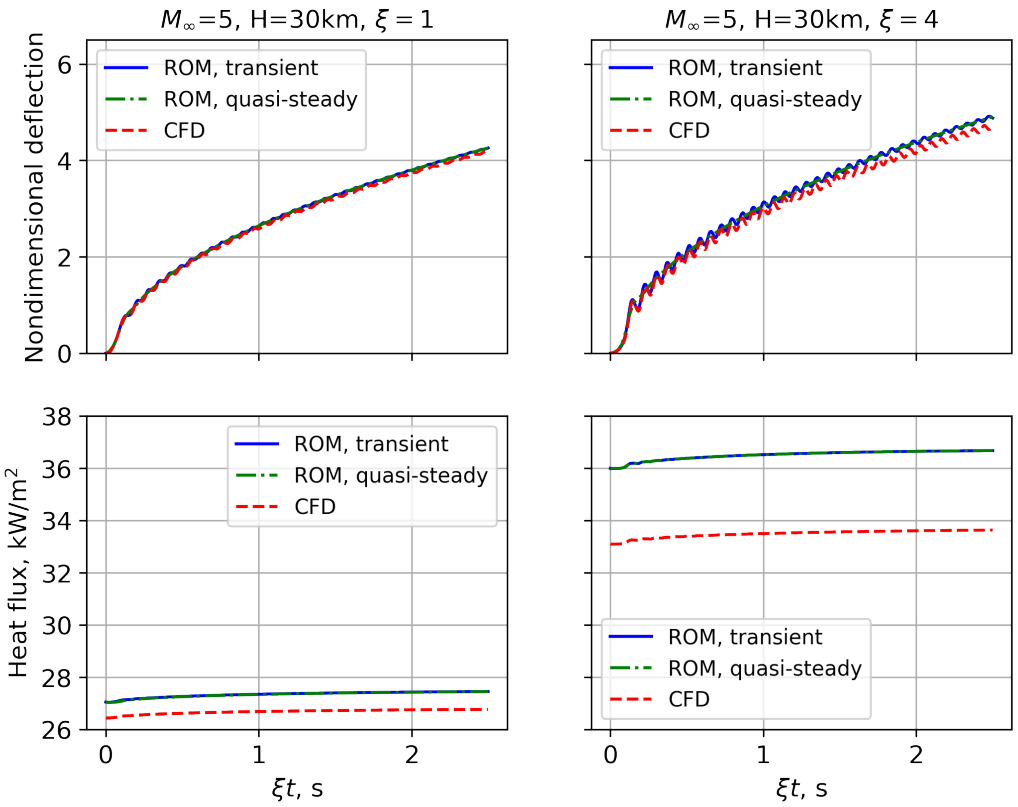

Figure 7.20: Structural and thermal responses for $M_\infty = 5.0$, $H = 30$km

The results for cases 1 and 2 demonstrate: (1) the transient aerothermoelastic response is approximated well by the quasi-steady response before the onset of instability, and (2) the aerothermoelastic responses at different flight conditions and geometric scales can be generated using the same ROM using the correction and scaling technique. Furthermore, the quasi-steady aerothermoelastic response is generated efficiently using the tightly-coupled scheme with a time step size that is ten times larger than that in a conventional loosely-coupled scheme. The onset of aerothermoelastic instability is accurately captured by the linearized stability analysis.

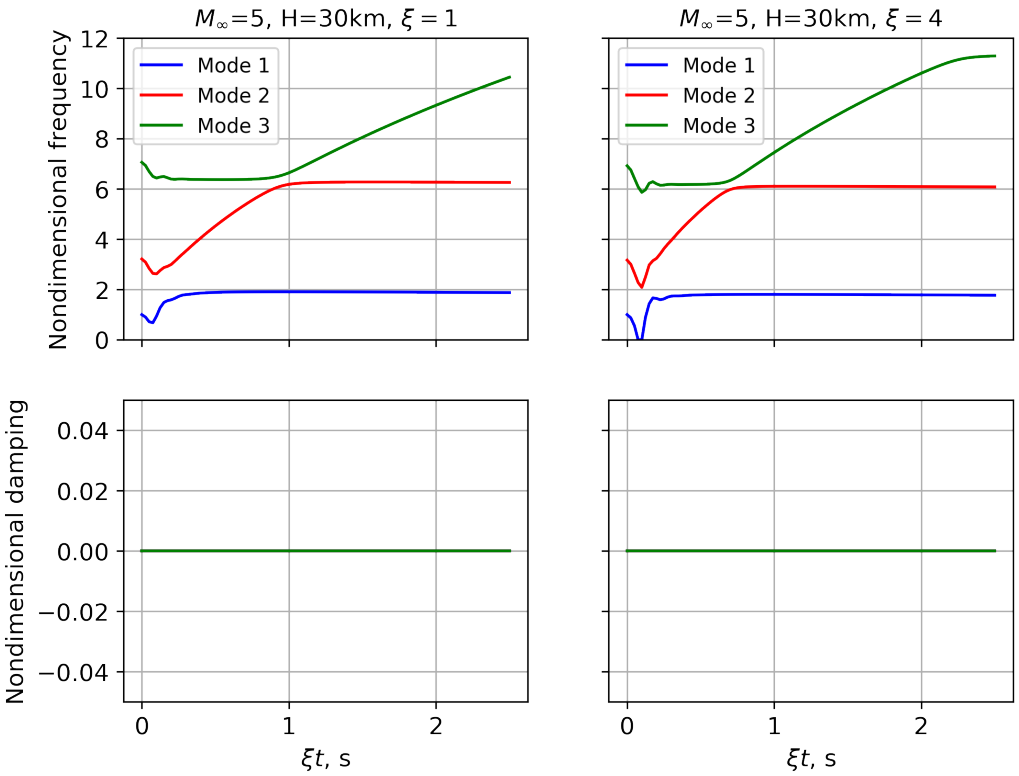

Figure 7.21: Eigenvalue solution for $M_\infty = 5.0$, $H = 30$km

CHAPTER 8

Results for Aerothermoelastic Behavior of Skin Panels

The HYPATE framework is used to examine the aerothermoelastic behavior of hypersonic skin panels so as to emphasize several important effects that have not been studied in detail by using a fully-coupled FSTI approach. First, the CFD-based aerothermoelastic simulation is employed to examine the effects of boundary layer thickness and aspect ratio on the responses of 2D and 3D panel configurations. Next, the ROM-based aerothermoelastic simulation is employed to examine the effects of flow orientation angle and material orthotropicity on the response of stiffened panel configurations, that may be used in practice on hypersonic vehicles that are currently in the design stages at various organizations.

8.1 Effect of Boundary Layer Thickness

8.1.1 Case Description

The effect of boundary layer thickness is examined using a 2D panel configuration, illustrated in Fig. 8.1. The flight condition is $M_\infty = 4.0$, $p_\infty = 2087.2\text{Pa}$, and $T_\infty = 266.7\text{K}$ that corresponds to $Re = 2.1 \times 10^6$. The boundary layer thickness on the panel is modified by adjusting wall length L_{le} in front of the panel. The four cases considered are shown in Table 8.1, so as to identify the influence of the boundary layer.

Table 8.1: Boundary layer thickness in the four cases

Case	L_{le}/a	δ/a
1	0.5	0.01
2	1.0	0.02
3	1.5	0.03
4	7.0	0.1

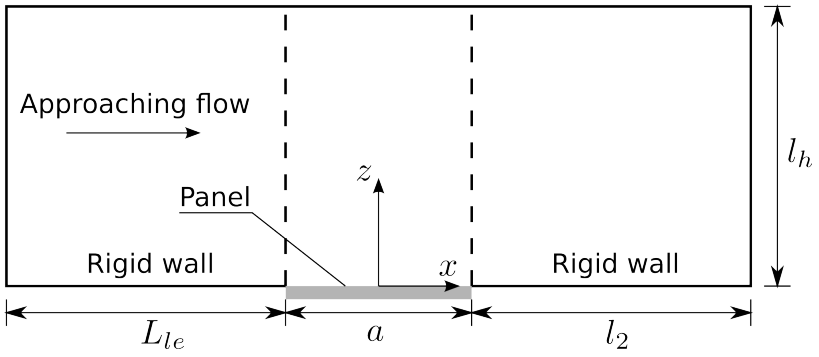

Figure 8.1: Geometrical configuration of a 2D panel for examining effect of boundary layer thickness

8.1.2 Aerothermoelastic Response

The aerothermoelastic responses of the 2D panel with different boundary layer thicknesses are shown in Fig. 8.2. The onset of aerothermoelastic instability is shown in Table 8.2. In the RANS result for $\delta/a = 0.01$, only the first 0.2 seconds of the panel response are presented, as the instability occurs immediately after the start of the simulation. The AM results correlate qualitatively well with the RANS results in cases 2 and 3, as the panel deforms into the flow and becomes unstable when snap-through occurs. However, the AM results fail to capture the immediate onset of instability in case 1 as well as the absence of instability in case 4.

Table 8.2: Time of onset for aerothermoelastic instability

Case	δ/a	RANS	AM
1	0.01	0.13s	1.98s
2	0.02	1.38s	2.02s
3	0.03	2.64s	2.04s
4	0.1	N/A	2.26s

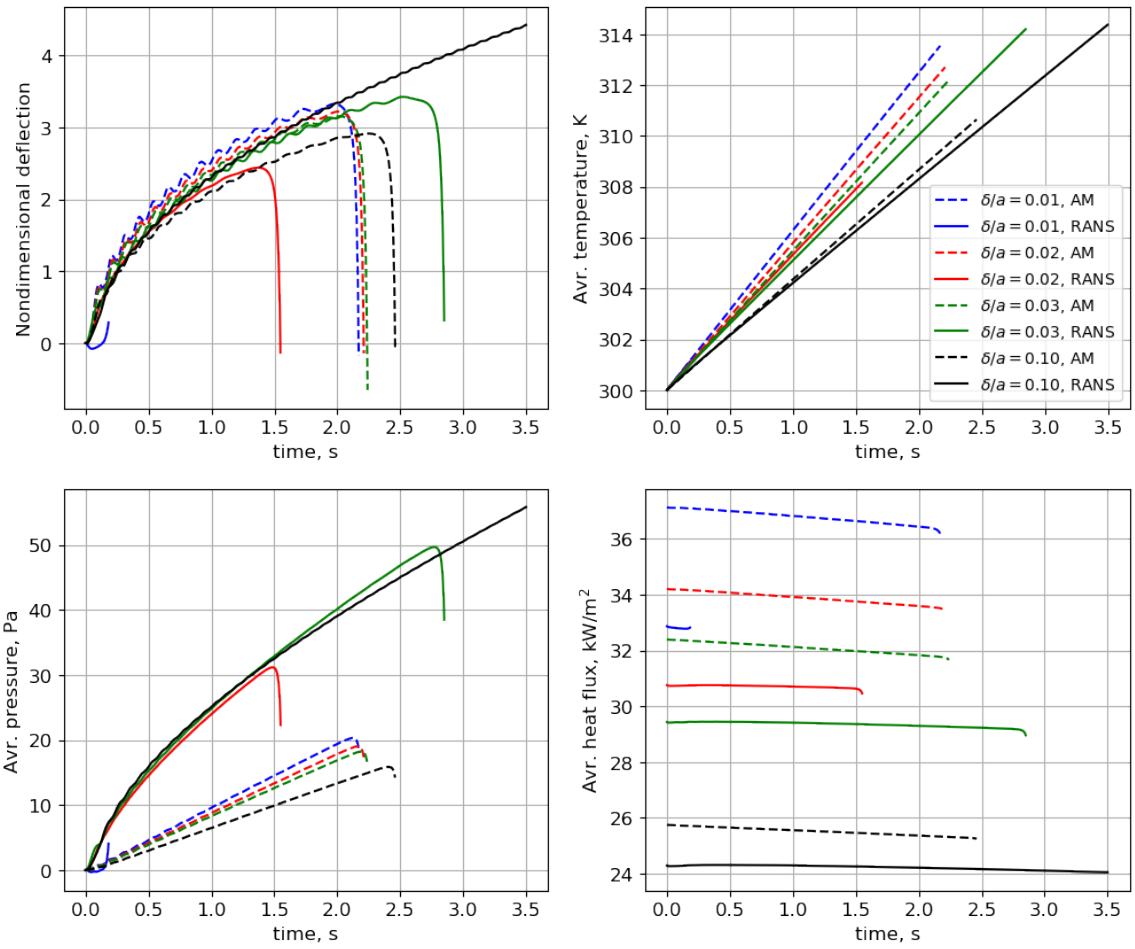

Figure 8.2: Effect of boundary layer thickness on the aerothermoelastic response of a 2D panel

The onset of snap-through type instability is controlled by two competing factors, the

temperature increase and the aerodynamic pressure. The increase in temperature causes the panel to deform into the flow, driving the panel away from snap-through. The pressure reduces the deflection, and causes snap-through when it is sufficiently large. Substantial differences exist in the temperature increase and the pressure between the RANS and AM results. The temperature increase is determined by the heat flux. As the boundary layer thickness δ/a increases from 0.01 to 0.1, the average heat flux drops by 30% in both the AM and RANS results. However, the drop in the heat flux in the AM results does not produce a dramatic change in the onset of the instability that is comparable to that is evident in the RANS results. Therefore, the difference between AM and RANS results is mainly due to the mismatch in the pressure distribution. This effect is due to the boundary layer that is neglected in the piston theory results.

The boundary layer effect on the pressure is illustrated in Figs. 8.3 and 8.4. Figure 8.3 depicts the pressure distributions over a panel with a prescribed deformation, so as to demonstrate the differences in the AM-based and RANS-based pressure distributions,

$$u_F/h = 3\cos(\pi x/a), \quad x/a \in [-0.5, 0.5] \tag{8.1}$$

The AM result, which represents the inviscid pressure distribution, is provided by third-order piston theory, Eq. (2.32b). The inviscid pressure distribution is characterized by

$$\begin{aligned}\frac{p^{PT3}(x)}{p_\infty} &= -\gamma K_1 \sin(\pi x/a) + \frac{\gamma(\gamma+1)}{4} K_1^2 \sin(\pi x/a)^2 \\ &\quad - \frac{\gamma(\gamma+1)}{12} K_1^3 \sin(\pi x/a)^3 \\ &= \underbrace{-\gamma K_1 \sin(\pi x/a)}_{\text{First order term}} + \underbrace{K_2 \cos(\pi x/a) + \cdots}_{\text{Higher-order terms}}\end{aligned} \tag{8.2}$$

where $K_1 = 3\pi M_\infty \frac{h}{a} \sim 10^{-1}$ and $K_2 = O(K_1^2)$. Equation (8.2) represents a qualitative analysis based on first-order piston theory, given by the first term of Eq. (8.2), and it is

linear in terms of $(u_{F,x}/h)$. However, this pressure distribution is modified by the additional "higher order terms" in Eq. (8.2). Note that the detailed Fourier series expansion of the higher-order terms are not given in detail. Therefore, the inviscid pressure distribution is dominated by the first term in Eq. (8.2) that is proportional to the slope of the deformed panel. The higher order nonlinear terms modify the dominant term by less than 5%.

The presence of boundary layer modifies the pressure distribution on the panel, as illustrated by Fig. 8.3, which shows the results for four different boundary layer thicknesses. Increasing the boundary layer thickness (δ/a) shifts the point where $c_p = 0$ towards the trailing edge. This trend can be approximated by a modified form of Eq. (8.2) given by

$$p(x) \approx p_I \cos(\pi x/a) + p_O \sin(\pi x/a) \tag{8.3}$$

which distinguishes between in-phase and out-of-phase components of the pressure, as explained next.

The pressure component p_I is proportional to the deformation and thus referred to as in-phase component. The pressure component p_O is proportional to the *slope* of the deformation and is referred to as out-of-phase component. In the RANS results, the boundary layer modifies the pressure distribution and produces a stronger in-phase pressure component when compared to the AM results. The values of p_I and p_O can be curve-fitted from the pressure distribution using Eq. 8.3. The impact of boundary layer effect on the pressure distribution is characterized by the *force ratio*

$$k_F = |p_I/p_O| \tag{8.4}$$

The legend in Fig. 8.3 provides the values of k_F associated with each boundary layer thickness, so as to quantify the effect of boundary layer thickness on the force ratio. When the boundary layer effect is absent, such as the AM case, the out-of-phase component

dominates the pressure distribution and force ratio is close to zero. Note that the force ratio in the AM case is nonzero due to the in-phase pressure component associated with the higher-order terms in the third-order piston theory, Eq. (2.30), producing a nonzero term. In the RANS case, the boundary layer introduces a stronger in-phase pressure component, which results in force ratios that are larger than those in the AM case.

Figure 8.4 illustrates the dependence of the force ratio on the increase in average temperature during aerothermoelastic response. The force ratio increases from 0.3 to 0.7 in cases 2-4 for the RANS results, and from 0.2 to 0.5 for the AM results. In case 1 for the RANS results, the force ratio increases rapidly and exceeds 4.0 at the start of the simulation. The results indicate that the force ratio depends on two factors. First, for both the AM and the RANS cases, larger thermally-driven structural deformation produces a larger force ratio. Second, in the RANS cases, the *growth rate* of the force ratio increases as the boundary layer thickness decreases. This trend is not present in the AM case, due to the absence of boundary layer.

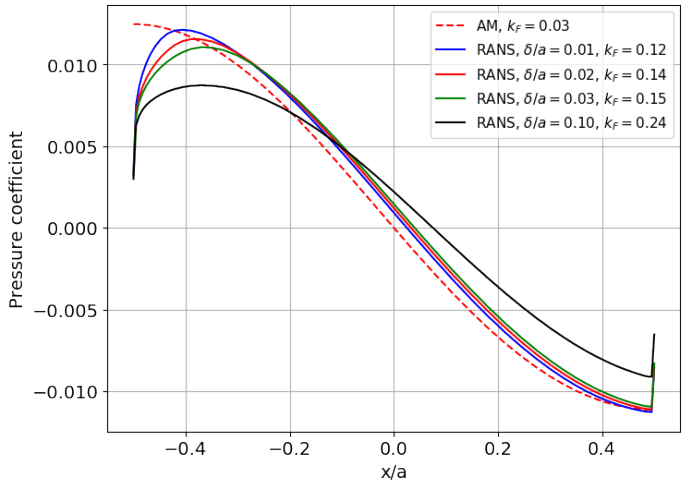

Figure 8.3: Effect of boundary layer thickness on pressure distribution for $M_\infty = 4.0$, $p_\infty = 2087.2\text{Pa}$, and $T_\infty = 266.7\text{K}$ with the fixed panel deformation given by Eq. (8.1)

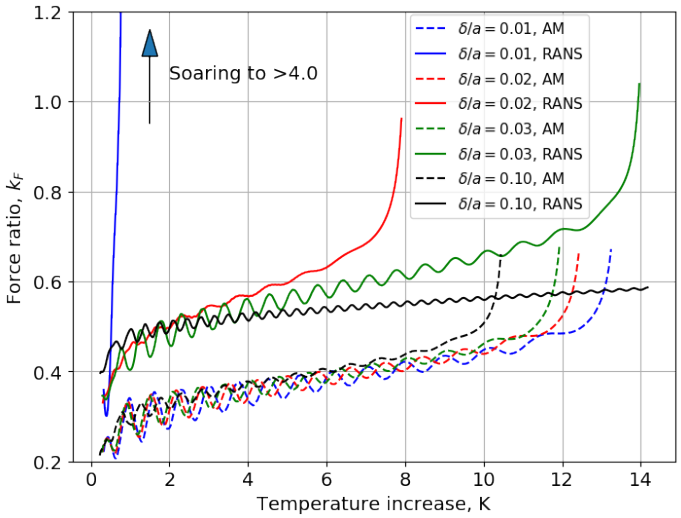

Figure 8.4: Variation in force ratio with different boundary layer thicknesses in the aerothermoelastic response of the 2D panel

8.1.3 A Simplified Model for Aerothermoelastic Stability

The LSA method is not applicable for determining the aerothermoelastic stability of a response generated by a CFD-based simulation. In this section, a simplified model representing the *static* thermoelastic response of a 2D panel is developed in order to capture the onset of its aerothermoelastic instability. The structural response of the simplified model only depends on the *prescribed* body temperature and pressure. The distributions of prescribed body temperature and pressure resemble the thermal and fluid solutions of the aerothermoelastic response. By decoupling the structural response from the thermal and fluid responses, the simplified model is used to examine the impact of average temperature increase and the force ratio of the pressure distribution on the aerothermoelastic stability of a 2D panel.

In the simplified model, the panel is simply-supported at its two ends and heated to a temperature that has a uniform distribution in the x-direction,

$$T(x,z) = T_w + \Delta T + k_z z \tag{8.5}$$

where ΔT and k_z are the average temperature increase and the temperature gradient along the thickness direction, respectively. The gradient is fixed to be $k_z = 120\mathrm{K/m}$, which is a typical value in the aerothermoelastic responses obtained in the previous section. Due to the temperature gradient, the panel deforms upward as ΔT increases.

A pressure distribution with a fixed force ratio is applied on the panel,

$$p(x) = k_F p_O \cos(\pi x/a) + p_O \sin(\pi x/a) \tag{8.6}$$

where $k_F p_O$ corresponds to the magnitude of the in-phase pressure component. The center of pressure is $x_{cp} = \frac{a}{\pi k_F}$, which is inversely proportional to k_F. The total force due to the pressure distribution is $F_{tot} = \frac{2a}{\pi} k_F p_O$. The pressure reduces the deflection of the panel.

For each combination of ΔT and k_F, there is a critical value of the out-of-phase pressure component, at which snap-through occurs and the panel deforms downward,

$$p_O = p_{cr}(\Delta T, k_F) \tag{8.7}$$

For given ΔT and k_F, the critical pressure p_{cr} is found by a grid search over a range of p_O. Figure 8.5 illustrates the cases for $k_F = 0.3$ and 0.7 at $\Delta T = 10\mathrm{K}$. For the case $k_F = 0.3$, the snap-through occurs at $p_{cr} = 332$Pa, or $F_{tot} = 63.41$N/m. For the case $k_F = 0.7$, the snap-through occurs at $p_{cr} = 213$Pa, or $F_{tot} = 94.92$N/m. As the force ratio increases, i.e. the center of pressure moves closer to the center of the panel, a larger total force is required to cause the snap-through. The net effect is that, the critical pressure decreases as the force ratio increases.

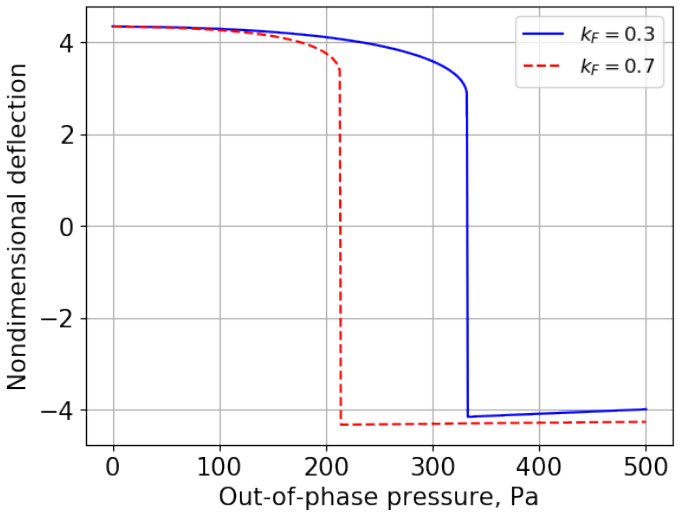

Figure 8.5: Snap-through of a 2D panel with a temperature increase of $10\mathrm{K}$ and a pressure distribution given by Eq. (8.6)

The aerothermoelastic response of the 2D panel is emulated by the static thermoelastic response of the simplified model using the following approach. First, for each time step of the aerothermoelastic response, the average temperature increase ΔT, the force ratio k_F and the out-of-phase pressure component p_O associated with the thermal and fluid solutions are computed. The quantities ΔT, k_F, and p_O define the magnitudes of the prescribed distributions of the body temperature and pressure in the the static thermoelastic response. Next, for each combination of ΔT and k_F, a critical pressure p_{cr} is computed using the simplified model Eq. (8.7). The snap-through type of aerothermoelastic instability of the 2D panel is expected to occur at the time step when the out-of-phase pressure component p_O exceeds p_{cr}.

The results for aerothermoelastic stability analysis using the simplified model are presented in Figs. 8.6 and 8.7. The AM cases are shown in Fig. 8.6. The solid lines represent the out-of-phase pressure component versus the average temperature increase. The dot-dashed lines represent the critical pressure of the simplified model with a *fixed* k_F versus the average temperature increase, which serves as an indicator of the stability of the aerother-

moelastic model. When the out-of-phase pressure component exceeds the critical pressure (i.e. above the dot-dashed line) the instability occurs. At the beginning of the aerothermoelastic simulation, $k_F = 0.2$. The out-of-phase pressure component in the aerothermoelastic response is below the critical pressure associated with $k_F = 0.2$ in the simplified static thermoelastic model. As the structure deforms due to increased temperature, k_F increases and the critical pressure decreases. Towards the onset of aerothermoelastic instability, k_F approaches 0.5. The instability occurs when the out-of-phase pressure component in the aerothermoelastic response reaches the critical pressure associated with $k_F = 0.5$ in the simplified static thermoelastic model.

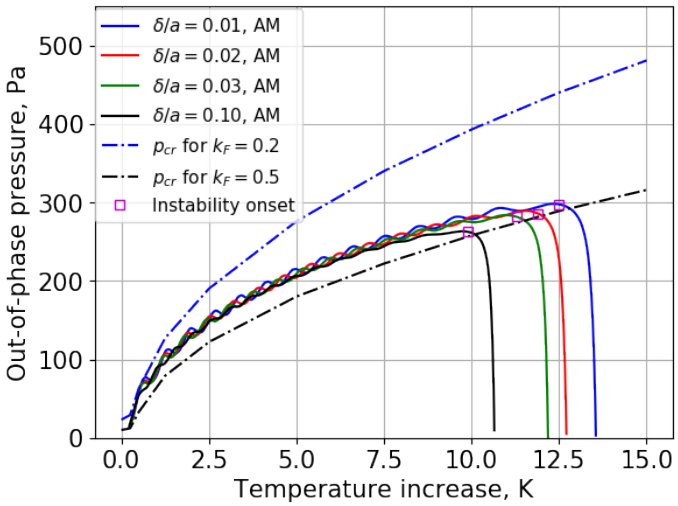

Figure 8.6: Out-of-phase pressure component from the AM-based aerothermoelastic results and the critical pressure from the static thermoelastic model

The RANS cases are shown in Figs. 8.7(a) and 8.7(b). The results of cases 2 and 3, shown in Fig. 8.7(a), are similar to the AM results. Both the force ratio and the out-of-phase component increase with the temperature. The out-of-phase component reaches the critical pressure for $k_F = 0.7$ when the instability occurs. The results for cases 1 and 4 are shown in Fig. 8.7(b). For case 1, the force ratio reaches 4.0 shortly after the start of the simulation. The out-of-phase component exceeds the critical pressure for $k_F = 4.0$, indicating the onset

of instability. For case 4, the force ratio is lower than 0.6 throughout the simulation, and the out-of-phase component never exceeds the critical pressure for $k_F = 0.6$. For $k_F < 0.6$, p_{cr} is even higher, and as a result, the panel remains stable in case 4.

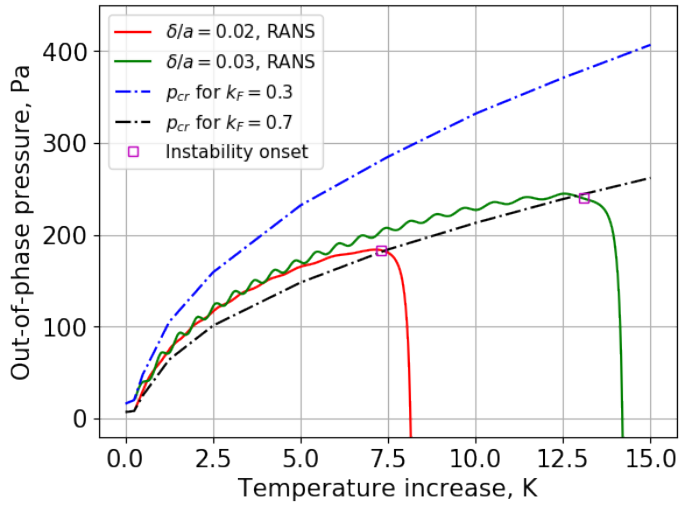

(a) Cases 2 and 3

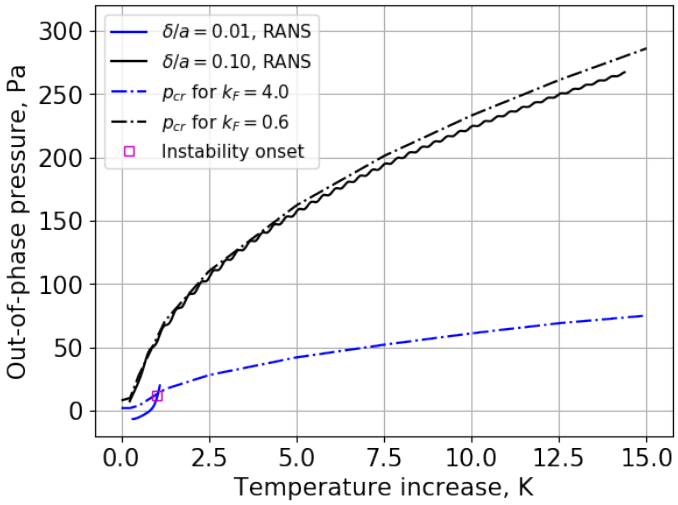

(b) Cases 1 and 4

Figure 8.7: Out-of-phase pressure component from the RANS-based aerothermoelastic results and the critical pressure from the static thermoelastic model

The analysis outlined above shows that the simplified model is useful for capturing the onset of the aerothermoelastic instability of the 2D panel, as well as explaining the differ-

ences between the aerothermoelastic responses of the AM and RANS cases. Specifically, three conclusions can be drawn from above discussion:

1. The aerothermoelastic instability that occurred in the 2D panel case is a snap-through of a heated structure. As the panel deforms due to the thermal stress, the force ratio of the pressure distribution increases, indicating that the snap-through type of instability is more likely to occur.
2. Increasing the boundary layer thickness suppresses the growth rate of the force ratio and delays the onset of snap-through. A sufficiently thick boundary layer *stabilizes* the panel.
3. An inviscid aerodynamic model such as the piston theory, which does not account for the boundary layer effect, is inaccurate for capturing the onset of aerothermoelastic instability, since it fails to capture the magnitude and the growth rate of the force ratio during the structural deformation.

8.2 Effect of Aspect Ratio

8.2.1 Case Description

The 2D panel is the same as the configuration in the previous section, as illustrated in Fig. 8.1. The 3D panel configuration is obtained by adding the third dimension to the 2D panel, resulting in a rectangular panel, illustrated in Fig. 8.8. The 2D and 3D panels share the same material properties, as shown in Table 7.5, and are both simply-supported along the edges. The flight conditions are $M_\infty = 4.0$, $p_\infty = 2087.2\text{Pa}$, and $T_\infty = 266.7\text{K}$, which corresponds to $Re = 2.1 \times 10^6$.

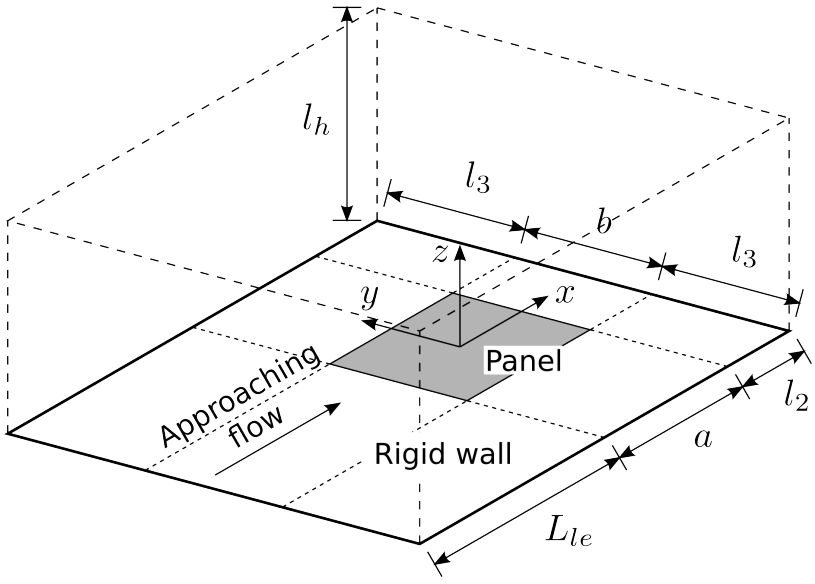

Figure 8.8: Geometrical configuration of a 3D panel for examining effect of aspect ratio

8.2.2 Aerothermoelastic response

The aerothermoelastic response of the 2D and 3D panels with $\delta/a = 0.02$ is depicted in Fig. 8.9. For comparison with the 2D case, the deformation, pressure, temperature and heat flux of the 3D cases are provided by the data extracted at the centerline $y = 0$. In the 2D and 3D cases, the AM results correlate qualitatively with the RANS results. Like the 2D case, the 3D panel deforms into the flow due to aerodynamic heating. However, the 2D panel becomes unstable within 2.5s, while the 3D panel remains stable up to the end of simulation, t =5.0s.

Further analysis of the structural deformation reveals fundamental differences between the 2D and 3D results, as shown in Fig. 8.10. The first two sinusoidal modal components are plotted as a function of the temperature. The two structural modes for the 3D case are,

$$u_{Fi}(x,y) = \sin\left[i\pi\left(\frac{x}{a}+\frac{1}{2}\right)\right]\cos\left(\frac{\pi y}{b}\right), \quad i = 1,2 \tag{8.8}$$

When the increase in the temperature is less than 1.4K, the modal components of 2D

and 3D results agree, indicating effect of the aspect ratio is negligible. When the temperature increase exceeds 1.4K, the amplitude of the second structural mode in the 3D case is much smaller than that for the 2D case. This change is due to the thermal stress in the spanwise direction in the 3D panel, which results in higher spanwise sinusoidal modes that are absent in the 2D case. When the new structual mode emerges, the pressure distribution becomes fundamentally different from that of the 2D case, as shown in Figs. 8.11 and 8.12. The in-phase pressure component in the 3D case grows much slower than that in the 2D case. As a consequence, the force ratio in 3D case drops from 0.5 to a value of 0.2, which is over 60% lower than that in the 2D case.

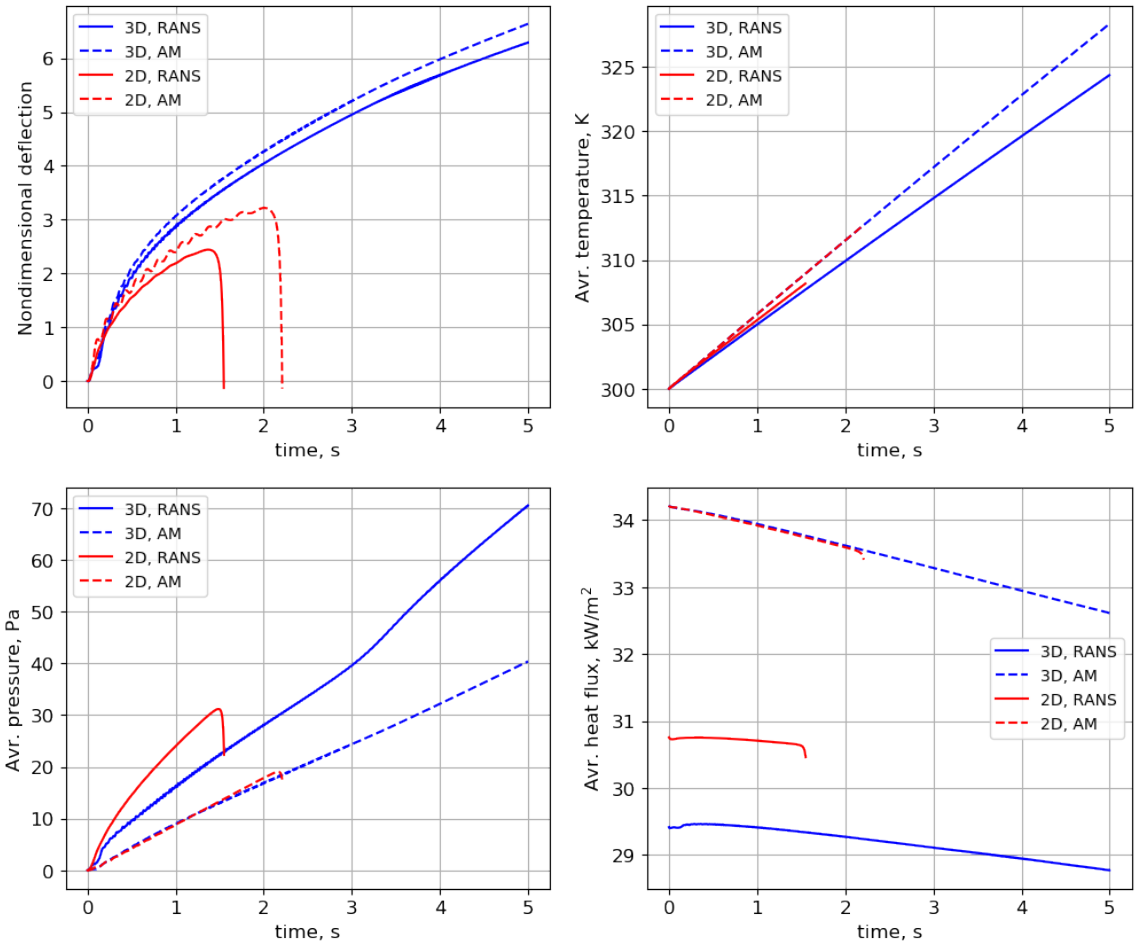

Figure 8.9: Aerothermoelastic responses of the 2D and 3D panels with $\delta/a = 0.02$

The structural stability is characterized by extending the static thermoelastic model to the 3D case. The temperature increase is the same as Eq. (8.5). The pressure distribution remains the same as Eq. (8.6), that is based on assuming that the pressure remains uniform in the spanwise direction. The assumption results in larger total load on the panel than that corresponding to the actual aerothermoelastic response, which implies that the critical pressure computed in this manner is conservative. The comparison between the out-of-phase pressure and the critical pressure is depicted in Fig. 8.13. Throughout the whole simulation, the out-of-phase pressure is far below the critical value, indicating the panel is stable.

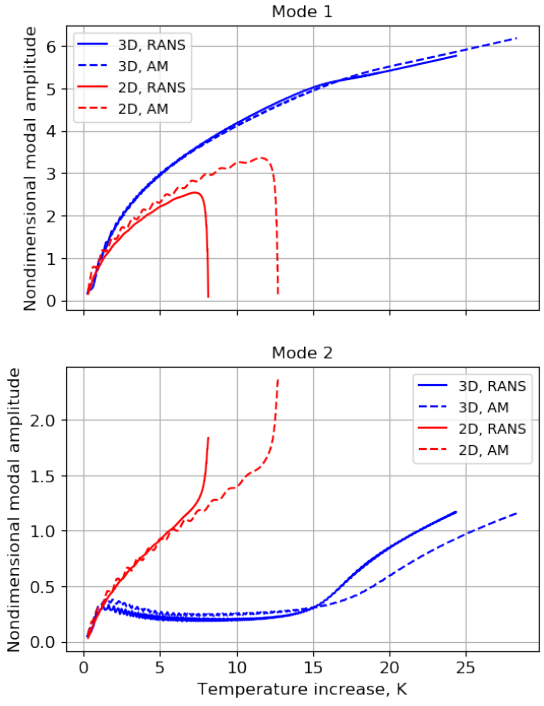

Figure 8.10: Modal responses of the 2D and 3D panels

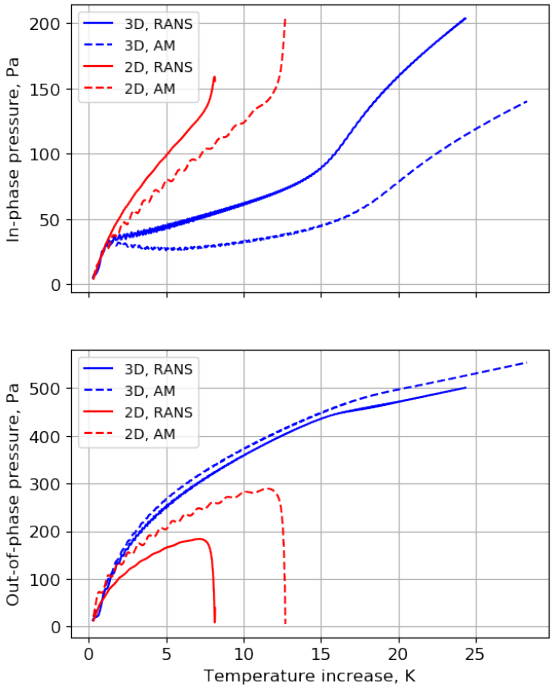

Figure 8.11: Pressure components of the 2D and 3D panels

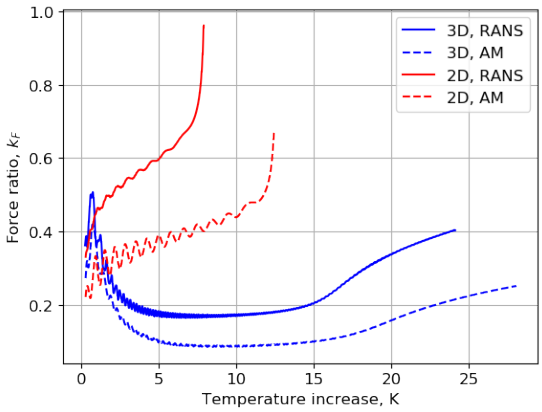

Figure 8.12: Variation in force ratio in the 2D and 3D results

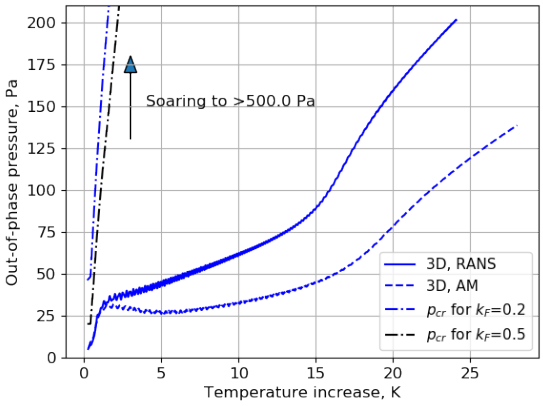

Figure 8.13: Critical pressure in the 3D RANS results

8.3 Combined Effects of Flow Orientation and Orthotropicity

8.3.1 Case Description

The panel configuration is adapted from the stiffened skin panel of a generic hypersonic vehicle studied in Ref. [2], as illustrated by Fig. 8.14. The panel is assumed to be square. Its dimensions are $1\mathrm{m} \times 1\mathrm{m}$ and it is simply supported along its edges. The panel is a thin metal sheet having a thickness of 1.5 mm reinforced by stiffeners having a height of 12 mm. The geometry of the stiffeners is illustrated in Fig. 8.15 and can be varied according to the parameters listed in Table 8.3. To examine the effect of panel orthotropicity, three types of stiffener configurations are considered, as shown in Fig. 8.15. In the first case, the metal sheet is stiffened by an orthogrid. The orthogrid has evenly spaced stiffeners distributed in both x- and y-directions. In the second and third cases, the stiffeners are evenly distributed either in x- or y-direction, respectively. The sheet and stiffeners are made from Inconel 718. The material properties are temperature dependent, with a the maximum service (MS)

temperature is $T_{MS} = 1200°F$ (1195K) [9]. Using a safety factor of 1.4, it is assumed that the material starts to fail at $T_{\max} = T_{MS}/1.4 \approx 850\text{K}$. The material properties at room temperature ($T = 300K$) are shown in Table 8.4 [6]. The emissivity of the upper surface is assumed to be 0.85, and the bottom and the sides of the panel are insulated.

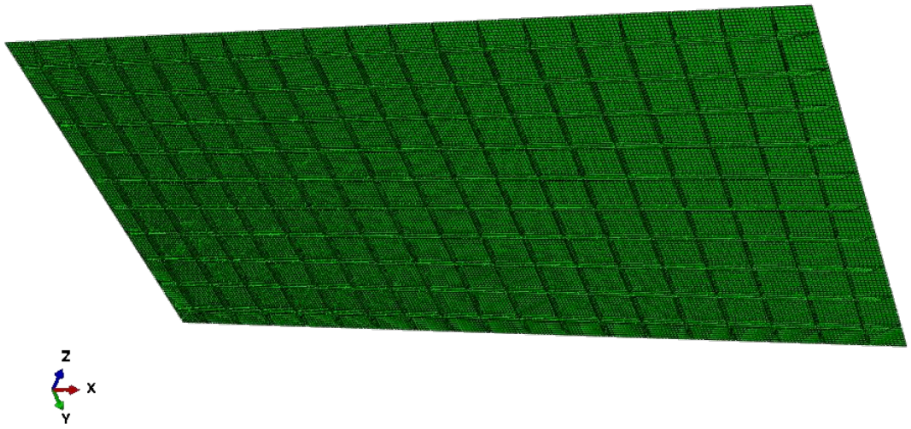

Figure 8.14: Stiffened panel configuration studied in Ref. [2]

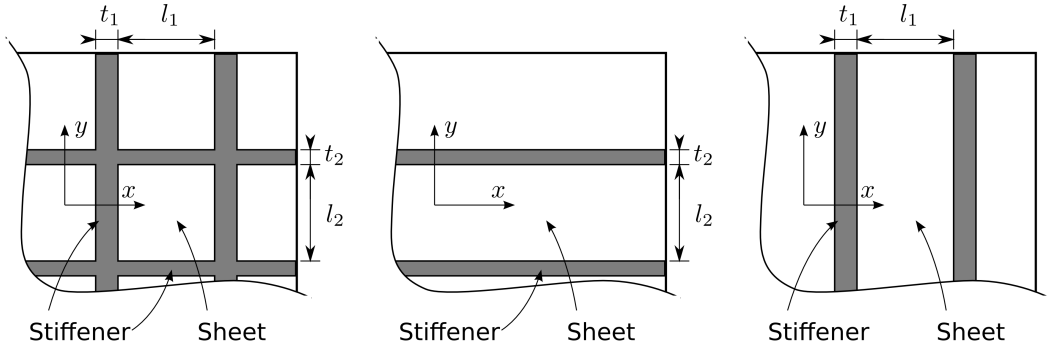

(a) Case 1 **(b) Case 2** **(c) Case 3**

Figure 8.15: Bottom view of the stiffened panel

Table 8.3: Geometrical parameters of the stiffeners

Case	t_1	l_1	t_2	l_2
1	2 mm	60 mm	2 mm	60 mm
2	4 mm	60 mm	0 mm	N/A
3	0 mm	N/A	4 mm	60 mm

Table 8.4: Material properties of Inconel 718 at $T = 300\text{K}$ [6]

ρ^s	E	ν	α	k^s	c_p^s
8220kg/m^3	204.0GPa	0.29	$1.237 \times 10^{-5}/\text{K}$	11.71W/mK	418.4J/kgK

8.3.2 Computational Models

8.3.2.1 Fluid Model

Three flow orientation angles are considered $\beta = 0, 15°, 30°$. For the case of $\beta = 15°, 30°$, the first 9 structural modes are used for ROM generation,

$$u_F(x)/h = \sum_{i=1}^{3}\sum_{j=1}^{3} a_{ij} \sin\left[i\pi\left(\frac{x}{a}+\frac{1}{2}\right)\right]\sin\left[j\pi\left(\frac{y}{b}+\frac{1}{2}\right)\right] \tag{8.9}$$

In the case for $\beta = 0°$, the structural response is symmetric about the centerline of the panel in the x-direction. Therefore, the 3 asymmetric modes in Eq. (8.9) are ignored, i.e. $a_{2j} = 0, j = 1, 2, 3$, and the remaining 6 symmetric modes are used for generating the ROM. The ranges of modal coordinates in the ROM samples are shown in Table 8.5. For all the ROM samples, the temperature is uniform with a range of $[200K, 1000K]$ and the flight conditions are $M_\infty = 6.0$ and $H = 25\text{km}$. For the case of $\beta = 0°$, 500 samples are generated for ROM training and 100 samples for ROM verification. The convergence plot is shown in Fig. 8.16. The ROM achieves convergence using 400 samples with the average NRMSE less than 0.5% for both the pressure and heat flux distributions. For the

Table 8.5: The ranges of sample parameters in the 3D ROM

β	$0°$	$15°$	$30°$
a_{11}	$[-0.5, 4.0]$	$[-0.5, 4.0]$	$[-0.5, 4.0]$
a_{12}	N/A	$[-0.5, 0.5]$	$[-0.5, 0.5]$
a_{13}	$[-0.35, 0.35]$	$[-0.5, 0.5]$	$[-0.5, 0.5]$
a_{21}	$[-0.75, 0.75]$	$[-0.75, 0.75]$	$[-0.75, 0.75]$
a_{22}	N/A	$[-0.3, 0.3]$	$[-0.3, 0.3]$
a_{23}	$[-0.35, 0.35]$	$[-0.3, 0.3]$	$[-0.3, 0.3]$
a_{31}	$[-0.75, 0.75]$	$[-0.75, 0.75]$	$[-0.75, 0.75]$
a_{32}	N/A	$[-0.3, 0.3]$	$[-0.3, 0.3]$
a_{33}	$[-0.3, 0.3]$	$[-0.3, 0.3]$	$[-0.3, 0.3]$

cases of $\beta = 15°, 30°$, 900 samples are generated for ROM training and 100 samples for ROM verification. The ROMs converge using 800 samples with the average NRMSE less than 1.5% for both the pressure and heat flux distributions.

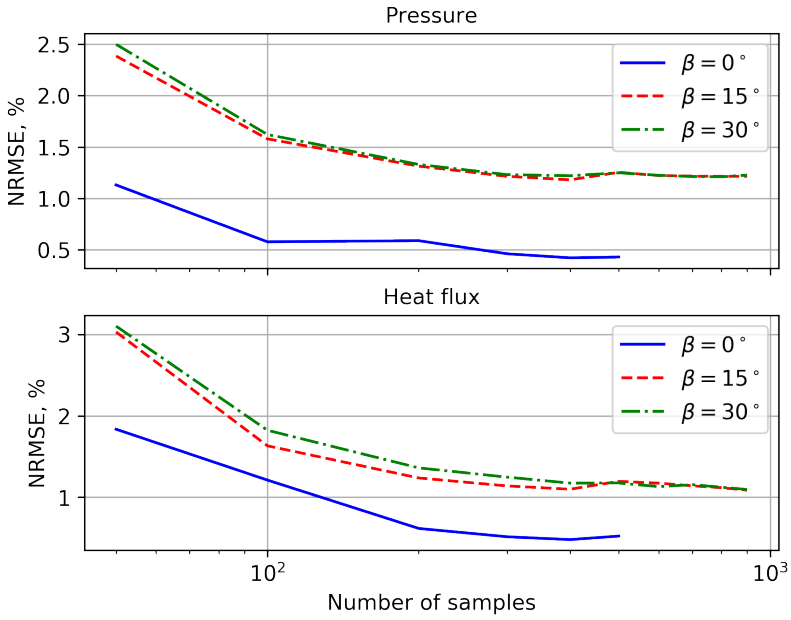

Figure 8.16: Convergence of the ROMs for the 3D panel

8.3.2.2 Structural Model

The thermal and structural properties of the orthogrid are incorporated in the model using the homogenization approach. Thus, the stiffeners can be treated as a homogenous

orthotropic layer in the composite panel analysis, as illustrated by Fig. 8.17. The homogenized layer is evenly divided into five laminae and the through-the-thickness distributions of temperature and thermal stress are resolved by a piecewise quadratic function using the finite element approach based on the layer-wise thermal lamination theory presented in Chapter 4.

The relation between the material properties of the stiffener and the homogenized layer are obtained in the following [203],

$$\begin{aligned}
&\rho^h = c_3\rho, \qquad c_p^h = c_p, \\
&E_i^h = c_i E, \qquad \nu_{3i}^h = \nu, \qquad G_{3i}^h = c_i G, \qquad k_i^h = c_i k, \qquad i = 1, 2 \\
&E_3^h = c_3 E, \qquad \nu_{12}^h = 0, \qquad G_{12}^h = 0, \qquad k_3^h = c_3 k \\
&\alpha_j^h = \alpha, \qquad j = 1, 2, 3
\end{aligned} \tag{8.10}$$

where,

$$c_1 = \frac{t_1}{t_1 + l_2}, \quad c_2 = \frac{t_2}{t_2 + l_1}, \quad c_3 = c_1 + c_2 \tag{8.11}$$

The orthotropicity of the homogenized layer is characterized by the ratio $R_{12} = \frac{E_1}{E_2}$. When $R_{12} = 1$, the layer is isotropic. When $R_{12} = 0$, $E_1 = 0$, and the panel is stiffened only in the y-direction. When $R_{12} = \infty$, $E_2 = 0$, i.e. the panel is stiffened only in the x-direction.

One of the objectives of the current study is to examine the impact of orthotropicity on the aerothermoelastic response of a skin panel. Therefore, homogenization of stiffeners is a simple and effective approach to obtaining orthotropic material properties with tunable parameters, such as stiffener properties and geometry. A thermally-loaded stiffened panel is known to have nonlinear behavior, such as local buckling, that cannot be captured by the homogenization approach [23]. To capture these nonlinear behaviors, a finite element analysis of the detailed stiffened panel structure has to be employed. However, this is not within the scope of the current study.

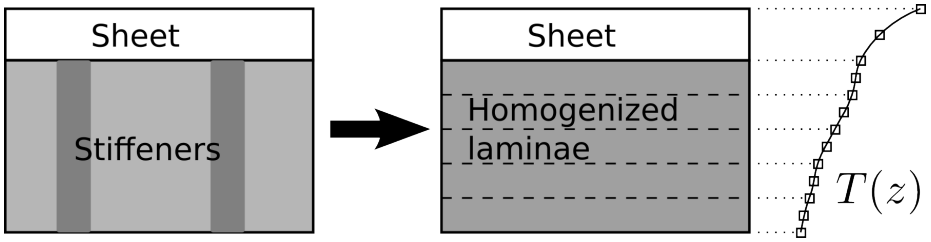

Figure 8.17: Homogenization of stiffeners

8.3.3 Typical Aerothermoelastic Response

First, the aerothermoelastic response for $\beta = 30°$, $R_{12} = \infty$, $M_\infty = 6.0$, $H = 25$km is examined. The response is divided into two stages: (1) the transient response in $t = 0 \sim 5$s with a time step size of $\Delta t = 0.001$s, and the quasi-steady response in $t = 5 \sim 100$s with a time step size of $\Delta t = 0.2$s.

8.3.3.1 Initial Transient Response

In the first stage, an unsteady heat conduction process occurs in the panel, as illustrated in Fig. 8.18a. The surface temperature of the panel increase rapidly due to aerodynamic heating while the temperature at the bottom of the panel is almost constant due to the low thermal conductivity of the stiffener layer. Different rates of temperature elevation in the thickness direction result in a rapid increase in the temperature gradient in the through-the-thickness direction of the panel, leading to a strong thermal force that drives the unsteady structural response.

The nondimensional center deflection of the panel is illustrated in Fig. 8.18b and four snapshots of the panel deformation are illustrated in Fig. 8.19. Initially, the panel is thermally buckled and the center portion of the panel deforms *out of* the flow. Due to the material orthotropicity, the deformation in the spanwise direction experiences a wavy pattern that is more noticeable than that in the streamwise direction. After a snap-through occurring at $t = 1.28$s, the entire panel deforms into the flow and the structural response

becomes quasi-steady. The snap-through results in a sudden change in both the aerodynamic heating and loading, as illustrated in Figs. 8.18c and 8.18d.

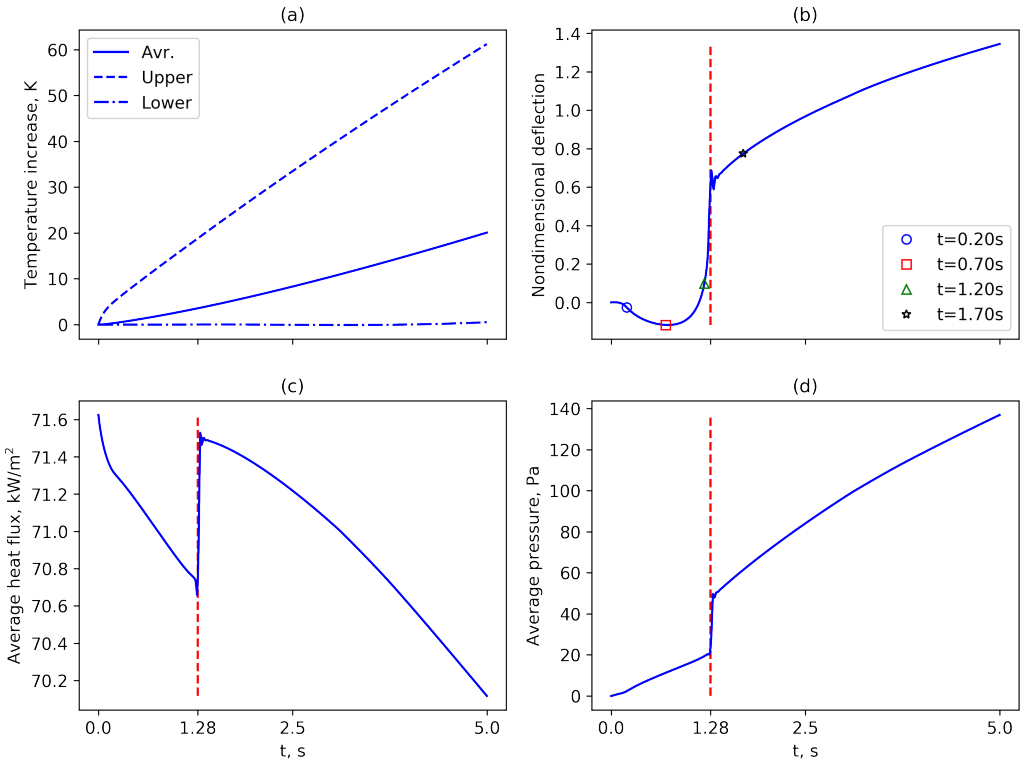

Figure 8.18: Transient aerothermoelastic response for $\beta = 30°$, $R_{12} = \infty$

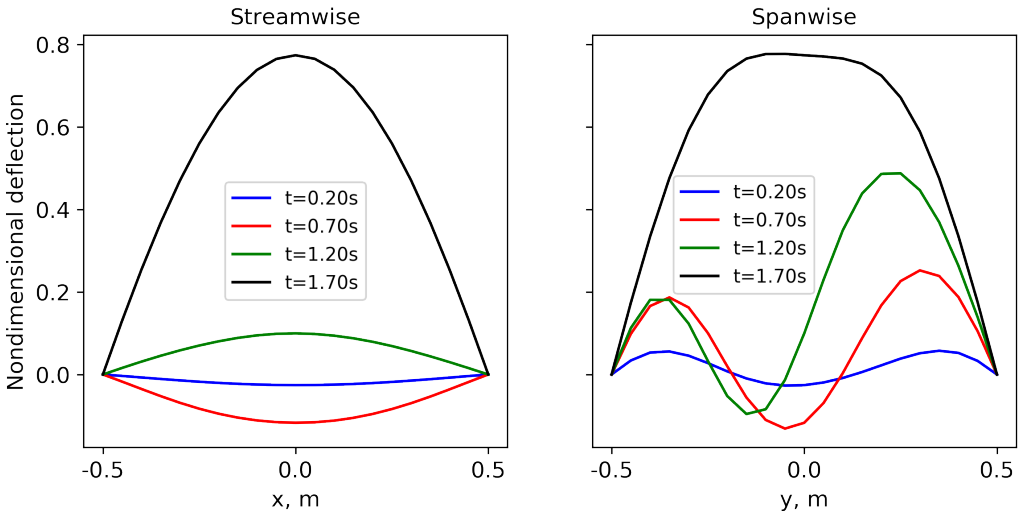

Figure 8.19: Comparison of streamwise and spanwise deflections at four time steps

8.3.3.2 Long-Term Quasi-Steady Response

The thermal and structural responses of the panel are shown in Fig. 8.20. In Figs. 8.20a and 8.20c, the heating rate decreases as the temperature increases, because the convective heating and radiative cooling at the upper surface approaches equilibrium. Initially, the upper surface temperature increases at a higher rate than the lower surface temperature due to the low thermal conductivity of the stiffener layer. The temperature difference between the upper and lower surfaces decreases as the upper surface temperature approaches equilibrium. Note that the *average* temperature remains below $T_{\max}$ of the material throughout the entire simulation. In Fig. 8.20b, the panel continues to deform into the flow due to aerodynamic heating and the deformation slows down as the panel approaches equilibrium temperature. The average pressure on the panel surface gradually increases as the panel deforms into the flow, as shown in Fig. 8.20d.

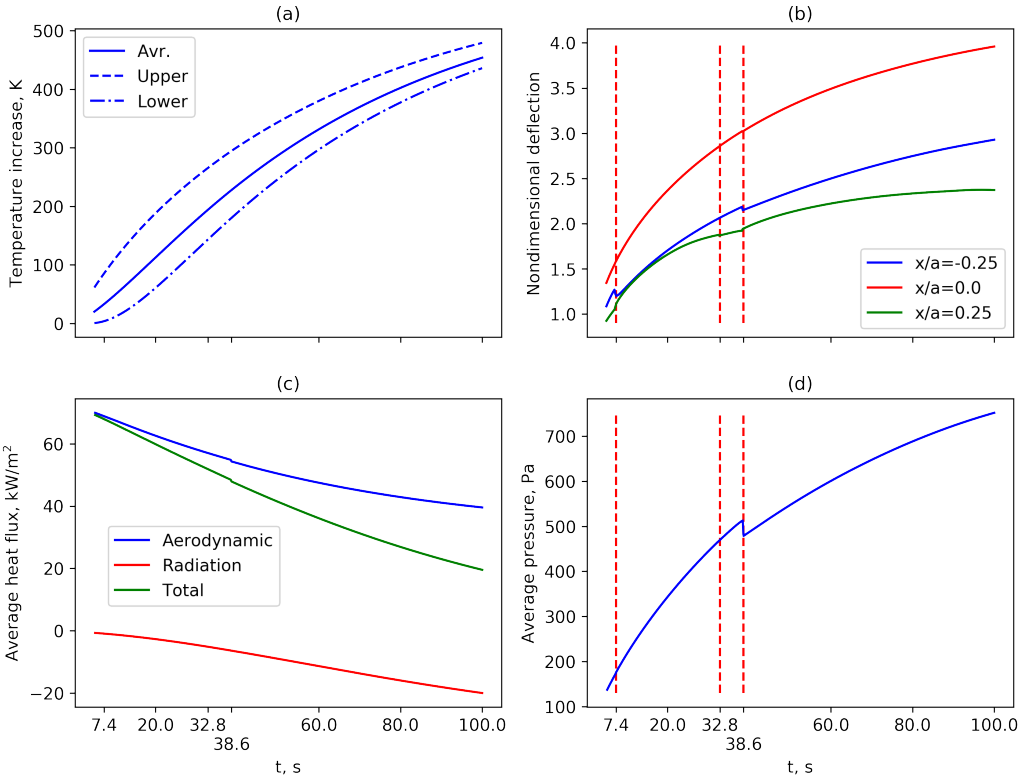

Figure 8.20: Quasi-steady aerothermoelastic response for $\beta = 30°$, $R_{12} = \infty$

The panel undergoes *non-smooth* deformation at three time steps, as indicated by the dashed red lines in Fig. 8.20b. The stability of the panel is examined using the LSA method, shown in Fig. 8.21. During most of the simulation, the frequencies of the aeroelastic modes are positive and the dampings remain zero, indicating that the panel is dynamically stable. At the three time steps associated with the non-smooth deformation, the frequency of the first mode becomes zero and the damping becomes positive. Therefore, the non-smooth deformation is a result of divergence, or snap-through.

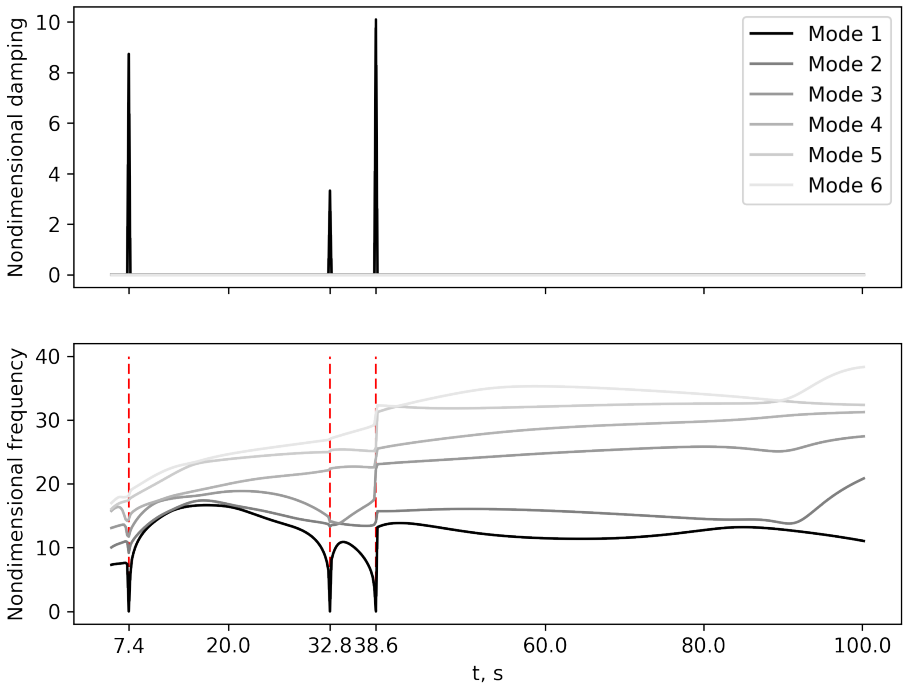

Figure 8.21: Eigenvalues of linearized stability analysis

Further analysis indicates that snap-through is a local instability that does not cause a deterioration in the aerothermoelastic stability of the panel. The snap-through at $t = 38.2$s is examined further. The transient aerothermoelastic simulation is restarted using the quasi-steady aerothermoelastic solutions before the onset of snap-through. The transient and quasi-steady structural responses of the panel during the snap-through are compared in Fig. 8.22(a). The snap-through at $t = 38.3$s triggers oscillation in the panel. However,

amplitudes of the oscillation are decreasing, indicating that the panel is dynamically stable. The average trend of the transient response is well captured by the quasi-steady response. The location of the snap-through is illustrated in Fig. 8.22(b). Unlike the snap-through at $t = 1.28\text{s}$ during the initial response, which occurs on the entire panel, the snap-through at $t = 38.2\text{s}$ occurs locally in Quadrant 1 of the panel (see Fig. 7.9 for definition of quadrants). The *localized* snap-through does not result in a divergence or flutter type of instability.

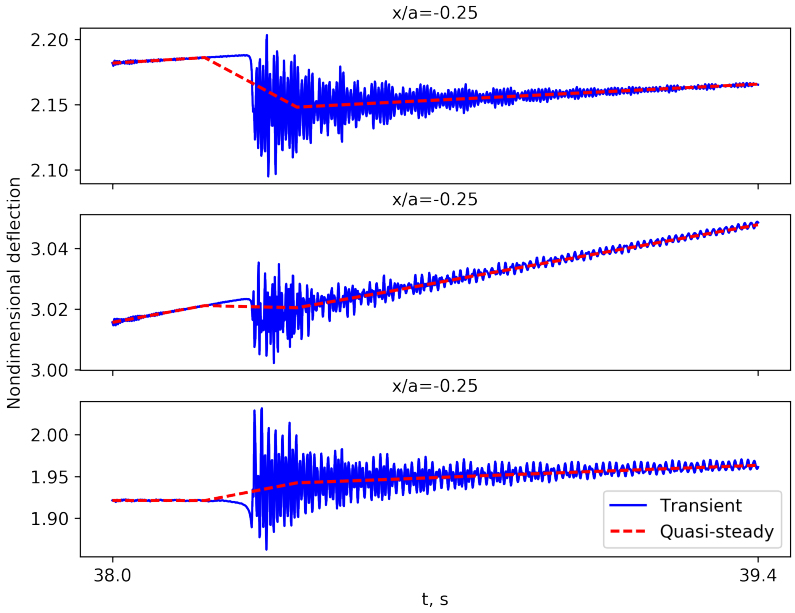

(a) Transient and quasi-steady responses

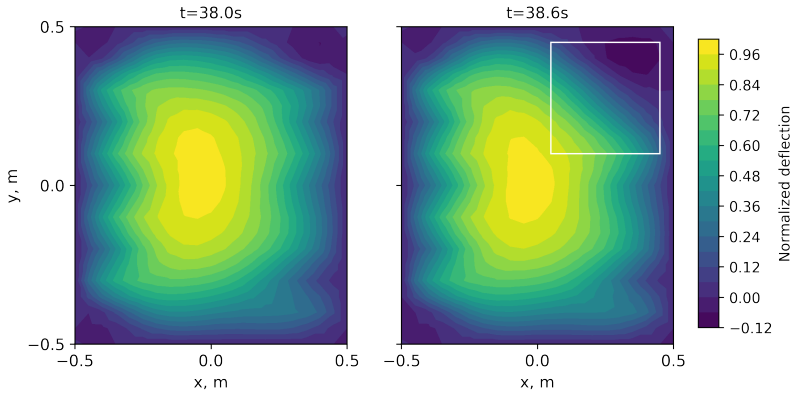

(b) Comparison of quasi-steady deformation

Figure 8.22: Snap-through during $t = 38.0\text{s} - 38.6\text{s}$

8.3.4 Aerothermoelastic Stability Boundary

Next, the effect of flow orientation angle and orthotropicity on the aerothermoelastic stability boundary is examined for $\beta = 0°, 15°, 30°$, and $R_{12} = 0, 1, \infty$ at flight conditions $M_\infty = 6$, $H = 25\text{km}$.

Account for material degradation with temperature, the aerothermoelastic stability boundary of the generic skin panel is defined as the time when the panel becomes dynamically unstable or the percentage of failed region exceeds 25%. The failed region is the region on the upper surface of the panel where the surface temperature exceeds the temperature of material failure $T_{\max} = 850\text{K}$. For all the cases, the panel fails due to material degradation. Localized snap-through does occur during the aerothermoelastic response, but it does not trigger unstable response of the panel.

8.3.4.1 Effect of Flow Orientation Angle

The aerothermoelastic response of an isotropic panel ($R_{12} = 1$) at different flow orientation angles $\beta = 0°, 15°, 30°$ are compared in Figs. 8.23-8.24. Figure 8.23 depicts the percentage of failed region on the surface of the panel for $\beta = 0°, 15°, 30°$. The panel reaches the temperature of material failure first in the case for $\beta = 0°$ at $t = 50\text{s}$. As β increases, the panel stays below the temperature of material failure for a longer time. However, at larger β, the area of failed region grows faster, reducing the aerothermoelastic stability boundary. At the end of the simulation, over 35% of the panel failed in the case for $\beta = 30°$, which is over 5% larger than that in the other two cases.

The aerothermoelastic responses of the skin panel are further examined in Fig. 8.24 at $t = 80\text{s}$, where the white contours in Fig. 8.24(b) illustrate the failed regions due to material degradation. In Fig. 8.24(a), the shape and amplitude of structural deformations in the three cases are similar. However, in Figs. 8.24(b) and 8.24(c), the heat flux distributions of the three cases, and thus the surface temperature distributions, are significantly different due to the varying flow orientation angles.

When $\beta = 0°$, the distributions of heat flux and surface temperature are symmetric about the x-axis. The aerodynamic heating is the most severe in Quadrants 2 and 3, i.e. the windward side of the panel. As a result, two temperature peaks of equal magnitude occur in Quadrants 2 and 3. The entire Quadrants 1 and 4 of the panel are on the leeward side and the temperature stays below $T_{\max}$. Increasing β to $15°$ results in stronger heat flux in Quadrant 2 of the panel. The distorted heat flux distribution leads to different amplitudes of the temperature peaks, as well as increased failed region areas in Quadrant 2. At $\beta = 30°$, the Quadrants 2 and 3 *as well as* Quadrant 1 of the panel are on the windward side of the panel and exposed to strong aerodynamic heating. The modified heat flux distribution results in a new failed region in Quadrant 1 and thereby increasing total failed region area of the panel.

To summarize, the structural deformation is insensitive to the change in flow orientation angle. However, at larger flow orientation angles, an increased portion of the panel is exposed to the approaching hypersonic flow. The increased exposure leads to stronger aerodynamic heating and higher surface temperature, and causes a reduction in the aerothermoelastic stability boundary of the panel.

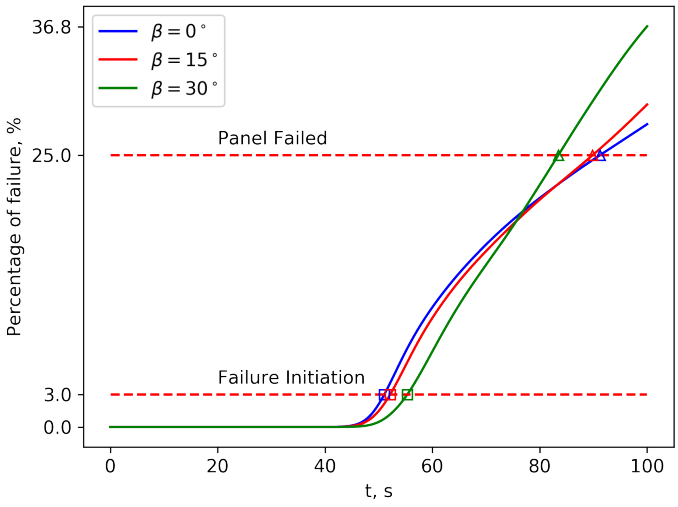

Figure 8.23: Percentage of upper surface area of failed region when $\beta = 0°$

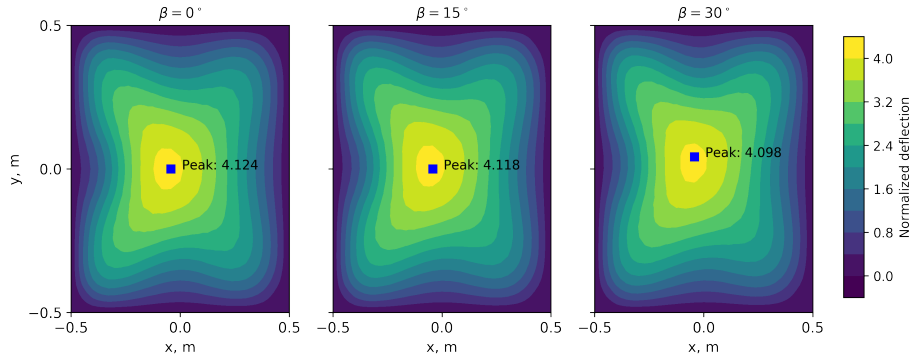

(a) Structural deformation

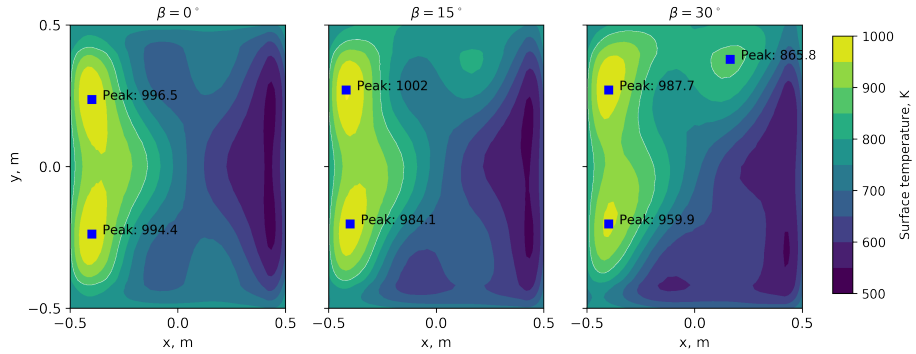

(b) Surface temperature

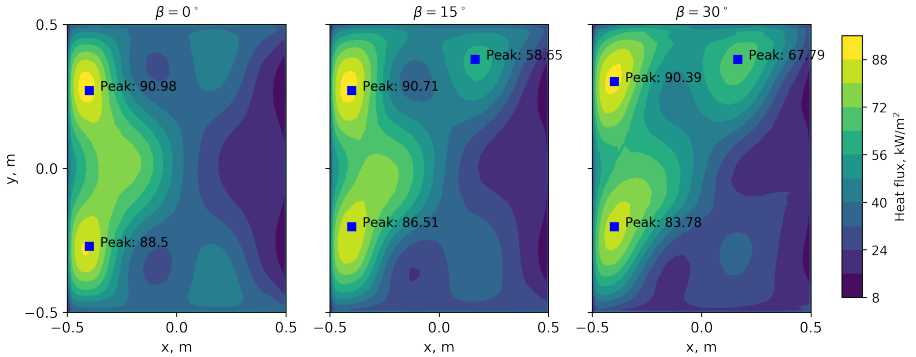

(c) Heat flux

Figure 8.24: Comparison of aerothermoelastic responses for $R_{12} = 1.0$ at $t = 80$s

8.3.4.2 Effect of Material Orthotropicity

The aerothermoelastic responses at $\beta = 0°$ of three panels of different material layups ($R_{12} = 0, 1, \infty$) are compared in Figs. 8.25-8.26. Figure 8.25 illustrates the percentage of

failed region on the surface of the panel for $R_{12} = 0, 1, \infty$. The failure is initiated first in the case for $R_{12} = 0$ at $t = 48s$. The initiation time of material failure is delayed as R_{12} increases. However, at larger R_{12}, the area of failed region grows faster, resulting in the reduction of aerothermoelastic stability boundary.

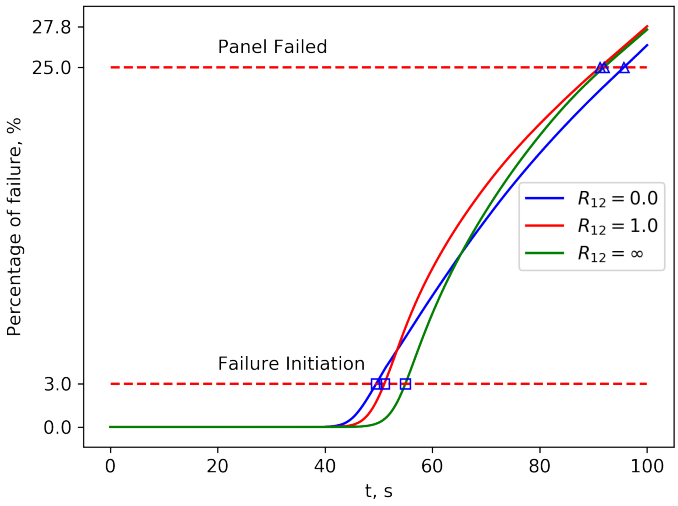

Figure 8.25: Percentage of upper surface area of failed region when $R_{12} = 1$

The aerothermoelastic response of the skin panel is examined further in Fig. 8.26, at $t = 80$s. The surface temperature distributions for all the three cases have a similar trend, illustrated in Fig. 8.26(a). The surface temperature distribution is symmetric about the x-axis, and two temperature peaks of equal magnitude occur in Quadrants 2 and 3 of the panel. The entire Quadrants 1 and 4 are on the leeward side and the temperature stays below $T_{\max}$. While the temperature distributions for the three cases are similar, different values of R_{12} result in significant differences in the structural deformation, as illustrated in Fig. 8.26(b). When $R_{12} = 1$, i.e. the panel is isotropic, the elevated temperature results in similar corrugation patterns in the x- and y-directions. When $R_{12} = 0$, the stiffness is maximized in the y-direction while the stiffness in the x-direction is almost negligible, resulting in a corrugation pattern with more waviness in the x-direction than in the y-direction. When $R_{12} = \infty$, on opposed to the case for $R_{12} = 0$, a wavy corrugation pattern

occurs in the y-direction due to the negligible stiffness in this direction.

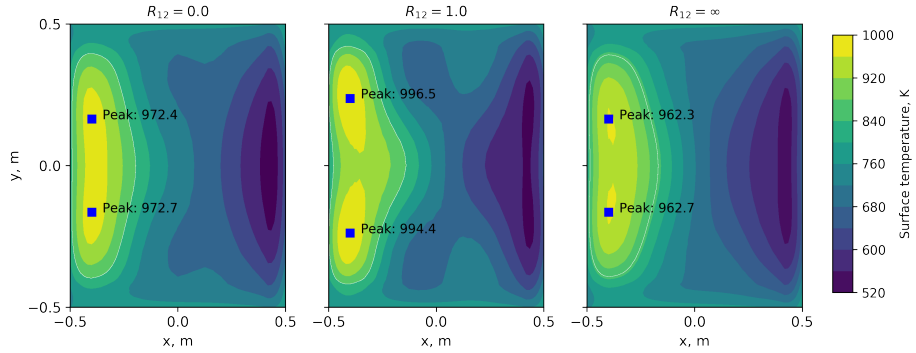

(a) Surface temperature

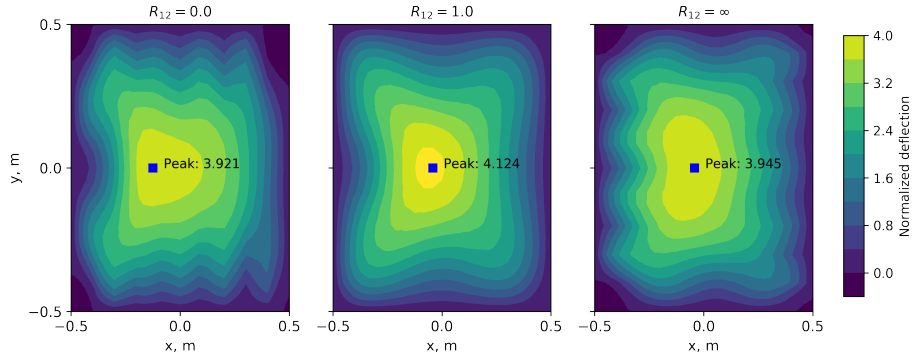

(b) Structural deformation

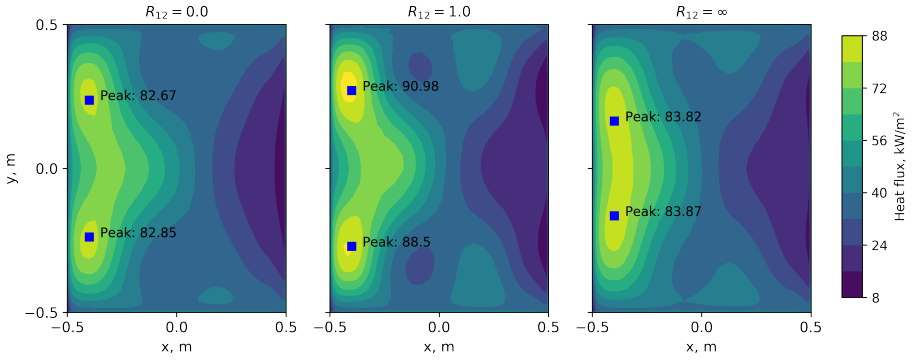

(c) Heat flux

Figure 8.26: Comparison of aerothermoelastic responses for $\beta = 0°$ at $t = 80$s

The different wavy corrugation patterns in the structural deformation result in different distributions of heat flux for the three cases, as illustrated in Fig. 8.26(c). For $R_{12} = 0, 1,$

the regions of high heat flux are concentrated near the two temperature peaks in Quadrants 2 and 3 of the panel. However, in the case for $R_{12} = \infty$, the wavy corrugation pattern in y-direction results in a region of high heat flux on the windward side of the panel that spans from Quadrant 2 to 3. The larger region of high heat flux results in faster increase of structural temperature and thus reduces the aerothermoelastic stability boundary of the panel.

8.3.4.3 Combined Effect of Flow Orientation Angle and Material Orthotropicity

The aerothermoelastic responses at $\beta = 0°, 15°, 30°$ are compared for the panels having different values of R_{12}. The percentage of failed region on the surface of the panel for all the nine cases are compared in Fig. 8.27. Recall that the results for $R_{12} = 1$ have been presented in Fig. 8.23, however they are included again in Fig. 8.27 for comparison.

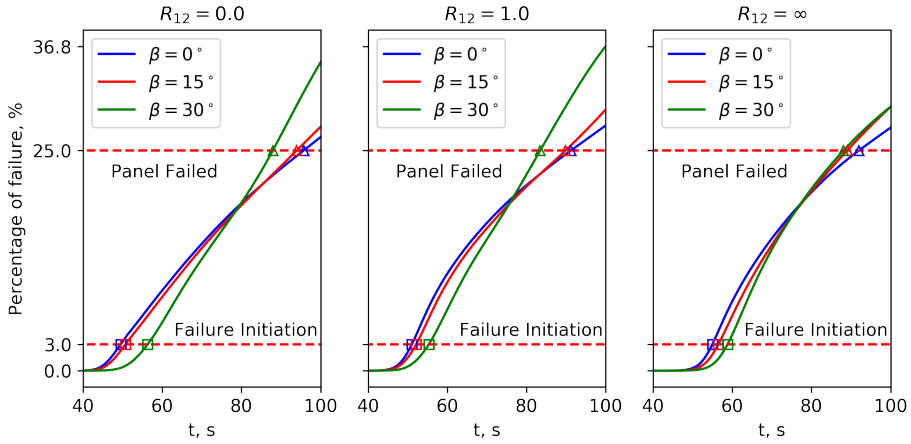

Figure 8.27: Percentage of upper surface area of failed region for combinations of β and R_{12}

The similar trend between the cases for $R_{12} = 0, 1, \infty$ up to the aerothermoelastic stability boundary indicates that the differences between the results for $\beta = 0°, 15°, 30°$ can be explained using the mechanism described in Section 8.3.4.1: The increased exposure to approaching flow at larger β leads to stronger aerodynamic heating on the windward side

of the panel and thus the decreased aerothermoelastic stability boundary. The quantitative differences between the results for $R_{12} = 0, 1, \infty$ are attributed to the effect of orthotropicity, as discussed in Section 8.3.4.2. A lower value of R_{12} results in earlier initiation of material failure, but extends the aerothermoelastic stability boundary.

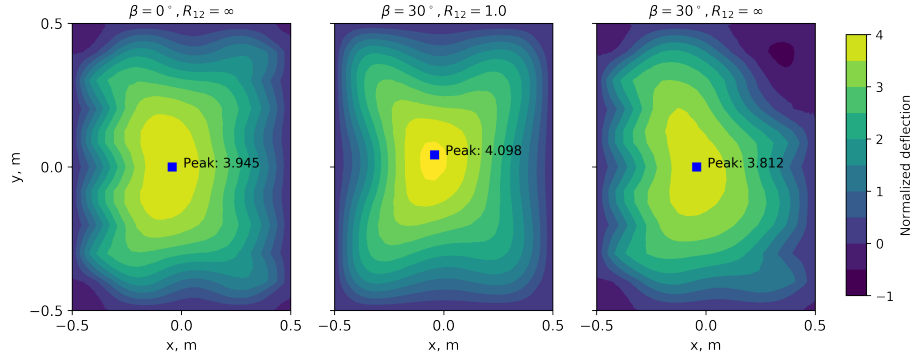

(a) Structural deformation

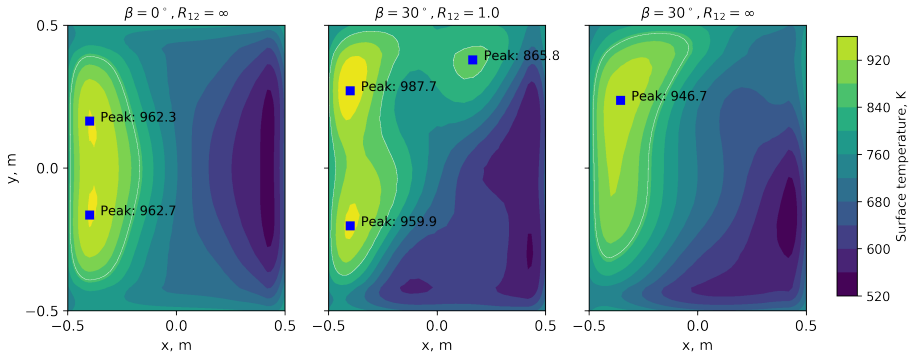

(b) Surface temperature

Figure 8.28: Comparison of aerothermoelastic responses for $\beta = 30°$ at $t = 80$s

In the cases for $R_{12} = 0, 1$, the final failed region for $\beta = 30°$ is approximately 30% larger than the failed regions for $\beta = 0°, 15°$. However, there is a distinctive trend of the result for $\beta = 30°$ and $R_{12} = \infty$ that the final failed region is approximately the same as the failed region for $\beta = 15°$. The distinctive result is explained by the *combined* effect of flow orientation angle and orthotropicity. The structural deformations and temperature distributions at $t = 80$s for $(\beta = 0°, R_{12} = \infty)$, $(\beta = 30°, R_{12} = 1)$ and $(\beta = 30°, R_{12} = \infty)$ are compared in Fig. 8.28. Compared with the structural deforma-

tion for ($\beta = 0^\circ, R_{12} = \infty$), a snap-through has occurred in the structural deformation for ($\beta = 30^\circ, R_{12} = \infty$), that significantly reduces the windward area in Quadrant 1 of the panel that is exposed to the approaching hypersonic flow. Comparing the temperature distributions for ($\beta = 30^\circ, R_{12} = 1$) and ($\beta = 30^\circ, R_{12} = \infty$), the decrease in the exposure area reduces the total heat load experienced by the panel and eliminates the temperature peak in Quadrant 1, which leads to the reduction of failed region on the panel.

8.4 Reduction of Computational Cost

The reduction in computer time due to the fluid ROM in the previous section is illustrated in Table 8.6. The computational costs are measured on a Dell® Precision 7000 Workstation using 5 Intel® Xeon X5650 2.67GHz processors.

For aerothermoelastic simulation, four cases are considered:

1. The CFD-based transient response using the LC scheme with $\Delta t = 1\text{ms}$.
2. The ROM-based transient response using the LC scheme with $\Delta t = 1\text{ms}$.
3. The ROM-based quasi-steady response using the TC scheme and the direct linear solver with $\Delta t = 0.2\text{s}$.
4. The ROM-based quasi-steady response using the TC scheme and the iterative linear solver with $\Delta t = 0.2\text{s}$.

The time step sizes for transient and quasi-steady responses are chosen based on the aeroelastic and aerothermal chracteristic times, respectively. It is impossible to complete the CFD-based transient aerothermoelastic solution for 100s on a workstation computer within a reasonable amount of time. Therefore, the computational cost of the CFD-based solution is estimated using the computational cost of the CFD-based simulation for 2s on the same workstation computer.

In case 2, the fluid solver is accelerated by the ROM by three orders of magnitude, resulting in a total reduction of computer time by a factor of $\sim$200. In case 3, the number

of time steps is reduced by a factor of 200 due to the increase in the time step size. However, due to the introduction of the stability solver and tightly-coupled structural solver, the computational cost per time step is increased by a factor of $\sim$20. Compared to case 2, the net reduction of computer time in case 3 is by a factor of less than 20. In case 4, using the more efficient iterative linear solver, the structural and stability solvers are accelerated by a factor of $\sim$8. As a result, compared to the CFD-based solution in case 1, the computational cost is reduced from several months to a few minutes and near-real-time aerothermoelastic simulation is enabled by the ROM-based tightly-coupled solver.

Table 8.6: Comparison of computational cost in aerothermoelastic simulation (* means extrapolation)

	CFD, LC	ROM, LC	ROM, TC	
			Direct	Iterative
Δt	1ms	1ms	0.2s	0.2s
Fluid	72s	30ms	33ms	33ms
Structural	145ms	145ms	1156ms	148ms
Thermal	134ms	134ms	187ms	187ms
Stability	N/A	N/A	1951ms	256ms
Cost	83.7 days*	8.58 hours	27.7 minutes	5.20 minutes
Acceleration	1	2.34×10^2	4.35×10^3	2.32×10^4

CHAPTER 9

Aerothermoelastic Scaling of Skin Panels

In this chapter, the effectiveness of two-pronged approach for generating numerical scaling laws is demonstrated using two cases. In the first case, the two-pronged approach is employed to generate the numerical scaling laws for the transient aeroelastic response of a uniformly heated panel. The aeroelastic case represents a simplified aerothermoelastic problem, for which the analytical scaling laws exist. The first case serves as a sanity check to demonstrate that the two-pronged approach can reproduce the analytical scaling laws via numerical optimization. In the second case, the two-pronged approach is used to develop aerothermoelastically scaled models for a generic panel representing skin of a hypersonic vehicle. This case illustrates the capability for generating numerical hypersonic ASL when considering wind tunnel and manufacturing constraints.

9.1 Scaling of Transient Aeroelastic Response

9.1.1 Problem Description

The "prototype" configuration is illustrated in Fig. 9.1. It consists of a simply-supported square panel with side length of 1 m and thickness of 2 mm. The flight conditions of the prototype are $M_\infty = 6.0$ and $p_\infty = 10^4 \text{Pa}$. The flow is aligned with the panel, i.e. the flow orientation angle is zero. Initially, the panel is uniformly heated up by $\Delta T = 1\text{K} \approx 2.425 T_{cr}$. The aerodynamics is assumed to be inviscid and full-order piston theory,

Eq. (2.30), is sufficient for the aeroelastic simulation. The simulation of the prototype is carried out using a time step size of 0.001s to capture the transient aeroelastic response of the panel. The prototype and model panels are made of two different materials Inconel 718 and Ti 6242, respectively, which makes the scaling problem more challenging. The material properties are assumed to be temperature *independent* and equal to the values at room temperature ($T = 300K$) as provided in Table 9.1. It is also assumed that the Mach numbers and heat capacity ratios associated with the prototype and the model are the same.

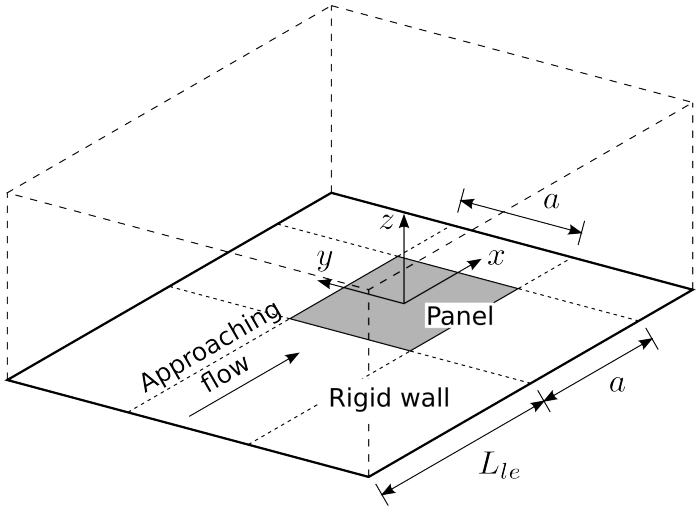

Figure 9.1: Geometrical configuration of a square panel for aeroelastic scaling

Table 9.1: Material properties of Inconel 718 and Ti 6242 for aeroelastic scaling

Material	ρ^s, $\mathrm{kg/m^3}$	E, GPa	ν	α, $\times 10^{-5}/\mathrm{K}$	k^s, $\mathrm{W/mK}$	c_p^s, $\mathrm{J/kgK}$
Inconel 718 [6]	8220	204.0	0.29	1.237	11.71	418.4
Ti 6242 [204]	4540	114.3	0.32	0.6975	6.937	459.4

9.1.2 Aeroelastic Scaling Laws

9.1.2.1 Analytical Similarity Parameters

Analytical aeroelastic scaling laws exist for a uniformly-heated thin isotropic plate with piston theory aerodynamics, involving the similarity parameters (pp. 85-88 of Ref. [49]),

$$\frac{\hat{h}}{\hat{L}}, \bar{\lambda}_F, \frac{\Delta\hat{T}\widehat{N}_{Tx}\hat{L}^2}{\widehat{D}_{xx}} \tag{9.1a}$$

$$\frac{\hat{I}\hat{L}^4}{\widehat{D}_{xx}\hat{t}^2} \tag{9.1b}$$

When the dimension of the scaled model L^m is given, the geometric scale ratio $\xi = \frac{L^p}{L^m}$, and the panel thickness, freestream pressure, and temperature increment associated with the scaled model are determined using Eq. (9.1a) as follows,

$$h^m = \frac{1}{\xi}h^p \tag{9.2a}$$

$$p_\infty^m = \xi^3 \frac{\widehat{D}_{xx}^m}{\widehat{D}_{xx}^p} p_\infty^p \tag{9.2b}$$

$$\Delta T^m = \xi^2 \frac{\widehat{D}_{xx}^m}{\widehat{D}_{xx}^p} \frac{\widehat{N}_{Tx}^p}{\widehat{N}_{Tx}^m} \Delta T^p \tag{9.2c}$$

The scaling factor for time is determined using Eq. (9.1b),

$$\Delta t^m = \frac{1}{\xi^2}\sqrt{\frac{\widehat{D}_{xx}^p}{\widehat{D}_{xx}^m}\frac{\hat{I}^m}{\hat{I}^p}}\Delta t^p \tag{9.3}$$

9.1.2.2 Numerical Scaling by Optimization

The numerical scaling laws of the aeroelastic problem are generated by finding the scaled models for different geometric scales. For each geometric scale, the model configuration is found by solving an SO problem. The objective is the difference between the nondimen-

sional structural responses of the prototype and the model, as in Eq. (6.4a),

$$J_u(\mathbf{d}; \{\mathbf{u}_i^m\}) = \sqrt{\sum_{i=1}^{100} \left\| \frac{\mathbf{u}_i^m}{\hat{u}^m} - \frac{\mathbf{u}_i^p}{\hat{u}^p} \right\|^2} \tag{9.4}$$

Note that in Eq. (9.4), the objective is computed based on the first 100 time steps of simulation, which corresponds to the first oscillation period of the aeroelastic response. The number of time steps is sufficiently large, so that the numerical result captures the characteristics of the aeroelastic responses associated with different model configurations. The number of time steps is also sufficiently small, so as to reduce the computational cost of sample generation in the BO algorithm.

An aeroelastically scaled model should result in a difference of zero, $J_u = 0$. The time step size for the aeroelastic simulation of the model is determined using Eq. (9.3). The time step size is the only quantity in the numerical scaling approach that is determined using an analytical similarity parameter.

The design variables include the thickness h, freestream pressure p_∞, and temperature increment ΔT associated with the model. The constraints of the design variables are summarized in Table 9.2.

The SO problem is solved using the BO algorithm. The optimizer employs the LCB acquisition function with $\upsilon = 1.0$. The optimization is initialized with 10 samples and run for 300 iterations. In the inner optimization loop, the acquisition function is minimized using a gradient-based solver with multiple starts.

Table 9.2: Constraints of the design variables for the aeroelastically scaled model

Design variables	h (mm)	p_∞ (kPa)	ΔT (K)
Range	$[0.2, 1.2]$	$[3.0, 11.0]$	$[0.5, 4.5]$

9.1.3 Numerical Scaling Results

The scaled models are generated for three different geometric scales, $\xi = 2, 3, 4$. In each case, the convergence history is illustrated in Fig. 9.2, and the optimizer successfully converges within 300 iterations.

The nondimensional aeroelastic responses of the prototype and the models are compared in Fig. 9.3. In the first 100 time steps, the responses are used for the numerical scaling with the objective Eq. (9.4), and the responses of the scaled models match very well with the prototype response with errors less than 4%. For the responses beyond the first 100 time steps, the model and prototype responses still match reasonably well, especially the frequency and amplitude of the oscillation. The similarity parameters associated with the prototype and the scaled models are almost identical, as shown in Table 9.3. Finally, the scaling of the design variables are compared in Fig. 9.4. It is clear that the two-pronged approach has successfully generated the numerical scaling laws that *recover* the analytical scaling laws for the aeroelastic problem considered in this section.

Finally, the results also show that the BO algorithm is effective in finding the global minimum of the non-convex optimization problem associated with the two-pronged approach. As an example, the contour of J_u w.r.t. variables p_∞ and ΔT for the case $\xi = 4$ is illustrated in Fig. 9.5. The distribution of the objective J_u is highly non-convex. While the global minimum of J_u is achieved at the point that corresponds to an aeroelastically scaled model, there are multiple local minima that can lead to incorrectly scaled models. Nevertheless, the BO algorithm is able to avoid the local minima and identify the global minimum successfully.

Table 9.3: Optimization results for different geometric scales

Parameters	$\frac{\hat{h}}{\hat{L}}$	$\bar{\lambda}_F$	$\frac{\Delta T \widehat{N}_{Tx} \hat{L}^2}{\widehat{D}_{xx}}$
Prototype	0.002	566.07	47.882
$\xi = 2$	0.00201 (0.379%)	566.85 (0.137%)	47.581 (0.629%)
$\xi = 3$	0.00200 (0.167%)	561.38 (0.829%)	47.759 (0.257%)
$\xi = 4$	0.00200 (0.166%)	566.69 (0.109%)	47.671 (0.439%)

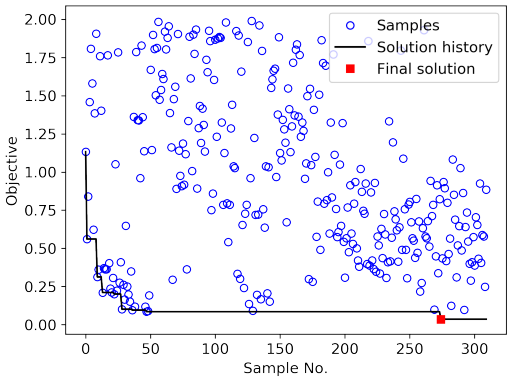

(a) $\xi = 2$

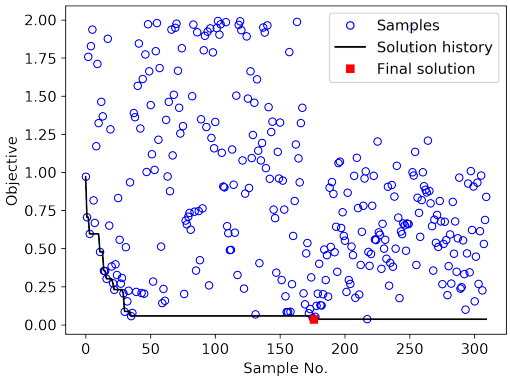

(b) $\xi = 3$

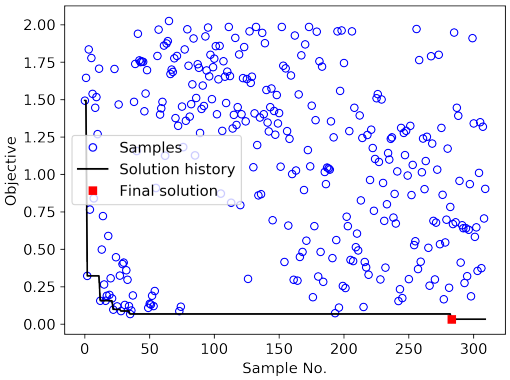

(c) $\xi = 4$

Figure 9.2: Convergence history of the cases for $\xi = 2, 3, 4$

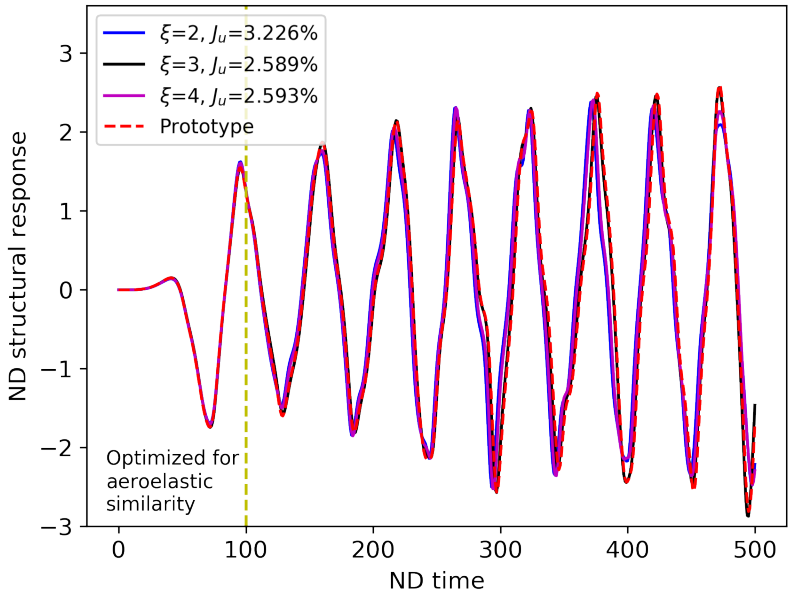

Figure 9.3: Nondimensional aeroelastic responses of the prototype and the scaled models

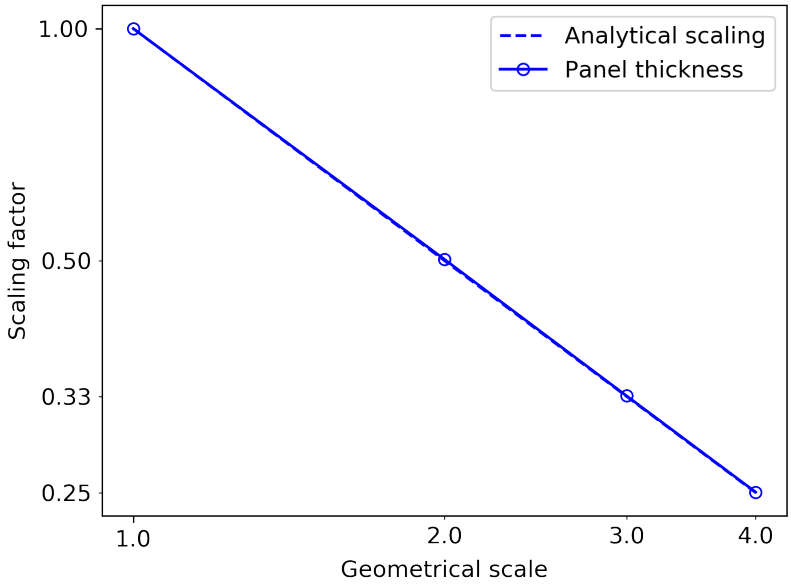

Figure 9.4: Comparison of analytical and numerical scaling

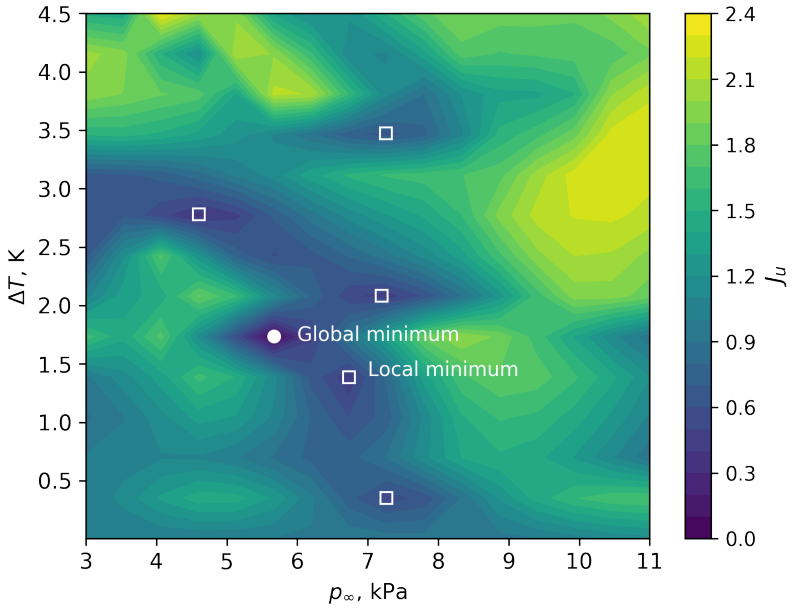

Figure 9.5: Contour of J_u at $h = 0.5$mm for the case $\xi = 4$

9.2 Scaling of Quasi-Steady Aerothermoelastic Response

9.2.1 Problem Description

9.2.1.1 Panel Configuration

The "prototype" configuration is illustrated in Fig. 9.6. The case consists of a simply-supported square panel with side length of 1m and front rigid wall length of 1m. The flow is aligned with the panel, i.e. the flow orientation angle is zero. The layup of the panel is shown in Table 9.4, which resembles the honeycomb sandwich panel used in Ref. [9]. It is assumed that (1) honeycomb cell is hexagonal, so the material properties of the honeycomb core are isotropic in the x and y directions; (2) the honeycomb core carries only the shear stress and transfers the load between the upper and lower surfaces through shear deformation. The effective transverse shear modulus is computed using the analytical relation provided in Ref. [203]. The thermal properties of the honeycomb is obtained using the

Swann-Pittman relation [205]. The effective thermal conductivity increases with temperature due to the radiative heat transfer. The emissivity of the upper surface is assumed to be 0.85. The "model" panel is a square *isotropic* panel made of Ti 6242. The material properties of both the prototype and the model are temperature dependent and the properties at room temperature ($T = 300K$) are provided in Table 9.5.

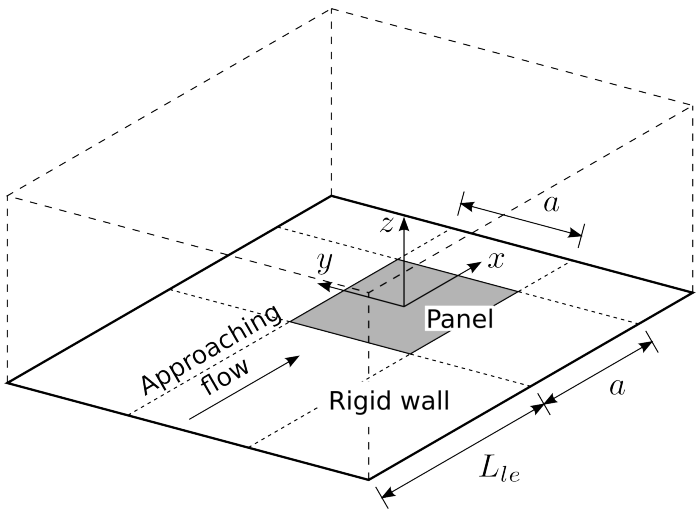

Figure 9.6: Geometrical configuration of a square panel for aerothermoelastic scaling

The objective of the scaling is to determine the geometrical dimensions of the model panel, as well as the experimental conditions of the wind tunnel, so that the aerothermoelastic response of the model in the wind tunnel is similar to the aerothermoelastic response of the prototype at a given flight condition. The error of the structural response J_u is quantified by the difference in the deflection at the center of the panel nondimensionalized by the thickness. The error of the thermal response J_T is quantified by the difference in the average body temperature nondimensionalized by the stagnation temperature. The duration of the response of the prototype is 160s and the initial temperature of the prototype is 300K.

The fluid ROM for the prototype panel configuration has been developed in Section 8.3, and it is employed in the numerical aerothermoelastic simulation of the prototype and the model. The ROM was generated for flight conditions $M_\infty = 6.0$ and $H = 25$km. When

combined with the correction and scaling technique, the ROM can be used to predict the aerodynamic loading and heating at different conditions for a flight envelope covering the range of $5.0 \leq M_\infty \leq 7.0$ and $20 \leq H \leq 30$km on the prototype as well as the model with a geometric scale $2 \leq \xi \leq 5$.

Table 9.4: Layup of the prototype panel

Component	Material	Thickness
Upper sheet	Inconel 718	1 mm
Honeycomb core	Inconel 718	16 mm
Lower sheet	Inconel 718	1 mm

Table 9.5: Material properties of Inconel 718 and Ti 6242 at $T = 300\mathrm{K}$

Material	ρ^s, $\mathrm{kg/m^3}$	E, GPa	ν	α, $\times 10^{-5}/\mathrm{K}$	k^s, $\mathrm{W/mK}$	c_p^s, $\mathrm{J/kgK}$
Inconel 718 [6]	8220	204.0	0.29	1.237	11.71	418.4
Ti 6242 [204]	4540	114.3	0.32	0.6975	6.937	459.4

9.2.1.2 Wind Tunnel Conditions

Several wind tunnels that are suitable for hypersonic aerothermoelastic testing are illustrated in Fig. 1.5. Among these wind tunnels, the hypersonic tunnel facility (HTF) at NASA Glenn Research Center is of interest [3, 31]. The HTF is a free-jet blow-down wind tunnel that is capable of simulating the flight conditions at multiple Mach numbers, $M_\infty = 5, 6, 7$, which are representative of the flight envelope of interest, as illustrated in Fig. 9.7. The test conditions at different Mach numbers are achieved using three nozzle configurations, all of which have an exit diameter of $42\mathrm{in} \approx 1.07\mathrm{m}$. The dimensions of the test section are $42\mathrm{in} \times 10\mathrm{ft} \approx 1.07\mathrm{m} \times 3.05\mathrm{m}$.

The constraints representing the operating envelope of the HTF are necessary for the optimization problem associated with refined aerothermoelastic scaling. However, the data

defining the *exact* operating envelope of the HTF is unavailable in the open literature. The only public data available is the upper and lower limits of the stagnation temperature and pressure of the operating envelope at $M_\infty = 5, 6, 7$ [3, 31]. Therefore, in the current study, three sets of "realistic" wind tunnel conditions are synthesized based on the available HTF data in public [3, 31], illustrated in Fig. 9.8 and listed in Table 9.6. Additionally, a set of "ideal" wind tunnel conditions is assumed based on the flight condition of $5 \leq M_\infty \leq 7$ and $20\text{km} \leq H \leq 30\text{km}$, which encompasses the ranges of the three sets of "realistic" wind tunnel conditions. For each set of the conditions, the Mach number is fixed and it is assumed that an arbitrary combination of the stagnation temperature and pressure in the given range is attainable.

Another constraining factor for the aerothermoelastic test is the operation time of the wind tunnel. In the quasi-steady aerothermoelastic problem, the scaling in time is determined by the Fourier number, as required by Eq. (6.3a),

$$t^m = \frac{1}{\xi^2} \frac{[\hat{k}^s]^p}{[\hat{\rho}^s \hat{c}_p^s]^p} \frac{[\hat{\rho}^s \hat{c}_p^s]^m}{[\hat{k}^s]^m} t^p \tag{9.5}$$

It means that the time duration of the the scaled test is inversely proportional to the square of the geometric scale ξ. When the time duration of the quasi-steady aerothermoelastic response is 160s, and the geometric scale ranges from 2 to 5, the time duration of the the scaled test is expected to be less than 40s. The operation time of the HTF depends on the test condition and ranges from 42s to 294s. Therefore, it is assumed that the wind tunnel can operate for sufficient time length so as to accommodate the aerothermoelastic test of any model with geometric scales of $2 \leq \xi \leq 5$. In other words, no constraint is needed for the time duration of the scaled test in the optimization problem associated with refined aerothermoelastic scaling.

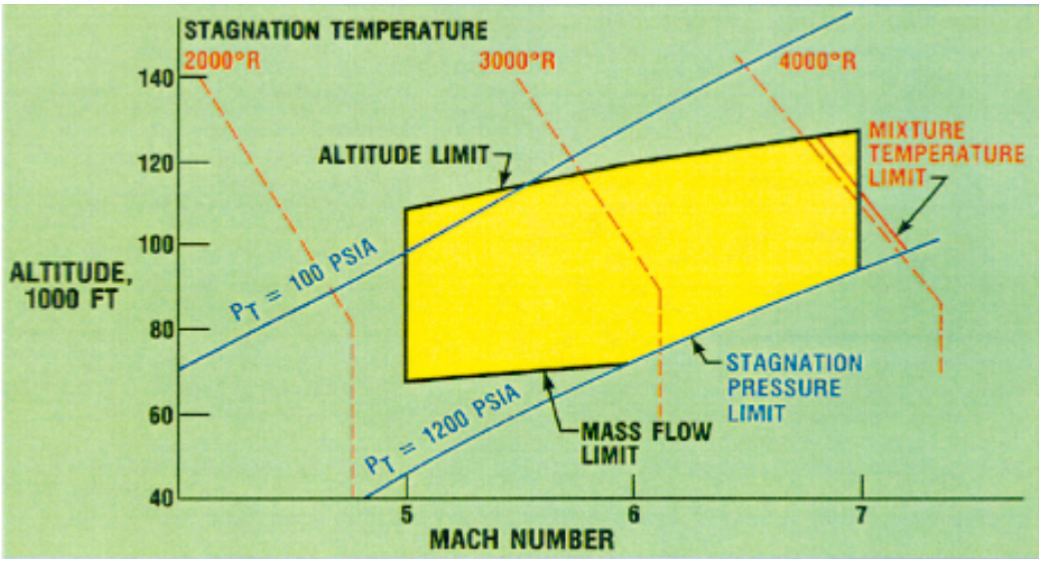

Figure 9.7: Operating envelope of the HTF (Figure 1 of Ref. [3])

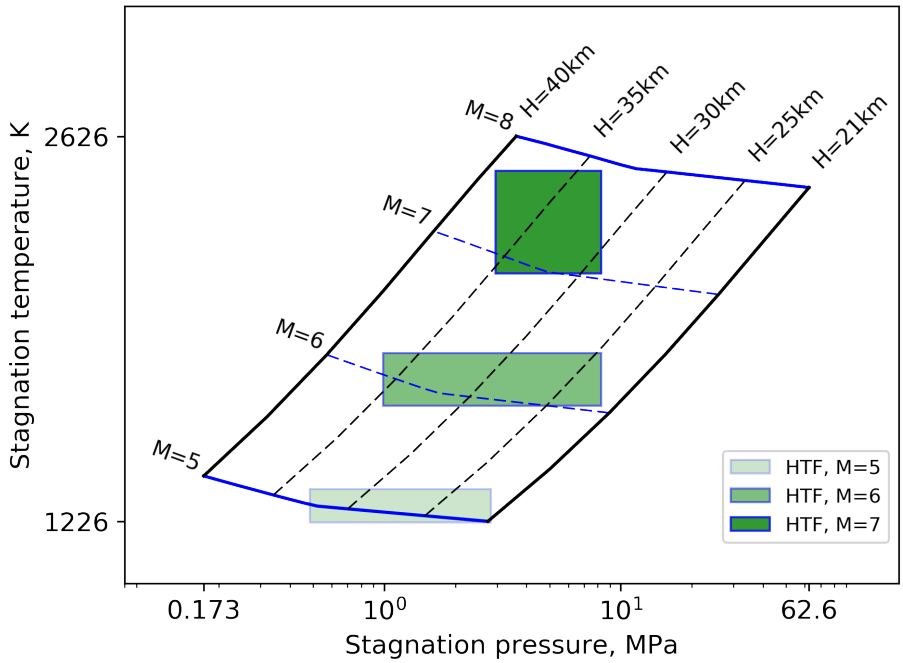

Figure 9.8: Envelopes of the HTF test conditions and typical hypersonic flight conditions

Table 9.6: Wind tunnel conditions

		M_∞	p_0 (MPa)	T_0 (K)
Ideal		$[5, 7]$	$[0.27579, 86.184466]$	$[416.483, 2500.0]$
Realistic	WT5	5	$[0.4860804, 2.82685]$	$[1222.22, 1344.44]$
	WT6	6	$[0.992845, 8.273709]$	$[1647.22, 1838.89]$
	WT7	7	$[2.96475, 8.273709]$	$[2127.778, 2500.0]$

9.2.1.3 Design Variables and Constraints

The design variables considered for the scaling of the skin panel, as well as their constraints, are summarized in Table 9.7. These design variables are selected from Table 6.1. The design variables consist of the wind tunnel conditions, geometrical parameters of the model, and the parameters for an external radiative heater. The constraints for the wind tunnel conditions have been provided in Table 9.6. In the constraints for the geometrical parameters, the upper limits are determined by the size of the wind tunnel test section and the lower limits are determined by the manufacturing constraints. The radiative heating is assumed to enable the discussion of the incomplete testing strategy. It is assumed that the radiation temperature T_{rad} is constant throughout the test and the surface emissivity of the model ε is uniformly distributed. The model is assumed to be aligned with the flow, so the inclination angle θ is zero. The model is built of a single material, Ti 6242, so the material properties are fixed and there is only one design variable h representing the thickness of the panel.

When parameter relaxation strategy is employed, only the similarity parameters in Eqs. (6.3a) and (6.3c) are imposed as equality constraints, and the matching of the similarity parameters in Eq. (6.3b) is not required. Equation (6.3a) defines the scaling of the time

Table 9.7: Design variables for the scaled model and their constraints

M_∞, p_0, T_0	L (m)	L_{le} (m)	h (m)	ε	T_{rad} (K)
See Table 9.6	$[0.1, 0.5]$	$[0.1, 2.0]$	$[0.001, 0.01]$	$[0.5, 1.0]$	$[300.0, 2500.0]$

step size during the simulation,

$$\Delta t^m = \frac{1}{\xi^2} \frac{[\hat{k}^s]^p}{[\hat{\rho}^s \hat{c}_p^s]^p} \frac{[\hat{\rho}^s \hat{c}_p^s]^m}{[\hat{k}^s]^m} \Delta t^p \tag{9.6}$$

Assuming $\hat{T}_T^p = \hat{T}_S^p = \hat{T}_w^p$ and $\hat{T}_F^p = T_\infty^p$ for the prototype, Eq. (6.3c) implies the following equality constraints on the design variables associated with reference temperatures,

$$\hat{T}_T^m = \hat{T}_S^m = \hat{T}_w^m, \quad \hat{T}_F^m = T_\infty^m, \quad \frac{T_w^m}{T_\infty^m} = \frac{T_w^p}{T_\infty^p} \tag{9.7}$$

9.2.2 Scaling With Ideal Wind Tunnel Conditions

First, the feasibility of numerical aerothermoelastic scaling is explored by generating scaled models for different geometric scales with ideal wind tunnel conditions. The flight conditions of the prototype are $M_\infty = 6.0$ and $H = 25$km. The parameter relaxation strategy is used and the design variables include $M_\infty, p_0, T_0, L_{le}, h$. Four different geometric scales are considered: $\xi = 2, 3, 4, 5$. For each case, 20 samples are generated to initialize the SBO algorithm and 50 iterations are conducted during the optimization.

The Pareto fronts for the four cases are shown in Fig. 9.9. The results show that, reducing the error of one of responses would result in a rapid increase in the error of the other response. Thus it illustrates the failure of the classical aerothermoelastic scaling. Nevertheless, for each geometric scale, it is possible to find a model configuration that satisfies approximately the aerothermoelastic similarity, as indicated by the solid points in Fig. 9.9. These points are assumed to be the final design points. The responses associated with these design points are shown in Figs. 9.10 and 9.11. In all the cases, the errors in the

aerothermoelastic responses are less than 10%.

The values of the design variables are listed in Table 9.8 and illustrated in Fig. 9.12. Figure 9.12 illustrates the differing scaling requirements of the geometrical variables h and L_{le}. The numerical scaling of the panel thickness h agrees with the analytical scaling requirements represented by the blue dashed line. However, the variable L_{le} increases as the panel dimension decreases, which is vastly different from the analytical scaling requirements. The scaling of L_{le} obtained numerically represents a refinement of the analytical scaling relation. Table 9.8 illustrates the activation of constraints at the design points. The constraints of h and L_{le} are active for the cases $\xi = 2$ and $\xi = 3$, respectively, due to the limitation in the size of the test section. Using the classical scaling approach, it is inconvenient to develop a scaled model that accounts for the inequality constraints. That is because, for the classical approach the scaling requirements are determined by the analytical similarity parameters. However, the derivation of these similarity parameters does not involve any inequality constraints. Nevertheless, the inequality constraints are treated efficiently using the two-pronged approach. A scaled model that satisfies all the constraints is obtained by the refined and systematic adjustment using the optimization process of the two-pronged approach.

To summarize, the results in this section show that it is possible to achieve refined ASL under ideal wind tunnel conditions using the two-pronged approach. Furthermore, the results obtained illustrate the advantages of the two-pronged approach over the classical scaling approach. First, the two-pronged approach can generate the requirements for aerothermoelastic scaling by refining the scaling requirements represented by the analytical similarity parameters. Second, the two-pronged approach can account for the inequality constraints representing the limitations of the wind tunnel and manufacturing capabilities, which cannot be treated efficiently using the classical approach.

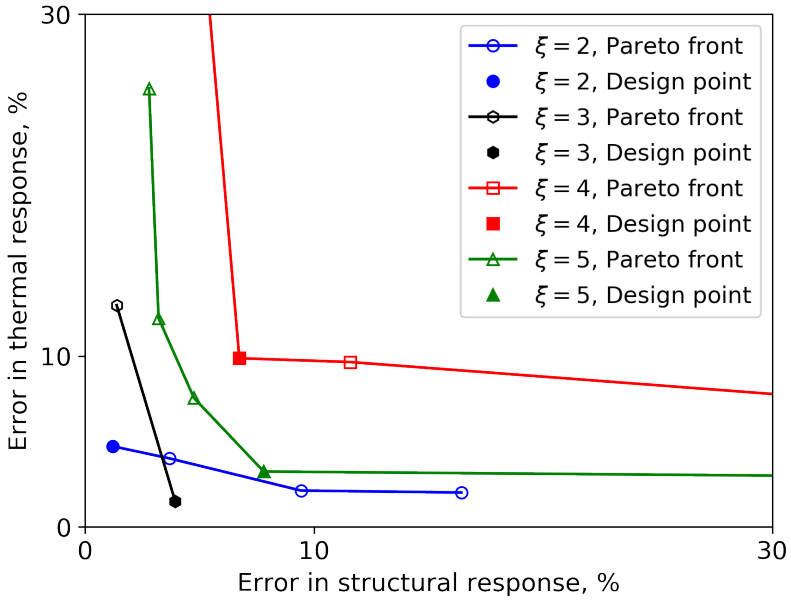

Figure 9.9: Pareto fronts for different geometric scales

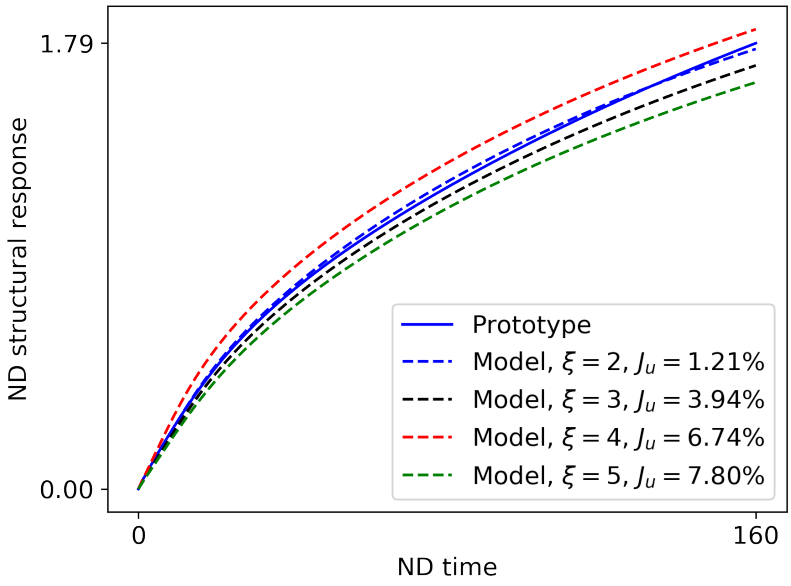

Figure 9.10: Comparison of nondimensional structural responses

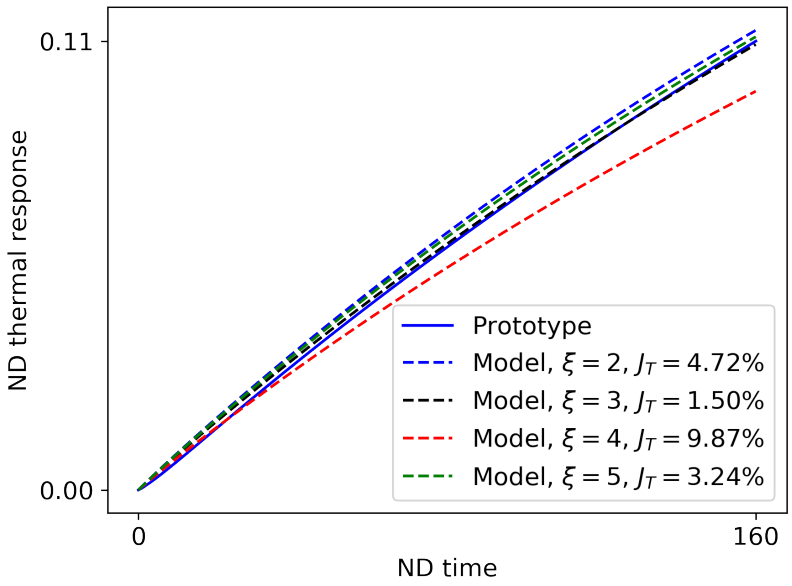

Figure 9.11: Comparison of nondimensional thermal responses

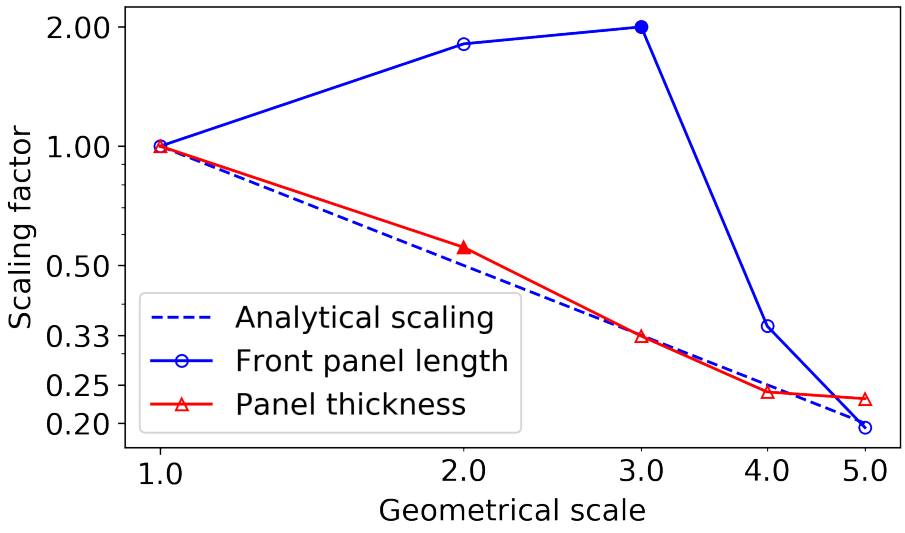

Figure 9.12: Analytical and numerical scaling of geometrical variables

Table 9.8: Design points for different geometric scales

Design variables	$\xi = 2$	$\xi = 3$	$\xi = 4$	$\xi = 5$
M_∞	6.841e+00	5.653e+00	5.407e+00	6.250e+00
p_0 (MPa)	6.476e+01	3.916e+01	3.858e+01	7.330e+01
T_0 (K)	2.280e+03	1.868e+03	2.130e+03	2.187e+03
L_{le} (m)	1.812e+00	2.000e+00	3.516e-01	1.950e-01
h (m)	1.000e-02	5.971e-03	4.317e-03	4.150e-03

9.2.3 Scaling With Realistic Wind Tunnel Conditions

Next, the scaling of the prototype is conducted with realistic wind tunnel conditions. The flight conditions of the prototype are $M_\infty = 6.0$ and $H = 25$km and the wind tunnel conditions WT5, WT6 and WT7 from Table 9.6 are used. Two cases are considered. For Case 1, pure parameter relaxation strategy is used and the design variables are p_0, T_0, L, L_{le}, h. For Case 2, combined strategy of parameter relaxation and incomplete testing is used and the design variables are $p_0, T_0, L, L_{le}, h, \varepsilon, T_{rad}$. For both cases, 20 samples are generated to initialize the SBO algorithm and 50 iterations are conducted for the optimization.

The Pareto fronts of the two cases are shown in Fig. 9.13. For Case 1, the two-pronged approach failed to find any good solution that have low errors in the structural and thermal responses for any realistic wind tunnel conditions. For Case 2, it is possible to find configurations that can satisfy approximately the aerothermoelastic similarity for all the three wind tunnel conditions. The differences between the two cases are explained by examining the design points in Tables 9.9-9.10. All the design points in Case 1 have reached the upper limit of p_0 for the realistic wind tunnel conditions, which is less than 10% of the maximum p_0 in the ideal wind tunnel conditions. As illustrated in Fig. 9.14, the low value of p_0 leads to insufficient heating on the model and produces a slow increase in the average temperature as well as the center deflection. The problem in Case 1 is resolved in Case 2 with

Table 9.9: Design points for realistic wind tunnel conditions in Case 1

Design variables	WT5	WT6	WT7
p_0 (MPa)	2.827e+00	8.274e+00	8.274e+00
T_0 (K)	1.267e+03	1.664e+03	2.317e+03
L (m)	5.000e-01	5.000e-01	5.000e-01
L_{le} (m)	7.601e-01	6.270e-01	6.419e-01
h (m)	7.034e-03	8.794e-03	1.000e-02

Table 9.10: Design points for realistic wind tunnel conditions in Case 2

Design variables	WT5	WT6	WT7
p_0 (MPa)	4.861e-01	9.928e-01	6.543e+00
T_0 (K)	1.222e+03	1.821e+03	2.220e+03
L (m)	5.000e-01	4.480e-01	4.448e-01
L_{le} (m)	2.000e+00	1.761e+00	1.717e+00
h (m)	7.500e-03	7.798e-03	8.210e-03
ε	5.000e-01	1.000e+00	1.000e+00
T_{rad} (K)	1.621e+03	1.492e+03	1.548e+03

the introduction of the external heating, which compensates for the low heating rate in the realistic wind tunnel conditions.

The comparison between Cases 1 and 2 shows that, using parameter relaxation and incomplete testing, the two-pronged approach can be used to generate aerothermoelastically scaled models with restrictive constraints of realistic wind tunnel conditions. However, it should be emphasized that achieving small errors in the structural and thermal responses is progressively more difficult as the Mach number decreases. When $M_\infty = 5$, the design point has most of the constraints active, indicating that the constraints imposed by the wind tunnel conditions WT5 are not suitable for the flight condition considered in the current problem.

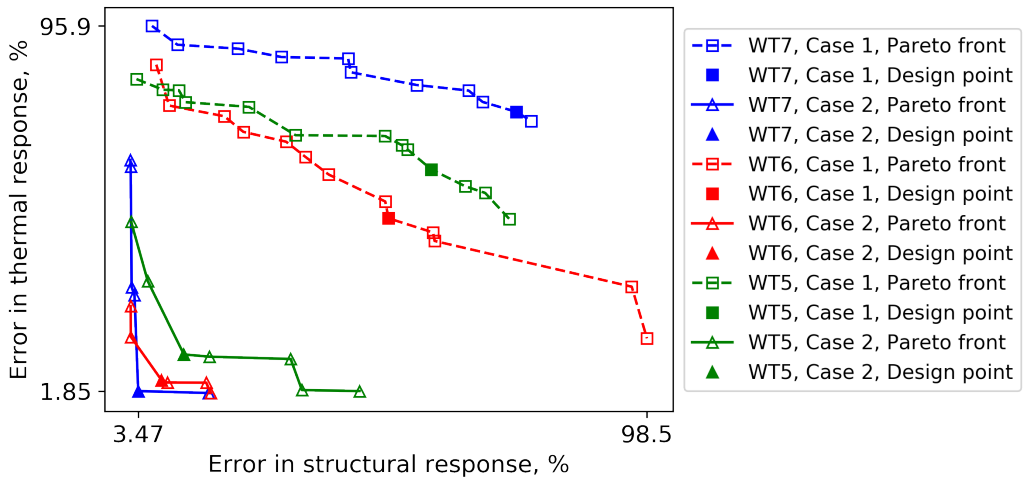

Figure 9.13: Pareto fronts for Cases 1 and 2

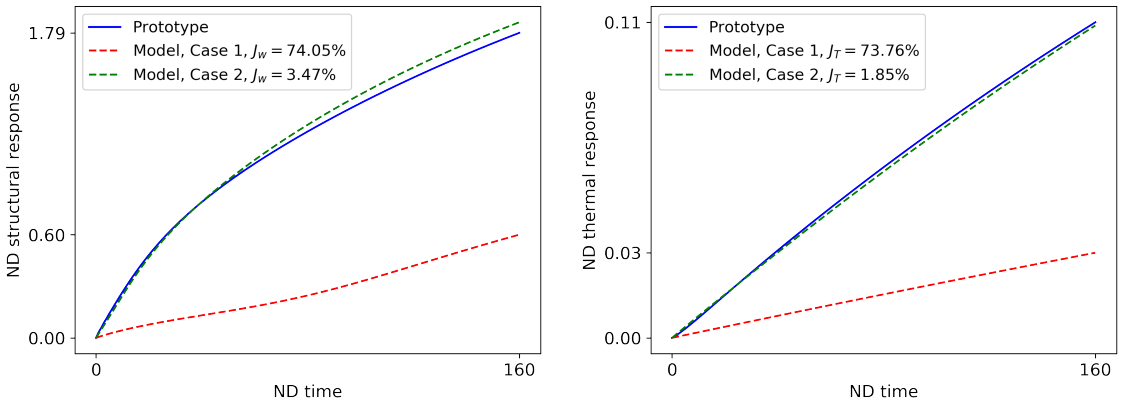

(a) Nondimensional structural response **(b) Nondimensional thermal response**

Figure 9.14: Comparison of prototype and model responses in Cases 1 and 2 for wind tunnel condition WT7.

9.2.4 Scaling for Multiple Flight Conditions in the Same Wind Tunnel

Finally, the two-pronged approach is used to generate scaled models for aerothermoelastic testing associated with different flight conditions using the same set of wind tunnel conditions. A range of flight conditions is considered: $M_\infty = 5.0, 5.5, 6.0, 6.5, 7.0$ and $H = 20, 22, 25, 28, 30$km. The wind tunnel condition WT7 in Table 9.6 is assumed. The

design variables are $p_0, T_0, L, L_{le}, h, \varepsilon, T_{rad}$, which are the same as those in the previous problem. However, in this problem, instead of solving the MO problem for each flight condition, an SO problem is solved for a combined objective function,

$$J_s = \sqrt{J_u^2 + J_T^2} \tag{9.8}$$

Solving SO problems requires fewer samples of numerical aerothermoelastic responses and thus saves a considerable amount of computer time. The SO problems are solved in a sequential manner. The first SO problem is initialized using 20 samples and 20 iterations are conducted. The next SO problems are solved using 20 iterations with the initial samples recycled from the previous SO problems.

The errors associated with different flight conditions are listed in Table 9.11. For all but five flight conditions, it is possible to find configurations that can approximately satisfy the aerothermoelastic similarity with errors of less than 5%. The errors exceed 5% in two cases: (1) high Mach number ($M_\infty = 6.5, 7.0$) and low altitude ($H = 20$km) and (2) low Mach number ($M_\infty = 5.0, 5.5$) and high altitude ($H = 28, 30$km).

Next, three typical cases are examined: (1) $M_\infty = 7.0, H = 20$km, ($J_s = 5.22\%$), (2) $M_\infty = 6.0, H = 22$km, ($J_s = 1.50\%$), (3) $M_\infty = 5.0, H = 30$km, ($J_s = 9.98\%$). Figure 9.15 illustrates the structural deformation and temperature distribution along the centerline at nondimensional times $t = 30, 90, 160$. For all the cases, aerothermoelastic similarity is achieved approximately. However, the temperature distribution of the prototype is more non-uniform than the model, because the heat sources on the model include both aerodynamic heating and external heating due to radiation. While the aerodynamic heating is stronger near the leading edge of the panel, the radiative heating is almost uniform over the panel. This produces a relatively uniform temperature distribution on the model. The temperature distribution becomes more non-uniform as the Mach number increases and the altitude decreases, because the aerodynamic heating becomes stronger at higher Mach

number and higher freestream pressure, i.e. lower altitude. As discussed in the previous chapter, in the long-term quasi-steady aerothermoelastic response, the panel deformation is mainly caused by the thermal effect. The maximum deflection of the panel increases as the average temperature increases and the location of the maximum deflection of the panel is closer to the leading edge when the temperature distribution is more non-uniform.

Among the three sets of flight conditions considered, the second one is a typical case where aerothermoelastic similarity is achieved approximately. The temperature distribution of the prototype is not highly non-uniform, so that the maximum deflections of the prototype and the model occur approximately at the center of the panel. The average temperatures of the prototype and the model are similar, resulting in similar amplitudes of structural deformation and smaller errors in the structural response. On the other hand, the first set of flight conditions represents a case where the aerodynamic heating is too strong and produces a highly non-uniform temperature distribution that causes the location of maximum deflection of the prototype to move from the center towards the leading edge. The mismatch in the shape of panel deflection produces an increased error in the nondimensional structural response. The third set of flight conditions represents the case where the aerodynamic heating is weak but the external heating is insufficient to accurately control the average temperature of the model. The mismatch in the average temperatures of the model and the prototype leads to the error in the magnitude of panel deflection and the increased error of structural response.

Within the current optimization framework, the sources of errors in the first and the third cases can be minimized or eliminated by refined adjustment of the model. For the first case, the *distribution* of the radiation temperature of the radiative heater can be optimized, so as to tune the distribution of the radiative heat flux to resemble the non-uniform distribution of the aerodynamic heat flux. Furthermore, the objective functions J_u and J_T can be modified to include the structural and thermal modal coordinates so as to ensure the matching of the distributions of deformation and temperature. For the third case, the time variation of

the radiation temperature during the wind tunnel test can be optimized, so as to accurately control the average temperature and thus the deformation of the panel.

Table 9.11: Errors in aerothermoelastic responses of differernt flight conditions (in %)

	$H = 20$km	$H = 22$km	$H = 25$km	$H = 28$km	$H = 30$km
$M_\infty = 5.0$	4.82	4.41	3.69	7.20	9.98
$M_\infty = 5.5$	3.40	2.95	3.34	4.51	5.47
$M_\infty = 6.0$	2.75	1.50	4.52	3.2	4.13
$M_\infty = 6.5$	6.16	2.15	3.24	2.25	2.81
$M_\infty = 7.0$	5.22	3.58	2.43	5.17	2.01

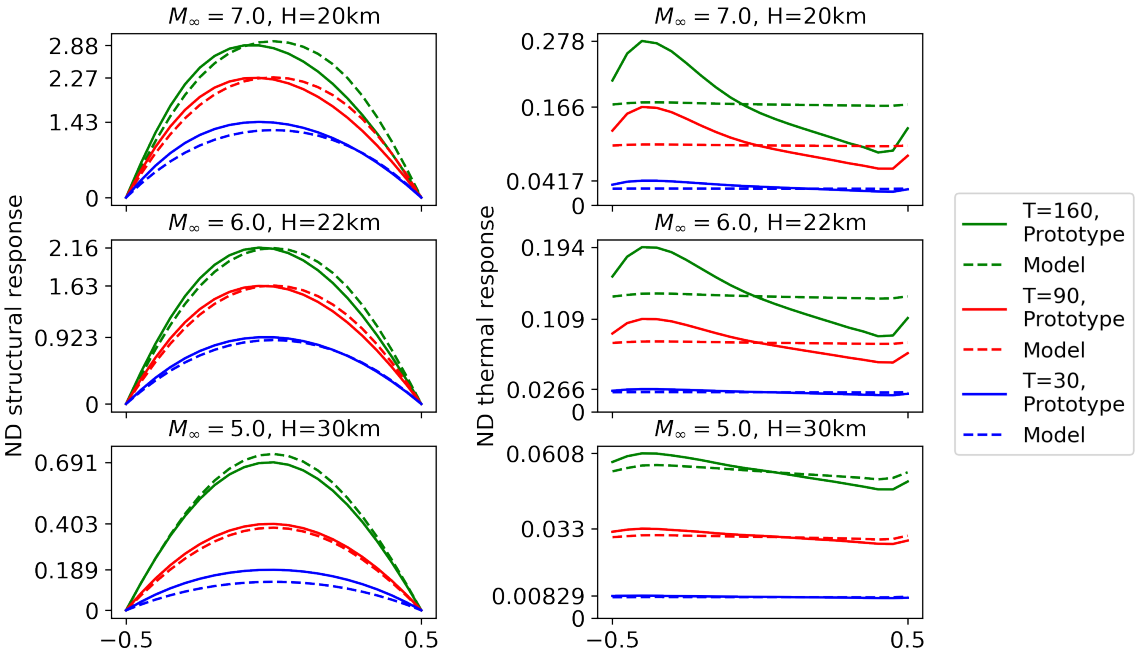

Figure 9.15: Nondimensional structural and thermal responses of selected cases

CHAPTER 10

Conclusions and Recommendations for Future Research

This dissertation has addressed the outstanding challenges associated with the aeroelastic and aerothermoelastic analysis of hypersonic structures. The primary objectives were: (1) enhancing our understanding of the aeroelastic and aerothermoelastic behavior of hypersonic structures by conducting a computational study, and (2) development of a new methodology for generating refined hypersonic ASL that are suitable for wind tunnel testing. The principal novel contributions of this dissertation are two-fold. First, an integrated computational framework HYPATE was developed to enable rapid long-time-duration aerothermoelastic simulation of hypersonic structures. Two novel approaches have been incorporated to accelerate the HYPATE framework: a fluid ROM enhanced using a correction and scaling technique, and a new computational approach combining a tightly-coupled scheme with linearized stability analysis. Second, a new, two-pronged approach to aerothermoelastic scaling is developed. It combines the classical scaling approach with augmentation from numerical simulations of the specific problem based on a constrained optimization formulation. In the optimization formulation, the strategies of parameter relaxation and incomplete testing are incorporated to assist the refinement of hypersonic aerothermoelastic scaling.

The aerothermoelastic analysis results highlight the impact of the effects of boundary layer thickness, aspect ratio, flow orientation angle, and material orthotropicity on the be-

havior of skin panels in hypersonic flow. The findings provide practical insight on the structural design of hypersonic vehicles. The new two-pronged approach was applied to the aerothermoelastic scaling of a skin panel in hypersonic flow. The aerothermoelastic similarity between the prototype and the scaled model was successfully obtained using a systematic optimization approach, which accounts for realistic constraints of the wind tunnel and manufacturing.

10.1 Conclusions

The results presented in this dissertation provide significant insight into the aeroelastic and aerothermoelastic behavior of panel in hypersonic flow and enhance our understanding of this complex multiphysics problem. The principal conclusions and contributions of this dissertation are summarized below:

1. The transient aerothermoelastic response is approximated well by the quasi-steady response generated using the tightly-coupled scheme with a time step size that is two orders of magnitude larger than those employed in the conventional loosely-coupled schemes.
2. The linearized stability analysis serves as an effective tool for the identification of aerothermoelastic instability. The LSA is capable of capturing flutter-type instabilities that results in unstable oscillatory response, as well as snap-through-type instability that does not necessarily develop into unstable response of the entire panel.
3. The correction and scaling technique developed was effective in improving the flexibility of a fluid ROM by accounting for both non-uniform temperature distribution and extrapolation to different flow conditions and geometric scales. The formulation does not rely on any specific forms of the ROM and thus can be applied to ROMs employing alternative methods that are different from POD-kriging.
4. The combination of the fluid ROM and the tightly-coupled scheme enables fast, high-

fidelity aerothermoelastic simulation that can be carried out on a typical workstation computer in *near-real-time*, instead of on a large-scale computing facility using weeks or months.

5. For aeroelastic stability and response in high supersonic, turbulent flow ($M_\infty = 4.0$), increasing boundary layer thickness has a beneficial effect on the flutter amplitude and a stabilizing effect on the panel by postponing the onset of instability. Failure to include the aspect ratio effect in the aeroelastic simulation may lead to erroneous predictions of the critical flutter parameter of a panel.
6. For the aerothermoelastic case, the snap-through type of instability is controlled by the force ratio, i.e. the ratio between the in-phase and out-of-phase components of the pressure distribution. The force ratio increases as the structure deforms due to temperature increase. The growth rate of the force ratio is higher when the boundary layer is thinner. As the force ratio increases, a lower value of out-of-phase pressure component is required to cause the snap-through.
7. For the aerothermoelastic case, the boundary layer does not necessarily stabilize the panel in contrast to the aeroelastic case. A sufficiently thin boundary layer can lead to high force ratio and the immediate onset of aerothermoelastic instability.
8. The aerothermoelastic response is sensitive to the boundary layer thickness. Furthermore, 2D panel models are not suitable for capturing the intricate nonlinear behavior present in 3D panels. Failure to include the boundary layer effect or the aspect ratio effect in the aerothermoelastic simulation may lead to erroneous predictions of the instability of a panel.
9. The flow orientation angle alters the regions of a panel exposed to hypersonic flow, leading to significant changes in the heat flux distribution, and thus the temperature distribution. Increasing the flow orientation angle from 0° to 30° can reduce the aerothermoelastic stability boundary by 10%.
10. The material orthotropicity alters the thermoelastic deformation of a panel, resulting

in modified distributions of heat flux and temperature. In addition, the combined effect of flow orientation angle and orthotropicity can result in nonlinear behavior of the panel, such as localized snap-through, that can influence the aerothermoelastic stability boundary.

11. When the wind tunnel is capable of simulating flight conditions with sufficiently high stagnation temperature and stagnation pressure, the aerothermoelastic scaling can be achieved using a parameter relaxation strategy. An aerothermoelastically scaled model is constructed by matching a partial set of the aerothermoelastic similarity parameters between the prototype and the model.
12. When the wind tunnel is limited and cannot provide high stagnation temperature or stagnation pressure, aerothermoelastic similarity can be still achieved by combining parameter relaxation with incomplete testing. Thus external loading and heating is introduced to compensate for the insufficient aerodynamic loading and heating capability of the wind tunnel.
13. Using one set of wind tunnel conditions, i.e. in the same wind tunnel, it is possible to adjust the scaled model in a refined manner, so as to conduct hypersonic aerothermoelastic testing for a range of flight conditions that are representative of the flight envelope of a hypersonic vehicle.

10.2 Recommendations for Future Research

This is a pioneering study that represents the first-ever effort to develop numerical ASL for hypersonic structures. The demonstration of the numerical scaling approach shows that it can be eventually applied to testing various components of a hypersonic vehicle. Furthermore, the approach can be also used to map aerothermoelastic results obtained in a scaled test on an actual vehicle to a vehicle having different geometric size. Therefore, it has the potential for saving considerable funds in the development process of future

hypersonic vehicles by replacing some flight tests with wind tunnel experiments.

However, the complexity of aerothermoelastic problem still has several facets that require additional work. In fact, it has just opened up a new area that requires the joint of the computational and experimental work to produce practical and reliable results. On the computational side, high-fidelity simulation should be carried out to assist the design of the scaled models for wind tunnel testing. The model design would require detailed modeling of the imperfections of the testing environment in the wind tunnel, such as structural boundary conditions, wind tunnel turbulence and wall interference effects, and imperfect radiative heating and cooling. On the experimental side, relevant testing and measurement techniques, such as simultaneous temperature and displacement measurement methods with high spatial and temporal resolutions [139], should be developed so as to conduct actual aerothermoelastic testing in a wind tunnel.

The ultimate goals of scaled aerothermoelastic testing is to predict the performance and reliability of structural components on a full-scale hypersonic vehicle. Such experimental results will also be an important source for data validation and uncertainty quantification of the computational tools. Two types of uncertainty have been defined for hypersonic aerothermoelastic problems: aleatory and epistemic uncertainty [1]. Aleatory uncertainty refers to variability inherent to input variables, e.g. uncertainty in atmospheric properties. Epistemic uncertainty encompasses uncertainty inherent to the modeling assumptions pertaining to a given analysis, e.g. the simplification introduced by the fluid ROM. While a systematic approach for the quantification of aleatory uncertainty has been developed for hypersonic aerothermoelasticity using surrogate-based stochastic collocation method [1], there are limited studies devoted to the quantification of epistemic uncertainty in aerothermoelastic analysis, especially when ROMs are employed. Strategies and computational tools have to be developed for the *robust* design of hypersonic vehicles that account for the model uncertainties.

The extensive numerical analysis and forth-coming experimental results can greatly

enhance the understanding of aerothermoelastic behavior of hypersonic structures, which can produce a paradigm shift in the structural design of hypersonic vehicles. The traditional hypersonic structures are relatively stiff and heavy, because they are designed to avoid any possible instabilities during hypersonic flight. The heavy structural weight represents a significant payload and performance penalty on the vehicle. In this dissertation, the study on the aerothermoelastic behavior of the skin panel indicates that, it is possible to optimize the stiffness distribution of the skin panel with respect to the flow orientation, and *exploit* some benign aerothermoelastic instabilities, such as local snap-through, so as to improve the aerothermoelastic stability boundary of hypersonic vehicle structural components.

Finally, a natural extension of this work is to consider the aerothermoelastic analysis that incorporates more complex flow physics, e.g. acoustic radiation of turbulent flow and shock wave/boundary layer interaction [63, 64]. These problems may involve shock-dominated flow that requires high spatiotemporal resolution, panel deformations containing a wide spectrum of structural modes, and highly nonlinear wall temperature distributions. To tackle these problems, the first step is to resolve complex flow phenomena using higher-fidelity tools such as LES. Next, more versatile fluid ROMs need be developed to capture the highly nonlinear and stochastic dynamics in the complex flow physics. It would be ideal to have a fluid ROM, or an approximate fluid solver, that can accurately predict the pressure and heat flux distributions on an arbitrary geometrical configuration with arbitrary structural deformations and temperature distributions. Once such a fluid solver is available, it can accelerate and enhance the aerothermoelastic design and analysis of hypersonic structures.

APPENDIX A

Kriging and Proper Orthogonal Decomposition

A.1 Kriging model

The key assumption of kriging method is that two sample points that are close to each other in the parameter space have similar errors. This assumption is feasible for an unknown black-box function defined by deterministic computer simulations, since no sources of random error exists in the sample data set [105, 107].

It suffices to consider kriging model for a function with vector input and scalar output. For a function with vector output, a kriging model can be constructed for each dimension of the output. With a given sample data set $\mathcal{D} = \{\mathbf{x}_i, y_i\}_{i=1}^m$, the kriging interpolation is characterized by a global approximation f corrected using local deviations Z,

$$y(\mathbf{x}) = f(\mathbf{x}) + Z(\mathbf{x}) \tag{A.1}$$

The global approximation f is a regression function representing the global trend of the unknown function,

$$f(\mathbf{x}) = \mathbf{f}(\mathbf{x})^T \boldsymbol{\beta}_f = \sum_{i=1}^{q} \beta_{fi} f_i(\mathbf{x}) \tag{A.2}$$

In practice, the basis functions $\mathbf{f}(\mathbf{x}) = [f_1(\mathbf{x}), \cdots, f_q(\mathbf{x})]$ are polynomials up to second-order. When the basis function is zeroth-order, i.e. the global trend is a constant value, the kriging model is usually referred to as "ordinary kriging". Ordinary kriging has been

applied widely in engineering designs, such as Ref. [106]. Linear and quadratic basis functions have been used in kriging models for fluid ROMs, such as Refs. [101, 102]. The results show that kriging model with quadratic basis functions generates more accurate results than the one with linear basis functions.

The local deviation Z is assumed to resemble the behavior of a Gaussian process with zero mean and variance of σ^2_{krg}. Using a correlation function $r(\mathbf{x}_i, \mathbf{x}_j)$, the covariance between two sample points is,

$$\mathrm{cov}[Z(\mathbf{x}_i, \mathbf{x}_j)] = \sigma^2_{krg} r(\mathbf{x}_i, \mathbf{x}_j) \tag{A.3}$$

The correlation function measures the "closeness" between two points: The function value decreases as $||\mathbf{x}_i - \mathbf{x}_j||$ increases. A typical choice of the correlation function is the Gaussian kernel,

$$r(\mathbf{x}_i, \mathbf{x}_j) = \exp\left[-(\mathbf{x}_i - \mathbf{x}_j)^T \boldsymbol{\Theta} (\mathbf{x}_i - \mathbf{x}_j)\right] \tag{A.4}$$

where $\boldsymbol{\Theta}$ is typically a diagonal matrix characterizing the strength of correlation.

The kriging prediction of the black-box function at an input $\mathbf{x}$ follows a Gaussian distribution,

$$\mathbf{y}^{krg} \sim \mathcal{N}(\mu(\mathbf{x}), \sigma^2(\mathbf{x})) \tag{A.5}$$

The predictive mean μ and variance σ^2 are, respectively,

$$\mu(\mathbf{x}) = \boldsymbol{\beta}_f^T \mathbf{f}(\mathbf{x}) + \boldsymbol{\beta}_r^T \mathbf{r}(\mathbf{x}) \tag{A.6a}$$

$$\sigma^2 = \sigma^2_{krg}[1 + \mathbf{t}(\mathbf{x})^T (\mathbf{F}^T \mathbf{R}^{-1} \mathbf{F})^{-1} \mathbf{t}(\mathbf{x}) - \mathbf{r}(\mathbf{x})^T \mathbf{R}^{-1} \mathbf{r}(\mathbf{x})] \tag{A.6b}$$

where,

$$[\mathbf{F}]_{ij} = f_i(\mathbf{x}_j) \tag{A.7a}$$

$$[\mathbf{R}]_{ij} = r(\mathbf{x}_i, \mathbf{x}_j) \tag{A.7b}$$

$$\boldsymbol{\beta}_r = \mathbf{R}^{-1}(\mathbf{y} - \mathbf{F}\boldsymbol{\beta}_f) \tag{A.7c}$$

$$\mathbf{r}(\mathbf{x}) = [R(\mathbf{x}, \mathbf{x}_1), \cdots, R(\mathbf{x}, \mathbf{x}_m)]^T \tag{A.7d}$$

$$\mathbf{t}(\mathbf{x}) = \mathbf{F}^T\mathbf{R}^{-1}\mathbf{r}(\mathbf{x}) - \mathbf{f}(\mathbf{x}) \tag{A.7e}$$

The variance provides a quantification of the error in kriging prediction. A lower variance corresponds to a more confident prediction of the black-box function.

Finally, the gradients of the mean and variance w.r.t. to the input variables are,

$$\frac{\partial \mu}{\partial \mathbf{x}} = \boldsymbol{\beta}_f^T \frac{\partial \mathbf{f}}{\partial \mathbf{x}} + \boldsymbol{\beta}_r^T \mathbf{R}^{-1} \frac{\partial \mathbf{r}}{\partial \mathbf{x}} \tag{A.8a}$$

$$\frac{\partial \sigma^2}{\partial \mathbf{x}} = 2\sigma_{krg}^2 \left[\mathbf{t}(\mathbf{x})^T (\mathbf{F}^T\mathbf{R}^{-1}\mathbf{F})^{-1} \frac{\partial \mathbf{t}}{\partial \mathbf{x}} - \mathbf{r}(\mathbf{x})^T \mathbf{R}^{-1} \frac{\partial \mathbf{r}}{\partial \mathbf{x}} \right] \tag{A.8b}$$

where the gradients of $\mathbf{f}$, $\mathbf{r}$, and $\mathbf{t}$ w.r.t. $\mathbf{x}$ can be computed analytically from Eq. (A.7).

A.2 Proper Orthogonal Decomposition

The POD method has been used for dimension reduction problems [93, 104]. It provides a means to reproduce the behavior of a full-order system using a lower-order model, and thus significantly reduces computational cost. The low-order model is constructed from a few "POD modes", which represent the dominating patterns in the responses of a full-order system. Reference [93] is the first study to apply POD in fluid problems. Reference [104] provides a detailed description of the POD method in general.

For fluid dynamics, the POD modes are usually constructed using the snapshot method [93]. Consider a sample data set of full-order solutions $\{\mathbf{y}_i\}_{i=1}^{N_s}$, the snapshot matrix is,

$$\mathbf{S}_P = [\mathbf{y}_1, \cdots, \mathbf{y}_{N_s}] \tag{A.9}$$

Take the singular value decomposition (SVD) of the snapshot matrix,

$$\mathbf{S}_P = \mathbf{U}\boldsymbol{\Delta}\mathbf{V}^T \tag{A.10}$$

where $\mathbf{U}$ and $\mathbf{V}$ are orthonormal matrices, whose columns are the left and right singular vectors of $\mathbf{S}_P$, respectively. The matrix $\boldsymbol{\Delta}$ is diagonal, and the nonzero entries are singular values of $\mathbf{S}_P$ in decreasing order.

Let the first N_p left singular vectors be the POD modes,

$$\boldsymbol{\Psi}_P = [\mathbf{u}_1, \cdots, \mathbf{u}_{N_p}] \tag{A.11}$$

The snapshot matrix is approximated by projection onto the space spanned by $\boldsymbol{\Psi}_P$,

$$\mathbf{S}_P \approx \boldsymbol{\Psi}_P \boldsymbol{\Psi}_P^T \mathbf{S}_P \tag{A.12}$$

A full-order solution $\mathbf{y}$ and its POD components $\mathbf{y}_P$ are related by POD transformation,

$$\mathbf{y}_P = \boldsymbol{\Psi}_P^T \mathbf{y}, \quad \mathbf{y} \approx \boldsymbol{\Psi}_P \mathbf{y}_P \tag{A.13}$$

The relative error of approximation is,

$$\epsilon_{POD} = \frac{\left\| \mathbf{S}_P - \boldsymbol{\Psi}_P \boldsymbol{\Psi}_P^T \mathbf{S}_P \right\|}{\|\mathbf{S}_P\|} = \left(\frac{\sum_{i=N_P+1}^{N_s} \sigma_i^2}{\sum_{i=1}^{N_s} \sigma_i^2} \right)^{1/2} \tag{A.14}$$

For the POD approximation, the number of POD modes N_P is chosen such that the approximation error ϵ_{POD} of the snapshot matrix is less than 0.5%. In the problems considered in this study, $N_P < 50 \ll N_s \sim 1000$, and therefore the POD is an effective approach for the dimension reduction of a full-order system.

APPENDIX B

Smart Ordering Scheme for Efficient Sample Generation

The smart ordering scheme presented in the following is developed for the parallel generation of N_s samples using N_C groups of CPUs. Each group of CPUs are used to compute a group of $\frac{N_s}{N_C}$ samples. That means, N_C samples are computed in parallel. In each group, the samples are carefully ordered to satisfy the requirements proposed in Section 2.4.5, so as to reduce the total computational cost for sample generation.

The parallel sample generation is beneficial since a typical parallelized CFD solver does not have perfect linear scalablility. That means, more than N CPUs have to be used to accelerate the computation of a CFD sample by a factor of N. As a result, in terms of total computational cost, it is more efficient to generate as many samples as possible in parallel with fewer CPUs, instead of using as many CPUs as possible to generate one sample at a time.

The procedure of the smart ordering scheme is presented in the following,

1. Use OLH sampling to generate N_s samples. An example dataset with two parameters is shown in Fig. B.1(a). The star indicates the parameter combination for naive flow solution $\mathbf{w}_0$, e.g. the flow solution associated with an undeformed skin panel.
2. Create the k-Nearest-Neighbour (kNN) graph [206] from the samples, as illustrated in Fig. B.1(b). The samples are represented by the vertices of the graph. Each sample is connected to its k nearest neighbours, which are its candidate reference solutions.

The distance between two samples is defined using Eq. (2.81). The number k is chosen such that the graph is fully connected.

3. Divide the samples into n_C equal-sized groups using standard graph partition algorithm from the METIS package [207], as illustrated in Fig. B.1(c).
4. Generate the minimum spanning tree (MST) for each group of samples, represented by a subgraph. In the MST, the graph is fully connected, but some samples are disconnected to each other, such that the sum of the distances between the connected samples are minimized.
5. Starting from the naive flow solution $\mathbf{w}_0$, determine the reference solution for each sample. The dependency is represented using arrows in Fig. B.1(d). The sample at the tail of the arrow is the reference solution for the sample at the head of the arrow.

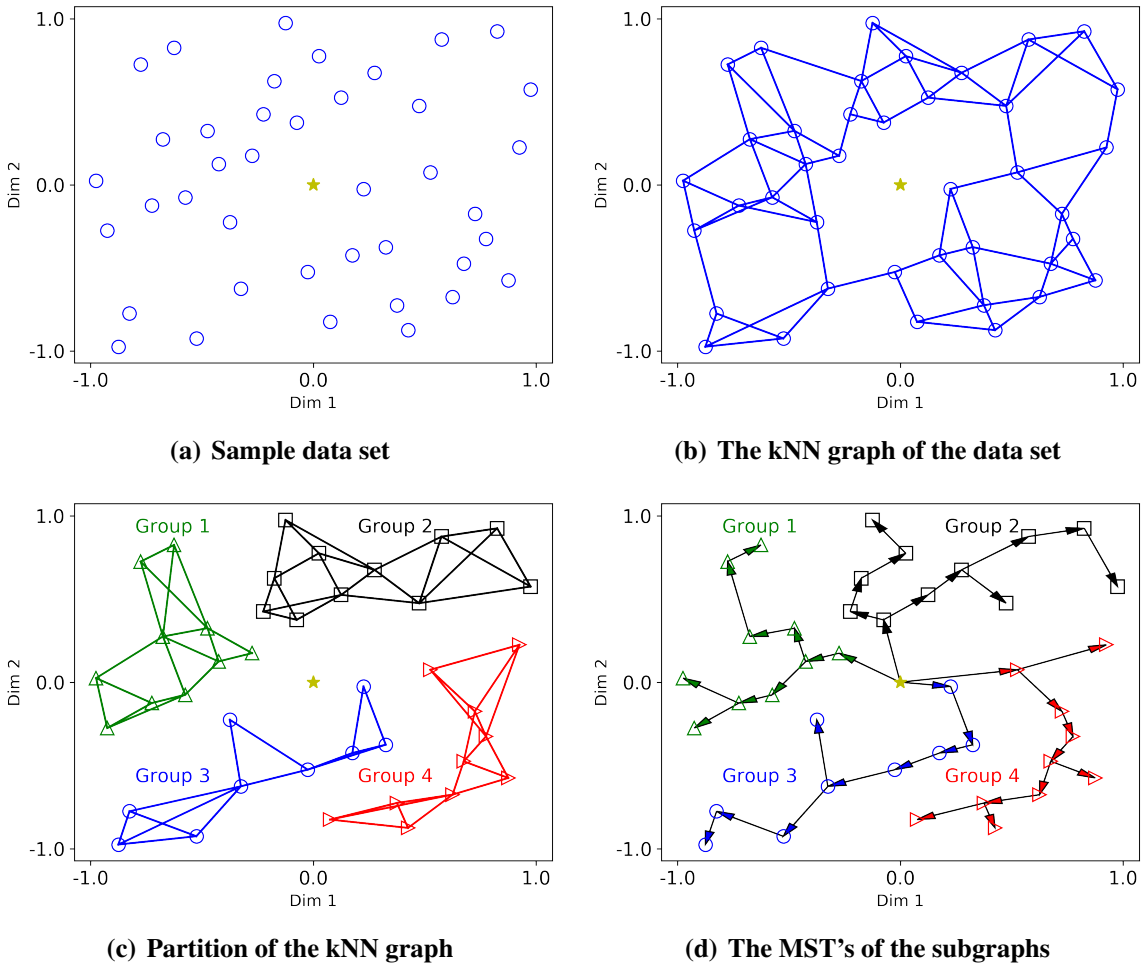

(a) Sample data set

(b) The kNN graph of the data set

(c) Partition of the kNN graph

(d) The MST's of the subgraphs

Figure B.1: Illustration of the smart ordering scheme

BIBLIOGRAPHY

[1] Lamorte, N. E., "Uncertainty Propagation in Hypersonic Vehicle Aerothermoelastic Analysis," Ph.D. thesis, University of Michigan, Ann Arbor, 2013.

[2] Gogulapati, A., Brouwer, K. R., Wang, X., Murthy, R., McNamara, J. J., and Mignolet, M. P., "Full and Reduced Order Aerothermoelastic Modeling of Built-Up Aerospace Panels in High-Speed Flows," *AIAA 2017–0180, 58th AIAA/ASCE/AHS/ASC Structures, Structural Dynamics, and Materials Conference*, Grapevine, TX, 2017, pp. 1–34. doi:10.2514/6.2017-0180.

[3] Woike, M., and Willis, B., "Mach 6 Integrated Systems Testing for the Hypersonic Tunnel Facility," *AIAA 2000–2446, 21st Aerodynamic Measurement Technology and Ground Testing Conference*, Denver, CO, 2000, pp. 1–10. doi:10.2514/6.2000-2446.

[4] Gaspers, P. A. J., Muhlstein, L. J., and Riddle, D. W., "An Experimental Study of the Influence of the Turbulent Boundary Layer on Panel Flutter," Tech. rep., NASA TN D-4486, Ames Research Center, Moffett Field, CA, 1968.

[5] U.S. Department of Defence, *Military Handbook, MIL–HDBK–5J: Metallic Materials and Elements for Aerospace Vehicle Structures*, U.S. Department of Defence, 1998, Chap. 3, pp. 368–426.

[6] U.S. Department of Defence, *Military Handbook, MIL–HDBK–5J: Metallic Materials and Elements for Aerospace Vehicle Structures*, U.S. Department of Defence, 1998, Chap. 6, pp. 51–76.

[7] George Tzong, Richard Jacobs, and Salvatore Liguore, "Predictive Capability for Hypersonic Structural Response and Life Prediction, Phase 1 – Identification of Knowledge Gaps, Volume I," Tech. Rep. AFRL-RB-WP-TR-2010-3068,V1, Wright-Patterson Air Force Base, Dayton, OH, Sep. 2010.

[8] McNamara, J. J., and Friedmann, P. P., "Aeroelastic and Aerothermoelastic Analysis in Hypersonic Flow: Past, Present, and Future," *AIAA Journal*, Vol. 49, No. 6, 2011, pp. 1089–1122. doi:10.2514/1.J050882.

[9] Zuchowski, B., "Predictive Capability for Hypersonic Structural Response and Life Prediction: Phase II – Detailed Design of Hypersonic Cruise Vehicle Hot-Structure," Tech. Rep. AFRL-RQ-WP-TR-2012-0280, Wright-Patterson Air Force Base, Dayton, OH, May 2012.

[10] Eason, T. G., and Spottswood, S., "A Structures Perspective on the Challenges Associated with Analyzing a Reusable Hypersonic Platform," *54th AIAA/ASME/ASCE/AHS/ASC Structures, Structural Dynamics, and Materials Conference*, Boston, MA, 2013, pp. 1–15. doi:10.2514/6.2013-1747.

[11] Bowcutt, K. G., "Physics Drivers of Hypersonic Vehicle Design," *AIAA 2018–5373, 22nd AIAA International Space Planes and Hypersonics Systems and Technologies Conference*, Orlando, FL, 2018, pp. 1–22. doi:10.2514/6.2018-5373.

[12] Walker, S. H., and Rodgers, F., "Falcon Hypersonic Technology Overview," *AIAA 20053253, AIAA/CIRA 13th International Space Planes and Hypersonics Systems and Technologies*, CIRA, Italy, 2005, pp. 1–7. doi:10.2514/6.2005-3253.

[13] McClinton, C. R., "X-43 Scramjet Power Breaks the Hypersonic Barrier: Dryden Lectureship in Research for 2006," *AIAA 20061, Proceedings of 44th AIAA Aerospace Sciences Meeting and Exhibit*, Reno, Nevada, 2006, pp. 1–18. doi: 10.2514/6.2006-1.

[14] Bolender, M. A., and Doman, D. B., "Nonlinear Longitudinal Dynamical Model of an Air-Breathing Hypersonic Vehicle," *Journal of Spacecraft and Rockets*, Vol. 44, No. 2, 2007, pp. 374–387. doi:10.2514/1.23370.

[15] Mansour, N., Pittman, J., and Olson, L., "Fundamental Aeronautics Hypersonics Project: Overview," *39th AIAA Thermophysics Conference*, Miami, FL, 2007, pp. 1–10. doi:10.2514/6.2007-4263.

[16] Dolvin, D., "Hypersonic International Flight Research and Experimentation (HiFiRE) Fundamental Science and Technology Development Strategy," *15th AIAA International Space Planes and Hypersonic Systems and Technologies Conference*, Dayton, OH, 2008, pp. 1–11. doi:10.2514/6.2008-2581.

[17] Shea, J. F., "Report of the Defense Science Board Task Force on the National Aerospace Plane (NASP)," Tech. Rep. ADA201124, Defense Science Board, Washington D.C., 1988.

[18] Bertin, J. J., *Hypersonic Aerothermodynamics*, AIAA Educational Series, 1994.

[19] Anderson, J. D., *Hypersonic and High Temperature Gas Dynamics*, AIAA, 2006.

[20] Culler, A. J., and McNamara, J. J., "Impact of Fluid-Thermal-Structural Coupling on Response Prediction of Hypersonic Skin Panels," *AIAA Journal*, Vol. 49, No. 11, 2011, pp. 2393–2406. doi:10.2514/1.J050617.

[21] McNamara, J. J., "Aeroelastic and Aerothermoelastic Behavior of Two and Three Dimensional Lifting Surfaces in Hypersonic Flow," Ph.D. thesis, University of Michigan, Ann Arbor, 2005.

[22] Brouwer, K. R., and McNamara, J. J., "Enriched Piston Theory for Expedient Aeroelastic Loads Prediction in the Presence of Shock Impingements," *AIAA Journal*, Vol. 57, No. 3, 2019, pp. 1288–1302. doi:10.2514/1.J057595.

[23] Blades, E., Shah, P. N., Nucci, M., and Miskovish, S., "Demonstration of Multiphysics Analysis Tools on Representative Hypersonic Vehicle Structures," *AIAA 2013–1746, Proceedings of the 54th Structures, Structural Dynamics, and Materials Conference*, Boston, Massachusetts, 2013, pp. 1–17. doi:10.2514/6.2013-1746.

[24] Dugundji, J., and Calligeros, J. M., "Similarity Laws for Aerothermoelastic Testing," *Journal of the Aerospace Sciences*, Vol. 29, No. 8, 1962, pp. 935–950. doi:10.2514/8.9663.

[25] Hank, J., Murphy, J., and Mutzman, R., "The X-51A Scramjet Engine Flight Demonstration Program," *AIAA 2008–2540, 15th AIAA International Space Planes and Hypersonic Systems and Technologies Conference*, Dayton, OH, 2008, pp. 1–13. doi:10.2514/6.2008-2540.

[26] "Meet the SR-72," http://www.lockheedmartin.com/us/news/features/2013/sr-72.html, 2013. Accessed: 03/27/2019.

[27] "Early Look: This Aircraft Concept Shows a Hypersonic Vehicle for Passengers," https://www.boeing.com/features/2018/06/hypersonic-concept-vehicle.page, 2018. Accessed: 11/16/2018.

[28] Lu, F. K., and Marren, D. E., *Advanced Hypersonic Test Facilities*, AIAA, 2002, Vol. 198, Chap. 10, pp. 279–314.

[29] Witeof, Z., "Exploratory Study on the Design of Combined Aero-Thermo-Structural Experiments in High Speed Flows," PhD Thesis, The Ohio State University, Columbus, OH, 2013. URL http://rave.ohiolink.edu/etdc/view?acc_num=osu1366213825.

[30] David, K., Gorham, J., Kim, S., Miller, P., and Minkus, C., "Aeronautical Wind Tunnels, Europe and Asia," Tech. rep., Federal Research Division Library of Congress, Washington, DC, 2006.

[31] Goodrich, M., and Gorham, J., "Wind Tunnels of the Western Hemisphere," Tech. rep., Federal Research Division Library of Congress, Washington, DC, 2008.

[32] Shih, P. K., Prunty, J., and Gopaul, N., "Thermostructural Concepts for Hypervelocity Vehicles," *Journal of Aircraft*, Vol. 28, No. 5, 1991, pp. 337–345. doi:10.2514/3.46032.

[33] Van Wie, D., Drewry, D., King, D., and Hudson, C., "The Hypersonic Environment: Required Operating Conditions and Design Challenges," *Journal of Materials Science*, Vol. 39, No. 19, 2004, pp. 5915–5924. doi:10.1023/B:JMSC.0000041688.68135.8b.

[34] Blosser, M., Poteet, C., Chen, R., Dorsey, J., Schmidt, I., Bird, R., and Wurster, K., "Development of Advanced Metallic-Thermal-Protection System Prototype Hardware," *Journal of Spacecraft and Rockets*, Vol. 41, No. 2, 2004, pp. 183–194. doi: 10.2514/1.9179.

[35] Poteet, C. C., Abu-Khajeel, H., and Hsu, S.-Y., "Preliminary Thermal-Mechanical Sizing of a Metallic Thermal Protection System," *Journal of Spacecraft and Rockets*, Vol. 41, No. 2, 2004, pp. 173–182. doi:10.2514/1.9174.

[36] Ellis, D., Pagel, L., and Schaeffer, D., "Design and Fabrication of a Radiative Actively Cooled Honeycomb Sandwich Structural Panel for a Hypersonic Aircraft." Tech. Rep. NASA CR 2957, Langley Research Center, Mar. 1978.

[37] Koch, L. C., and Pagel, L., "High Heat Flux Activity Cooled Honeycomb Sandwich Structural Panel for a Hypersonic Aircraft." Tech. rep., McDonnell Douglas Corp., 1978.

[38] Thornton, E. A., *Thermal Structures for Aerospace Applications*, American Institute of Aeronautics and Astronautics, Reston, VA, 1996.

[39] Collier, C., "Thermoelastic Formulation of Stiffened, Unsymmetric Composite Panels for Finite Element Analysis of High Speed Aircraft," *Proceedings of 35th AIAA/ASME/ASCE/AHS/ASC Structures, Structural Dynamics, and Materials Conference*, New Orleans, LA, 1994, pp. 2076–2086. doi:10.2514/6.1994-1579.

[40] Blosser, M. L., "Development of Metallic Thermal Protection Systems for the Reusable Launch Vehicle," *AIP Conference Proceedings*, Vol. 387, No. 1, 1997, pp. 1125–1144. doi:10.1063/1.51930.

[41] Gogu, C., Bapanapalli, S. K., Haftka, R. T., and Sankar, B. V., "Comparison of Materials for an Integrated Thermal Protection System for Spacecraft Reentry," *Journal of Spacecraft and Rockets*, Vol. 46, No. 3, 2009, pp. 501–513. doi:10.2514/1.35669.

[42] Martinez, O. A., Sharma, A., Sankar, B. V., Haftka, R. T., and Blosser, M. L., "Thermal Force and Moment Determination of an Integrated Thermal Protection System," *AIAA Journal*, Vol. 48, No. 1, 2010, pp. 119–128. doi:10.2514/1.40678.

[43] Ravishankar, B., Sankar, B. V., and Haftka, R. T., "Homogenization of Integrated Thermal Protection System with Rigid Insulation Bars," *AIAA 2010-2687, Proceeding of the 51st AIAA/ASME/ASCE/AHS/ASC Structures, Structural Dynamics, and Materials Conference*, Orlando, Florida, 2010, pp. 1–12. doi:10.2514/6.2010-2687.

[44] Zuchowski, B., "Predictive Capability for Hypersonic Structural Response and Life Prediction Phase 1 - Identification of Knowledge Gaps," Tech. Rep. AFRL-RB-WP-TR-2010-3069, Wright-Patterson Air Force Base, Dayton, OH, August 2010.

[45] Mei, C., Abdel-Motagaly, K., and Chen, R., "Review of Nonlinear Panel Flutter at Supersonic and Hypersonic Speeds," *Applied Mechanics Reviews*, Vol. 52, No. 10, 1999, pp. 321–332. doi:10.1115/1.3098919.

[46] Fung, Y., "On Two-Dimensional Panel Flutter," *Journal of the Aerospace Sciences*, Vol. 25, No. 3, 1958, pp. 145–160. doi:10.2514/8.7557.

[47] Dowell, E. H., "Nonlinear Oscillations of a Fluttering Plate," *AIAA Journal*, Vol. 4, No. 7, 1966, pp. 1267–1275. doi:10.2514/3.3658.

[48] Friedmann, P., and Hanin, M., "Supersonic Non Linear Flutter of Orthotropic or Isotropic Panels with 'arbitrary' Flow Direction," *Israel Journal of Technology*, Vol. 6, 1968, pp. 46–57.

[49] Dowell, E. H., *Aeroelasticity of Plates and Shells*, Vol. 1, Springer Science & Business Media, 1974. doi:10.1115/1.3423871.

[50] Dowell, E. H., and Ilgamov, M., *Studies in Nonlinear Aeroelasticity*, Springer-Verlag, New York, 1988, Chap. 5, pp. 163–186.

[51] Lighthill, M., "Oscillating Airfoils at High Mach Number," *Journal of the Aeronautical Sciences*, Vol. 20, No. 6, 1953, pp. 402–406. doi:10.2514/8.2657.

[52] Ashley, H., and Zartarian, G., "Piston Theory – a New Aerodynamic Tool for The Aeroelastician," *Journal of the Aeronautical Sciences*, Vol. 23, No. 12, 1956, pp. 1109–1118. doi:10.2514/8.3740.

[53] Xue, D. Y., and Mei, C., "Finite Element Nonlinear Panel Flutter With Arbitrary Temperatures in Supersonic Flow," *AIAA Journal*, Vol. 31, No. 1, 1993, pp. 154–162. doi:10.2514/3.11332.

[54] Cheng, G., "Finite Element Modal Formulation for Panel Flutter at Hypersonic Speeds and Elevated Temperatures," Ph.D. thesis, Old Dominion University, Norfolk, VA, 2002.

[55] Cheng, G., Lee, Y. Y., and Mei, C., "Flow Angle, Temperature, and Aerodynamic Damping on Supersonic Panel Flutter Stability Boundary," *Journal of Aircraft*, Vol. 40, No. 2, 2003, pp. 248–255. doi:10.2514/2.3116.

[56] Bein, T., Friedmann, P., Zhong, X., and Nydick, I., "Hypersonic Flutter of a Curved Shallow Panel with Aerodynamic Heating," *AIAA Paper 93-1318, 34th AIAA/ASME/ASCE/AHS/ASC Structures, Structural Dynamics and Materials Conference AIAA/ASME Adaptive Structures Forum*, La Jolla, CA, 1993, pp. 1–16. doi:10.2514/6.1993-1318.

[57] Nydick, I., Friedmann, P. P., and Zhong, X., "Hypersonic Panel Flutter Studies on Curved Panels," *AIAA Paper 95-1485-CP, Proceedings of 34th AIAA/ASME/ASCE/AHS/ASC Structures, Structural Dynamics, and Materials Conference*, New Orleans, LA, 1995, pp. 2995–3011.

[58] Klock, R., and Cesnik, C. E., "Aeroelastic Stability of High-Speed Cylindrical Vehicles," *58th AIAA/ASCE/AHS/ASC Structures, Structural Dynamics, and Materials Conference*, Grapevine, TX, 2017, pp. 1–13. doi:10.2514/6.2017-0406.

[59] Gordnier, R. E., and Visbal, M. R., "Development of a Three-Dimensional Viscous Aeroelastic Solver for Nonlinear Panel Flutter," *Journal of Fluids and Structures*, Vol. 16, No. 4, 2002, pp. 497–527. doi:10.1006/jfls.2000.0434.

[60] Gordnier, R. E., and Visbal, M. R., "Computation of Three-Dimensional Nonlinear Panel Flutter," *Journal of Aerospace Engineering*, Vol. 16, No. 4, 2003, pp. 155–166. doi:10.1061/(ASCE)0893-1321(2003)16:4(155).

[61] Hashimoto, A., Aoyama, T., and Nakamura, Y., "Effects of Turbulent Boundary Layer on Panel Flutter," *AIAA Journal*, Vol. 47, No. 12, 2009, pp. 2785–2791. doi: 10.2514/1.35786.

[62] Miguel R. Visbal, "Viscous and Inviscid Interactions of an Oblique Shock With a Flexible Panel," *Journal of Fluids and Structures*, Vol. 48, 2014, pp. 27–45. doi: 10.1016/j.jfluidstructs.2014.02.003.

[63] Gogulapati, A., Deshmukh, R., Crowell, A., and etc., "Response of a Panel to Shock Impingement: Modeling and Comparison with Experiments," *AIAA 2014–0148, Proc. 55th AIAA/ASME/ASCE/AHS/ASC Structures, Structural Dynamics and Materials Conference*, National Harbor, Maryland, 2014, pp. 1–23. doi:10.2514/6.2014-0148.

[64] Gogulapati, A., Deshmukh, R., McNamara, J. J., Vyas, V., Wang, X. Q., Mignolet, M., Beberniss, T., Spottswood, S. M., and Eason, T. G., "Response of a Panel to Shock Impingement: Modeling and Comparison with Experiments - Part 2," *AIAA Paper 2015-0685, 56th AIAA/ASCE/AHS/ASC Structures, Structural Dynamics, and Materials Conference*, Kissimmee, Florida, 2015, pp. 1–27. doi:10.2514/6.2015-0685.

[65] Nathan R. Boyer, Jack J. McNamara, and Miguel R. Visbal, "Study on Shock-Induced Panel Flutter in 2-D Laminar Flow," *AIAA 2016-1091, 15th Dynamics Specialists Conference*, San Diego, CA, 2016, pp. 1–14. doi:10.2514/6.2016-1091.

[66] Culler, A. J., "Coupled Fluid-Thermal-Structural Modeling and Analysis of Hypersonic Flight Vehicle Structures," Ph.D. thesis, The Ohio State University, 2010.

[67] Eckert, E. R. G., "Survey of Boundary Layer Heat Transfer at High Velocities and High Temperatures," Tech. rep., Minnesota. Univ., Minneapolis. Heat Transfer Lab., 1960.

[68] Dugundji, J., "Theoretical Considerations of Panel Flutter at High Supersonic Mach Numbers," *AIAA Journal*, Vol. 4, No. 7, 1966, pp. 1257–1266. doi:10.2514/3.3657.

[69] Donea, J., Giuliani, S., and Halleux, J., "An Arbitrary Lagrangian-Eulerian Finite Element Method for Transient Dynamic Fluid-Structure Interactions," *Computer Methods in Applied Mechanics and Engineering*, Vol. 33, No. 1, 1982, pp. 689–723. doi:10.1016/0045-7825(82)90128-1.

[70] Morton, S. A., Melville, R. B., and Visbal, M. R., "Accuracy and Coupling Issues of Aeroelastic Navier-Stokes Solutions on Deforming Meshes," *Journal of Aircraft*, Vol. 35, No. 5, 1998, pp. 798–805. doi:10.2514/2.2372.

[71] Bartels, R. E., "Mesh Strategies for Accurate Computation of Unsteady Spoiler and Aeroelastic Problems," *Journal of Aircraft*, Vol. 37, No. 3, 2000, pp. 521–525.

[72] Biedron, R. T., and Thomas, J. L., "Recent Enhancements to the FUN3D Flow Solver for Moving-Mesh Applications," *AIAA Paper 2009-1360, 47th AIAA Aerospace Sciences Meeting Including The New Horizons Forum and Aerospace Exposition*, Orlando, Florida, 2009, pp. 1–19.

[73] Felippa, C. A., Park, K., and Farhat, C., "Partitioned Analysis of Coupled Mechanical Systems," *Computer Methods in Applied Mechanics and Engineering*, Vol. 190, No. 24, 2001, pp. 3247–3270. doi:10.1016/S0045-7825(00)00391-1.

[74] Farhat, C., Geuzaine, P., and Grandmont, C., "The Discrete Geometric Conservation Law and the Nonlinear Stability of ALE Schemes for the Solution of Flow Problems on Moving Grids," *Journal of Computational Physics*, Vol. 174, No. 2, 2001, pp. 669–694. doi:10.1006/jcph.2001.6932.

[75] Farhat, C., Van der Zee, K. G., and Geuzaine, P., "Provably Second-Order Time-Accurate Loosely-Coupled Solution Algorithms for Transient Nonlinear Computational Aeroelasticity," *Computer Methods in Applied Mechanics and Engineering*, Vol. 195, No. 17, 2006, pp. 1973–2001. doi:10.1016/j.cma.2004.11.031.

[76] Farhat, C., Lesoinne, M., and Le Tallec, P., "Load and Motion Transfer Algorithms for Fluid/Structure Interaction Problems With Non–Matching Discrete Interfaces: Momentum and Energy Conservation, Optimal Discretization and Application to Aeroelasticity," *Computer Methods in Applied Mechanics and Engineering*, Vol. 157, No. 1–2, 1998, pp. 95–114. doi:10.1016/S0045-7825(97)00216-8.

[77] Bendiksen, O. O., "A New Approach to Computational Aeroelasticity," *AIAA paper 91–0939, Proceedings of AIAA/ASCE/AHS/ASC 32nd Structures, Structural Dynamics and Materials Conference*, Baltimore, MD, 1991, pp. 1712–1727. doi: 10.2514/91-0939.

[78] Piperno, S., and Farhat, C., "Partitioned Procedures for the Transient Solution of Coupled Aeroelastic Problems – Part II: Energy Transfer Analysis and Three-Dimensional Applications," *Comput. Methods in Applied Mechanics and Engineering*, Vol. 190, No. 24, 2001, pp. 3147–3170. doi:10.1016/S0045-7825(00)00386-8.

[79] Tran, H., and Farhat, C., "An Integrated Platform for the Simulation of Fluid-Structure-Thermal Interaction Problems," *AIAA 2002-1307, 43rd AIAA/ASME/ASCE/AHS/ASC Structures, Structural Dynamics, and Materials Conference*, Denver, Colorado, 2002, pp. 1–9. doi:10.2514/6.2002-1307.

[80] Miller, B. A., Crowell, A. R., and McNamara, J. J., "Loosely Coupled Time-Marching of Fluid-Thermal-Structural Interactions," *AIAA 2013-1666, 54th AIAA/ASME/ASCE/AHS/ASC Structures, Structural Dynamics, and Materials Conference*, Boston, Massachusetts, 2013, pp. 1–17. doi:10.2514/6.2013-1666.

[81] Miller, B. A., and McNamara, J. J., "Time-Marching Considerations for Response Prediction of Structures in Hypersonic Flows," *AIAA Journal*, Vol. 53, No. 10, 2015, pp. 3028–3038. doi:10.2514/1.J053872.

[82] Miller, B. A., and McNamara, J. J., "Efficient Fluid-Thermal-Structural Time Marching with Computational Fluid Dynamics," *AIAA Journal*, Vol. 56, No. 9, 2018, pp. 3610–3621. doi:10.2514/1.J056572.

[83] Gaitonde, D. V., "Progress in Shock Wave/Boundary Layer Interactions," *Progress in Aerospace Sciences*, Vol. 72, 2015, pp. 80–99. doi:10.1016/j.paerosci.2014.09.002.

[84] Brouwer, K. R., Gogulapati, A., and McNamara, J. J., "Interplay of Surface Deformation and Shock-Induced Separation in Shock/Boundary-Layer Interactions," *AIAA Journal*, Vol. 55, No. 12, 2017, pp. 4258–4273. doi:10.2514/1.J056030.

[85] Hodges, D. H., and Pierce, G. A., *Introduction to Structural Dynamics and Aeroelasticity*, Cambridge University Press, 2011, Vol. 15, Chap. 5, pp. 175–200. doi:10.1017/CBO9780511997112.

[86] Cunningham, H. J., Batina, J. T., and Bennett, R. M., "Modern Wing Flutter Analysis by Computational Fluid Dynamics Methods," *Journal of Aircraft*, Vol. 25, No. 10, 1988, pp. 962–968. doi:10.2514/3.45686.

[87] Pak, C.-G., and Friedmann, P., "New Time-Domain Technique for Flutter Boundary Identification," *AIAA Paper 92–2102–CP, Proceedings of AIAA Dynamics Specialists Conference*, Dallas, TX, 1992, pp. 201–214.

[88] Torii, H., and Matsuzaki, Y., "Flutter Margin Evaluation for Discrete-Time Systems," *Journal of Aircraft*, Vol. 38, No. 1, 2001, pp. 42–47. doi:10.2514/2.2732.

[89] Raveh, D. E., "Identification of Computational-Fluid-Dynamics Based Unsteady Aerodynamic Models for Aeroelastic Analysis," *Journal of Aircraft*, Vol. 41, No. 3, 2004, pp. 620–632. doi:10.2514/1.3149.

[90] McNamara, J. J., and Friedmann, P. P., "Flutter Boundary Identification for Time-Domain Computational Aeroelasticity," *AIAA Journal*, Vol. 45, No. 7, 2007, pp. 1546–1555. doi:10.2514/1.26706.

[91] Crowell, A. R., McNamara, J., and Miller, B., "Hypersonic Aerothermoelastic Response Prediction of Skin Panels Using Computational Fluid Dynamic Surrogates," *Journal of Aeroelasticity and Structural Dynamics*, Vol. 2, No. 2, 2011. doi:10.3293/asdj.2011.11.

[92] Carlberg, K. T., "Model Reduction of Nonlinear Mechanical Systems via Optimal Projection and Tensor Approximation," Ph.D. thesis, Stanford University, 2011.

[93] Sirovich, L., "Turbulence and the Dynamics of Coherent Structures, Part I: Coherent Structures," *Quarterly of Applied Mathematics*, Vol. 45, No. 3, 1987, pp. 561–571. doi:10.1090/qam/910462.

[94] Berkooz, G., Holmes, P., and Lumley, J. L., "The Proper Orthogonal Decomposition in the Analysis of Turbulent Flows," *Annual Review of Fluid Mechanics*, Vol. 25, 1993, pp. 539–575. doi:10.1146/annurev.fl.25.010193.002543.

[95] Hall, K. C., Thomas, J. P., and Dowell, E. H., "Proper Orthogonal Decomposition Technique for Transonic Unsteady Aerodynamic Flows," *AIAA Journal*, Vol. 38, No. 2, 2000, pp. 1853–1862. doi:10.2514/2.867.

[96] Epureanu, B. I., "A Parametric Analysis of Reduced Order Models of Viscous Flows in Turbomachinery," *Journal of Fluids and Structures*, Vol. 17, No. 7, 2003, pp. 971–982. doi:10.1016/S0889-9746(03)00044-6.

[97] Thomas, J. P., Dowell, E. H., and Hall, K. C., "Three-Dimensional Transonic Aeroelasticity Using Proper Orthogonal Decomposition-Based Reduced Order Models," *Journal of Aircraft*, Vol. 40, No. 3, 2003, pp. 544–551. doi:10.2514/2.3128.

[98] Amsallem, D., and Farhat, C., "An Interpolation Method for Adapting Reduced-Order Models and Application to Aeroelasticity," *AIAA Journal*, Vol. 46, No. 7, 2008, pp. 1803–1813. doi:10.2514/1.35374.

[99] Rowley, C. W., Colonius, T., and Murray, R. M., "Model Reduction for Compressible Flows Using POD and Galerkin Projection," *Physica D: Nonlinear Phenomena*, Vol. 189, No. 1, 2004, pp. 115–129. doi:10.1016/j.physd.2003.03.001.

[100] Kalashnikova, I., Arunajatesan, S., Barone, M. F., van Bloemen Waanders, B. G., and Fike, J. A., "Reduced Order Modeling for Prediction and Control of Large-Scale Systems," Tech. Rep. Report SAND2014-4693, Sandia National Lab., 2014.

[101] Crowell, A. R., McNamara, J. J., Kecskemety, K. M., and Goerig, T., "A Reduced Order Aerothermodynamic Modeling Framework for Hypersonic Aerothermoelasticity," *AIAA Paper 2010-2969, 51th AIAA/ASCE/AHS/ASC Structures, Structural Dynamics, and Materials Conference*, 2015, pp. 1–22. doi:10.2514/6.2010-2969.

[102] Falkiewicz, N. J., S. Cesnik, C. E., Crowell, A. R., and McNamara, J. J., "Reduced-Order Aerothermoelastic Framework for Hypersonic Vehicle Control Simulation," *AIAA Journal*, Vol. 49, No. 8, 2011, pp. 1625–1646. doi:10.2514/1.J050802.

[103] Crowell, A. R., and McNamara, J. J., "Model Reduction of Computational Aerothermodynamics for Hypersonic Aerothermoelasticity," *AIAA Journal*, Vol. 50, No. 1, 2012, pp. 74–84. doi:10.2514/1.J051094.

[104] Lucia, D. J., Beran, P. S., and Silva, W. A., "Reduced-Order Modeling: New Approaches for Computational Physics," *Progress in Aerospace Sciences*, Vol. 40, No. 1, 2004, pp. 51–117.

[105] Rasmussen, C. E., and Williams, C. K. I., *Gaussian Processes for Machine Learning*, The MIT Press, Cambridge, MA, 2006.

[106] Bryan Glaz, "Active/Passive Optimization of Helicopter Rotor Blades for Improved Vibration, Noise, and Performance Characteristics," Ph.D. thesis, University of Michigan, Ann Arbor, 2008.

[107] Forrester, A., Sobester, A., and Keane, A., *Engineering Design Via Surrogate Modelling: A Practical Guide*, John Wiley & Sons, 2008. doi:10.2514/4.479557.

[108] Skujins, T., and Cesnik, C. E., "Reduced-Order Modeling of Hypersonic Vehicle Unsteady Aerodynamics," *Proceedings of the 2010 AIAA Guidance, Navigation, and Control Conference*, Toronto, Ontario Canada, 2010, pp. 1–15. doi:10.2514/6.2010-8127.

[109] Skujins, T., and Cesnik, C. E. S., "Reduced-Order Modeling of Unsteady Aerodynamics Across Multiple Mach Regimes," *Journal of Aircraft*, Vol. 51, No. 6, 2014, pp. 1681–1704. doi:10.2514/1.C032222.

[110] McNamara, J. J., Crowell, A. R., Friedmann, P. P., Glaz, B., and Gogulapati, A., "Approximate Modeling of Unsteady Aerodynamics for Hypersonic Aeroelasticity," *Journal of Aircraft*, Vol. 47, No. 6, 2010, pp. 1932–1945. doi:10.2514/1.C000190.

[111] Smarslok, B. P., "Quantifying Confidence in Model Predictions for Hypersonic Aircraft Structures," Tech. Rep. AFRL-RQ-WP-TR-2015-0069, Air Force Research Laboratory, Mar. 2015.

[112] Spain, C. V., Zeiler, T. A., Bullock, E., and Hodge, J. S., "A Flutter Investigation of All-Moveable NASP-Like Wings at Hypersonic Speeds," *AIAA-93-1315, 34th AIAA/ASME/ASCE/AHS/ASC Structures, Structural Dynamics and Materials Conference*, La Jolla, CA, 1993, pp. 1–9. doi:10.2514/6.1993-1315.

[113] Crowell, A. R., "Model Reduction of Computational Aerothermodynamics for Multi-Discipline Analysis in High Speed Flows," Ph.D. thesis, The Ohio State University, 2013.

[114] Crowell, A. R., Miller, B. A., and McNamara, J. J., "Robust and Efficient Treatment of Temperature Feedback in Fluid–Thermal–Structural Analysis," *AIAA Journal*, Vol. 52, No. 11, 2014, pp. 2395–2413.

[115] Buckingham, E., "On Physically Similar Systems; Illustrations of the Use of Dimensional Equations," *Physics Review*, Vol. 4, 1914, pp. 345–376.

[116] Bridgman, P. W., *Dimensional Analysis*, Yale University Press, 1922.

[117] Bisplinghoff, R. L., Ashley, H., and Halfman, R. L., *Aeroelasticity*, Addison-Wesley Publishing Company, 1955.

[118] Wasserman, L. S., and Mykytow, W. J., "Model Construction, Part IV," *AGARD Manual on Aeroelasticity*, Vol. 7, 1963, pp. 1–30.

[119] Ivanco, T. G., "Unique Testing Capabilities of the NASA Langley Transonic Dynamics Tunnel, an Exercise in Aeroelastic Scaling," *AIAA 2013-2625, Ground Testing Conference*, 2013, pp. 1–23.

[120] French, M., "An Application of Structural Optimization in Wind Tunnel Model Design," *AIAA-90-0956-CP, 31st Structures, Structural Dynamics and Materials Conference*, Long Beach, CA, 1990, pp. 127–134.

[121] French, M., and Eastep, F., "Aeroelastic Model Design Using Parameter Identification," *Journal of Aircraft*, Vol. 33, No. 1, 1996, pp. 198–202.

[122] Richards, J., Suleman, A., Canfield, R., and Blair, M., "Design of a Scaled RPV for Investigation of Gust Response of Joined-Wing Sensorcraft," *50th AIAA/ASME/ASCE/AHS/ASC Structures, Structural Dynamics, and Materials Conference 17th AIAA/ASME/AHS Adaptive Structures Conference 11th AIAA No*, Palm Springs, CA, 2009, pp. 1–14. doi:10.2514/2009-2218.

[123] Mas-Colomer, J., "Aeroelastic Similarity of a Flight Demonstrator via Multidisciplinary Optimization," Ph.D. thesis, Universite de Toulouse, Toulouse, French, 2018.

[124] Bond, V. L., Canfield, R. A., Suleman, A., and Blair, M., "Aeroelastic Scaling of a Joined Wing for Nonlinear Geometric Stiffness," *AIAA Journal*, Vol. 50, No. 3, 2012, pp. 513–522.

[125] Wan, Z., and Cesnik, C. E., "Geometrically Nonlinear Aeroelastic Scaling for Very Flexible Aircraft," *AIAA Journal*, Vol. 52, No. 10, 2014, pp. 2251–2260.

[126] Ricciardi, A. P., "Geometrically Nonlinear Aeroelastic Scaling," Ph.D. thesis, Virginia Tech, Blacksburg, Virginia, 2014.

[127] Pototzky, A., "Scaling Laws Applied to a Modal Formulation of the Aeroelastic Equations," *43rd AIAA/ASME/ASCE/AHS/ASC Structures, Structural Dynamics, and Materials Conference*, Denver, CO, 2002, pp. 1–11. doi:10.2514/2002-1598.

[128] Friedmann, P., Guillot, D., and Presente, E., "Adaptive Control of Aeroelastic Instabilities in Transonic Flow and Its Scaling," *Journal of Guidance, Control, and Dynamics*, Vol. 20, No. 6, 1997, pp. 1190–1199.

[129] Friedmann, P. P., "Innovative Scaling Laws for Study of Nonlinear Aeroelastic and Aeroservoelastic Problems." Tech. Rep. AFRL-SR-BL-TR-98-0564, Univ. of California, Dept. of Mechanical and Aerospace Engineering, Los Angeles, CA, Apr. 1998.

[130] Friedmann, P., and Presente, E., "Active Control of Flutter in Compressible Flow and Its Aeroelastic Scaling," *Journal of Guidance, Control, and Dynamics*, Vol. 24, No. 1, 2001, pp. 167–175.

[131] Friedmann, P., "Aeroelastic Scaling for Rotary-Wing Aircraft With Applications," *Journal of Fluids and Structures*, Vol. 19, No. 5, 2004, pp. 635–650. doi:10.1016/j.jfluidstructs.2004.03.003.

[132] Molyneux, W., "A Consideration of the Similarity Requirements for Aerothermoelastic Test on Reduced Scale Models," Tech. rep., Ministry of Aviation, Royal Aircraft Establishment, RAE Farnborough, 1962.

[133] Scruton, C., and Lambourne, N., "Similarity Requirements for Flutter Model Testing, Part IV," *AGARD Manual on Aeroelasticity*, Vol. 6, 1963, pp. 1–26.

[134] Tsien, H.-S., "Similarity Laws of Hypersonic Flows," *Studies in Applied Mathematics*, Vol. 25, No. 1–4, 1946, pp. 247–251.

[135] Hayes, W. D., and Probstein, R. F., "Viscous Hypersonic Similitude," *Journal of the Aerospace Sciences*, Vol. 26, No. 12, 1959, pp. 815–824.

[136] Calligeros, J. M., and Dugundji, J., "Similarity Laws Required for Experimental Aerothermoelastic Studies," Tech. Rep. TR 75–1, Office of Naval Research, 1959.

[137] Calligeros, J. M., and Dugundji, J., "Similarity Laws Required for Experimental Aerothermoelastic Studies. Part 2 Hypersonic Speeds," Tech. Rep. TR 75–2, Office of Naval Research, 1961.

[138] Lamorte, N., Friedmann, P. P., Dalle, D. J., Torrez, S. M., and Driscoll, J. F., "Uncertainty Propagation in Integrated Airframe–Propulsion System Analysis for Hypersonic Vehicles," *Journal of Propulsion and Power*, Vol. 31, No. 1, 2014, pp. 54–68.

[139] Riley, Z. B., Perez, R. A., Bartram, G. W., Spottswood, S. M., Smarslok, B. P., and Beberniss, T. J., "Aerothermoelastic Experimental Design for the AEDC/VKF Tunnel C: Challenges Associated With Measuring the Response of Flexible Panels in High-Temperature, High-Speed Wind Tunnels," *Journal of Sound and Vibration*, Vol. 441, 2019, pp. 96–105. doi:10.1016/j.jsv.2018.10.022.

[140] Ostoich, C., "Aerothermal and Aeroelastic Response Prediction of Aerospace Structures in High-Speed Flows Using Direct Numerical Simulation," Ph.D. thesis, University of Illinois at Urbana-Champaign, 2013.

[141] Wilcox, D. C., *Turbulence Modeling for CFD*, DCW Industries, La Cañada, CA, 2006, Chap. 5, pp. 239–302.

[142] Spalart, P., and Allmaras, S., "A One-Equation Turbulence Model for Aerodynamic Flows," *30th Aerospace Sciences Meeting and Exhibit*, Reno, NV, 1992, pp. 1–17. doi:10.2514/6.1992-439.

[143] Roy, C. J., and Blottner, F. G., "Review and Assessment of Turbulence Models for Hypersonic Flows," *Progress in Aerospace Sciences*, Vol. 42, No. 7-8, 2006, pp. 469–530. doi:10.1016/j.paerosci.2006.12.002.

[144] Bartels, R. E., Rumsey, C. L., and Biedron, R. T., "CFL3D Version 6.4, General Usage and Aeroelastic Analysis," Tech. rep., NASA Langley Research Center, 2006.

[145] Thomas, P., and Lombard, C., "Geometric Conservation Law and Its Application to Flow Computations on Moving Grids," *AIAA Journal*, Vol. 17, No. 10, 1979, pp. 1030–1037. doi:10.2514/3.61273.

[146] Geuzaine, P., Grandmont, C., and Farhat, C., "Design and Analysis of ALE Schemes With Provable Second-Order Time-Accuracy for Inviscid and Viscous Flow Simulations," *Journal of Computational Physics*, Vol. 191, No. 1, 2003, pp. 206–227. doi:10.1016/S0021-9991(03)00311-5.

[147] Huang, D., Rokita, T., and Friedmann, P. P., "An Integrated Aerothermoelastic Analysis Framework With Application to Skin Panels," *AIAA Journal*, 2018. doi: 10.2514/1.J056677.

[148] Huang, D., and Friedmann, P. P., "An Integrated Aerothermoelastic Analysis Framework for Predicting the Response of Composite Panels," *AIAA 2016-1090, 15th Dynamics Specialists Conference*, San Diego, CA, 2016, pp. 1–37. doi:10.2514/6. 2016-1090.

[149] van der Weide, E., Kalitzin, G., Schluter, J., and Alonso, J. J., "Unsteady Turbomachinery Computations Using Massively Parallel Platforms," *AIAA Paper 2006–0421, 44th AIAA Aerospace Sciences Meeting and Exhibit*, Reno, NV, 2006, pp. 1–16. doi: 10.2514/2006-0421.

[150] Kenway, G. K. W., Secco, N., Martins, J. R. R. A., Mishra, A., and Duraisamy, K., "An Efficient Parallel Overset Method for Aerodynamic Shape Optimization," *AIAA 2017–0357, Proceedings of the 58th AIAA/ASCE/AHS/ASC Structures, Structural Dynamics, and Materials Conference, AIAA SciTech Formum*, Grapevine, TX, 2017, pp. 1–30. doi:10.2514/2017-0357.

[151] Deshmukh, R., Culler, A. J., Miller, B. A., and McNamara, J. J., "Response of Skin Panels to Combined Self-And Boundary Layer-Induced Fluctuating Pressure," *Journal of Fluids and Structures*, Vol. 58, 2015, pp. 216–235. doi:10.1016/j.jfluidstructs. 2015.08.008.

[152] Cox, R. N., and Crabtree, L. F., *Elements of Hypersonic Aerodynamics*, Academic Press, 1965, Chap. 7, pp. 177–180. doi:10.1063/1.3048343.

[153] Pope, S. B., *Turbulent Flows*, IOP Publishing, Cambridge, UK, 2001, Chap. 7, pp. 298–321. doi:10.1017/cbo9780511840531.

[154] Boley, B. A., "Approximate Analyses of Thermally Induced Vibrations of Beams and Plates," *Journal of Applied Mechanics*, Vol. 39, No. 1, 1972, pp. 212–216.

[155] Queipo, N. V., Haftka, R. T., Shyy, W., Goel, T., Vaidyanathan, R., and Tucker, P. K., "Surrogate-Based Analysis and Optimization," *Progress in Aerospace Sciences*, Vol. 41, No. 1, 2005, pp. 1–28. doi:10.1016/j.paerosci.2005.02.001.

[156] Reddy, J. N., *Mechanics of Laminated Composite Plates and Shells: Theory and Analysis*, CRC Press, New York, 2004.

[157] Qatu, M. S., "Recent Research Advances in the Dynamic Behavior of Shells: 1989-2000, Part 1: Laminated Composite Shells," *Applied Mechanics Reviews*, Vol. 55, No. 4, 2002, pp. 325–350.

[158] Hughes, T. J., *The Finite Element Method: Linear Static and Dynamic Finite Element Analysis*, Prentice Hall, Englewood Cliffs, New Jersey, 1987. doi:10.1016/0045-7825(87)90013-2.

[159] Bathe, K.-J., *Finite element procedures*, Prentice Hall, Englewood Cliffs, New Jersey, 1996.

[160] Newmark, N. M., "A Method of Computation for Structural Dynamics," *Journal of the Engineering Mechanics Division*, Vol. 85, No. 3, 1959, pp. 67–94.

[161] Hilber, H. M., Hughes, T. J. R., and Taylor, R. L., "Improved Numerical Dissipation for Time Integration Algorithms in Structural Dynamics," *Earthquake Engineering & Structural Dynamics*, Vol. 5, No. 3, 1977, pp. 283–292. doi:10.1002/eqe.4290050306.

[162] Chung, J., and Hulbert, G. M., "A Time Integration Algorithm for Structural Dynamics With Improved Numerical Dissipation: The Generalized–α Method," *Journal of Applied Mechanics*, Vol. 60, No. 2, 1993, pp. 371–375. doi:10.1115/1.2900803.

[163] Dewalque, F., Rochus, P., and Brüls, O., "Importance of Structural Damping in the Dynamic Analysis of Compliant Deployable Structures," *Acta Astronautica*, Vol. 111, 2015, pp. 323–333. doi:10.1016/j.actaastro.2015.03.003.

[164] Kaviany, M., *Principles of Heat Transfer*, John Wiley & Sons, 2002, Chap. 1, pp. 24–32.

[165] Noor, A. K., and Burton, W. S., "Computational Models for High-Temperature Multilayered Composite Plates and Shells," *Applied Mechanics Reviews*, Vol. 45, No. 10, 1992, pp. 419–446.

[166] Argyris, J., and Tenek, L., "Recent Advances in Computational Thermostructural Analysis of Composite Plates and Shells With Strong Nonlinearities," *Applied Mechanics Reviews*, Vol. 50, No. 5, 1997, pp. 285–306.

[167] Bose, A., and Surana, K., "Piecewise Hierarchical P-Version Curved Shell Finite Element for Heat Conduction in Laminated Composites," *Computers & Structures*, Vol. 49, No. 2, 1993, pp. 283–300.

[168] Muliana, A. H., and Kim, J. S., "A Two-Scale Homogenization Framework for Nonlinear Effective Thermal Conductivity of Laminated Composites," *Acta Mechanica*, Vol. 212, No. 3-4, 2010, pp. 319–347.

[169] Lewis, R. W., Morgan, K., Thomas, H., and Seetharamu, K., *The Finite Element Method in Heat Transfer Analysis*, John Wiley & Sons, 1996, Chap. 1, pp. 13–28.

[170] Jaiman, R. K., Jiao, X., Geubelle, P. H., and Loth, E., "Conservative Load Transfer Along Curved Fluid–Solid Interface With Non–Matching Meshes," *Journal of Computational Physics*, Vol. 218, No. 1, 2006, pp. 372–397. doi:10.1016/j.jcp.2006.02.016.

[171] Khalil, H. K., *Nonlinear Systems*, Prentice-Hall, New Jersey, 1996.

[172] Verhulst, F., *Methods and Applications of Singular Perturbations: Boundary Layers and Multiple Timescale Dynamics*, Springer Science & Business Media, 2005, Vol. 50, Chap. 8, pp. 93–120.

[173] Huang, D., Rokita, T., and Friedmann, P. P., "Efficient Reduced-Order Modeling for Skin Panels in Hypersonic Flow and Its Application to Generating Aerothermoelastic Scaling Laws," *International Forum on Aeroelasticity and Structural Dynamics*, Como, Italy, 2017, pp. 1–29.

[174] Stewart, G. W., "A Krylov–Schur Algorithm for Large Eigenproblems," *SIAM Journal on Matrix Analysis and Applications*, Vol. 23, No. 3, 2002, pp. 601–614. doi:10.1137/s0895479800371529.

[175] Hernandez, V., Roman, J. E., and Vidal, V., "SLEPc: A Scalable and Flexible Toolkit for the Solution of Eigenvalue Problems," *ACM Trans. Math. Software*, Vol. 31, No. 3, 2005, pp. 351–362. doi:10.1145/1089014.1089019.

[176] Amestoy, P. R., Duff, I. S., Koster, J., and L'Excellent, J.-Y., "A Fully Asynchronous Multifrontal Solver Using Distributed Dynamic Scheduling," *SIAM Journal on Matrix Analysis and Applications*, Vol. 23, No. 1, 2001, pp. 15–41. doi:10.1137/s0895479899358194.

[177] Trefethen, L. N., and Bau III, D., *Numerical Linear Algebra*, SIAM, 1997, Vol. 50, Chap. 4, pp. 172–178. doi:10.1137/1.9780898719574.

[178] Saad, Y., *Iterative Methods for Sparse Linear Systems*, SIAM, 2003, Vol. 82, Chap. 9, pp. 261–282. doi:10.1137/1.9780898718003.

[179] Trussell, D. H., and Weidman, D. J., "A Radiant Heater to Simulate Aerodynamic Heating in a Wind Tunnel," Tech. Rep. NASA TN D–530, NASA Langley Research Center, Langley Field, VA, November 1960.

[180] Jones, D. R., Schonlau, M., and Welch, W. J., "Efficient Global Optimization of Expensive Black-Box Functions," *Journal of Global Optimization*, Vol. 13, No. 4, 1998, pp. 455–492.

[181] Goel, T., Vaidyanathan, R., Haftka, R. T., Shyy, W., Queipo, N. V., and Tucker, K., "Response Surface Approximation of Pareto Optimal Front in Multi-Objective Optimization," *Computer Methods in Applied Mechanics and Engineering*, Vol. 196, No. 4-6, 2007, pp. 879–893. doi:10.1016/j.cma.2006.07.010.

[182] Regis, R. G., "Constrained Optimization by Radial Basis Function Interpolation for High-Dimensional Expensive Black-Box Problems with Infeasible Initial Points," *Engineering Optimization*, Vol. 46, No. 2, 2014, pp. 218–243. doi: 10.1080/0305215X.2013.765000.

[183] Sasena, M. J., "Flexibility and Efficiency Enhancements for Constrained Global Design Optimization with Kriging Approximations," Ph.D. thesis, University of Michigan, Ann Arbor, 2002.

[184] Mockus, J., "Application of Bayesian Approach to Numerical Methods of Global and Stochastic Optimization," *Journal of Global Optimization*, Vol. 4, No. 4, 1994, pp. 347–365.

[185] Martinez-Cantin, R., "Bayesopt: A Bayesian Optimization Library for Nonlinear Optimization, Experimental Design and Bandits," *The Journal of Machine Learning Research*, Vol. 15, No. 1, 2014, pp. 3735–3739.

[186] Knowles, J., "ParEGO: A Hybrid Algorithm With Online Landscape Approximation for Expensive Multiobjective Optimization Problems," *IEEE Transactions on Evolutionary Computation*, Vol. 10, No. 1, 2006, pp. 50–66. doi:10.1109/TEVC.2005.851274.

[187] Emmerich, M., "Single-and multi-objective evolutionary design optimization assisted by gaussian random field metamodels," Ph.D. thesis, Universitt Dortmund, Dortmund, Germany, 2005. URL https://eldorado.tu-dortmund.de/bitstream/2003/21807/1/Doktorarbeitneu.pdf.

[188] Gelbart, M. A., "Constrained Bayesian Optimization and Applications," Ph.D. thesis, Harvard University, Graduate School of Arts & Sciences, Cambridge, MA, 2015.

[189] Kushner, H. J., "A New Method of Locating the Maximum Point of an Arbitrary Multipeak Curve in the Presence of Noise," *Journal of Basic Engineering*, Vol. 86, No. 1, 1964, pp. 97–106. doi:10.1115/1.3653121.

[190] Lizotte, D. J., "Practical Bayesian Optimization," Ph.D. thesis, University of Alberta, Edmonton, Alta., Canada, 2008.

[191] Cox, D. D., and John, S., "A Statistical Method for Global Optimization," *Systems, Man and Cybernetics, 1992., IEEE International Conference on*, IEEE, 1992, pp. 1241–1246. doi:10.1109/ICSMC.1992.271617.

[192] Brochu, E., Cora, V. M., and De Freitas, N., "A Tutorial on Bayesian Optimization of Expensive Cost Functions, with Application to Active User Modeling and Hierarchical Reinforcement Learning," *arXiv preprint arXiv:1012.2599*, 2010.

[193] Emmerich, M., and Klinkenberg, J.-w., "The Computation of the Expected Improvement in Dominated Hypervolume of Pareto Front Approximations," Tech. Rep. LIACS-TR 9-2008, Rapport Technique, Leiden University, The Netherlands, 2008.

[194] Ponweiser, W., Wagner, T., Biermann, D., and Vincze, M., "Multiobjective Optimization on a Limited Budget of Evaluations Using Model-Assisted S-Metric Selection," *International Conference on Parallel Problem Solving from Nature*, Vol. 5199, Springer, Berlin, Heidelberg, 2008, pp. 784–794. doi:10.1007/978-3-540-87700-4_78.

[195] Couckuyt, I., Deschrijver, D., and Dhaene, T., "Fast Calculation of Multiobjective Probability of Improvement and Expected Improvement Criteria for Pareto Optimization," *Journal of Global Optimization*, Vol. 60, No. 3, 2014, pp. 575–594. doi:10.1007/s10898-013-0118-2.

[196] Hupkens, I., Deutz, A., Yang, K., and Emmerich, M., "Faster Exact Algorithms for Computing Expected Hypervolume Improvement," *International Conference on Evolutionary Multi-Criterion Optimization*, Springer, 2015, pp. 65–79. doi:10.1007/978-3-319-15892-15.

[197] Deb, K., Pratap, A., Agarwal, S., and Meyarivan, T., "A Fast and Elitist Multiobjective Genetic Algorithm: NSGA-II," *IEEE Transactions on Evolutionary Computation*, Vol. 6, No. 2, 2002, pp. 182–197. doi:10.1109/4235.996017.

[198] Zitzler, E., Laumanns, M., and Thiele, L., "SPEA2: Improving the Strength Pareto Evolutionary Algorithm," Tech. Rep. TIK-Report 103, Eidgenössische Technische Hochschule Zürich (ETH), Institut für Technische Informatik und Kommunikationsnetze (TIK), 2001. URL 10.3929/ethz-a-004284029.

[199] Pedregosa, F., Varoquaux, G., Gramfort, A., Michel, V., Thirion, B., Grisel, O., Blondel, M., Prettenhofer, P., Weiss, R., Dubourg, V., Vanderplas, J., Passos, A., Cournapeau, D., Brucher, M., Perrot, M., and Duchesnay, E., "Scikit-Learn: Machine Learning in Python," *Journal of Machine Learning Research*, Vol. 12, 2011, pp. 2825–2830.

[200] Jones, D. R., "The DIRECT Global Optimization Algorithm," *Encyclopedia of Optimization*, Springer, 2001, pp. 431–440.

[201] Jones, E., Oliphant, T., Peterson, P., et al., "SciPy: Open Source Scientific Tools for Python," http://www.scipy.org/, 2001–.

[202] LaFontaine, J. H., Gogulapati, A., Miller, B. A., and McNamara, J. J., "Effects of Strain Hardening on Fluid–Thermal–Structural Interactions," *AIAA Paper 2015–1629, 56th AIAA/ASCE/AHS/ASC Structures, Structural Dynamics, and Materials Conference*, Kissimmee, FL, 2015, pp. 1–17. doi:10.2514/2015-1629.

[203] Gibson, L. J., and Ashby, M. F., *The Mechanics of Honeycombs*, Cambridge University Press, 1999, Chap. 4, pp. 69–119. doi:10.1017/cbo9781139878326.006.

[204] U.S. Department of Defence, *Military Handbook, MIL–HDBK–5J: Metallic Materials and Elements for Aerospace Vehicle Structures*, U.S. Department of Defence, 1998, Chap. 5, pp. 43–50.

[205] Swann, R. T., and Pittman, C. M., "Analysis of Effective Thermal Conductivities of Honeycomb-Core and Corrugated-Core Sandwich Panels," Tech. Rep. TN D-714, NASA, 1961.

[206] Altman, N. S., "An Introduction to Kernel and Nearest-Neighbor Nonparametric Regression," *The American Statistician*, Vol. 46, No. 3, 1992, pp. 175–185. doi: 10.2307/2685209.

[207] Karypis, G., and Kumar, V., "A Fast and High Quality Multilevel Scheme for Partitioning Irregular Graphs," *SIAM Journal on Scientific Computing*, Vol. 20, No. 1, 1998, pp. 359–392. doi:10.1137/s1064827595287997.